

A Tight Binding Study of Dislocations in Iron and Their Interaction with Hydrogen

Edmund Luke Simpson

Department of Physics

King's College London

A thesis submitted in partial fulfilment of the requirements for the
degree of Doctor of Philosophy.

December 2018

Abstract

At low temperatures, the plastic deformation of body centred cubic (BCC) iron is governed by the motion of screw dislocations. In order to understand the effect of hydrogen on the mechanical properties of iron, it is then crucial to extend the understanding of its influence on screw dislocation mobility. The work carried out during this study was to provide both the data and the machinery required for large-scale simulations of hydrogen in iron, primarily with a view to further specify a kinetic Monte Carlo (kMC) model of screw dislocation motion in the presence of hydrogen. The extensions envisaged for the kMC model were to include the process of vacancy emission by the climb of jog segments, which could account for the increase in lattice vacancies after plastic deformation with hydrogen, and to describe the regions of high strain around a crack-tip, where the effect of hydrogen will be most significant. All of this work was carried out with methods based upon the Tight Binding Hamiltonian, making use of both the large scale achievable with the Bond Order Potential (BOP) and the accuracy of direct diagonalisation.

First, a set of parameters, originally fit for use within direct diagonalisation Tight Binding, are tested within the BOP; the results from dislocation simulations are close to values from *ab-initio* models in the literature and the structures involved generally match well with those found by employing a well-established BOP model for the same simulations. These parameters are then used within BOP for Nudged Elastic Band (NEB) simulations of edge dislocation climb, finding that the barrier for vacancy emission depends both on the orientation of the path and the edge core structure. In an attempt to decrease the dependence of this kMC model on results from the literature, single kinks on screw dislocations are then simulated, with the idea of calculating kink-pair formation rates; however, these structures are found to require a scale beyond that attainable with this BOP model.

Direct diagonalisation Tight Binding is then employed to calculate the variation of the hydrogen binding to screw dislocations with tensile and compressive strains. The locations and binding energies of the hydrogen trap-sites surrounding the unstrained

core are shown to be of a similar accuracy to previous *ab-initio* results. Estimations of the hydrogen effect in these regions are then made based on the mechanics of the defactant model; finding that the effects of enhanced kink-pair nucleation and solute-drag on kinks will be greatly enhanced in tensile regions. The chance of hardening by the collision of crossed-kinks, to form a jog, is estimated by comparing the nucleation and annihilation rate of kinks on a straight screw dislocation for a range of hydrogen concentrations and temperatures, generally observing a greatly increased incidence with tension that was accentuated at lower temperatures. These results represent almost all the data required to extend the kMC model to these strained regions; however, NEB simulations of the Peierls barrier indicate that the kink-pair nucleation rate should vary significantly with strain, and so must be calculated before these results can be included. The diffusion barriers between these trap-sites are also calculated with NEB across the range of strains; finding that the jump rate between sites is orders of magnitude lower than between bulk sites and hydrogen is too unstable in the screw core for the "pipe-diffusion" mechanism, or accelerated diffusion along the dislocation line, to have much effect.

An attempt was then made to implement a method that would allow the simulation of hydrogen in iron at a scale and accuracy not previously realised with Tight Binding methods. This method involves seamlessly embedding a region described with direct diagonalisation Tight Binding within another described with the Bond Order Potential, allowing accurate simulations of a small portion of the cell coupled to a large, surrounding area for stress dissipation. It was found that the disparity between the parameter set used by the Bond Order Potential and that required for the description of hydrogen in iron was too great, resulting in unbalanced forces at the interface and electronic disturbances that permeate the inner region. If a consistent basis set is used throughout the cell, however, the inner region converges to results from a full direct diagonalisation simulation within a short distance of the interface. This method will then be invaluable in the future for large-scale simulations of problems in which a similar basis set may be used throughout.

List of Abbreviations

appm	Atomic Parts Per Million
CI	Climbing Image
PES	Potential Energy Surface
MEP	Minimum Energy Path
DFT	Density Functional Theory
TB	Tight Binding
BOP	Bond Order Potential
b	Burgers vector
GGA	Generalised Gradient Approximation
LDA	Local Density Approximation
QM/MM	Quantum Mechanics/Molecular Mechanics
DD	Direct Diagonalisation
ECC	Easy Core Configuration
HCC	Hard Core Configuration
MD	Molecular Dynamics
GF	Green Function
MRSSP	Maximum Resolved Shear Stress Plane
LSDA	Local Spin Density Approximation
PBC	Periodic Boundary Conditions
GFBC	Green Function Boundary Conditions
NEB	Nudged Elastic Band
GB	Grain Boundary
BCC	Body Centred Cubic
kMC	kinetic Monte Carlo
EAM	Embedded Atom Method
FS	Finnis-Sinclair
ZPE	Zero Point Energy

Table of contents

Abstract	1
Table of contents	4
List of figures	6
List of tables	9
1 Introduction	10
1.1 Dislocations in Iron	10
1.2 Defect Modelling Schemes	13
1.3 Hydrogen Embrittlement of Metals	17
1.4 Overview and Objectives	24
2 Theory	27
2.1 Dislocations	27
2.2 Electronic Structure Methods	32
2.2.1 Tight Binding	32
2.2.2 Bond Order Potential	43
2.2.3 Self-Consistency	50
3 Preliminary Dislocation Calculations	56
3.1 Introduction	56
3.2 Methods	58
3.3 Screw Dislocations	63
3.4 Edge Dislocations	78
3.5 Conclusions	95

Table of contents

4 Screw Dislocation Kink Structures	100
4.1 Introduction	100
4.2 Results and Discussion	103
4.3 Conclusion	109
5 Including Broyden Mixing	112
5.1 Introduction	112
5.2 Schemes	113
5.3 Results & Discussion	115
5.4 Conclusion	116
6 Hydrogen Interactions With Screw Dislocations	118
6.1 Introduction	118
6.2 Methods	120
6.3 Results and Discussion	124
6.3.1 Unstrained Case	124
6.3.2 Effects of Strain	127
6.3.3 Hydrogen Diffusion Around a Screw Core	145
6.4 Conclusion	150
7 Embedding a Self-Consistent Tight Binding Cluster Within Bond Order Potential	156
7.1 Introduction	156
7.2 Implementations	159
7.3 Simulation Details	162
7.4 Results & Discussion	164
7.4.1 Preliminary Tests	164
7.4.2 Hydrogen Solution Energy	177
7.5 Conclusions	180
8 Conclusion	183

List of figures

2.1	Burgers circuits for edge and screw dislocations	29
2.2	Dislocation responses to stress	31
2.3	Possible bond integrals formed between s , p and d orbitals	35
3.1	Differential displacement plot of screw dislocation quadrupole	64
3.2	Magnetic moment distribution around screw dislocation quadrupole . .	65
3.3	Peierls barrier for screw dislocation	67
3.4	Screw dislocation core trajectory during Peierls transition	69
3.5	Path of isolated screw dislocations under simple shear stress	72
3.6	Common forms of the $\Sigma 3\{112\}$ grain boundary	75
3.7	Screw dislocation interaction with $\Sigma 3(112)$ grain boundary under applied simple shear stress	76
3.8	Differential displacement plots of Paxton screw transmission through $\Sigma 3(112)$ grain boundary	77
3.9	Differential displacement plot of $\Sigma 3(112)$ grain boundary structure after screw dissociation for both parameter sets	78
3.10	Edge dislocation simulation cells	79
3.11	Displacement functions and differential displacements for atoms around $\frac{a}{2}\{112\}$ edge dislocation	80
3.12	Displacement functions and differential displacements for atoms around $\frac{a}{2}\{110\}$ edge dislocation	82
3.13	Interaction energy between vacancies	84
3.14	Interaction energy between a vacancy and an edge dislocation	87
3.15	Variation with cell radius in interaction energies between an edge dislocation and a vacancy or an interstitial	89
3.16	Variation with cell length in interaction energy between an edge dislocation and an interstitial	89

List of figures

3.17 Initial and final images from NEB simulations of $\frac{a}{2}\langle 111 \rangle\{112\}$ edge dislocation climb	93
3.18 Barriers for vacancy migrations associated with climb	94
3.19 Vacancy migration barriers in bulk lattice	94
4.1 Kink core structures	105
4.2 Kink formation energy against cell length and radius	105
4.3 Atomic columns used to estimate kink width	106
4.4 Graphical representation of kink structures	107
4.5 Change in bond length for $\langle 111 \rangle$ column of atoms along kink core	109
6.1 Trap sites around screw core	121
6.2 Variation of H - Screw binding energy with strain	129
6.3 Critical temperatures for significant kink-pair nucleation enhancement .	131
6.4 Lower critical shear stresses required to escape H-kink trapping for several bulk concentrations	133
6.5 Lower critical shear stresses required to escape H-kink trapping against strain	134
6.6 Variation of hydrogen kink trapping energy with effective shear stress .	136
6.7 Average kink velocity with effective shear, strain and hydrogen content	138
6.8 Kink-pair nucleation rate over kink annihilation rate for several hydrogen concentrations and temperatures against strain	143
6.9 Screw Peierls barrier at several strains	144
6.10 Variation of screw core energy difference with strain	145
6.11 Hydrogen transition barriers between sites at several strains	147
6.12 Hydrogen pipe diffusion path through screw core	148
6.13 Barriers for hydrogen pipe diffusion	149
7.1 Speed-up of embedding calculations after parallelisation with increased processor number	164
7.2 Phonon dispersion and density of states from direct diagonalisation and Bond Order Potential	166
7.3 Energy gradients and forces on displaced atoms from embedding models	169
7.4 Cell used for force comparisons between the embedding implementations, BOP and SCTB	170

List of figures

7.5 A comparison of the forces from <i>d</i> -orthogonal embedding, BOP and <i>d</i> -orthogonal SCTB DD	171
7.6 A comparison of the atomic charge in the DD portion of a fully <i>d</i> -orthogonal embedding cell and <i>d</i> -orthogonal SCTB	172
7.7 A comparison of the forces from <i>sd</i> -nonorthogonal embedding, BOP and <i>sd</i> -nonorthogonal SCTB DD	173
7.8 A comparison of the forces from <i>sd</i> -nonorthogonal embedding, BOP and <i>sd</i> -nonorthogonal SCTB DD	174
7.9 Average atomic charges from <i>sd</i> -nonorthogonal embedding models and Tight Binding	175
7.10 A comparison of the forces from a embedding with a fully <i>sd</i> -nonorthogonal cluster, BOP and <i>sd</i> -nonorthogonal SCTB	176
7.11 Force and energy gradients with atom displacement in embedding cell with fully <i>sd</i> -nonorthogonal cluster	177
7.12 Calculated hydrogen solution energy against embedded region size	178
7.13 Average atomic charges sorted by distance from centre of embedded cluster	179

List of tables

3.1	Sequential binding energies of vacancies to an edge dislocation	91
5.1	Comparison of Broyden and Anderson mixing schemes	116
6.1	Trap sites around screw dislocations	125
6.2	Binding energy of two hydrogen atoms to a screw dislocation.	126
6.3	Binding energy of three hydrogen atoms to a screw dislocation.	126
6.4	Hydrogen barriers and jump frequencies between sites at several strains	148
6.5	Barriers and jump frequencies for hydrogen pipe diffusion along an ECC screw	150

Chapter 1

Introduction

1.1 Dislocations in Iron

Due to the abundance of iron ore, its relatively simple refinement process, strength and the low temperatures at which it may be formed, iron has been an important structural material for humanity for thousands of years. However, a valid description of the plasticity in iron, and indeed all BCC materials, came much later than that for FCC or HCP structures. The first systematic experimental measurements of plastic flow were carried out in FCC crystals, finding that deformation generally occurred by the sliding of the the most widely spaced close-packed atomic planes, or $\{111\}$, in the direction of the densest atomic packing, or $\langle 110 \rangle$ [1]. Analysis of these results, along with further tests in HCP crystals, led to the formulation of the Schmid law that dictated the conditions for the onset of slip[2]. There are two parts to this law: first, that a given slip system, defined by the direction of slip and the slip plane, will become active when the resolved shear stress on that system reaches a critical value, known as the Critical Resolved Shear Stress (CRSS); and second, that this CRSS is a constant, independent of the sense of slip, the system involved or any elements of the stress tensor that do not give rise to stresses on this system.

However, it was already known that BCC materials did not deform in the same way as FCC: studies of α -iron[3] and β -brass[4] showed significant deviations from this law. Although these materials were also found to deform by the sliding of atomic planes parallel to the direction of closest atomic packing, $\langle 111 \rangle$, the slip plane was not well defined. Furthermore, the CRSS varied both with the loading orientation and between tension and compression, a property known as "tension/compression asymmetry". It was found in later deformation tests that the CRSS for BCC materials also changed

with the sense of stress[5–8], known as "twinning/anti-twinning asymmetry". These deviations from Schmid law, along with the much lower levels of ductility observed in BCC materials, implied a fundamental difference in the deformation mechanisms. The asymmetries could be explained by details of the BCC crystal lattice[9], but the low ductility and ill-defined slip planes observed could only be explained by the variation in dislocation structure.

The concept of dislocations did not originate as a crystal defect, but rather as an abstract mathematical formulation used to consider the properties of singularities by performing cuts and displacements in a continuous solid body[10]. These defects were proposed to be the carriers of plastic deformation in crystals, allowing planes of atoms to slide over each other gradually; their existence was later confirmed with Transmission Electron Microscopy[11–14]. According to *Neumann's* principle[15] any kind of symmetry possessed by the crystal structure of a material will also be possessed by any physical property of that material. Dislocations in BCC materials with their line along the direction of closest atomic packing, or $\langle 111 \rangle$, would then have the same three-fold screw symmetry as the crystal does along that axis. It was realised by *Hirsch*[16] that this could imply that the screw dislocation core spreads into several of the planes intersecting this axis, so that the core must be changed from this low-energy sessile form into a high-energy glissile form before it could glide on a plane. This structure was confirmed with the first atomistic simulations of the screw core, carried out with simple pair potentials; however, they also predicted that it had two energetically degenerate forms, related by the $\langle 110 \rangle$ diad[17–19]. Later, more sophisticated models found that screw dislocations in BCC metals generally also possess this diad symmetry, and so only have one, non-degenerate form[20–22]. This non-planar core provided a good explanation of both the low ductility of BCC metals, as this will be determined by the dislocation segments with the lowest mobility, and the fact that the slip plane could change easily. It was found that stresses other than those parallel to the slip direction would have effects on the core structure, leading to variation in the CRSS and preferred slip direction[23, 24]. In contrast, the relatively low stacking fault energy in most FCC metals means that the dislocations can dissociate into partials on the close packed planes, so that they have a planar character and move at lower applied stresses on a well-defined plane. Experimentally, no stable stacking faults have been found in the BCC lattice, and it was shown with atomistic calculations that they are unlikely to exist[25–27].

It became clear that the behaviour of dislocations was primarily determined by

Introduction

their core structure. Unfortunately, while linear elasticity theory may provide a good description of the dislocation stress field far from the core, it is not applicable to the large displacements within the core itself. This problem was first tackled by *Peierls*[28]: by employing a model that combined elements of atomistic and elastic descriptions of the dislocation core he was able to perform the first detailed calculation of the resolved shear stress required to move a straight dislocation through a crystal in the absence of thermal fluctuations. This stress was then known as the Peierls stress, and the associated energetic barrier the Peierls barrier. This model was later improved by *Nabarro*[29] and *Eshelby*[30]; it basically consisted of describing the core of a planar dislocation as the balance between the distribution of the compression along the glide plane and the disregistry of atoms on either side of this plane. The energy may then be obtained as a sum of the elastic energies of the blocks on either side of the glide plane and an approximation to the misfit energies across it. Rigid shifts of the distribution of compression will provide the energy as a function of the dislocation core position along the glide plane, and the Peierls stress will be the maximum gradient of this energy.

Shockley[31] considered that these dislocations needn't remain as straight lines, but that the activation energy for dislocation movement could be greatly reduced if they had steps, sections of the line for which slip had proceeded further than the rest of the line. The short segments of the dislocation line lying across the Peierls barrier were known as kinks, and were predicted to have a low enough formation energy to exist on the line in thermal equilibrium. Motion of the kinks along the dislocation line could then move more of the line into the next Peierls valley, reducing the energy for the process analogously to how dislocations reduced the energy for atomic planes to slide over each other. The nucleation of a kink-pair is a thermally activated process, fluctuations in the dislocation line throwing a length over to the next Peierls valley, and this process was later applied to explain the strong temperature dependence of the flow stress observed in BCC materials[32].

This dependence had been observed for a number of BCC materials[8, 33, 34] by employing a procedure developed by *Cottrell and Stokes*[35]. Essentially this consisted of applying stress to the sample to establish the deformation at one temperature, halting it and resuming at a lower temperature. The results for BCC materials uniformly showed the existence of a "knee temperature", below which the flow and yield stresses increased sharply with further cooling; above this temperature the dependence was weak. These results could be well explained if the ductility were dependent on a

thermally activated process; it is now generally accepted that, for finite temperature and stresses below the Peierls stress, screw dislocations in BCC metals move by the repeated nucleation of kink-pairs.

1.2 Defect Modelling Schemes

It is clear then that the movement of dislocations in the lattice is intimately related to the details of bond breaking and formation at the core. The energetics of the dislocation translation is primarily determined by the displacement of these core atoms due to the highly non-linear character of their interactions. This has meant that atomistic calculations have been critical to extending the understanding of plastic deformation, ranging from calculations of the small number of atoms directly surrounding the dislocation core to the interaction and evolution of huge ensembles of dislocations.

Simulation techniques may be broadly divided by whether or not they are dynamic; that is, whether or not they provide a physically-meaningful path for the system on its way to equilibrium. Dynamic methods, such as Molecular Dynamics (MD), provide an approximation to this path; they give a phase space trajectory for the system toward thermal dynamic equilibrium at finite temperature. This enables the measurement of dislocation mobility in a way that is otherwise impossible: experimental measurement of the velocity of individual dislocations may be difficult, but observation of the atomistic processes involved is far beyond current capabilities. Molecular Dynamics may also be employed as a relaxation method, avoiding metastable minima, or to determine equilibrium properties by sampling from a statistical mechanical ensemble. Temperature may be included, by sampling the initial atomic velocities randomly from the Maxwell-Boltzmann distribution, and maintained with some thermostat procedure. The system is allowed to evolve according to Newton's equations of motion; some method will be required to numerically integrate these equations, with an accuracy that will be determined by the time-step chosen. This numerical integration is a computationally heavy step and so either limits the description of the interactions to simplistic models or the simulation to small systems. Furthermore, for many simulations the required time-step is so small that simulation of large time-scales would be prohibitively expensive. The limitation to a short time-scale makes simulation of rare events difficult and often means that non-physical strain rates must be employed in deformation studies.

Another common dynamic method is Discrete Dislocation Dynamics, which can

provide a mesoscopic description of the evolution of dislocation microstructure. Crystallographic and elastic properties of the lattice must be specified, as well as a range of dislocation characteristics like the character-dependent mobility and core energy[36]. Straight segments of the dislocations are characterised by the relative orientation between the line and Burgers vector; forces between them are then determined within elasticity theory. Additional core forces, determined by the variation of the core energy between each dislocation type, may also be included. The velocity of each segment will then be determined by the mobilities provided, possibly including a full description for each type and, in the more sophisticated models, the non-conservative motion of dislocations out of their glide planes, known as climb. Temperature may be included with temperature-dependent drag effects on the mobilities and appropriate probability dependent waiting times for the thermally activated processes[37]. This model requires extensive atomistic simulation to fully specify the dislocations but, provided these characteristics are correct, it can provide an invaluable tool to both interpret the origins of experimentally observed microstructures and approximate their variation with a finely controlled environment.

On the other hand, Molecular Statics and Monte Carlo simulations provide a physically-meaningful equilibrium state but the transient intermediate states are not necessarily close to the pathway the system would take. Monte Carlo is a generic term for an algorithm based on random sampling; a sub-set known as Kinetic Monte Carlo models sample processes based upon their rates. The accuracy of these models is dependent on the fact that all possible processes are included in this sampling, so that the method is ergodic. Again, atomistic simulations are commonly employed to obtain these rates, or at least the energetic barriers for an event to occur, the rate may then be obtained from transition state theory[38]. A vast number of these calculations are then generally required to fully specify a kinetic Monte Carlo model.

Molecular Statics simulations are based upon finding the equilibrium state of the system at a temperature of zero degrees Kelvin. Some description of the interaction energies and forces is required, an optimisation algorithm will then be employed to minimise these forces so that the system reaches an energy minimum. The optimal method employed to calculate these interactions will depend on the problem at hand: simple models will be able to simulate large areas of the lattice but will be limited in the structures and materials they can accurately describe. Conversely first-principles models, such as Density Functional Theory, are able to simulate a large range of structures and interactions, providing a truly quantum-mechanical description, but

are limited in their scale.

Some of the simplest models used in these calculations are empirical potentials, generally produced by selecting some functional form and adjusting their parameters to reproduce *ab-initio* or experimental data, such as the energies of various structures or elastic coefficients. This essentially equates to "integrating out" the electronic degrees of freedom so that the effects of complex electronic phenomena, such as charge transfer and bond formation, is hoped to be contained within the fitting of this function[39]. Due to the simplicity of this approach, huge numbers of atoms can be simulated efficiently and the origin of structural features easily interpreted; the analytic form of the potential also confers advantages in MD from the ease of integration. The reliability of these potentials may be improved by including more terms in these interactions, such as three and four-body terms, but it is still difficult to determine how applicable they are to situations beyond those included in their fitting[40]. Furthermore, systems in which these electronic effects become important are generally not well described by these potentials[41].

The Embedded Atom Model and Finnis-Sinclair are more advanced interatomic potentials, including many-body interactions in that the interaction between any two atoms depends also on their surrounding neighbours. The EAM is made up of a pair-potential and a term that represents the energy required to embed each atom into an environment with the same local electronic density as at its site; the form of this density term will differ depending on the details of the model. The FS model also includes a pair potential term, but the second term is deduced from the second-moment approximation to the density of states in the Tight Binding method, described below. The density of states defines the number of states in a given interval of energy, and each moment will describe a further property of its distribution. The first two moments will include a description of the width and centre of gravity, and so these methods make an approximation that the energetics of the material described are not greatly affected by any finer detail. Both of these models have been successfully applied to dislocation studies in the past and, importantly, both now routinely predict the same non-degenerate core structure for screw dislocations in BCC metals as found with *ab-initio* methods[21, 24, 42].

Among the more accurate methods, a particularly common one is *Kohn-Sham* Density Functional Theory, a collection of accurate and fully quantum-mechanical *ab-initio* models that provide a reliable description of atomic interactions[43]. In very basic terms, these models consist of constructing an energy functional of the electron

density for a non-interacting system of electrons and variationally minimising it to obtain the ground state density; an effective potential is included in the functional to represent the other electrons and nuclei. This procedure is justified by the *Hohenberg-Kohn* theorems which state that the total energy of the system is a unique functional of the electron density, and that the density that minimises this functional is the exact ground state density[44]. The models differ in how they approximate the exchange-correlation energy from electron interactions: the most simple is the Local Density Approximation (LDA) in which these terms are approximated with those calculated for a homogeneous electron gas with the same density as that seen by each electron, while the Generalised Gradient Approximation (GGA) is a more sophisticated method that also includes the gradients of the density.

An issue with these methods is the limitation to small system sizes: advances in computational resources have allowed the simulation of up to 10^5 atoms, but the incredible computational expense involved limits most defect simulations to a few hundred. In general, this is only large enough to simulate the most ordered of structures; which can still be indispensable for the calculation of the basic properties of materials and the parameterisation of more coarse-grained models. The group of *Ventelon* tackled this problem by arranging screw dislocations in a periodic array, first quantifying the errors of such an arrangement[45] and then employing the cells to calculate the Peierls surfaces for a screw dislocations in a range of BCC materials[46, 47]. Perhaps a more flexible method is to employ DFT to simulate a small number of atoms around the defect core, and include the effect of the surrounding lattice with some other model; this allows the simulation of isolated defects and has been employed successfully by many groups to simulate screw[48, 49] and edge[50] dislocations in BCC iron.

The empirical Tight Binding model lies somewhere between these methods in terms of accuracy, although closer to DFT than the interatomic potentials: the atomic interactions are still parameterised but are done so in a way that preserves their quantum-mechanical nature. Instead of rigorously calculating them from the basis set and Hamiltonian operator, the matrix elements of the Hamiltonian are constructed from a set of parameterised bond integrals, dependent on bond angle and length. These bond integrals, as well as a repulsive pair-potential term, will require an extensive fitting strategy; the accuracy and reliability of the method will depend on this step. The flexibility of this method and the basis in quantum-mechanics has enabled accurate approximations to atomic polarisation[51], magnetism[52] and many other electronic phenomena. These models have been utilised to describe cases as diverse as the phases

of water[53] and electric currents in nanostructures[54]. The simplicity of these models also lends an ease of interpretation to processes like bond formation and breaking that may be obscured in more complex or extensively parameterised models.

The Bond Order Potential method[55–57] is based on a moments-expansion of empirical Tight Binding, constructing an approximation to the density of states from the Hamiltonian matrix elements. This basis in TB means that it contains a correct description of bonding, while avoiding the computationally heavy step of diagonalising the Hamiltonian. The moments are calculated from the local atomic environment, so can be calculated independently for each atom and scale linearly with system size. A Bond Order Potential for iron has been able to incorporate ferromagnetism[58], and was found to reproduce DFT results well[59]. Although these models lose some of the accuracy of full direct diagonalisation TB, generally limited to Local Charge Neutrality self-consistency and orthogonal basis states, their simplicity and scaling has meant that they can simulate defects at a much greater scale.

1.3 Hydrogen Embrittlement of Metals

Hydrogen embrittlement is an umbrella term referring to the deleterious effects of hydrogen in the lattice: degradation of mechanical properties such as strength, ductility and toughness. The ubiquity of hydrogen, along with the wide range of metallic structures in which these effects are significant, means that hydrogen-induced catastrophic damage of structural components is a common problem for industry. Ingress is likely to occur during manufacturing, application of coatings through electrochemical means, cleaning with harsh chemicals or simply during the structure's working lifetime. Hydrogen's small mass leads to a host of complications in both experiment and simulation: it has one of the highest atomic diffusivities in metals, and will exhibit strong quantum-mechanical effects at low temperature, meaning that classical treatments may not be appropriate[60]. Furthermore, it is almost impossible to image with standard experimental techniques, such as electron or x-ray diffraction or Transmission Electron Microscopy. Generally, experimental observations are not then of hydrogen itself, but of the effects it has on the lattice; these include the observations of the effect on yield stresses, dislocation velocity and so on. The results of these experiments require interpretation that can only be provided with atomistic simulation.

The effects of hydrogen embrittlement were first recorded in a scientific paper in 1875 by *Johnson*[61], who observed the changes in strength and ductility in samples

Introduction

of iron and steel after immersion in hydrochloric or sulphuric acid. Since then, there has been a proliferation of theories to explain the effects of hydrogen but the multiple time and length scales involved has meant that no one theory satisfactorily encompasses them all. It is more likely that a number of mechanisms are active at any one time, depending on the hydrogen concentration, temperature, strain-rate, stress and of course the properties and fabrication processes of the material in question.

One of the first theories was Hydrogen Induced Decohesion (HID); it is postulated to occur due to the weakening of bonds in the presence of hydrogen, resulting in the brittle failure of the lattice. Hydrogen tends to follow the stress gradient in the lattice and so it would accumulate in stressed regions, such as crack tips, where failure is likely to occur. This was originally proposed to explain the reduced tensile strength of iron samples, showing brittle fracture across intercrystalline boundaries or interatomic planes[62]. Later, it was explained by *Oriani*[63] from a consideration of the reduction of surface free energy of iron by hydrogen, and the relation between that and the cohesive energy of the lattice, implying that hydrogen reduces the average cohesive force between iron atoms. Supporting evidence came from two experiments by *Vehoff and Neumann*[64] and *Vehoff and Rothe*[65] in which the crack-tip opening angle in single crystals of Fe-2.6wt.% Si and nickel with applied tension were related to the hydrogen concentration. The samples being composed of single crystals meant that the mechanism of crack advance was the same along its length, and the samples were carefully prepared such that the stress was confined to a small area in front of the crack tip. With in-situ SEM observations they could determine the crack tip opening angle, and later examine the fracture surface. They found that in vacuum the crack-tip would blunt by the emission of dislocations, but in the presence of hydrogen it remained sharp and was always along a cleavage plane; this led them to conclude that failure occurred by the weakening of bonds.

Evidence of this effect has been found in simulation: *Du et al.*[66] employed GGA-DFT to simulate the binding energy of hydrogen to trap sites in a number of close-packed and open structure grain boundaries in both ferritic and austenitic iron. A number of both types were found to provide favourable traps for hydrogen. They calculated the energies of the free surfaces that would form if the grain boundaries were to separate, along with the binding energy of hydrogen to these surfaces. *Griffith's* criterion[67] provides an estimate of the critical stress required for fracture based on the surface energy of the crack that would be formed. The decrease to the surface energy with hydrogen was calculated in each case and used to estimate the reduction in

the critical stress. For all the grain boundaries that provided favourable binding sites, they found significant reductions in the critical stress. This decrease was the largest for cases with the largest difference in binding energies between the grain boundary and free surface. The effect was also seen to increase with hydrogen coverage.

The process of cleavage was simulated by *Katzarov and Paxton*[68], employing Tight Binding to find the variation of the hydrogen binding sites and cohesive strength of iron across a (111) plane as it was separated. They calculated the hydrogen binding energy to sites on this plane at different applied strains and for a range of different configurations, then calculated the chemical potential of the hydrogen in these configurations and used it to obtain the rate of diffusion to the surface from the bulk. The binding energy of the cell at each applied stress was defined as the difference between the total energy of the supercell with a cleavage zone and that of an equivalent supercell that was homogeneously stretched with no cleavage. The derivative of this binding energy with respect to the opening of the cleavage zone then provided traction curves, the maximum of which could be identified as the critical stress for rupture. They estimated that the ideal cohesive strength of α -Fe could be reduced from 30GPa to 22GPa by the introduction of hydrogen, which would represent a significant reduction in the plastic work of fracture.

McEniry et al.[69] carried out *ab-initio* simulations of cleavage across the interphase boundary between ferrite and cementite, which would occur abundantly in high-carbon steel. Strong hydrogen trapping sites were found, along with much stronger sites on either free surface; again this implies that hydrogen would lower the thermodynamic stability of the structure. Tensile strain was then incrementally applied normal to the surface until it separated, with varying amounts of hydrogen at the interface. The tensile strain required for rupture was found to decrease by $\sim 15\%$ with full hydrogen coverage, indicating that the dilatation of hydrogen also has an effect on the decohesion. The chemical potential of hydrogen for these sites was again calculated and used to obtain the relative concentration of hydrogen in these sites to the bulk, they concluded that these effects would be significant even for low bulk concentrations.

A recent theory, the Hydrogen Enhanced Stress Induced Vacancy (HESIV) model, is based upon the formation and agglomeration of vacancies being more favourable in the presence of hydrogen rather than a direct effect of hydrogen itself. These excess vacancies are stabilised and have their mobility reduced by forming complexes with hydrogen, and so form clusters that lead to failure at a lower stress. It was proposed by

Nagumo[70] in response to a number of experiments that evidenced increased vacancy concentrations after straining in the presence of hydrogen, observed with Thermal Desorption Analysis and Positron Annihilation Spectroscopy[71]. Thermal Desorption Analysis (TDA) involves heating a hydrogen charged specimen at a constant rate and measuring the rate at which hydrogen is degassed; both the amount of hydrogen released and the temperatures at which the peak rates occur can provide information on the hydrogen trapping. However, attributing a peak to a specific trap is indirect: the temperature at which these peaks occur will be increased both with trap depth and density, and the size of the specimen can also have an effect. A more direct method is Positron Annihilation Spectroscopy (PAS), in which positrons are introduced into the sample and the γ -rays emitted, given off when they annihilate with electrons, are analysed. The lifetime of these positrons will depend on their path through the lattice; those that encounter vacancies will have a particularly long lifetime due to the low electron density. Further analysis of the lifetime spectrum can reveal more of the nature of the defects in the lattice[72]. These increases in vacancy concentrations with plastic strain in hydrogen have been found by a number of groups using these methods[73–76]. *Takai et al.* [74] carried out TDA along with other tests on iron and a nickel-based alloy that showed these effects more directly: they applied strain to hydrogen charged and uncharged samples, allowed hydrogen to diffuse out of the samples and then tested them to fracture. They found that the charged samples had significant reductions in fracture strength even though their hydrogen content was similar to the uncharged ones, implying that the effects of hydrogen on the microstructure had already occurred. The strength of the samples could be almost completely recovered by annealing out the defects at 200°C, which implied that the effects were caused by vacancy-type defects.

Hydrogen Enhanced Localised Plasticity (HELP) is another of the most widely accepted theories; the first form of it was proposed by *Beachem*[77] from the observation of ductile features on fracture surfaces. He theorised that hydrogen in front of a crack tip aided in deformation mechanisms in that region. Evidence for hydrogen enhancing the mobility of dislocations came from in-situ TEM observations of deformation tests carried out within an environmental cell[78–80]; these tests involved observing the effect of hydrogen introduction on either the velocity of moving dislocations at a constant strain rate or stationary dislocations at a constant strain. The results indicated that hydrogen enhanced the mobility of dislocations, showing an increase of velocity in the first case and a resumption of movement in the second. The effect on

the dislocation velocity were also found to be reversible, as the dislocations decelerated when hydrogen charging ceased.

Birnbaum and Sofronis[81] later postulated that this occurred due to a hydrogen atmosphere forming around dislocations. These atmospheres were supposed to create a dilatational stress field and shield the dislocation from interactions with surrounding defects by responding to the stress. They stated that this reduction of the repulsive force between defects should increase the mobility of individual dislocations and result in macroscopic softening, at least in the range of strain rates and temperatures at which the atmospheres remain with the dislocations as they move. A common picture shown as evidence for this theory is that of *Ferreira et al.*[82], an in-situ TEM observation of the effect of hydrogen on dislocation pile-ups in stainless steel with a constant load applied. They found that the dislocations in pile-ups moved closer together with the introduction of hydrogen and remained in those positions upon its removal. Note however that the TEM requires a thin film sample and so it is difficult to gauge the effect of the sample geometry. These effects on dislocation mobility have been observed in a large number of tests by now[83], as well as evidence of slip localisation in SEM images which have also been interpreted as being HELP-related[84].

This softening was also observed by *Matsui et al.*, finding that the flow stress of high-purity iron samples decreased sharply immediately after beginning electrolytic charging with hydrogen, reaching a steady value after decreases of up to 50%[85]. When charging was ceased the sample could recover close to its original flow stress, considered to rule out the effects of the charging mechanism from being the culprit. *Matsui et al.* concluded that the softening was likely due to the enhancement of kink-pair nucleation on screw dislocations; they also observed a hardening effect below 190K and concluded that this was due to the trapping effect of hydrogen on kinks. *Jagodzinski et al.*[86] estimated the elastic effect of hydrogen in dislocation pile-ups in iron within the framework of elasticity theory by calculating the force between two edge dislocations and including the effect of the dilatational field from the surrounding atmospheres of hydrogen atoms. They used these results to estimate the effect on the flow stress and found that, in order to reproduce the results of *Matsui et al.* with this shielding effect alone, hydrogen concentrations far above those that can possibly be achieved in experiment are required.

Recently, *Song and Curtin* performed MD simulations with EAM potentials to simulate an edge dislocation pile up under stress and quantify the effect of differing concentrations of hydrogen[87]. They found that, while the hydrogen did form a dense

Introduction

Cottrell atmosphere around each of the edge cores, they actually exerted a significant resistance to dislocation movement due to solute drag. However, it is difficult to say if this effect is due to the rapid application of stress required by MD models: in this case the stress was either applied in a single pulse of 200/400MPa and the steady-state velocity observed for 1.2ns before the dislocations reached the obstacle, or applied in steps of 50MPa with 2ns between them. After the dislocations formed the pile-up, they found that hydrogen concentration had no effect on the spacing, concluding that the hydrogen stress field did not affect the interactions between dislocations.

A related theory regarding the effect of hydrogen on dislocation mobility was proposed by *Kirchheim*[88–90]; known as the defactant concept, it is based on a thermodynamic consideration of the interactions between solutes and defects. It is considered that some of the effects of hydrogen on material plasticity may occur because hydrogen lowers the formation energy of defects. This is particularly important when considering plasticity in BCC materials at finite temperatures and low stresses: this will be primarily dependent on the screw component of dislocations, and the mobility of screw dislocations will be mediated by the thermal activation of kink-pairs. With increasing hydrogen concentration this theory predicts that the effect in BCC metals will first be macroscopic softening, as the hydrogen reduces the kink-pair formation energy, and then hardening, as the excess concentration of hydrogen results in drag on the migrating kinks[91].

Barnoush and Vehoff[92] performed nano-indentation experiments on a range of materials, including Fe-3wt.%Si, with and without hydrogen charging. These experiments involved measuring the force required to push a hard tip into the surface of a sample, both with and without hydrogen charging; the area of this tip is on the order of tens of nanometres. The probed volume will then be so small that it may be considered to be dislocation free and so the material will continue to load elastically, approaching the theoretical shear strength of the material[93], until dislocations are nucleated under the tip. The load required for this to occur was universally reduced by the charging of hydrogen, and because of the lack of other dislocations the HELP mechanism will not be relevant. *Barnoush and Vehof* concluded that these results were well described with the defactant concept, theorising that the elastic energy, and so the formation energy, of the dislocations was reduced by the segregation of hydrogen.

In an attempt to quantify the effects of hydrogen on screw dislocation mobility in the light of the defactant concept, *Itakura et al.*[48] simulated the interaction between

hydrogen and screw dislocations for a range of binding sites around the core with GGA-DFT. These binding energies could be used to estimate the kink trapping energy of hydrogen, due to the change in binding site as the kink sweeps past, and the enhancement of the kink-pair nucleation process. This second term was calculated with the use of a line tension model of a dislocation line, calculating the enthalpy for kink-pair nucleation with and without hydrogen. The line tension model involves breaking the dislocation line into segments with a length of a Burgers vector along the $\langle 111 \rangle$ direction and calculating the energy of each segment individually; this energy is made up a sum of terms that are based upon the dislocation line energy, the intersection of each segment with the Peierls surface of the screw and the interaction of any external stress with each segment. This group previously employed this formulation to calculate the kink-pair activation energy and found good agreement with previous MD results, and now simply included a term to account for the interaction with hydrogen as the kink-pair is formed[94]. These kink-pair nucleation enhancement and kink trapping energies enabled *Itakura et al.* to produce estimates of the effect of hydrogen on the screw dislocation mobility, these contributions are considered in more detail in chapter 6. From the results of this model, they predicted that the effect of hydrogen would change from macroscopic softening to hardening at lower temperatures, in qualitative agreement with the experimental results of *Matsui et al.*[85] mentioned above.

Katzarov et al.[95] employed a kMC model to simulate the effect of hydrogen on the screw dislocation velocity in iron. As mentioned, at finite temperature and low stresses the movement of screw dislocations proceeds by the nucleation, migration and annihilation of kinks; the rates of each of these processes, and their variation with stress, hydrogen content and temperature formed inputs for the model. These rates were obtained by employing transition state theory with the barrier data from the aforementioned papers of *Itakura et al.*; kinks were allowed to nucleate on any of the three $\{110\}$ glide planes intersecting the screw $\langle 111 \rangle$ slip direction and then propagated along the dislocation with a velocity determined by the stress, the phonon drag coefficient and the effect of hydrogen trapping calculated by *Itakura et al.* Kinks on different glide planes could then collide to form immobile jogs on the dislocation line, short sections that do not share the glide plane of the parent line. These jogs can only move with the rest of the line by the non-conservative process of climb, and so form strong pinning-points for the dislocation. Climb was not included within this model, although the dislocation line could cross above the immobile jogs, thus cutting them from the line and leaving behind a prismatic dislocation loop. This kMC model

allowed a quantitative description of the effect of hydrogen on dislocation dynamics, demonstrating the regimes of stress, temperature and hydrogen content in which the dislocation mobility would be enhanced or diminished.

1.4 Overview and Objectives

The primary objective of this thesis was to provide both data and the machinery to carry out large scale calculations on the effect of hydrogen in iron, with the intent to extend the work carried out by *Katzarov et al.*[95], on the effect of hydrogen on dislocation mobility, and that by *Katzarov and Paxton*[68], on the decohesive effect of hydrogen. Both of these papers provide methods to predict the effect of hydrogen but require large amounts of underlying data to produce these predictions.

A limitation of the kMC model used by *Katzarov et al.*[95] was that it was dependent on the results from the literature, and the abstraction to a line tension model. This method could be applied to a number of different environments in iron, where the effect of hydrogen would almost certainly be different, if the input data for the changing hydrogen/screw interactions and kink-pair nucleation energies were available. A region of particular interest would be the dense pile-up of screw dislocations in the region around a crack-tip where failure is likely to originate. It may also be of interest to include the energetics of jog, or edge dislocation, climb in this model; the drag of immobile jogs can result in the emission of vacancies and so could help to account for the abundance of vacancies observed in hydrogen-charged samples after plastic deformation[73–76]. This model could then enable predictions of the temperature, hydrogen content and stress at which the Hydrogen Enhanced Stress Induced Vacancy (HESIV) mechanism described above becomes important. It would be of interest to extend the calculations on the decohesive effect of hydrogen carried out by *Katzarov and Paxton*[68] to a number of common grain boundaries, as well as other materials. As noted above, these calculations required a large number of configurational simulations to obtain the variation of the binding energy with plane separation, requiring the variation of the hydrogen trap energy in various arrangements at each separation. It was considered that methods of accelerating these kinds of simulations, as well as extending the capability of TB to larger, more disordered structures, would be of great use.

The body of chapter 3 is based around the testing of a BOP parameter set, which was originally fit for use within direct-diagonalisation Tight Binding, and learning how

to carry out large-scale defect simulations. These tests are particularly important as this parameter set is used for later simulations and formed an integral part of the scheme attempted in chapter 7. The energetics of jog climb are also calculated at the end of this chapter; a range of vacancy/edge binding energies are calculated along with the energetic barriers required to extend the kMC model to include climb. An attempt is then made, in chapter 4, to calculate the structure and formation energies of kinks on screw dislocations. These calculations were intended to be extended to provide the energetics of kink-pair formation, which would have reduced the dependence of the kMC model on literature results and possibly allowed the calculation of the variation of this rate with strain.

Chapter 5 details the inclusion and testing of the Broyden accelerated mixing procedure[96] in TBE calculations. Calculations in α -Fe are complicated by the requirement to accurately describe magnetism in the structure: the energy of the system is weakly dependent on these magnetic moments and so they converge slowly compared to the charges. The range of possible simulations that could be carried out effectively could be extended by accelerating the convergence of these moments. Attempts are also made to further accelerate this convergence by altering the structure of the mixing cycle.

The central results of this thesis are contained within chapter 6: empirical Tight Binding was employed to estimate the changing interaction between hydrogen and screw dislocations with tension and compression. Due to the driving forces associated with stress gradients on the diffusion of hydrogen, it is known to accumulate in the high-stress areas around a crack-tip[97, 98]. The area around a crack-tip is then both the site where failure is most likely to originate and where the effect of hydrogen will be maximised. It is then crucial to extend the understanding of all aspects of hydrogen effect in these areas; these results were focussed on providing input for the kMC model used by *Katzarov et al.* Extending this model to describe the evolution of a dislocation around a crack-tip could provide indispensable information on the failure mechanism associated with enhanced plasticity.

Finally, an attempt was made to include hydrogen at a scale never before achieved with a truly quantum-mechanical method. Simulations of the interaction between defects and hydrogen generally require both large cells, to relax long-range stress fields, and quantum-mechanical accuracy, to describe hydrogen. It was considered that a method of this type would be invaluable for these studies, Chapter 7 describes the formulation, implementation and testing of two methods of embedding: seamlessly

Introduction

connecting an inner region described with direct-diagonalisation Tight Binding within a much larger region described with the Bond Order Potential. Although the Bond Order Potential used is restricted to local charge neutrality self-consistency it is still more than accurate enough to describe the large area of slightly-displaced atoms surrounding a defect. The fact that both of these models can share the same Hamiltonian also means that bonds across the surface are not terminated in a non-physical way, but may be naturally included in the calculation.

Chapter 2

Theory

2.1 Dislocations

Crystalline materials have a periodic arrangement of atoms in three dimensions, which may be defined with respect to a three dimensional grid formed by three sets of parallel lines. The parallelepipeds formed by this grid are known as unit cells, repeating blocks that make up the lattice of atoms such that each intersection of the grid has identical surroundings. However, no perfect crystalline structure exists in nature but are filled with defects that disrupt the periodicity. It is helpful to classify these defects by their dimension: a point defect will be a defect that disturbs the symmetry at an isolated position, such as a vacant site where an atom should be or an extra atom in the area between atomic sites. Line defects, or dislocations, are then whole lines through the solid of anomalously arranged atoms; surface defects are two-dimensional, such as the boundary between two areas of the crystal with a differing orientation to their crystal structure, known as grain boundaries; and finally volume defects may be a group of agglomerated vacancies or foreign particles which form a three dimensional defected area.

The properties of a crystal will be partially determined by these defects, it is therefore crucial to understand their effect and interaction in order to quantify the effect on the behaviour of the crystal as a whole, particularly with regard to mechanical properties. Plastic deformation of the crystal involves large numbers of atoms sliding over one another; generally the most closely packed planes with the widest spacing between them will be the preferred planes for this slip to occur. However, the stress required for these planes to slip rigidly over one another would be far above the actual yield stresses observed in materials[99]. This discrepancy may be explained with the

existence of dislocations, the movement of which allows the slip of small areas of the atomic plane at a time and so requires a far smaller stress[11–13].

A dislocation may be defined by the relative orientation between the discontinuity it produces in the lattice, or its Burgers vector, and the line along which this discontinuity repeats through the crystal. There are two types of pure dislocation: edge dislocations, with a Burgers vector perpendicular to the dislocation line; and screw dislocations which have them parallel. The edge dislocation may be thought of an extra half plane of atoms, inserted between planes; this will result in compressive stress in the areas to either side of the extra plane and a tensile stress after its end, the edge of this half plane then defines the dislocation line. Screw dislocations instead distort the planes normal to the dislocation line such that they form a helix around it, like a spiral staircase; the dislocation line will be at the centre of this distortion.

The Burgers vector may be found by carrying out a Burgers circuit around the area of the crystal containing the dislocation; this involves hopping between sites around the dislocation that may be recognisably mapped to sites in the perfect lattice, then carrying out the same circuit in the perfect lattice. The vector by which the circuit fails to close in the perfect lattice will define the sum of the Burgers vectors for all dislocations contained within the circuit, as shown in figure 2.1. It is essential to maintain a convention when using the Burgers circuit as this will define the sign of the Burgers vector; if a consistent dislocation line sense is defined the circuit may then always be carried out clockwise when looking down the positive direction of the line and the Burgers vector defined by the vector from the finish to the start of the circuit in the perfect crystal. This consistency is required as the direction of the Burgers vector will partially define the properties of the dislocation: oppositely signed dislocations of the same type will move in opposite directions under the same applied stress (as will be seen below) and will annihilate if brought together.

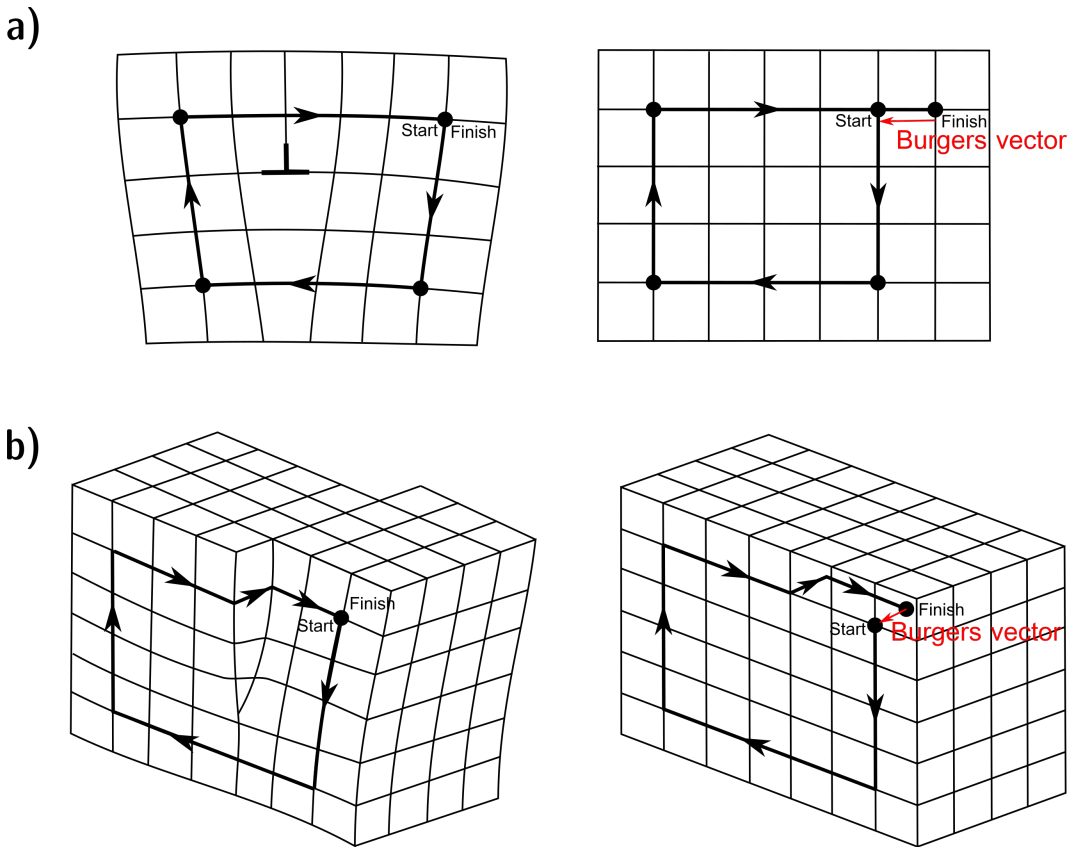


Fig. 2.1: Burgers circuit construction for **a)** edge and **b)** screw dislocations in a simple cubic structure; a closed circuit is constructed between lattice sites that may be recognisably mapped to sites in the perfect lattice then that same circuit is carried out in the perfect lattice; the closure failure will then define the total Burgers vector of all dislocations enclosed by the circuit. The core of the edge dislocation is marked as the bottom of the extra half plane of atoms.

The Burgers vector is a fundamental property of a dislocation, it is invariant along the dislocation line or as the dislocation moves. However the orientation relation between the Burgers vector and dislocation line is not invariant: the dislocation line may curve, having both edge and screw character depending on the angle between the line and the Burgers vector at each point. The Burgers vector is also conserved: a dislocation cannot terminate in an otherwise perfect area within the crystal, but must end in a closed loop, a junction of other dislocations, a free surface, a grain boundary or some other defect. When the dislocation ends in a node, or a junction of other dislocations, the vector total of the Burgers vector in from any of the dislocations must equal the vector total out from the others, similar to Kirchoff's law of current conservation in junctions.

A dislocation may move conservatively, without the addition or removal of atomic sites, in any plane which contains both the Burgers vector and the dislocation line; for an edge dislocation this will uniquely define a single plane, but for a screw it will be any atomic plane that contains the dislocation line. This plane is known as the glide plane, and as the dislocation glides along it the atoms on one side of the plane will be displaced by a Burgers vector relative to those on the other side, the dislocation line then marks the division between the areas where these relative displacements have occurred and those where they have not. The potential energy landscape for the movement of a straight dislocation line on the glide plane will be made up of periodic hills and troughs, known as Peierls barriers and valleys respectively. The Peierls barrier is the energy cost to move the dislocation line from one Peierls valley to another, arising from the lattice friction; Peierls valleys are simply the minima where the majority of the dislocation line will lie. The dislocation may also move normal to the glide plane but this motion, known as climb, will be non-conservative and so requires the addition or removal of material. In the context of the edge dislocation, we may picture this as the extra half-plane of atoms moving upward or downward by the addition or removal of atoms. Therefore edge dislocations will act as a source and sink of vacancies and interstitial atoms; however the self diffusion of atoms through the lattice is a slow process and so climb is unlikely to occur at low temperatures.

A dislocation will move in response to stress, whether by the application of an external load or by the presence of another defect causing an internal stress, and this movement will do work on the crystal. Therefore the force on a dislocation may be defined as the amount of work done over the distance travelled, this force is not physical but simply a method of describing dislocations' response to applied stress. The direction of this force will depend on the slip produced by the dislocation, and so the direction of the Burgers vector; dislocations of opposite Burgers vector will move in opposite directions under the same applied stress, as shown in figure 2.2. The sign of the Burgers vector for the edge dislocations in figure 2.2 **a)** are implied by the direction of the symbol at either side of the dislocation line, and so the diagram contains two edges of opposite sign. The steps on either side of the cuboid show what would happen if either dislocation were to reach the free surface that they are travelling toward: a step with a width of the dislocation's Burgers vector. Figure 2.2 **b)** shows the behaviour of two screw dislocations with oppositely signed Burgers vectors; also shown is the steps that would result if either end of the dislocation were to terminate in a free surface. The force between dislocations may also be understood by the fact

that if the stress fields of the dislocations tend to reinforce each other then it will increase the energy of the configuration and so the dislocations will repel; however if the stress fields tend to cancel it will decrease the energy of the configuration and the dislocations will attract. Dislocations of opposite Burgers vector will then tend to attract each other and annihilate if they meet.

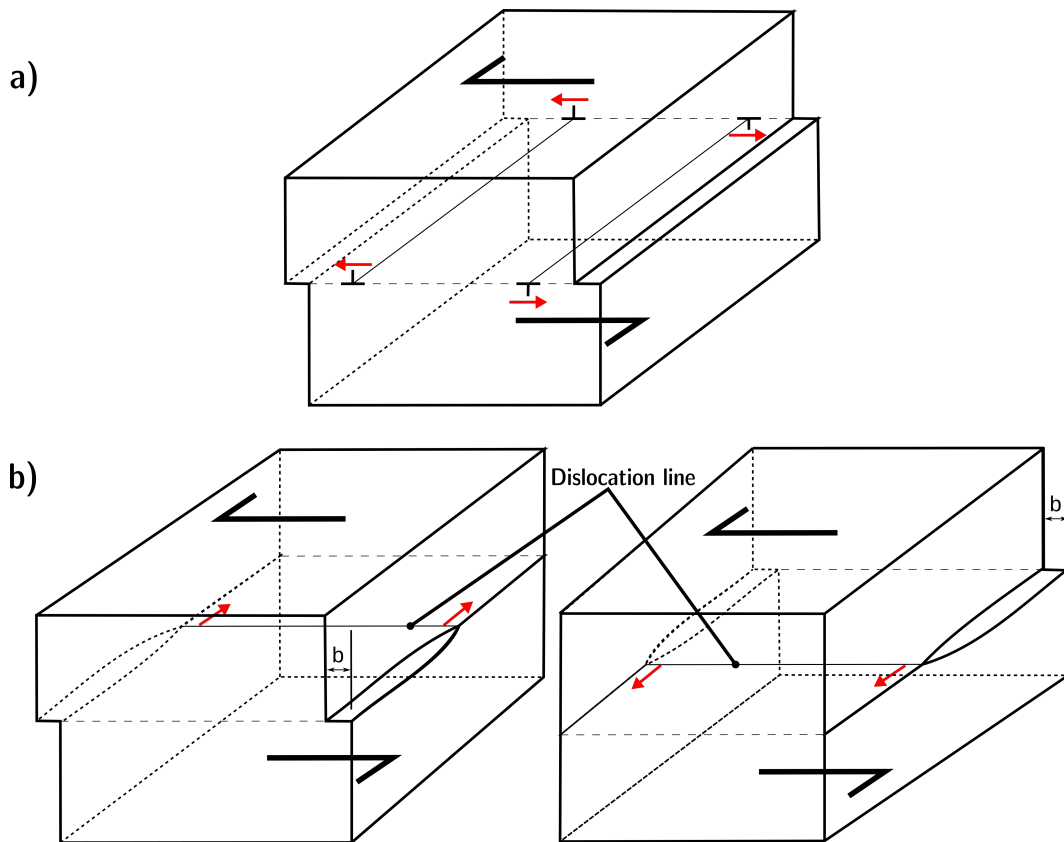


Fig. 2.2: Shown is the response of **a)** edge dislocations and **b)** screw dislocations to applied stress. The black half-arrows show the applied shear and the red arrows show the resultant direction of motion for each dislocation line.

The movement of the dislocation, whether it be by slip or by climb, will not occur for the full line at once but rather stepwise, moving small sections of the line then possibly expanding them until the full line has moved. If the new section of dislocation lies within the same glide plane as the parent then it is known as a kink, if it lies out of the glide plane it is known as a jog. These defects may also be formed by the intersection of two dislocations: the passage of a dislocation line displaces material on either side of the glide plane relatively by a Burgers vector, therefore the intersection of two dislocation lines will cause the formation of a kink or jog on each line of the

same magnitude and direction as the other's Burgers vector. Kinks and jogs share the same Burgers vector as the rest of the line; therefore kinks will not impede glide of the dislocation as they already lie on the glide plane. Jogs also will not impede the glide of an edge dislocation but on screw dislocations they will only be able to glide along the dislocation line; glide of the screw dislocation will require climb of the jog segment. Jogs then form pinning points on screw dislocations, preventing the movement of that section of the line due to the high energy cost associated with climb and requiring the absorption or emission of vacancies for each unit step.

2.2 Electronic Structure Methods

2.2.1 Tight Binding

In order to carry out any calculations for the wave function of a system, one of the first approximations to be applied is that the motion of electrons and nuclei in a system may be decoupled, assuming that the electrons react instantly to any motion of the nuclei. Known as the Born-Oppenheimer approximation[100], it works well because of the disparity in mass between electrons and nuclei; this means that electrons will remain in the lowest energy state, or ground state, as the atomic structure is changed. The ground state of the system may then be obtained from the time-independent Schrödinger equation below by minimisation of the energy with respect to the wave function.

$$\hat{H}\Psi = E\Psi \quad (2.1)$$

where \hat{H} is the Hamiltonian operator, made up of kinetic and potential energy operators, and Ψ is the wave function of the system, containing all information on its state. If the further assumption is made that the electrons may be modelled as independent particles, moving in an effective potential representing the other electrons and nuclei, then the Schrödinger equation for the non-interacting system of electrons separates to give one-electron equations of the form:

$$\hat{H}\psi_n(\vec{r}) = \left[-\frac{\hbar^2}{2m} \nabla^2 + V_{eff}(\vec{r}) \right] \psi_n(\vec{r}) = \varepsilon_n \psi_n(\vec{r}) \quad (2.2)$$

\hat{H} now represents the single-particle Hamiltonian operator: the kinetic energy operator $-\frac{\hbar^2}{2m} \nabla^2$ reproduces the kinetic energy of a system of non-interacting electrons with the

same density and the effective potential $V_{eff}(\vec{r})$ seen by each electron is independent of the others. This potential contains terms to approximate the many body effects, such that the ground-state charge density is the same as in the interacting system[43]. Each single-particle state, n , is described by its wave function, ψ_n , and its energy, ε_n , which are obtained as the eigenfunctions and eigenvalues of the single particle Hamiltonian respectively. Equation 2.2 may be simplified somewhat by assuming that the single-particle wave functions of the system are made up of a linear combination of localised atomic-orbital like basis states, ϕ_{RL} ; where R labels each atomic site by its position and $L = l, m$ is a combined angular momentum index labelling each orbital type. Representing ψ_n with n and ϕ_{RL} with RL , this expansion may be written in Dirac bra-ket notation as:

$$|n\rangle = \sum_{RL} C_{RL}^n |RL\rangle \quad (2.3)$$

C_{RL}^n are the expansion coefficients of the basis set. The problem has now been simplified from one of finding unknown functions, ψ_n , to one of finding these unknown coefficients.

Generally equation 2.2 is treated as a matrix eigenvalue problem, and so the operators are rewritten in matrix form. the Hamiltonian matrix elements are conceived as integrals of the basis states with the Hamiltonian operator.

$$H_{RLR'L'} = \int \phi_{RL}(\vec{r}) \hat{H} \phi_{R'L'}(\vec{r}) d^3\vec{r} = \langle RL | \hat{H} | R'L' \rangle \quad (2.4)$$

The basis states on neighbouring atoms are not necessarily orthogonal, and so may have an associated overlap matrix:

$$S_{RLR'L'} = \int \phi_{RL}(\vec{r}) \phi_{R'L'}(\vec{r}) d^3\vec{r} = \langle RL | R'L' \rangle \quad (2.5)$$

In the case of orthogonal orbitals, or those that have been orthogonalised by some procedure such as the Löwdin method[101], each occurrence of the overlap matrix in the following equations may be replaced with the identity matrix.

The input density, ρ^0 , is commonly taken to be a superposition of spherically symmetric, atomic charge densities and so a related approximation is made in most empirical Tight Binding models that the effective potential may be represented as a sum of atom-centred contributions. These integrals are now made up of two orbitals and a potential centred on three sites: one-centre integrals have all three terms centred

on the same site; two-centre, or hopping, integrals have the orbitals centred on two sites and the potential sharing one of these positions; and finally there are three-centre terms which have all three centred on different sites. The next approximation is to neglect the three-centre integrals, not just because their calculation is difficult and would obscure the physical clarity of the model, but also due to the fact that this two centre approximation is implicit in the structure of the bond integrals described below and in the calculation of forces[102]. Other combinations, such as having both orbitals centred on one site and the potential on another, may or may not be included depending on the model. The remaining integrals are treated as adjustable parameters, fitted to reproduce previous results; the Hamiltonian will be made up of terms representing the orbital on-site energies and interactions between orbitals on neighbouring atoms. In the interest of speed, further approximations are commonly made to restrict the interaction range to the first few shells of neighbours and the orbitals involved to those close to the energy range of interest, approximations which will anyway be more slight than discarding the three-centre terms[103].

There would still be a large number of bond integral parameters to fit but the number of independent elements may be reduced greatly using the convention laid down by *Slater and Koster*[104]. For a matrix element between two given orbitals on different atoms, spherical coordinate systems are constructed such that the vector between the atoms lies along the z -axis and the origin is centred on either atom; in integrating these functions over the spherical coordinates it is found that only those states that share the same component of angular momentum with respect to the bond axis will have a non-vanishing contribution to the integral. These components are labelled with σ , π and δ in analogy to the s , p and d orbitals; such that s orbitals may form σ bonds, p form σ and π bonds and d form σ , π and δ bonds, as illustrated in figure 2.3. The angular part of the bond integrals between any orbitals on neighbouring atoms is then a linear combination of these parametrised fundamental integrals depending on the direction cosines of the bond between the atoms, as laid out for several structures in *Slater and Koster*'s paper.

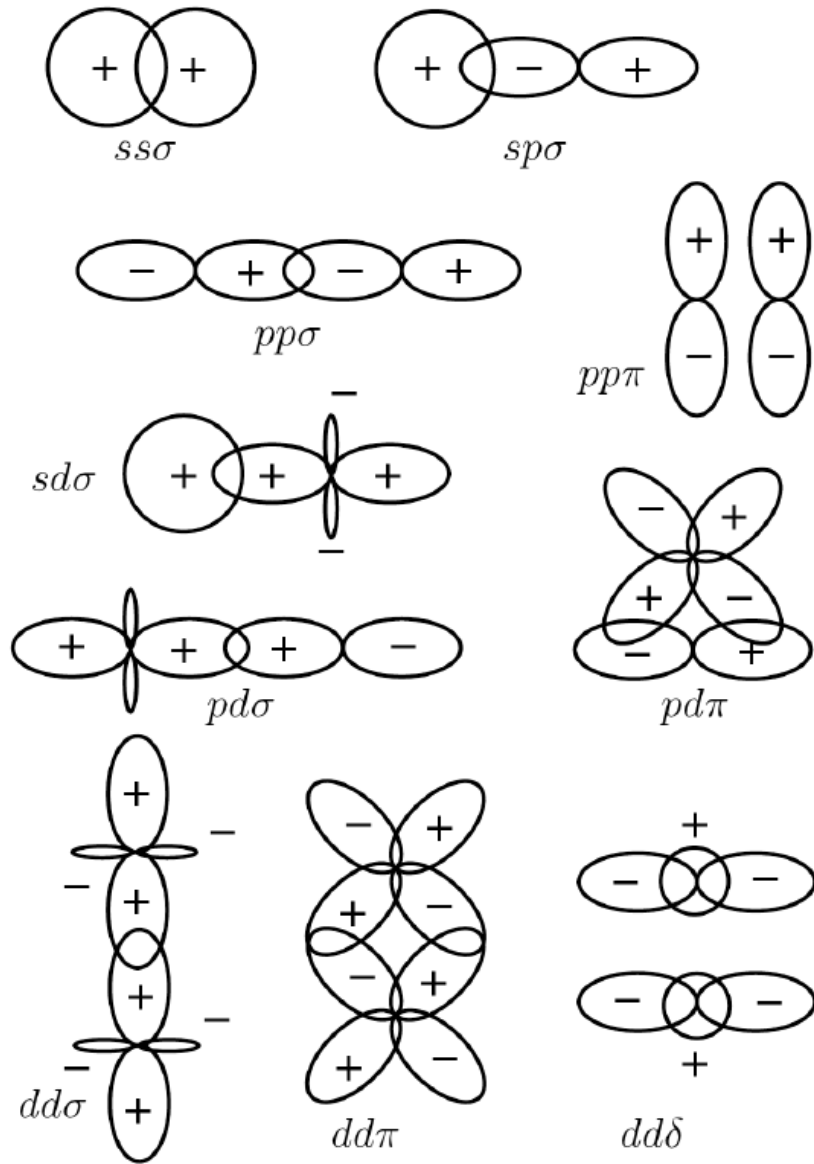


Fig. 2.3: Fundamental bond integrals that can be formed in a basis of *s*, *p* and *d* orbitals; the Latin letters label the orbitals involved and the Greek letter denotes the component of angular momentum they share with respect to the bond axis.

The Hamiltonian and overlap matrices can then be written as:

$$H_{RRL'R'L'}^0 = \begin{cases} \epsilon_{RL}\delta_{LL'} & R = R' \\ f_{RRL'R'L'}(|R' - R|) & R \neq R' \end{cases} \quad (2.6)$$

$$S_{RRL'R'L'} = \begin{cases} \delta_{LL'} & R = R' \\ f_{RRL'R'L'}^{ovl}(|R' - R|) & R \neq R' \end{cases} \quad (2.7)$$

The superscript label on the Hamiltonian denotes that it is the non-self-consistent input Hamiltonian, before any of its elements have been altered by the self-consistency procedures that will be described below. The on-site terms (ϵ_{RL}) are parameters which must be chosen for each orbital type; the two-centre terms ($f_{RRL'R'L'}(|R' - R|)$ and $f_{RRL'R'L'}^{ovl}(|R' - R|)$) are the hopping integrals, which have an angular dependence from the linear combination of fundamental bond integrals, described above, multiplied by some function with a dependence on bond length. This function will constitute more parameters to fit, and is of great importance as the gradient of these integrals will partially determine the interatomic forces and so the stability of various structures. The functional form must be quite short ranged, going to zero beyond the first shells of neighbours without any discontinuity, but still flexible enough to fit to other results. These requirements may be met by with the use of two functions: one fitted to reproduce the previous results, and a cutoff function that matches the value, slope and curvature at some point and then smoothly reduces it to zero at a reduced range[105]. Another option is to use some function which has an increasing decay rate beyond a certain point, such as the Goodwin-Skinner-Pettifor function[106].

The input Hamiltonian and overlap matrices have now been fully defined, and so the problem may be written as a linear eigenproblem and solved to obtain the band energies, ε_n , and expansion coefficients, C_{RL}^n , as the eigenvalues and eigenvectors respectively.

$$\sum_{R'L'} H_{RRL'R'L'} C_{R'L'}^n = \varepsilon_n \sum_{R'L'} S_{RRL'R'L'} C_{R'L'}^n \quad (2.8)$$

The state of the system may be represented with the use of the density operator, defined by:

$$\hat{\rho} = \sum_n f_n |n\rangle \langle n| \quad (2.9)$$

Occupancy of the eigenstates is defined by f_n : at zero temperature this would be a step function, equal to two below the Fermi level and zero above in materials with degenerate spins. Finite electron temperature may be included with the Fermi-Dirac function below, although this will involve an additional entropic contribution to the energy (described at the end of section 2.2.2).

$$f_F(\varepsilon) = \frac{1}{1 + \exp(\frac{\varepsilon - \varepsilon_F}{k_B T})} \quad (2.10)$$

where k_B is the Boltzmann constant, T the electron temperature and ε_F the Fermi level; the occupancy function in spin-degenerate systems is given by $f_n = 2f_F(\varepsilon_n)$. In materials with non-degenerate spins, i.e. magnetic materials, a separate Hamiltonian and so density matrix is produced for each spin σ , and so this occupancy function will vary between zero and one instead of zero and two, or $f_n^\sigma = f_F(\varepsilon_n)$. This essentially means that in non-magnetic, spin-degenerate systems equation 2.8 can be solved once for both spins, while for magnetic, spin-polarised systems equation 2.8 must be solved twice, once for each spin; this also means that all the terms below that involve the density matrix must also be calculated for each spin and summed. The difference between the spin-polarised Hamiltonians will be dealt with in more detail when considering self-consistency in section 2.2.3 below.

The expansion coefficients of the Hamiltonian can then be used to calculate the expansion coefficients of the density operator for the electrons in each state.

$$\rho^{RLR'L'} = \sum_n^\infty f_n C_{RL}^n C_{R'L'}^{n*} \quad (2.11)$$

These density expansion coefficients may also be obtained through the use of the Green function, a particularly useful relation as other methods exist to approximate it (such as the Bond Order Potential approximation). The Green function operator is defined by:

$$\hat{G}(\varepsilon) = \sum_n^\infty |n\rangle \frac{1}{\varepsilon - \varepsilon_n} \langle n| \quad (2.12)$$

This will be, by definition, equivalent to the inverse of the operator $(\varepsilon \hat{I} - \hat{H})$:

$$(\varepsilon \hat{I} - \hat{H}) \cdot \hat{G}(\varepsilon) = \hat{I} \quad (2.13)$$

The Green function operator is also related to the operator for the density of states,

$\hat{D}(\varepsilon)$:

$$\hat{D}(\varepsilon) = -\frac{1}{\pi} \lim_{\eta \rightarrow 0} \text{Im} \frac{1}{\varepsilon + i\eta - \varepsilon_n} = -\frac{1}{\pi} \lim_{\eta \rightarrow 0} \text{Im} \hat{G}(\varepsilon + i\eta) \quad (2.14)$$

where η is a small, positive value that is taken to zero from above. The density of states is related to the density by integration:

$$\hat{\rho} = \int_{-\infty}^{\infty} f(\varepsilon) \hat{D}(\varepsilon) d\varepsilon \quad (2.15)$$

$f(\varepsilon)$ is simply the occupancy f_n taken as a function of the energy, and so it is given by $f(\varepsilon) = 2f_F(\varepsilon)$ for a spin-degenerate material or $f^\sigma(\varepsilon) = f_F(\varepsilon)$ for spin-polarised. Finally this relation provides the link between the Green function and the density expansion coefficients:

$$\rho^{RLR'L'} = -\frac{1}{\pi} \lim_{\eta \rightarrow 0} \text{Im} \int_{-\infty}^{\infty} f(\varepsilon) G^{RLR'L'}(\varepsilon + i\eta) d\varepsilon \quad (2.16)$$

$G^{RLR'L'}(\varepsilon + i\eta)$ are the expansion coefficients of the Green function operator in the local basis:

$$G^{RLR'L'}(\varepsilon) = \sum_n^{\infty} \frac{C_{RL}^n C_{R'L'}^{n*}}{\varepsilon - \varepsilon_n} \quad (2.17)$$

Additionally, the expansion coefficients of the Green function may be used to obtain the local density of states $D_{RL}(\varepsilon)$, or the projection of the total density of states on orbital RL :

$$D_{RL}(\varepsilon) = -\frac{1}{\pi} \lim_{\eta \rightarrow 0} \text{Im} \sum_{R'L'} G^{RLR'L'}(\varepsilon + i\eta) S_{R'L'RL} \quad (2.18)$$

Once the density expansion coefficients have been obtained the charge in the system may be apportioned between atoms using Mulliken population analysis[107]; in an orthogonal system this simply amounts to a summation over the diagonal elements of the density matrix but with a non-orthogonal basis there will be a "bond charge" between atoms which must be included by multiplying by the overlap matrix:

$$q_R = \sum_L q_{RL} = \sum_{LR'L'} \rho^{RLR'L'} S_{R'L'RL} \quad (2.19)$$

If the summation were also over R this would have an identical form to the trace of the density operator.

The band energy, or the sum of the energies of occupied states, may then be obtained from either the eigenvalues or the density coefficients:

$$E_{band} = \sum_n f_n \varepsilon_n = Tr \hat{\rho} \hat{H}^0 = \sum_{RLR'L'} \rho^{RLR'L'} H_{R'L'RL}^0 \quad (2.20)$$

In the TB Band Model this energy forms part of the total energy of the solid, which *Chadi*[108] expressed as:

$$E_{tot} = E_{ee} + E_{ei} + E_{ii} \quad (2.21)$$

where E_{ee} , E_{ei} and E_{ii} are the electron-electron, electron-ion and ion-ion interaction energies respectively. Unfortunately the band structure energy includes the E_{ee} interaction more than once since, in summing over the one-electron states, the energy of each electronic interaction will be included from the perspective of each electron. The TB band model total energy was written as:

$$E_{tot} = E_{band} + E_{clas}^{band} \quad (2.22)$$

where E_{clas}^{band} is a repulsive pairwise term, originally interpreted to represent the ion-ion interactions and compensating for the double counting of the electron-electron interaction:

$$E_{clas}^{band} = \frac{1}{2} \sum_{R \neq R'} V_{RR'}(|R' - R|) \quad (2.23)$$

The Tight Binding Bond Model instead approximates the difference in energy between the condensed and free atom states[109]. The binding energy may then be expressed as:

$$E_{bind} = Tr(\rho - \rho^0) \hat{H}^0 + E_{clas}^{bond} \quad (2.24)$$

As mentioned, ρ^0 generally represents a superposition of, non-interacting, free atomic charge densities; the first term then arises from the bonding and charge redistribution in forming the solid; E_{clas}^{bond} has the same form as E_{clas}^{band} but represents different terms: It was demonstrated by *Sutton et al.*[109], with the use of the 1st order density functional defined by *Harris*[110] and *Foulkes*[111], that E_{clas}^{bond} now represents the change in electrostatic energy (including all electron-electron, electron-ion and ion-ion electrostatic interactions) and the exchange and correlation energies as the atoms

are condensed, and that these terms may be well approximated by a pair potential. Exchange represents the reduction in total energy due to the antisymmetry of the electron wave functions, preventing electrons of the same spin from sharing spatial states and so reducing Coulomb repulsion; while correlation is a measure of how the motion of one electron is affected by the presence of others around it. These terms are not calculated explicitly but rather fitted to reproduce some structural properties, such as the bulk moduli or lattice parameter. The Bond Model has now superseded the Band model in most applications, and forms the starting point for the Bond Order Potential, and so it is what I will continue with here.

In a real orbital basis ρ^0 will have no off-diagonal terms, and so the first term in equation 2.24 may be picked apart into on-site and inter-site parts. The on-site part, or promotion energy, defines the energy cost for the change in orbital occupancy from the free atom values, $(\rho^0)^{RLRL}$ (or N_{RL}), to those in the condensed state, ρ_{RLRL} .

$$E_{prom} = \sum_{RL} (\rho_{RLRL} - N_{RL}) H_{RLRL}^0 \quad (2.25)$$

The inter-site part of the band energy is equivalent to the bond energy, or a sum over the energies of all bonds in the system; it represents the largest contribution to the cohesion of the solid.

$$E_{bond} = \sum_{\substack{RLR'L' \\ R \neq R'}} \rho_{RLR'L'} H_{R'L'RL}^0 \quad (2.26)$$

The sum of the bond and promotion energies is then clearly equivalent to the band energy minus some reference energy of free atoms, $E_{ref} = \sum_{RL} N_{RL} \epsilon_{RL}$.

As mentioned, in the case of non-orthogonal orbitals a bond charge will build up between atoms, and so the promotion energy in equation 2.25 will not include all of the charge in the system; this may be rectified by replacing the ρ_{RLRL} in this equation with the q_{RL} from equation 2.19, so that the promotion energy is now:

$$E_{prom} = \sum_{RL} (q_{RL} - N_{RL}) H_{RLRL}^0 \quad (2.27)$$

This results in a new definition for the bond energy, the covalent energy[112]:

$$E_{cov} = \sum_{\substack{RLR'L' \\ R \neq R'}} \rho^{RLR'L'} (H_{R'L'RL}^0 - S_{R'L'RL} H_{RLRL}^0) \quad (2.28)$$

The overlap term is included so that the identity $E_{prom} + E_{cov} = E_{band} - E_{ref}$ still holds.

In order to actually use the TB model for atomistic simulations some prescription is required to calculate the force, which is defined as the gradient of the binding energy with respect to atomic displacement. The derivative of the band energy part, or the trace of the product of the density matrix and Hamiltonian, may be obtained by making use of the Hellmann-Feynman theorem[113, 114] to write it as the trace of the product of the density matrix and derivative of the Hamiltonian, or:

$$\frac{\partial}{\partial r_R} (Tr \hat{\rho} \hat{H}^0) = Tr \hat{\rho} \frac{\partial}{\partial r_R} \hat{H}^0 \quad (2.29)$$

where r_R represents the coordinates of atom R . This derivative of \hat{H}^0 is not actually known, but it may be rewritten in terms of derivatives of the hopping integrals and overlap matrix elements:

$$Tr \hat{\rho} \frac{\partial}{\partial r_R} \hat{H}^0 = \sum_n^\infty f_n C_{RL}^n C_{R'L'}^{n*} \left[\frac{\partial H_{R'L'RL}^0}{\partial r_R} - \varepsilon_n \frac{\partial S_{R'L'RL}}{\partial r_R} \right] \quad (2.30)$$

Due to the two-center approximation applied previously these derivatives are not difficult to obtain. ρ^0 consists solely of on-site terms and so $Tr \hat{\rho}^0 \frac{\partial}{\partial r_R} \hat{H}^0$ will just be a summation over the diagonal. The derivative of the binding energy will then have the form:

$$\frac{\partial E_{bind}}{\partial r_R} = Tr \hat{\rho} \frac{\partial}{\partial r_R} \hat{H}^0 - \sum_{RL} (\rho^0)^{RLRL} \frac{\partial H_{RLRL}^0}{\partial r_R} + \sum_{R' \neq R} \frac{\partial V_{RR'}}{\partial r_R} \quad (2.31)$$

The final term is the derivative of the pair potential, which is trivial to obtain due to its analytic form. The on-site terms of \hat{H}^0 do not vary with atomic displacement and so only gradients of the inter-site terms must be included in this calculation; the force on each atom R is then given by:

$$\begin{aligned}
 F_R = & - \sum_{\substack{LR'L' \\ R \neq R'}} \rho^{RLR'L'} \frac{\partial H_{R'L'RL}^0}{\partial r_R} \\
 & + \sum_{\substack{LR'L' \\ R \neq R'}} E_{RLR'L'}^B \frac{\partial S_{R'L'RL}}{\partial r_R} \\
 & - \sum_{R' \neq R} \frac{\partial V_{RR'}}{\partial r_R}
 \end{aligned} \tag{2.32}$$

The term $E_{RLR'L'}^B$ represents the band energy split into specific contributions:

$$\begin{aligned}
 E_{RLR'L'}^B &= \sum_n^\infty f_n C_{RL}^n C_{R'L'}^{n*} \varepsilon_n \\
 &= -\frac{1}{\pi} \lim_{\eta \rightarrow 0} \int_{-\infty}^\infty f(\varepsilon) \varepsilon \text{Im} G^{RLR'L'}(\varepsilon + i\eta) d\varepsilon
 \end{aligned} \tag{2.33}$$

The formalism presented so far has been for finite systems, which may be sufficient for some calculations if the simulation cell is large enough but often the calculation could be greatly reduced with the use of periodic boundary conditions. For crystalline materials the atomic structure, and so the Hamiltonian and density matrix, has a repeating pattern for a given size of unit cell. The bulk properties of the crystal may then be calculated per unit cell by making the approximation that the crystal is infinite and carrying the calculation out in k -space rather than real space. This is accomplished by replacing each local orbital with a Bloch sum that runs over the periodic images of that orbital. The Bloch-transformed Hamiltonian and overlap matrices are then:

$$H_{RLR'L'}(\vec{k}) = \sum_T e^{(i\vec{k}\cdot T)} H_{(R+T)L'R'L'} \tag{2.34}$$

$$S_{RLR'L'}(\vec{k}) = \sum_T e^{(i\vec{k}\cdot T)} S_{(R+T)L'R'L'} \tag{2.35}$$

where T are the translation vectors of the lattice or some integer combination of them; the summation runs over the infinite unit cells of the system but the number that actually have non-zero contributions will be determined by the range of the hopping-integrals. R and R' run over the atoms in the unit cell, so $T = 0$ would refer to matrix elements between atoms within the same unit cell, like in the finite system. The generalised eigenproblem (equation 2.8) can now be rewritten in terms of these

Bloch-transformed matrices:

$$\sum_{R'L'} H_{RLR'L'}(\vec{k}) C_{R'L'}^n(\vec{k}) = \varepsilon_n(\vec{k}) \sum_{R'L'} S_{RLR'L'}(\vec{k}) C_{R'L'}^n(\vec{k}) \quad (2.36)$$

\vec{k} is restricted to values that lie within the first Brillouin zone, a primitive cell in k -space defined by the volume that is closer to the central Γ -point ($\vec{k} = 0$) than any of the surrounding reciprocal lattice points. The eigenvalues of the Hamiltonian are only unique within the first Brillouin zone, and so it is unnecessary to consider k -points beyond it. The previous quantities obtained from the diagonalisation, such as the density matrix, must now be obtained as a summation over all of the allowed k -points; however, an infinite lattice will result in an infinite number of these points. This summation would then be equivalent to the integration of some continuous function of \vec{k} over the volume of the first Brillouin zone, which can be carried out by sampling at carefully selected points and weighting them accordingly[103, 115]. This is an acceptable solution as the eigenvalues of the Hamiltonian vary smoothly with \vec{k} , so that only a finite number of points need to be treated; although a higher variation with \vec{k} will mean that a higher density sampling mesh is required for the convergence of results. The computational expense involved in the solution of the eigenproblem means that it is of interest to reduce the number of k -points that need be sampled and there are a number of sophisticated sampling methods to improve this convergence[116, 117].

2.2.2 Bond Order Potential

The BOP model is based on the same TB Hamiltonian but bypasses the computationally heavy matrix equation (equation 2.8) by generating the Green function matrix from the moments of the local density of states associated with each orbital. Each successive moment of the density of states will describe a further property of the distribution, such as its norm, its centre of gravity, its mean square width and skewness[118, 119]. The p^{th} moment of the local density of states for an orbital RL may be expressed as:

$$\mu_{RL}^p = \int_{-\infty}^{\infty} \varepsilon^p D_{RL}(\varepsilon) d\varepsilon = \langle RL | \hat{H}^p | RL \rangle \quad (2.37)$$

This expression may be expanded through the insertion of the identity operator, de-

fined by $\sum_{RL} |RL\rangle \langle RL| = \hat{I}$, between the \hat{H} terms ($p - 1$) times.

$$\mu_{RL}^p = \sum_{R^{(1)}L^{(1)}R^{(2)}L^{(2)}\dots} \langle RL | \hat{H} | R^{(1)}L^{(1)} \rangle \langle R^{(1)}L^{(1)} | \hat{H} | R^{(2)}L^{(2)} \rangle \dots \langle R^{(p-1)}L^{(p-1)} | \hat{H} | RL \rangle \quad (2.38)$$

This relation then shows an explicit link between the p^{th} moment of the local density of states for an orbital RL and the sum of all hopping paths of length p through the lattice starting and ending with orbital RL . The moments of the local density of states for each orbital may then be calculated independently, depending only on the value of p rather than the total atom number, and so this calculation will scale linearly with system size. Also, since the electronic properties are generated from the local atomic environment, periodic boundary conditions may be approximated by surrounding the cell with a sufficient width of images to saturate the hopping paths; the calculation may then be carried out entirely in real-space.

However, recovering a function from its moments is difficult to accomplish; the recursion method[120, 121] is commonly used to do this in a stable and convergent way. Starting with each state being considered, the Hamiltonian operator is recursively applied to generate a chain of orthogonal states, known as recursion orbitals.

$$|\widetilde{i+1}\rangle = \hat{H} |i\rangle - a_i |i\rangle - b_i |i-1\rangle \quad (2.39)$$

a_i and b_i are known as recursion coefficients, the tilde is used to mark that the new state has not yet been normalised. Starting from $i = 0$, this relation becomes:

$$|\widetilde{1}\rangle = \hat{H} |0\rangle - a_0 |0\rangle \quad (2.40)$$

since it is known that $| -1 \rangle = 0$. The state $|\widetilde{1}\rangle$ is required to be orthogonal to $|0\rangle$, and $|0\rangle$ is already normalised so operating from the left with it results in a definition for a_0 :

$$a_0 = \langle 0 | \hat{H} | 0 \rangle \quad (2.41)$$

The state $|\widetilde{1}\rangle$ is then normalised by introducing the factor b_1 such that:

$$|1\rangle = \frac{1}{b_1} |\widetilde{1}\rangle \quad (2.42)$$

which defines $b_1^2 = \langle \widetilde{1} | \widetilde{1} \rangle$. An alternate definition for b_1 may be given by operating on

equation 2.40 from the left with $\langle 1|$:

$$b_1 = \langle 1 | \tilde{1} \rangle = \langle 1 | \hat{H} | 0 \rangle = \langle 0 | \hat{H} | 1 \rangle \quad (2.43)$$

This procedure may then be repeated for the subsequent values of i and acts to tridiagonalise the Hamiltonian, it is known as the Lanczos algorithm[122]. The Hamiltonian elements are now given by:

$$\begin{aligned} H_{ii} &= a_i \\ H_{i+1,i} &= H_{i,i+1} = b_{i+1} \end{aligned} \quad (2.44)$$

The problem has now been mapped onto a linear chain of states, with on-site elements a_i and hopping integrals b_i between nearest neighbours only. The purpose of this transformation is that the first diagonal element of the Green function matrix for this system may be represented exactly by a continued fraction.

$$G_{00}(\varepsilon) = \cfrac{b_0^2}{\varepsilon - a_0 - \cfrac{b_1^2}{\varepsilon - a_1 - \cfrac{b_2^2}{\dots}}} \quad (2.45)$$

Note that $b_0^2 = 1$. Each additional level of this continued fraction corresponds to adding a further 2 moments to the density of states distribution, where an infinite number of levels would be an exact solution of the TB model[123].

If the density of states is made up of a single band with a finite width, such as that of a TB model with a single d -orbital, then the recursion coefficients will eventually converge to constant values (a_∞ and b_∞) and so may be used to terminate the continued fraction after a given level of accuracy has been obtained. This terminator must satisfy the relation:

$$t(\varepsilon) = \cfrac{1}{\varepsilon - a_\infty - \cfrac{b_\infty^2}{\dots}} = \cfrac{1}{\varepsilon - a_\infty - b_\infty^2 t(\varepsilon)} \quad (2.46)$$

This has the form of a quadratic equation, that can be solved for the terminating function, known as the square root terminator[120].

$$t(\varepsilon) = \cfrac{\varepsilon - a_\infty}{2b_\infty} \left(1 - \sqrt{1 - \left(\cfrac{2b_\infty}{\varepsilon - a_\infty} \right)^2} \right) \quad (2.47)$$

This terminator essentially couples the finite chain to an infinite effective medium[103].

If the recursion operations are started on one of the basis states, ($|0\rangle = |RL\rangle$) then this continued fraction will correspond to the diagonal Green function matrix element for this orbital ($G_{RLRL}(\varepsilon)$), and so this constitutes a rapid method of obtaining the diagonal density matrix elements.

Obtaining the inter-site Green function matrix elements is more complex, and so only the key points will be summarised here; the full derivation may be found in the papers of *Horsfield et al*[55, 56]. First, an auxiliary space is defined, spanned by vectors $|e_{RL}^\Lambda\rangle$, with the inner product[124]:

$$(e_{RL}^\Lambda | e_{R'L'}^\Lambda) = \Lambda_{RLR'L'} \quad (2.48)$$

where $\sum_{RL} \Lambda_{RLRL} = 1$ and $\Lambda_{RLR'L'}$ has no physical meaning but serves to label bonds; each of these vectors in auxiliary space $|e_{RL}^\Lambda\rangle$ will have a unique corresponding vector in the Hilbert space of the TB basis set, $|RL\rangle$. A product space between the auxiliary space and the Hilbert space is also defined, in order to produce the composite vectors:

$$|W_0^\Lambda\rangle = \sum_{RL} |e_{RL}^\Lambda\rangle |RL\rangle \quad (2.49)$$

The expectation value of the Green function defined with respect to this vector is then:

$$\begin{aligned} G_{00}^\Lambda(\varepsilon) &= \frac{\{W_0^\Lambda | \hat{G}(\varepsilon) | W_0^\Lambda\}}{\{W_0^\Lambda | W_0^\Lambda\}} \\ &= \frac{\sum_{RLR'L'} G_{RLR'L'}(\varepsilon) \Lambda_{RLR'L'}}{\sum_{RL} \Lambda_{RLRL}} \\ &= \sum_{RLR'L'} G_{RLR'L'}(\varepsilon) \Lambda_{RLR'L'} \end{aligned} \quad (2.50)$$

where quantities in the auxiliary space are labelled with a superscript Λ and the fact that operators in the Hilbert space (such as $\hat{G}(\varepsilon)$) do not act upon the vectors in auxiliary space is used during this derivation. The off-diagonal elements of the Green function matrix can then be obtained by differentiating with respect to $\Lambda_{RLR'L'}$, resulting in the relation:

$$\begin{aligned}
 G_{RLR'L'}(\varepsilon) &= \sum_{i=0}^{\infty} \frac{\partial G_{00}^{\Lambda}(\varepsilon)}{\partial a_i^{\Lambda}} \frac{\partial a_i^{\Lambda}}{\partial \Lambda_{RLR'L'}} \\
 &\quad + \sum_{i=1}^{\infty} \frac{\partial G_{00}^{\Lambda}(\varepsilon)}{\partial b_i^{\Lambda}} \frac{\partial b_i^{\Lambda}}{\partial \Lambda_{RLR'L'}} \\
 &\quad + G_{00}^{\Lambda}(\varepsilon) \delta_{RR'} \delta_{LL'}
 \end{aligned} \tag{2.51}$$

The $G_{00}^{\Lambda}(\varepsilon)$, a_i^{Λ} and b_i^{Λ} can be found by applying the recursion method (equation 2.39) with a composite vector $|W_0^{\Lambda}\rangle$ as the starting state.

The Dyson equation is then employed to obtain relations for the derivatives of $G_{00}^{\Lambda}(\varepsilon)$, which relates the change in the Green function to that in the Hamiltonian:

$$\begin{aligned}
 \hat{G}(\varepsilon) &= \hat{G}_0(\varepsilon) + \hat{G}_0(\varepsilon) \delta \hat{H} \hat{G}(\varepsilon) \\
 &= \hat{G}_0(\varepsilon) + \hat{G}_0(\varepsilon) \delta \hat{H} \hat{G}_0(\varepsilon) + \dots
 \end{aligned} \tag{2.52}$$

Taking the variation in the Green function to first order in $\delta \hat{H}$ and expressing it in matrix form gives:

$$\delta G_{ij}(\varepsilon) = \sum_{kl} G_{ik}(\varepsilon) \delta H_{kl} G_{lj}(\varepsilon) \tag{2.53}$$

Therefore the derivatives of $G_{00}^{\Lambda}(\varepsilon)$ with respect to the tridiagonalised Hamiltonian elements are given by:

$$\frac{\partial G_{00}(\varepsilon)}{\partial a_i} = G_{0i}(\varepsilon) G_{i0}(\varepsilon) \tag{2.54}$$

$$\frac{\partial G_{00}(\varepsilon)}{\partial b_i} = G_{0i}(\varepsilon) G_{i-1,0}(\varepsilon) + G_{0,i-1}(\varepsilon) G_{i,0}(\varepsilon) \tag{2.55}$$

The $G_{0i}(\varepsilon)$ (which are equal to $G_{i0}(\varepsilon)$) elements may be obtained by taking the definition of the Green function $(z - \hat{H})\hat{G} = \hat{I}$ and inserting the elements of the tridiagonal Hamiltonian to obtain another recursion relation:

$$(\varepsilon - a_i) G_{ij} - b_i G_{i-1,j}(\varepsilon) - b_{i+1} G_{i+1,j}(\varepsilon) = \delta_{ij} \tag{2.56}$$

which can be rearranged to obtain:

$$G_{i+1,j}(\varepsilon) = \frac{\varepsilon - a_i}{b_{i+1}} G_{ij}(\varepsilon) - \frac{b_i}{b_{i+1}} G_{i-1,j}(\varepsilon) - \frac{\delta_{ij}}{b_{i+1}} \quad (2.57)$$

Each new element of $G_{ij}(\varepsilon)$ can then be obtained from the diagonal element $G_{00}(\varepsilon)$. Finally equation 2.51 may be rewritten as:

$$\begin{aligned} G_{RLR'L'}(\varepsilon) &= \sum_{i=0}^{\infty} G_{0i}^{\Lambda}(\varepsilon) G_{i0}^{\Lambda}(\varepsilon) \frac{\partial a_i^{\Lambda}}{\partial \Lambda_{RLR'L'}} \\ &\quad + 2 \sum_{i=1}^{\infty} G_{0,i-1}^{\Lambda}(\varepsilon) G_{i0}^{\Lambda}(\varepsilon) \partial b_i^{\Lambda} \frac{\partial b_i^{\Lambda}}{\partial \Lambda_{RLR'L'}} \\ &\quad + G_{00}^{\Lambda}(\varepsilon) \delta_{RR'} \delta_{LL'} \end{aligned} \quad (2.58)$$

The derivation for the derivatives of the recursion coefficients with respect to $\Lambda_{RLR'L'}$ is quite involved and so will not be included here, but again may be found in [55, 56].

There are several points in this method that require the evaluation of an integral with the Fermi-Dirac function (such as equations 2.16 and 2.68); this may be carried out in the complex plane by summing up an infinite series over the Matsubara poles, but the convergence of this series is very slow[55]. This convergence may be greatly improved by using a modified Matsubara scheme[125], beginning with an approximation to the exponential function:

$$\exp(Z) \approx \left(1 + \frac{Z}{n}\right)^n \quad (2.59)$$

which becomes exact as n tends to infinity. This approximation leads to an alternate representation of the Fermi-Dirac function (equation 2.10):

$$f_F(\varepsilon) = \frac{1}{1 + \exp(\beta(\varepsilon - \varepsilon_f))} \approx \frac{1}{\left(1 + \frac{\beta(\varepsilon - \varepsilon_f)}{2M}\right)^{2M} + 1} \quad (2.60)$$

where $\beta = \frac{1}{k_B T}$. This approximation to the Fermi-Dirac function has $2M$ poles in a circle in the complex plane off the real axis, these poles are given by:

$$E_p = \varepsilon_F + \frac{2M}{\beta}(z_p - 1) \quad (2.61)$$

$$z_p = \exp\left(\frac{i\pi(2p+1)}{2M}\right) \quad p = 0, 1, \dots, 2M-1 \quad (2.62)$$

The integral of some function $A(\varepsilon)$, that is defined in the complex plane, with the Fermi-Dirac function may now be given as a summation over the poles of the approximated Fermi function:

$$\lim_{\eta \rightarrow 0} \text{Im} \int_{-\infty}^{\infty} f_F(\varepsilon) A(\varepsilon + i\eta) d\varepsilon = -\frac{2\pi}{\beta} \text{Re} \left[\lim_{M \rightarrow \infty} \sum_{p=0}^{M-1} z_p A(E_p) \right] \quad (2.63)$$

The relation between the density matrix and the Green matrix (equation 2.16) can then be replaced with:

$$\rho^{RLR'L'} = \frac{2}{\beta} \text{Re} \left[\sum_{p=0}^{M-1} z_p G^{RLR'L'}(E_p) \right] \quad (2.64)$$

For non-magnetic systems with degenerate spins this density matrix must be doubled, while in magnetic systems it is calculated with the Green matrix of each spin individually.

As mentioned, finite electron temperature may be included with the Fermi-Dirac distribution; note that this is unrelated to the temperature of the solid as the motion of the electrons and nuclei are uncoupled. Increasing electron temperature will decrease the range of the density matrix and dampen long-range Friedel oscillations in metals, and so fewer moments will be required to accurately evaluate the local density of states[126]. Also, it has the effect of reducing the number of poles required for convergence in the modified Matsubara scheme. Using a finite temperature means that, instead of just the band energy $E_{band}(T)$, the band free energy $F_{band}(T)$ must be calculated by including the contribution from the entropy:

$$F_{band}(T) = E_{band}(T) - TS(T) \quad (2.65)$$

This entropic term accounts for the variation in states of the electrons near the Fermi energy, it is given by:

$$S(T) = \sum_{RL} \int D_{RL}(\varepsilon) s(\varepsilon) d\varepsilon \quad (2.66)$$

Again, this contribution must be doubled for spin degenerate systems or calculated for

each spin and summed otherwise. s represents the entropic density function, which is:

$$s(\varepsilon) = -k_B \{ f_F(\varepsilon) \log[f_F(\varepsilon)] + (1 - f_F(\varepsilon)) \log[1 - f_F(\varepsilon)] \} \quad (2.67)$$

This contribution has no effect on the evaluation of the forces provided that they are evaluated at a constant number of electrons[55].

2.2.3 Self-Consistency

Neglect of the self consistency can cause inaccuracy in the energy and forces due to the lack of charge conservation and an improper treatment of the potential variation from charge flow[109].

Local Charge Neutrality is implemented in many TB models as the simplest form of self-consistency. It is based on the insight that each atom will remain neutral, or that the charge associated with it is fixed; this is a good approximation for metallic materials as excess charge associated with atoms would be neutralised due to the screening of the electron gas[127]. This scheme may be effected in practice by iteratively updating the on-site elements of the Hamiltonian: atoms with an excess of charge will have their energy levels increased by an amount proportional to the excess and vice versa for those with a deficit. This continues until the charge transfer between atoms has been minimised to a certain degree, although charge transfers may still occur between orbitals on the same atom.

A good estimate for these energy shifts can come from the susceptibilities, which may be calculated for each orbital from the diagonal elements of the Green function:

$$\begin{aligned} \chi_{00,00} &= \frac{1}{\pi} \lim_{\eta \rightarrow 0} \text{Im} \int f(\varepsilon) G_{00}(\varepsilon + i\eta) G_{00}(\varepsilon - i\eta) d\varepsilon \\ &= -\frac{1}{2} \frac{\partial q_{RL}}{\partial a_0} \end{aligned} \quad (2.68)$$

a_0 will be equal to the first on-site element in the linear recursion chain produced from each orbital, and so this may be rewritten as:

$$\chi_{00,00(RL)} = -\frac{1}{2} \frac{\partial q_{RL}}{\partial \epsilon_{RL}} \quad (2.69)$$

The shifts to the Hamiltonian for each orbital will then have the form:

$$H'_{RLRL} = \frac{\delta q_R}{2 \sum_L \chi_{00,00}(RL)} \quad (2.70)$$

These shifts in the on-site potentials must be included in the energy; the promotion energy with LCN self-consistency is then modified so that it includes the updated Hamiltonian rather than the input:

$$E_{\text{prom}}^{\text{LCN}} = \sum_{RL} (q_{RL} H_{RLRL} - N_{RL} H_{RLRL}^0) \quad (2.71)$$

This would now mean that the calculation for the atomic forces, or $\frac{\partial E_{\text{bind}}}{\partial r_R}$, would change: the on-site terms of the Hamiltonian in the promotion energy now vary with atomic separation and so their gradients would have to be included. Following *Sutton et al.*[109], this may be avoided by adding and subtracting $\sum_{RL} N_{RL} H_{RLRL}$ so that the promotion energy becomes:

$$E_{\text{prom}}^{\text{LCN}} = \sum_{RL} (q_{RL} - N_{RL}) H_{RLRL} \quad (2.72)$$

The energy splitting between orbitals on the same atom is maintained during the LCN cycle, and so this term could be restructured as:

$$E_{\text{prom}}^{\text{LCN}} = \sum_R H'_{RLRL} \sum_L (q_{RL} - N_{RL}) + \sum_{RL} (q_{RL} - N_{RL}) H_{RLRL}^0 \quad (2.73)$$

Due to the LCN requirements $\sum_L (q_{RL} - N_{RL}) = 0$, and the second term is constant with atomic displacement; therefore there is no contribution to the atomic force from this new promotion energy. The additional term that arises from this reshuffle, $\sum_{RL} N_{RL} (H_{RLRL} - H_{RLRL}^0)$, is assumed to be absorbed in the fitting of the pairwise potential, although this assumption would only be justified for potentials that were originally fit for LCN self-consistency.

A description of magnetism is essential for the simulation of magnetic iron phases, with an important contribution to the relative stability of each phase[128]. Magnetism may be included with the Stoner theory for itinerant ferromagnetism[129, 130], which includes the presence of local exchange fields as a contribution to the band energy. The magnetic moments are determined by the difference in occupation between states with spins parallel or anti-parallel to the resultant field; these electrons will see a different on-site potential depending on this orientation, giving Hamiltonian updates

of the form:

$$H'_{RLRL} = \frac{\delta q_R}{2 \sum_L \chi_{00,00}(RL)} \pm \frac{1}{2} I_R m_R \quad (2.74)$$

I_R here represents the Stoner parameter, another ingredient of the model which must be fitted to reproduce the correct magnetic behaviour; the \pm sign gives the value of these on-site terms for the spin-polarised Hamiltonians, depending on whether the spin is parallel or anti-parallel to the local magnetic moment. This means each spin now has a different Hamiltonian and so density matrix, which must be summed, the occupancy function is now given by $f(\varepsilon) = f_F(\varepsilon)$. The magnetic moments must now also be made self-consistent like the charges; this procedure may be carried concurrently with the charge self-consistency procedure, although it is generally found that the magnetic moments converge more slowly than the charges and so there may be advantages in separating them. The magnetic contribution to the band energy will then have the form:

$$E_{mag}^{LCN} = \sum_R -\frac{1}{4} I_R m_R^2 \quad (2.75)$$

Polarisable Ion Tight Binding enables the description of charge transfer between atoms and the formation of point-multipoles on each atom[51]. The point multipoles are described through the inclusion of off-diagonal, on-site terms in the Hamiltonian, which act to couple orbitals of different angular momentum on the same site[131]. The Hamiltonian is adjusted iteratively with the potential generated by this charge distribution, until the charge difference between iterations is minimised beyond a certain degree and so the potential matches the induced charges.

At each step of the self-consistency cycle the charge multipoles are calculated.

$$Q_{RL} = \begin{cases} \sqrt{\frac{1}{4\pi}} \delta q_R & L = 0 \\ \sum_{L'L''} \rho_{RL'L''} \Delta_{l'l''l} C_{L'L''L} & L > 0 \end{cases} \quad (2.76)$$

The parameters $\Delta_{l'l''l}$ must be set for the model, defining the strength of the l -multipole from the coupling of the orbitals with angular momentum l' and l'' . $C_{L'L''L}$ are the Gaunt coefficients, integrals over three real spherical harmonics Y_L , which may be

written as:

$$C_{L'L''L} = \int \int Y_L Y_{L'} Y_{L''} d\Omega \quad (2.77)$$

These coefficients may be calculated in the beginning and reused; the Gaunt coefficients will also decide the selection rules, limiting the number of coupling "strength" parameters that are required[102].

If the assumption is made that the charges are sufficiently localised around the atomic sites, then the angular components of the electrostatic potential at an atomic site R may be related to the multipole moments of the charges on all atoms in the system:

$$V_{RL}^M = \sum_{\substack{R'L' \\ R \neq R'}} \tilde{B}_{RLR'L'}(|R - R'|) Q_{R'L'} \quad (2.78)$$

The $\tilde{B}_{RLR'L'}(|R - R'|)$ represents a matrix of structure constants, defined by:

$$\tilde{B}_{RLR'L'}(|R - R'|) = 16\pi^2 \sum_{L''} (-1)^l \frac{(2l'' - 1)!!}{(2l + 1)!!(2l'' + 1)!!} C_{L'L''L} K_{L''}(|R - R'|) \quad (2.79)$$

where the summation is restricted to values for which $L'' = L + L'$ and the $K_{L''}(r) = r^{-l-1} Y_L(r)$ are solid Hankel functions.

There is also a Hubbard potential, which represents the on-site self-interaction of the atomic charge.

$$V_R^U = \delta q_R U_R \quad (2.80)$$

The Hubbard U_R parameter will be another parameter to be fitted for each species: a greater U will incur a greater energy cost for the accumulation of charge on any one site, and indeed the LCN approximation could be taken as the limit of having an infinite U .

The updates to the Hamiltonian due to these potentials will then have the form:

$$H'_{RL'RL''} = e^2 \sum_L V_{RL}^M \Delta_{l'l''l} C_{L'L''L} + V_R^U \delta_{L'L''} \quad (2.81)$$

This will result in a 2nd order contribution to the energy, representing all of the

electron-electron interactions:

$$E_2 = \frac{1}{2} \sum_R (e^2 \sum_L Q_{RL} V_{RL}^M + \delta q_R V_R^U) \quad (2.82)$$

Finally the force on an atom R due to these inter-site electrostatic interactions will be given by:

$$F_R^M = -\frac{e^2}{2} \sum_L Q_{RL} \nabla_R V_{RL}^M \quad (2.83)$$

In the case when only charge transfer is considered (without the formation of point multipoles) the Madelung potential is simply restricted to the monopole moment:

$$V_{R0}^M = \sum_{\substack{R' \\ R' \neq R}} \sqrt{4\pi} \frac{\delta q_{R'}}{|R - R'|} \quad (2.84)$$

The Hamiltonian updates and energy contribution then become:

$$H'_{RLRL}^{(CT)} = e^2 \sum_{R'} \frac{\delta q_{R'}}{|R - R'|} + V_R^U \quad (2.85)$$

$$E_2^{(CT)} = \frac{1}{2} \sum_R (e^2 \sum_{R'} \frac{\delta q_R \delta q_{R'}}{|R - R'|} + \delta q_R V_R^U) \quad (2.86)$$

The updates to the Hamiltonian are now strictly diagonal: the off-diagonal, on-site terms that coupled orbitals of different angular momenta become zero.

Again the Stoner theory of itinerant ferromagnetism[129] is employed to include magnetic effects, resulting in two spin-polarised Hamiltonians and a additional contribution to the band energy. The Hamiltonian increments and 2^{nd} order contributions to the energy for a magnetic PITB model would then have the form:

$$H'_{RLRL} = e^2 \sum_L V_{RL}^M \Delta_{l'l''l} C_{L'L''L} + ((U_R - \frac{1}{2} I_R) \delta q_R \pm \frac{1}{2} I_R m_R) \delta_{L'L''} \quad (2.87)$$

$$E_2 = \frac{1}{2} \sum_R (e^2 \sum_L Q_{RL} V_{RL} + (U_R - \frac{1}{2} I_R) \delta q_R^2 - \frac{1}{2} I_R m_R^2) \quad (2.88)$$

Note that in this case there is an additional contribution to the potential and energy from the Stoner terms that acts to reduce the Hubbard on-site interactions; this repre-

Theory

sents the degree to which the on-site Coulomb repulsion is reduced for electrons with like spins due to exchange[52].

In the case of non-orthogonal orbitals there will also be off-site contributions to the Hamiltonian due to the presence of bond charge.

$$H'_{RLR'L'}^M = \frac{1}{2} O_{RLR'L'} (V_{R0}^M + V_{R'0}^M) \quad (2.89)$$

$$H'_{RLR'L'}^U = \frac{1}{2} O_{RLR'L'} (V_R^U + V_{R'}^U) \quad (2.90)$$

This will result in additional contributions to the forces:

$$\partial \rho_{RR'}^S = \sum_{LL'} \rho^{RLR'L'} \frac{\partial S_{RLR'L'}}{\partial r} \quad (2.91)$$

$$F_R^M = - \sum_{R'} (V_{R0}^M + V_{R'0}^M) \partial \rho_{RR'}^S \quad (2.92)$$

$$F_R^U = - \sum_{R'} (V_R^U + V_{R'}^U) \partial \rho_{RR'}^S \quad (2.93)$$

The origin of these forces can be understood by considering a pair of atoms moving relative to each other in a system: as the separation of the atoms changes so will their overlap, and so the bond charge that can be attributed to each atom. It is this change in charge, and so Hubbard potential, that gives rise to the Hubbard contribution to the force. The changing bond charge will also change the monopole moment on each atom, and so the Madelung contribution arises from the change in electrostatic interaction between these two sites and all other sites[52].

Chapter 3

Preliminary Dislocation Calculations

3.1 Introduction

As mentioned, the plastic deformation of a crystalline material is dependent on the movement and interaction of defects in the lattice. Although High Resolution Electron Microscopy can provide close to atomic resolution, experimental observation of these defects is still quite limited in scope and the preparation of samples can influence the measurement of bulk properties[132]. The stress fields of these defects are generally well described within continuum elasticity, but interactions that involve the core region require an atomistic description. A reliable description of atomic interactions can be guaranteed with first-principle methods, such as DFT, but then the structures that may be described are limited either to a perfect lattice or a closely spaced array of defects, due to the limitation in block sizes and the periodic boundary conditions imposed by a k -space treatment. The goal then is to apply enough approximation that the structure of the defect is not affected by the size of the cell, but not so much that important physics in the description is obscured.

Large cell sizes may be achieved with the use of interatomic potentials, which remove the electronic degrees of freedom and describe atomic interaction with a complexity that ranges from simple pairwise functions, fit to reproduce mechanical properties, to central-force many-body potentials such as the Embedded Atom Model[133] or Finnis-Sinclair potentials[134]. These potentials can work well to describe materials with bonding dominated by s - and p -electrons, and so nearly-free-electron in character, but may have difficulty with materials in which the angular dependence of the

bonding becomes important. The bonding of transition metals, such as iron, is mediated by the d -electrons due to the partially filled d -band; it has a mixed covalent and nearly-free-electron character and so will be strongly dependent on the bond angles, and generally are not well described with these potentials[41]. Removing these electronic degrees of freedom will also preclude the possibility of an accurate description of magnetism, which requires an accurate description of the density of states near the Fermi level. This is particularly important in iron and, as mentioned, can determine the relative stability of structural phases[128].

In general, BOP models describing transition metals or transition metal compounds have been limited to orthogonal basis states, and so must compensate for the neglect of valence s -electrons by adjusting the number of d -electrons. It is the filling of the d -band that determines the bonding in these materials and so the ground state structure, and so this restriction to orthogonal p - and d -states works well[135]. The basis in TB means that the BOP correctly describes the angular variation of bonding; furthermore it captures the physics of bond formation and breaking, saturated and unsaturated bonds, as well as dangling and radical bonds[123]. Indeed there have been a number of successes for BOP models describing transition metals, such as finding the explanation for preferred prism slip of screw dislocations in titanium: the high energy of stacking faults on the basal plane was due to the angular bonding of first neighbours and so could not be obtained with the interatomic potentials that do not include this dependence[136].

This chapter details the use of the BOP model to describe defect structures in α -iron. There were two motivations behind these simulations: first, to fully test the validity and flexibility of a d -orthogonal parameter set for iron, fitted for direct-diagonalisation TB by *Paxton and Elsässer*[105], for use in BOP simulations. Although BOP is based on the TB approximation, the parameter sets used within it are generally fitted both for BOP and a specific number of moments, which is not the case for these parameters. This is particularly important as this parameter set is used for subsequent BOP simulations and formed an integral part of the embedding model described in chapter 7. Secondly, these simulations were intended to deepen my understanding of large-scale defect simulations; in the introduction of dislocations, structuring simulation cells, calculating their interactions and so on. These methods are used extensively in later chapters, and some of the structures produced form the basis for future work.

A number of defect simulations are first carried out with both the Paxton parameter

set and another, fitted for use within BOP by *Mrovec et al.*[58] and found to reproduce DFT results well[59]. The use of the Mrovec set allowed direct comparison with an established model, simulating exactly the same processes; the results from these simulations are also compared to previous results from the literature where available. Finally, the Paxton set is employed in the description of the two most common edge dislocations in the α -iron lattice, first calculating their structure and estimating their interactions with vacancies in the lattice. One of these structures is then employed to calculate the energetics of the climb process, simulations which could only be carried out with a model that is so economical in its calculations.

3.2 Methods

Pure Dislocations in Anisotropic Linear Elasticity Theory

The following derivation follows that laid out in reference [137]. The summation convention will be used such that summation will be implied for repeated Latin suffixes (i, j, etc.) but not for Greek (α , β etc.).

The stress tensor σ_{ij} gives the force element acting along the positive x_j axis through the area element with unit normal x_i , and will be symmetric such that $\sigma_{ij} = \sigma_{ji}$. The displacement field from the undeformed state of a body is designated u_i and, when its spatial variation is sufficiently small, the strain tensor may be defined as:

$$e_{ij} = \frac{1}{2} \left(\frac{\partial u_i}{\partial x_j} + \frac{\partial u_j}{\partial x_i} \right) \quad (3.1)$$

The relation between the stress and the strain in an anisotropic medium is then given by generalised Hooke's law:

$$\sigma_{ij} = C_{ijkl} e_{kl} \quad (3.2)$$

where C_{ijkl} is a fourth-rank tensor of elastic constants related to the mechanical properties of materials. In the case of static equilibrium the following condition may be defined from the equation of motion:

$$\frac{\partial \sigma_{ij}}{\partial x_i} + f_j = 0 \quad (3.3)$$

Taking the body force, f_j , to be zero and making use of the relations above gives:

$$C_{ijkl} \frac{\partial^2 u_k}{\partial x_l \partial x_j} = 0 \quad (3.4)$$

Obtaining the displacement field for a dislocation in anisotropic media is then equivalent to solving equation 3.4 with some associated boundary and initial conditions. First the displacement field is taken to be invariant along the dislocation line and the following form is assumed:

$$u_k = A_k f(\mathbf{m} \cdot \mathbf{x} + p \mathbf{n} \cdot \mathbf{x}) \quad (3.5)$$

where \mathbf{x} is the position vector and a new mutually orthogonal, basis of unit vectors $(\mathbf{m}, \mathbf{n}, \mathbf{t})$ is defined such that \mathbf{t} lies along the axis of the dislocation. f in equation 3.5 is an analytic function with complex variables; this equation may then be taken and substituted into 3.4 to obtain:

$$\{C_{ijkl}(m_i + pn_i)(m_l + pn_l)\}A_k = 0 \quad (3.6)$$

If A_k and p are chosen such that they satisfy this equation then the displacement field defined in equation 3.5 will be an admissible solution to the static equilibrium conditions for any analytic function f . There will only be non-trivial solutions for A_k if $\det|C_{ijkl}(m_i + pn_i)(m_l + pn_l)| = 0$; this forms a sixth order polynomial which yields three complex conjugate pairs as solutions. A general solution to the displacement field may then be written as a linear combination of the solutions to this polynomial.

$$u_k = \sum_{\alpha=1}^6 D_\alpha A_{k\alpha} f(\mathbf{m} \cdot \mathbf{x} + p_\alpha \mathbf{n} \cdot \mathbf{x}) \quad (3.7)$$

where D_α are constants which must be determined by the boundary conditions of the problem. Equation 3.6 may be solved as an eigenvalue problem; this is done by first defining a new vector L_α :

$$L_{j\alpha} = -n_i C_{ijkl} (m_l + p_\alpha n_l) A_{k\alpha} \quad (3.8)$$

Another expression for $L_{j\alpha}$ may be obtained by expanding equation 3.6 and substituting in 3.8:

$$L_{j\alpha} = \frac{1}{p_\alpha} m_i C_{ijkl} (m_l + p_\alpha n_l) A_{k\alpha} \quad (3.9)$$

These two equations may then be rewritten as:

$$(nm)_{jk}A_{k\alpha} + L_{j\alpha} = -p_\alpha(nn)_{jk}A_{k\alpha} \quad (3.10)$$

$$(mm)_{jk}A_{k\alpha} = -p_\alpha(mn)_{jk}A_{k\alpha} + p_\alpha L_{j\alpha} \quad (3.11)$$

where the notation $(nm)_{jk} = n_i C_{ijkl} m_l$ has been used for the sake of brevity. In terms of six-dimensional matrices these two equations are:

$$\begin{bmatrix} (\mathbf{nm}) & \mathbf{I} \\ (\mathbf{mm}) & \cdot \end{bmatrix} \begin{bmatrix} \mathbf{A}_\alpha \\ \mathbf{L}_\alpha \end{bmatrix} = p_\alpha \begin{bmatrix} -(\mathbf{nn}) & \cdot \\ -(\mathbf{mn}) & \mathbf{I} \end{bmatrix} \begin{bmatrix} \mathbf{A}_\alpha \\ \mathbf{L}_\alpha \end{bmatrix} \quad (3.12)$$

where " \cdot " represents blocks of zeroes and the matrix of \mathbf{A}_α and \mathbf{L}_α is a six-component column vector of $A_{k\alpha}$ and $L_{j\alpha}$. This equation may be converted into a eigenvalue problem by multiplying from the left by:

$$\begin{bmatrix} -(\mathbf{nn})^{-1} & \cdot \\ -(\mathbf{mn})(\mathbf{nn})^{-1} & \mathbf{I} \end{bmatrix} \quad (3.13)$$

so it becomes:

$$-\begin{bmatrix} (\mathbf{nn})^{-1}(\mathbf{nm}) & (\mathbf{nn})^{-1} \\ (\mathbf{mn})(\mathbf{nn})^{-1}(\mathbf{nm}) - (\mathbf{mm}) & (\mathbf{mn})(\mathbf{nn})^{-1} \end{bmatrix} \begin{bmatrix} \mathbf{A}_\alpha \\ \mathbf{L}_\alpha \end{bmatrix} = p_\alpha \begin{bmatrix} \mathbf{A}_\alpha \\ \mathbf{L}_\alpha \end{bmatrix} \quad (3.14)$$

Diagonalising this problem will then yield p_α as the eigenvalues and the Stroh vectors, \mathbf{A}_α and \mathbf{L}_α , as the eigenvectors, which are normalised:

$$2A_{k\alpha}L_{k\alpha} = 1 \quad (3.15)$$

The following orthogonality relation is then valid for the \mathbf{A}_α and \mathbf{L}_α vectors:

$$A_{k\alpha}L_{k\beta} + A_{k\beta}L_{k\alpha} = \delta_{\alpha\beta} \quad (3.16)$$

An admissible form for the displacement field is then given by:

$$u_k = \frac{1}{2\pi i} \sum_{\alpha=1}^6 D_\alpha A_{k\alpha} \ln(\mathbf{m} \cdot \mathbf{x} + p_\alpha \mathbf{n} \cdot \mathbf{x}) \quad (3.17)$$

where the sign in front of the summation is taken to match that of the imaginary part

of p_α . D_α may then be obtained from the boundary conditions of the problem: u_k will change by a Burgers vector in an infinitesimal distance across the dislocation cut, or in the formalism used here, from $\mathbf{n} \cdot \mathbf{x} = 0^+$ to $\mathbf{n} \cdot \mathbf{x} = 0^-$, while $\mathbf{m} \cdot \mathbf{x} > 0$. The logarithmic function in the displacement relation will then change across this cut by:

$$\ln(\mathbf{m} \cdot \mathbf{x} + p_\alpha \mathbf{n} \cdot \mathbf{x}) \longrightarrow \ln(\mathbf{m} \cdot \mathbf{x}) \pm i0 \quad \text{as } \mathbf{n} \cdot \mathbf{x} \longrightarrow 0^+ \quad (3.18)$$

$$\longrightarrow \ln(\mathbf{m} \cdot \mathbf{x}) \pm i2\pi \quad \text{as } \mathbf{n} \cdot \mathbf{x} \longrightarrow 0^- \quad (3.19)$$

and so the following expression may be obtained[138]:

$$u_i(\mathbf{m} \cdot \mathbf{x} > 0; \mathbf{n} \cdot \mathbf{x} = 0^-) - u_i(\mathbf{m} \cdot \mathbf{x} > 0; \mathbf{n} \cdot \mathbf{x} = 0^+) = \sum_{\alpha=1}^6 \pm A_{i\alpha} D_\alpha = b_i \quad (3.20)$$

where b_i represents the Burgers vector. Using the orthogonality relation of the $A_{i\alpha}$ and $L_{i\alpha}$ vectors (along with the stress function corresponding to the displacement) yields an expression for D_α :

$$D_\alpha = \pm L_{i\alpha} b_i \quad (3.21)$$

The displacement field for a pure dislocation is then fully defined[139].

$$u_k = \pm \frac{1}{2\pi i} \sum_{\alpha=1}^6 A_{k\alpha} L_{i\alpha} b_i \ln(\mathbf{m} \cdot \mathbf{x} + p_\alpha \mathbf{n} \cdot \mathbf{x}) \quad (3.22)$$

where the sign is taken to match that of the imaginary part of p_α . And so, given the elastic constants of the lattice and the dislocation Burgers vector, the displacement field may be defined and used to introduce a dislocation to the lattice, excluding the core region. In this region the spatial variation of the displacement field may no longer be considered small, and so linear elasticity may not be applied. Atomistic relaxation is required to obtain the core structure.

The Nudged Elastic Band method

The transition rates for many dynamic processes may be obtained directly from static simulations using a statistical approach. If the minimum energy path (MEP) between the reactant and product state is obtained, transition state theory may be employed

to produce accurate estimates of these reaction rates[38]. The initial and final states of a process will be local minima in the potential energy surface (PES); the MEP between these minima will then have the properties that the tangent to the MEP at any point will be the same as the gradient of the PES at that point, and the gradient of the PES for any degree of freedom perpendicular to the MEP at any point will be zero. The highest point on the MEP is known as the saddle-point, and it will define the activation energy for the process being simulated.

The Nudged Elastic Band (NEB) method represents a simple and robust method of obtaining this MEP: the initial and final states of the system must be provided, the algorithm then places a chain of replica states between these points, equidistant in configurational space, and adjusts them simultaneously toward the MEP with an optimisation algorithm[140]. The images are prevented from falling back down the PES with a spring force between neighbours, defined for each image i by a spring constant k_i and the separation between it and the neighbouring images. However, without some adjustment of the forces, this method would not produce a good approximation to the reaction path: the components of the spring force that aren't parallel to the chain would push images out of the MEP, while the element of the true force, or PES gradient, parallel to the chain would cause images to slide down the PES and possibly miss the saddle point[141]. The NEB method avoids this issue by projecting out the perpendicular elements of the spring force and the parallel elements of the true force, so that the force on each image is given by:

$$\mathbf{F}_i = -\nabla V(\mathbf{R}_i) |_{\perp} + \mathbf{F}_i^s |_{\parallel} \quad (3.23)$$

where \mathbf{R}_i represents the reactive coordinates of each image in configurational space, $\nabla V(\mathbf{R}_i)$ is the gradient of the PES at image i and \mathbf{F}_i^s is the spring force on that image, which is obtained and separated into its parallel element with:

$$\mathbf{F}_i^s |_{\parallel} = ([k_{i+1}(\mathbf{R}_{i+1} - \mathbf{R}_i) - k_i(\mathbf{R}_i - \mathbf{R}_{i-1})] \cdot \hat{\tau}_i) \hat{\tau}_i \quad (3.24)$$

$\hat{\tau}_i$ represents the unit vector tangent to the chain of images, it may be determined using the coordination of the neighbouring images. The perpendicular component of the true force may be obtained by subtracting the element of the true force projected along the chain of images from the total, local PES gradient.

$$\nabla V(\mathbf{R}_i) |_{\perp} = \nabla V(\mathbf{R}_i) - (\nabla V(\mathbf{R}_i) \cdot \hat{\tau}_i) \hat{\tau}_i \quad (3.25)$$

At the end of the optimisation the images will all lie along a line for which $\nabla V(\mathbf{R}_i) |_{\perp} = 0$ and the choice of k will only affect the distribution of images within this path. This represents one of the first implementations of the NEB method, and there have been many improvements suggested, such as an alternate definition of the tangent to prevent kinks in the line[142]. One of the most useful improvements has been the climbing image NEB (CI-NEB), which guarantees that, if the chain converges to the MEP, the maximum image will be at the saddle-point[143]. In this method the start of the NEB simulation proceeds as normal: the path is optimised for a given number of iterations until a good enough approximation to the MEP has been found. The image with the maximum energy is then selected, and the force on this image is modified to:

$$\mathbf{F}_{i_{max}} = -\nabla V(\mathbf{R}_{i_{max}}) + 2(\nabla V(\mathbf{R}_{i_{max}}) \cdot \hat{\tau}_{i_{max}})\hat{\tau}_{i_{max}} \quad (3.26)$$

This image is now not affected by the spring forces at all, and the only effect of the surrounding images is in defining which degree of freedom is parallel to the chain. This new force will cause the climbing image to move down the PES perpendicular to the band and up the PES parallel to the band, and so toward the saddle-point.

3.3 Screw Dislocations

Simulation Cells

The Paxton parameter BOP simulations used four recursion levels and had an electron temperature of 0.0272eV in these, and subsequent, simulations.

Two sizes of square cell were constructed (containing 270 or 546 atoms) such that they were periodic in every direction; they had a depth of a Burgers vector and lengths of $(15/21)\frac{2a}{\sqrt{6}}$ and $(18/26)\frac{\sqrt{2}a}{2}$ in the [112] and [110] directions for the small/large cell respectively. Anisotropic linear elasticity theory was then used to introduce a quadrupolar array of screw dislocations to the cells, so that the separation between dislocations in their glide plane, (110), was either $\sim 17\text{\AA}$ or $\sim 24\text{\AA}$. This almost equivalent to the cells used by *Ventelon et al.*[46] to examine the Peierls barrier for screw dislocations in iron with DFT; those authors included a shift along z between dipoles to ensure the displacement fields matched smoothly. This was neglected in these cells: the results of these simulations are primarily for comparison and the effect in the quadrupolar cell was not considered to be large. A differential displacement (DD) plot [144] of the smaller quadrupole of screw dislocations is shown in figure 3.1: each

circle represents a $[11\bar{1}]$ column of atoms, coloured according to the $(11\bar{1})$ plane it belongs to; the arrows then represent the difference in displacement along $[11\bar{1}]$ between the columns, the length of the arrows is scaled such that the longest represent a difference in displacement of a third of a Burgers vector. Burgers circuits of the plot could be performed by summing the length of the arrows in the circuit, and so each screw core is centred between three arrows representing a difference in displacement of a third of a Burgers vector each.

The cells were then relaxed using the steepest descent method until the maximum force on an atom was less than $10^{-4}\text{eV}\text{\AA}^{-1}$; both parameter sets resulted in the non-degenerate core structure shown in 3.1. This is the same as the structure found by *Ventelon et al.* and previous DFT studies of screw dislocations in bcc transition metals[20], in contrast to the structure with two energetically degenerate forms commonly found with central force potentials[145].

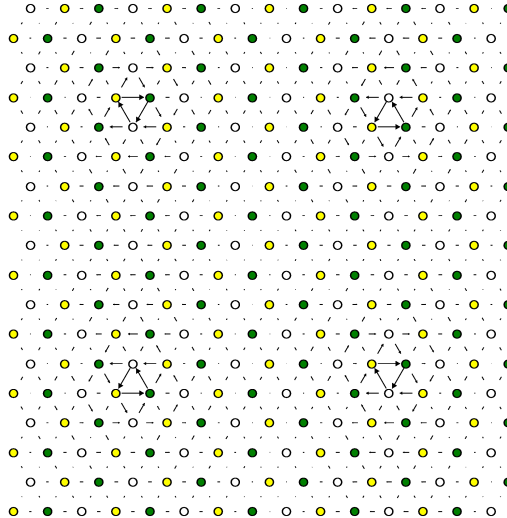


Fig. 3.1: A differential displacement (DD)[144] plot of the quadrupole of screw dislocations. The atoms are coloured according to the $(11\bar{1})$ plane they belong to and the arrows between atoms represent the difference in displacement along $[11\bar{1}]$ between them.

Colour maps of the resultant magnetic moments for a) the Paxton parameters and b) the Mrovec parameters are shown in figure 3.2, with the cores of the screw dislocations marked in black. The distribution of magnetic moments in a) is similar to that found by *Ventelon et al.* with Plane-Wave Self Consistent FIeld (PWSCF)[146] GGA-DFT: in both the three core atoms of each screw have the greatest moment in the cell, and both have a similar 3-fold pattern surrounding the core. However

the pattern formed here isn't quite as symmetrical as that found by *Ventelon et al.*, with slightly greater values in the areas between cores centred in triangles that point towards each other, possibly indicating an increased elastic interaction between cores due to the neglect of the shift between dipoles. The shifts in magnetic moments for the TB parameters were also not quite as large as the DFT results: the three core atomic moments increased by $0.05\mu_B$, less than a third of the PWSCF GGA increase ($0.18\mu_B$). The average moment change for the entire cell for the TB parameters was again much lower than the PWSCF GGA, at $0.004\mu_B/atom$ compared to $0.022\mu_B/atom$; however overall the the general configuration of the magnetic moments was reproduced quite well.

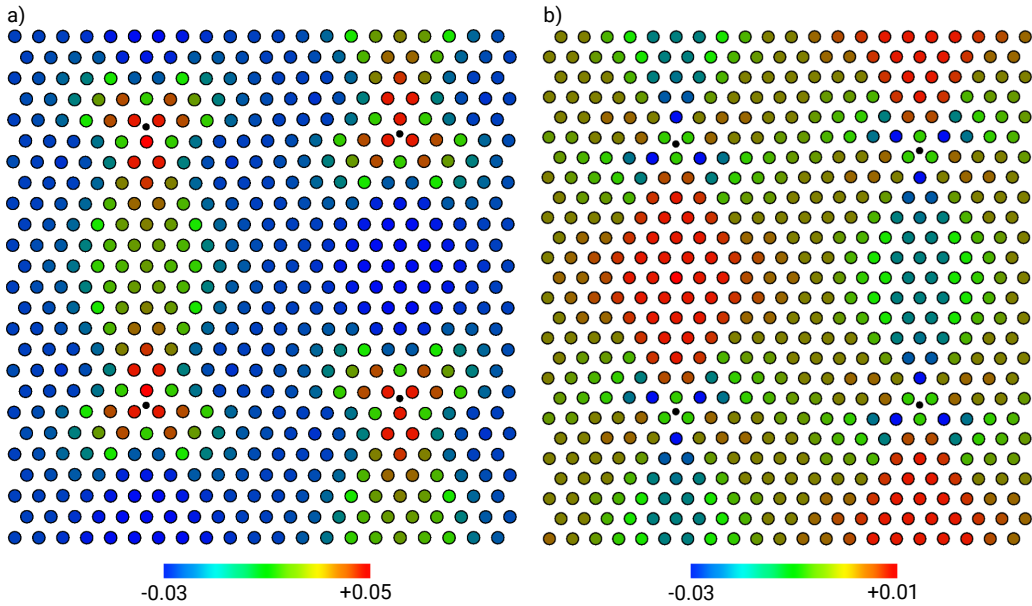


Fig. 3.2: A colour map of the magnetic moments for the fully relaxed 576 atom cell screw quadrupole with a) Paxton parameters and b) Mrovec parameters. The screw dislocation cores are marked with a black dot. Note also that the scale for each map is different and the moments are expressed in μ_B .

The Mrovec parameters were actually more distant from DFT: they showed a decrease in the core atom moments of $-0.008\mu_B$, and the secondary atoms surrounding the core had the largest decrease of the cell at $-0.03\mu_B$. The range of moments for the Mrovec parameters was around half that of the Paxton parameters, however the average change was almost equal in magnitude at $-0.003\mu_B/atom$. The maximum changes for both are quite small as most the structural changes associated with a screw dislocation are to do with the bond angle, rather than the bond length. Note

that the bulk magnetic moments for the d -orthogonal BOP models were both greater than those found for DFT at $2.92\mu_B$ and $2.85\mu_B$ for the Paxton and Mrovec parameters respectively (while those reported by *Ventelon et al.* were $2.18\mu_B$), this is generally accepted to be due to the neglect of sd -hybridisation[105, 147].

Calculation of the Peierls Barrier

In order to produce an end point for a Nudged Elastic Band (NEB) simulation of the Peierls barrier, the atoms in the relaxed cell were shifted by $+\frac{a\sqrt{3}}{6}$ in the $[11\bar{1}]$ direction and $+\frac{2a}{\sqrt{6}}$ in the $[112]$ direction (or a third of a Burgers vector and the $[112]$ separation between Peierls valleys respectively), atoms that went beyond the limits of the cell were then folded back by a cell vector. This results in an identical cell with all the screw dislocations moved to the neighbouring Peierls valley. The NEB method with variable springs was then used to find the MEP between these images and obtain an estimate for the Peierls barrier at zero stress.

The results are shown in figure 3.3 along with the saddle-point calculated using GGA-DFT by *Ventelon et al.*; both parameter sets resulted in a single humped barrier, with no metastable state in the middle of the transition as is found with some interatomic potentials[46]. The change in barrier height between cell sizes was $< 2\%$ for both parameter sets, implying that the interaction between the cores was already small and that the neglected elastic interaction was not significant. The result from the Mrovec parameters matches almost exactly with that from GGA-DFT, although the Paxton result is only 15meV smaller. Interestingly, the Paxton parameters match almost exactly with the result found by *Ventelon et al.* using SIESTA[148] GGA-DFT; although they considered this to be an underestimation due to the reduced localised basis set and inaccurate magnetic moments. This barrier was also estimated by *Zhao and Lu*[49], using NEB and the QM/MM method to move an isolated screw dislocation, and found it to be $60\text{meV}/b$; they postulated that the results found by *Ventelon et al.* were possibly inaccurate due to interactions of dislocations in the array or even just a difference in DFT methods. Other estimations for this barrier have been $35\text{meV}/b$ by both *Dezerald et al.*[47] and *Itakura et al.*[94] using GGA-DFT or, from experiment, a range of $27 - 48\text{meV}/b$ by *Caillard*.[149] The Mrovec parameters then result in a barrier slightly closer to previous results, but both sets are within an acceptable range.

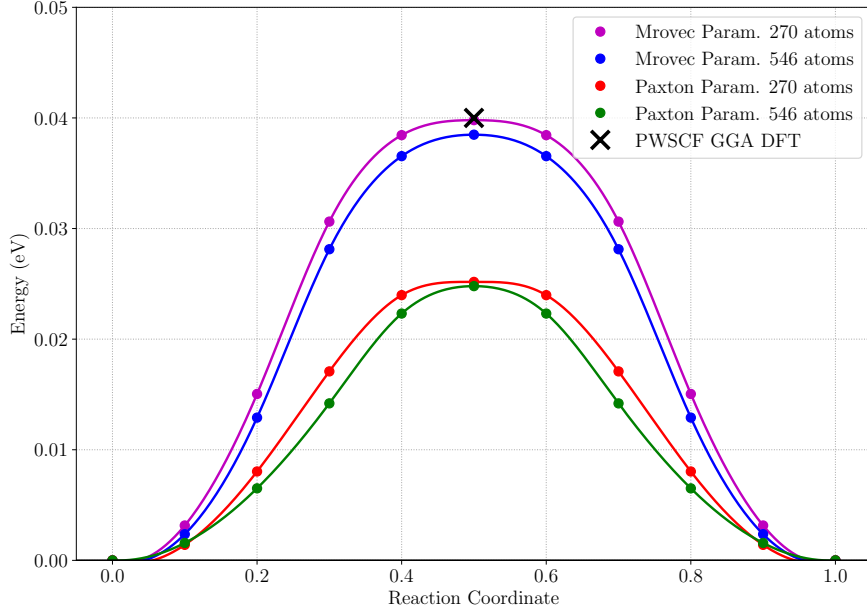


Fig. 3.3: Peierls barrier for the movement of a screw dislocation calculated using the NEB method within BOP for two cell sizes with two sets of parameters; those from *Paxton and Elsässer* [105] fitted for use within DD-TB and those of *Mrovec et al.*[58] fitted for use within BOP. Also shown is the saddle-point calculated using DFT by *Ventelon et al.* [46]

The cost-function method detailed in the paper of *Ventelon et al.* was then used to estimate the core position for the screw dislocations during the transition. For each NEB image, a cost-function was defined that was dependent on the difference in atomic displacements between the image and those obtained from anisotropic linear elasticity theory. This cost function was minimised by varying the coordinates of the screw core positions in the anisotropic linear elasticity equations; it is defined by:

$$C(dx_1, dy_1, dx_2, dy_2) = \sqrt{\sum_i^{N_{atom}} (\delta_{z_i} - \delta_{z_i}^{el}(dx_1, dy_1, dx_2, dy_2))^2} \quad (3.27)$$

where δ_{z_i} are the z displacements of each atom i in the NEB image and $\delta_{z_i}^{el}(dx_1, dy_1, dx_2, dy_2)$ are the displacements obtained from anisotropic linear elasticity with the screw cores displaced from their initial ECC positions by (dx_1, dy_1) and (dx_2, dy_2) . The minimisation of this function then essentially finds the coordinates of the anisotropic linear elasticity displacement field cores that most closely corresponds to these results. The coordinates of the oppositely-signed cores were varied indepen-

dently, but those with the same sign were assumed to have identical displacements.

The results are shown in figure 3.4: the large white circles represent the $[11\bar{1}]$ atomic columns surrounding the neighbouring easy core positions while the red circles are the minimised cost-function positions for the core positions in each image. The positions corresponding to the easy core configuration (ECC), the midpoint between easy cores, the split core and the hard core configuration (HCC) are labelled with a E, M, S and H respectively. Both methods show an asymmetric path between easy core positions, which would imply that there is significant interaction between the cores possibly affecting the accuracy of the results; however the separation between the cores along $[112]$ was found to vary by $< 1\%$ during the transition. This could also imply that the method of estimating the core position was inaccurate, and possibly different paths would be estimated if the coordinates of all four cores were allowed to vary independently; however the increased degrees of freedom would increase the expense of this calculation greatly. The Paxton parameters' path is closer to the DFT results reported by *Ventelon et al.*: an almost straight path between the ECC positions with little to no deviation toward the split core. The Mrovec parameters result in a path that dips toward the split core configuration, slightly closer to the trajectory *Ventelon et al.* found with interatomic potentials; however those potentials' path passed directly through the split core. *Itakura et al.*[94] also found that the path should pass through the midpoint between ECC positions; however, they found that the energy landscape was fairly flat between the midpoint and HCC position and so the path could pass above the midpoint as well. Both parameter sets then produce a good approximation to the transition path, with the Paxton parameters coming slightly closer to accepted DFT results.

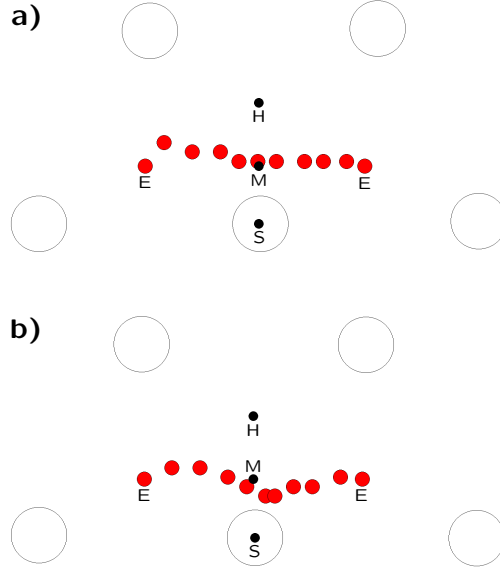


Fig. 3.4: Shown are the postions of the screw core for each image of a NEB simulation of a Peierls transition simulated using BOP with **a)** Paxton and Elsässer's DD-TB parameters and **b)** Mrovec *et al.*'s BOP parameters. The position of the screw core in each image is labelled with a red circle, while the white circles are [11-1] columns of iron atoms. The positions that correspond to the easy-core, hard-core, mid-point between easy-cores and split-core are labelled with an E, H, M and S respectively.

The Peierls stress may then be estimated as the maximum gradient of the Peierls barrier with respect to displacement of the core along the transition pathway (as $\frac{1}{b}(\frac{\delta E}{\delta x})_{max}$), making the assumption that the barrier is not altered by applied stress[150]. This results in a barrier of 3.25GPa for the Mrovec parameters and 1.33 Gpa for the Paxton set; while the estimates from DFT using this method range from 1-1.4 GPa[46, 47, 94]. Again the Paxton parameters give a result closer to the accepted DFT results; however this method will produce a fairly inaccurate estimate of the Peierls stress, due to the assumption mentioned and the dependence on the accuracy of the dislocation core position, and serves here only as a comparison with DFT. The lower bound for the Peierls stress may also be estimated from the difference in energy and position between the initial and saddle points as $\frac{1}{b^2}\frac{\Delta E}{\Delta x}$. This results in values of 0.78GPa and 0.54GPa for the Mrovec and Paxton parameters respectively, both of which compare well to a previous DFT estimation of 0.69GPa[94].

Applying Stress

A cell was made with 1729 atoms as an extended disk with a depth of a Burgers vector and a surrounding border of inert atoms, as shown in figure 3.5; this cell has periodic boundary conditions only along [11̄]. A screw dislocation was then introduced to one side of the cell with anisotropic linear elasticity and pure shear stress was applied such that the maximum resolved shear stress plane (MRSSP) was (1̄10), with a stress tensor defined by:

$$\sigma = \begin{pmatrix} 0 & 0 & 0 \\ 0 & 0 & -1 \\ 0 & -1 & 0 \end{pmatrix} \quad (3.28)$$

This matrix is normalised by the shear modulus for each parameter set in the dislocation coordinate system, denoted by C_{44} , which had a value of 70.02GPa for the Paxton parameters and 72.42GPa for the Mrovec parameters. The corresponding strain matrix may then obtained from relation 3.2; for the Paxton parameters this matrix was:

$$\mathbf{E}_p = \begin{pmatrix} 0 & -0.537 & 0 \\ -0.537 & 0 & -1.420 \\ 0 & -1.420 & 0 \end{pmatrix} \quad (3.29)$$

The Mrovec parameters resulted in:

$$\mathbf{E}_m = \begin{pmatrix} 0 & -0.451 & 0 \\ -0.451 & 0 & -1.312 \\ 0 & -1.312 & 0 \end{pmatrix} \quad (3.30)$$

This matrix may then be used to update the atomic coordinates in increments of $0.001C_{44}$, relaxing the cell with the steepest descent algorithm between increments.

The Peierls stress, or applied stress at which the dislocation moved, was $0.020C_{44}$ (1.44GPa) and $0.030C_{44}$ (2.17GPa) for the Paxton and Mrovec parameter sets respectively. The CRSS for screw dislocations in α -iron has been calculated previously using the Mrovec parameters[151], and yielded a value ~ 90 MPa greater than that found here, or around one step of the stress application; this was considered a small enough difference to be possibly due to the difference in relaxation scheme or stress increment (which were FIRE and $0.0005C_{44}$ respectively in the previous paper) and that these cells were still valid for the comparison of parameter sets. Previous estimates for the Peierls stress from interatomic potentials for iron range between 740 – 1820MPa, al-

though most are $< 1300\text{ MPa}$ [24, 145, 152]. As mentioned, the DFT estimates of the Peierls stress from the slope of the barrier range from $1 - 1.4\text{ GPa}$ [46, 47, 94]; the value estimated for the Paxton parameters using this method differed from the calculate value by $\sim 100\text{ MPa}$, but that for the Mrovec parameters differed by $\sim 1\text{ GPa}$, possibly affected by inaccuracy in the estimation of the core position. All of these estimates are several times larger than those obtained by extrapolating experimental measurements of the yield stress and flow measurements at low temperature to $0K$, which commonly range between $360 - 440\text{ MPa}$ [153, 154]. This is a feature common to all BCC atomistic simulations and a number of explanations have been offered; such as the interactions with other dislocations lowering the measured Peierls stress[155].

The Paxton parameters then produce a satisfactory estimate for the Peierls stress, but the glide had an anomalous pattern. The Peach-Koehler force on the dislocation for this stress should point solely in the [112] direction, and so the dislocation should glide only along the MRSSP, or $(\bar{1}10)$; this is the case for the Mrovec screw but the Paxton screw repeatedly cross-slips along (101) . The first step for the Paxton case was actually along (101) , and then it continued to take steps along both $(\bar{1}10)$ and (101) such that its average glide plane was close to $(2\bar{1}1)$, as shown in figure 3.5. This form of glide, in response to pure shear, has been observed previously for several atomistic potentials for α -iron[145, 152], as well as other BCC metals[156]; however it disagrees with the results found from experiment[157], which show that average glide at low temperatures is primarily along $\{110\}$ planes except when the MRSSP is close a $\{112\}$ plane. These experimental results have been replicated with the DFT-parameterised line tension model of *Itakura et al.*[94], which also predicted slip along the $\{110\}$ MRSSP with a deviation of less than 2° . When the MRSSP was a $\{112\}$ plane this model predicted average slip on that plane by random successive migrations on the two equivalent $\{110\}$ planes.

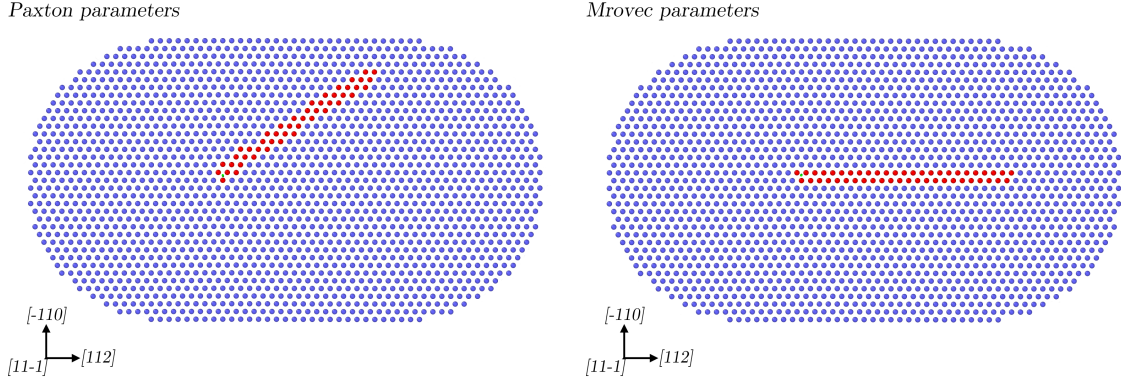


Fig. 3.5: Shown in red is the path the screw dislocation followed under the action of pure shear stress (σ_{yz}) for both sets of parameters; the starting position is marked with a green circle. Only active atoms are shown, marked in blue.

The EAM potential of *Wen et al.*[145] showed the same form of anomalous slip as the Paxton parameters, but yielded a degenerate core structure instead of the non-degenerate form found with the Paxton parameters and widely accepted to be correct. This difference in core structure is particularly important because the zig-zag path was theorised to be due to the two degenerate forms of the core: the barriers between these variants became non-equivalent under stress and so it became energetically favourable to repeatedly cross-slip to bypass the higher barrier. *Xia et al.*[152] used an EAM potential that reproduced the non-degenerate core structure to observe the effects of non-glide stresses on screw dislocation glide; this potential was found to follow the yield criteria established for BCC materials by previous BOP results at 0K[158]. In the case of pure shear stress the screw dislocation had the same compound $\{112\}$ glide as observed with the Paxton parameters, but only required small amounts of shear along the plane perpendicular to the glide plane (non-Schmid stress) for the screw dislocation to switch to gliding on the MRSSP. It was also found that in the case of pure shear strain (only $e_{yz} \neq 0$) the screw remained in the MRSSP, which would also include non-glide stresses in the stress tensor; however when this form of strain was applied for the Paxton parameters the average glide plane remained as $(2\bar{1}1)$.

Comparison may also be made with the results of *Ito and Vitek*[156], who used interatomic potentials to model the response of screw dislocations to stress for a range of BCC materials. In the case of tantalum the screw dislocation had a non-degenerate core structure and also moved along a $\{112\}$ plane when the MRSSP was $\{110\}$. They interpreted this slip as being either due to sequential jumps along the equivalent $\{110\}$

planes, to give an average $\{112\}$ glide, or the formation of three partials on the three adjacent $\{112\}$ planes, forming a microtwin, which then glides along that plane.

Chen et al.[151] found this $\{112\}$ glide with a BOP model with the Mrovec parameters previously: they found that the application of both the pure shear stress and non-Schmid stresses perpendicular to the glide direction could make glide along the horizontal MRSSP less favourable until both it and the diagonal $\{110\}$ slip systems were activated. This was also found by *Chaussidon et al.*[24] using an interatomic potential that reproduced the non-degenerate core and glide along the MRSSP: even small deviations in the angle of the MRSSP such that it sheared the $\{112\}$ planes in the twinning sense would result in average glide along a $\{112\}$ plane. They found that, when the lattice is sheared parallel to a $\{112\}$ plane, the asymmetry of the lattice across this plane caused additional tensile stresses which, if prevented from relaxing by rigid boundaries, can then generate shear components perpendicular to the glide direction. However the shear applied in this case was pure shear on the $(01\bar{1})$ plane, which is symmetric and so should not generate these additional non-Schmid stresses. Nonetheless, some simulations were run without inert boundary atoms to test whether image forces could be affecting the glide, but there was no change in result.

The BOP with both sets of parameters was then used to simulate the stress induced transmission of screw dislocations through grain boundaries (GBs). A simple, symmetric $\Sigma 3$ $[\bar{1}10]$ tilt GB was introduced to the cell by reversing the z -ordering of the atoms in the $(\bar{1}10)$ planes beyond a certain point such that the GB was along a (112) plane with a tilt angle of 70.53° . The structure of this GB is mirror-symmetrical, and so the slip systems on either side of the boundary are equivalent. The screw dislocation was then introduced to the cell using the solutions of anisotropic linear elasticity and the same stress was applied as in the previous simulation.

The formation energy for the $\Sigma 3(112)$ grain boundary was 0.38 Jm^{-2} and 0.45 Jm^{-2} for the Paxton and Mrovec parameters respectively. Both of these results fall within the range set by previous GGA-DFT simulations of $0.34 - 0.47 \text{ Jm}^{-2}$ [66, 159–161], interatomic potentials on the other hand tend to fall within the lower range of $0.26 - 0.38 \text{ Jm}^{-2}$ [161–163]. Interatomic potentials tend to underestimate the energy of this GB due to their central force character: the structural variation from the bulk for first and second neighbours is solely angular, with no difference in atomic separation. If the interatomic potential does not take bond-angle dependence into account then it will only be the more distant neighbours that contribute to the energy[164]. The low formation energy of this GB is reflected in the small amount of atomic distortion

Preliminary Dislocation Calculations

associated with it, which may also be seen by the small variation in magnetic moments: the Paxton and Mrovec parameters showed an increase of only $0.07\mu_B$ and $0.05\mu_B$ respectively for the interface atoms, although *Du et al.*[66] found a slightly greater increase of $0.15\mu_B$ for these atoms with GGA-DFT.

Studies on this GB structure generally find that it has two forms that are nearly energetically degenerate: they are known as the "reflection" and "isosceles" and are illustrated in figure 3.6. The reflection structure refers to the form that is mirror-symmetric across the GB plane, while the isosceles form may be obtained by displacing the lower grain by $-\frac{a}{12}[11\bar{1}]$, where a is the lattice parameter. The form that is preferred energetically depends both on the material and the model applied: *Mrovec et al.*[165] found with environment-dependent DD-TB that the preferred form differed in Nb and Mo, but had the opposite preference when simulated with mixed-basis pseudo potentials, while screened-BOP showed the isosceles form to be preferential for both. In iron, *Bristowe and Crocker*[166] simulated this boundary with interatomic potentials and found that the isosceles structure was preferred by 0.003Jm^2 without volume relaxation, or the reflection structure was preferred by 0.002Jm^2 if the volume was relaxed. *Papon et al.*[167] also found the reflection structure to be preferred by $0.054 - 0.129\text{Jm}^2$ using a moment-expansion of the DOS based on a d -orthogonal TB Hamiltonian, depending on the parameters used. Both sets of parameters used here gave a lower energy for the isosceles form, by 0.028Jm^2 and 0.073Jm^2 for the Paxton and Mrovec parameters respectively; however, the reflection form will still be used in the following, both because it has been observed with electron microscopy in α -iron[168] and to facilitate comparison with a previous BOP study of $\Sigma 3\{112\}$ grain boundary/screw dislocation interactions[164].

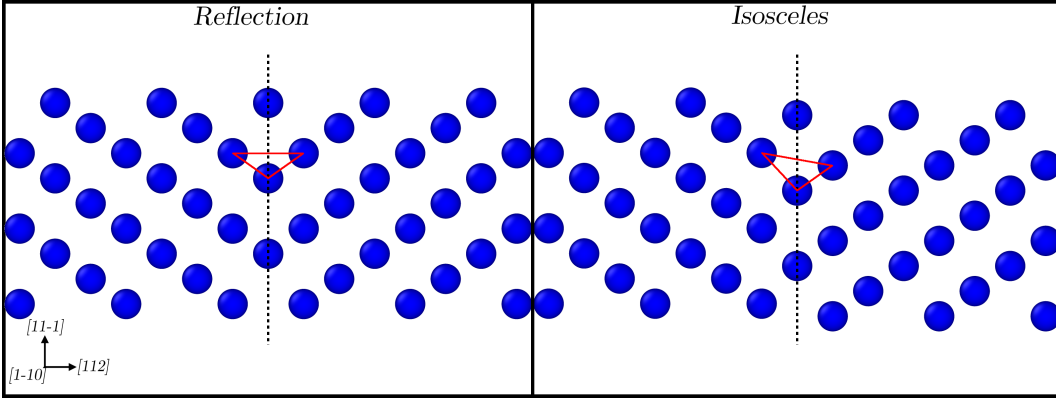


Fig. 3.6: Shown are the two common forms found for the $\Sigma 3(112)$ grain boundary in BCC materials, the GB plane is marked with a dashed line.

There may be several outcomes for a dislocation impinging on a GB, depending on the geometry of both: the dislocation may be transmitted directly, the transmission may involve some translation, the dislocation may be absorbed or residual dislocations may be left behind after transmission. Since the slip systems on either side of the boundary are equivalent residual dislocations are not required to conserve the Burgers vector, and so the last outcome is unlikely. The screw dislocation glide will also be affected by interaction with the GB: as seen from the previous results, the glide of a screw dislocation is very unstable and can easily cross slip on each of the $\{110\}$ planes if the applied stress generates corresponding components of the glide force. The GB stress field may induce additional glide forces that assist in the cross-slip on another $\{110\}$ glide plane, and so the direction of motion could be affected by the GB structure.

The results for the interaction between the $\Sigma 3(112)$ boundary and screw dislocation for the Paxton and Mrovec parameters are shown in figure 3.7: **a)** shows the path of the dislocation and **b)** shows the resulting structure at the end of the simulation. The Mrovec case showed a slight decrease of $0.01C_{44}$, or 72MPa, to the glide stress, possibly due to a slight attraction between the dislocation and the GB, while the Paxton screw showed no change in Peierls stress. The Paxton screw impinged on the GB at $0.054C_{44}$ and was transmitted at $0.060C_{44}$. No residual dislocations were left at the GB, as expected, but the dislocation was translated up to the next $(\bar{1}10)$ plane during transmission. In the case of the Mrovec parameters the dislocation impinged on the GB at an applied stress of $0.033C_{44}$ but was not re-emitted, instead forming a step-like structure in the GB slightly above the absorption site, as shown in figure

3.7 b). This structure has a width of two (112) atomic planes, with the boundary displaced in opposite directions above and below the step.

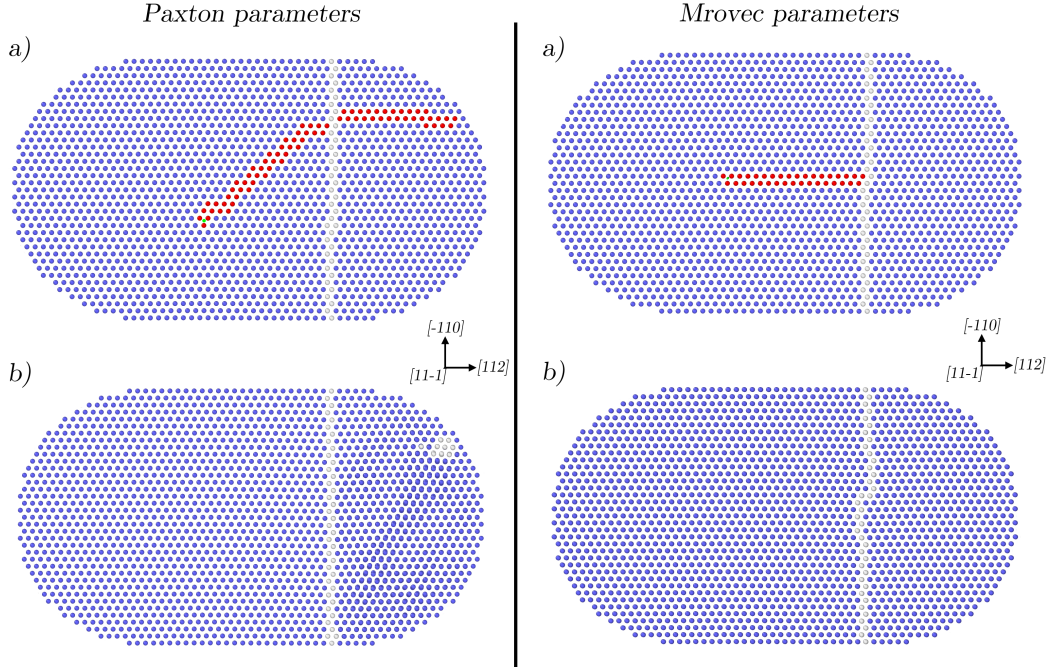


Fig. 3.7: Shown in a) is the path taken by the screw dislocation under pure shear stress with a $\Sigma 3(112)$ grain boundary; defected atoms, such as those of the GB, are marked in grey. b) shows the cell at the maximum applied stress, which was $0.068C_{44}$ and $0.057C_{44}$ for the Paxton and Mrovec parameters respectively.

Mrovec *et al.*[164] simulated the interaction of screw dislocations with a $\Sigma 3(11\bar{2})$ GB in BCC tungsten using both the BOP and interatomic potentials. They found that the screw initially moved at the same Peierls stress in the bulk as with the GB and so their interaction did not influence the Peierls barrier of the dislocation. The screw dislocation, upon impinging on the GB, immediately dissociated into three partial dislocations with Burgers vectors of $\frac{a}{6}[111]$; these partial dislocations are geometrically admissible at the GB and may move conservatively along the GB plane. One partial then remains at the dissociation site while the two others repel and propagate in opposite directions along the GB, which displaces the GB such that a step of two $\{112\}$ interplanar spacings was formed at this point. This simulation was repeated with the interatomic potential so that several dislocations could be stressed into the GB, and it was found that the step increased in size for each dislocation absorbed; in this case the cell had free boundaries so that the partials could leave the GB.

This is clearly what occurred in the case of the Mrovec parameters; although, judging from the undisplaced portions of the GB, the partials seem to have only separated by ~ 13 $(\bar{1}10)$ inter-planar spacings at the maximum applied stress, possibly due to interaction with the inert boundaries. This dissociation also seems to occur for the Paxton parameter screw: the step structure forms while the dislocation is still within the GB but, as can be seen in figure 3.8, disappears when the dislocation is transmitted. This implies that the dislocation dissociated but then recombined with increasing stress; this is possibly due to the elements of the force that caused the dislocation to repeatedly cross-slip, so that the force on the partials has elements that tend to move them back together, slightly above the dissociation site. This step structure may be seen more clearly if the partials are allowed to fully separate before they are forced to recombine, by removing the boundary of inert atoms so that the partials may leave the cell. The screw dislocation is then not transmitted through the GB, but an almost identical step structure as that found for the Matous parameters is left behind, shown in figure 3.9.

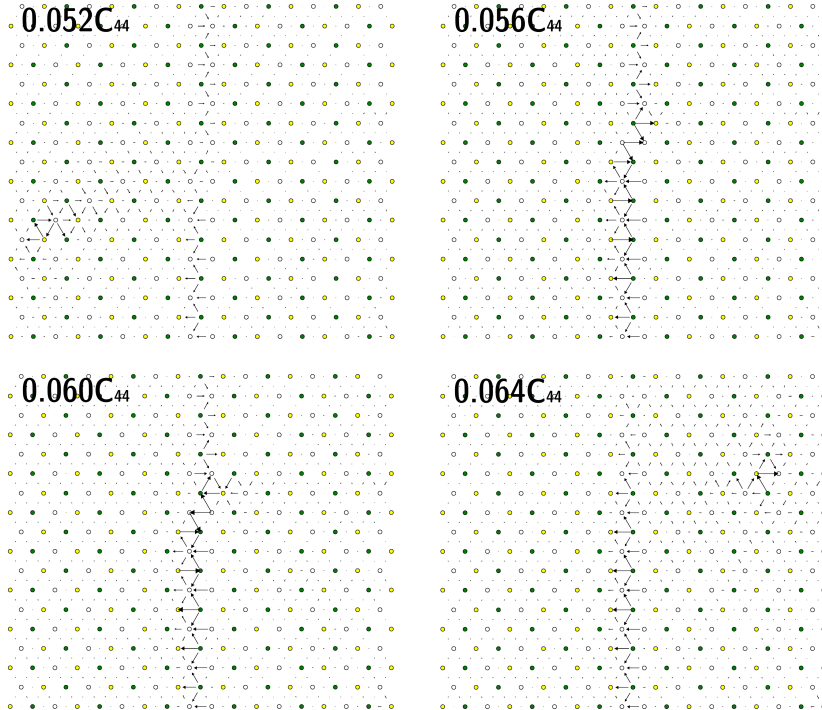


Fig. 3.8: Sequence of differential displacement plots for the transmission of the Paxton parameter screw dislocation through the $\Sigma 3(112)$ grain boundary with increasing stress.

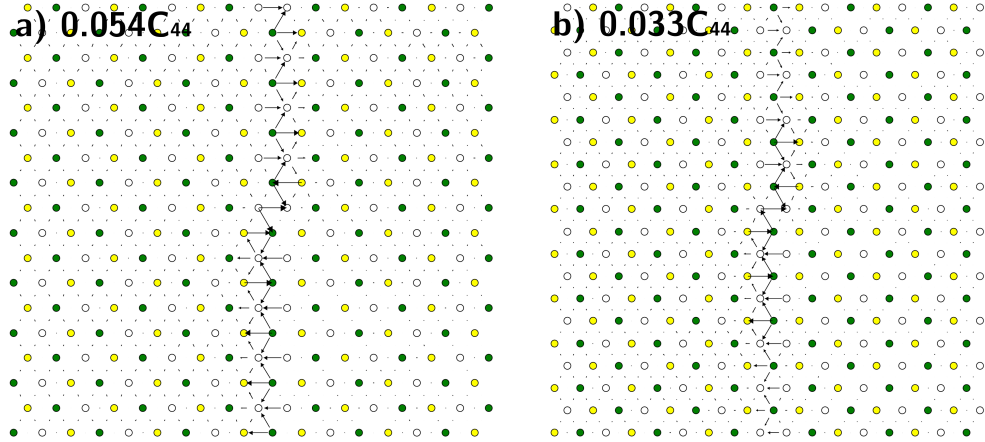


Fig. 3.9: Shown for the **a)** Paxton parameters and **b)** Mrovec parameters with free boundary conditions is the differential displacement plot of the step structure left in the GB after the dissociation of the screw dislocation.

3.4 Edge Dislocations

Simulation Cells

Simulation cells for the two primary types of edge dislocation in BCC materials were produced within BOP using the TB matrix elements. These edge dislocations share the same Burgers vector with the screw dislocation (i.e. $\frac{a}{2}\langle 111 \rangle$) but differ in their glide plane: with one gliding along $\{110\}$ and the other $\{112\}$. The dislocations were again produced using anisotropic linear elasticity: a large, cylindrical cell with a depth of the smallest repeating distance along the dislocation line was produced for each edge (of radius 65Å and containing 7278 atoms for the $\{110\}$ edge and 85Å containing 7774 atoms in the $\{112\}$ case) and the displacement field applied to introduce an edge to the centre. The atoms were then relaxed, apart from a 8Å rim of frozen atoms, using the steepest-descent scheme until the maximum force on an atom was less than $2 \times 10^{-4} \text{ eV}\text{\AA}^{-1}$; a smaller cell of radius 25/30Å was then cut from it for the $\{110\}/\{112\}$ cases, as shown in figure 3.10.

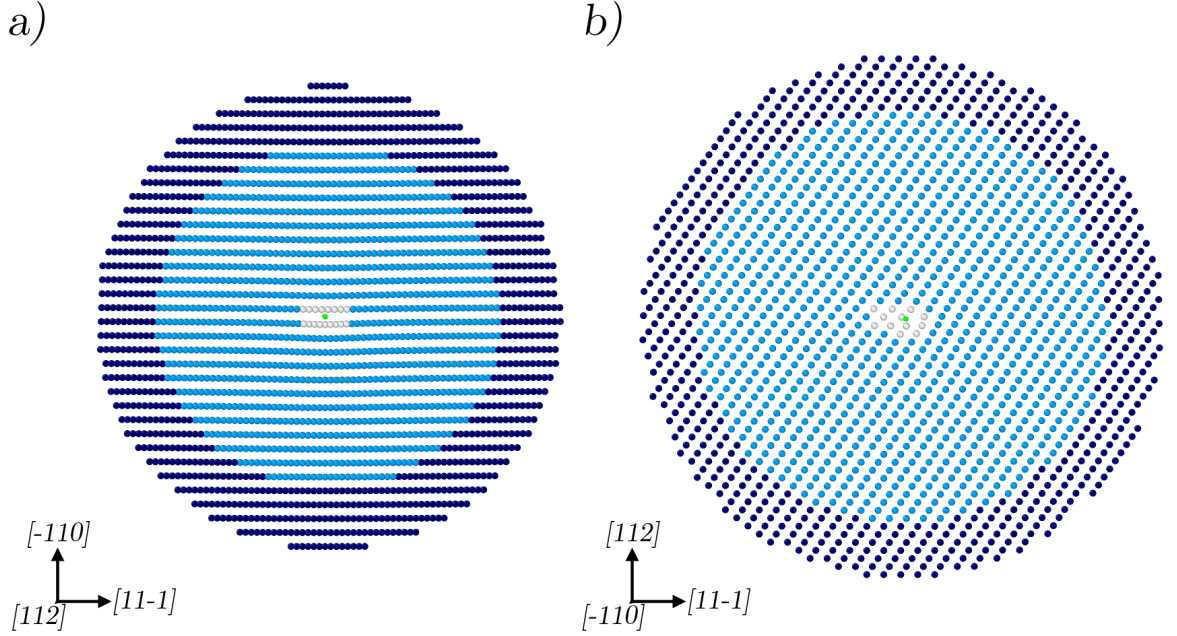


Fig. 3.10: Shown are the simulation cells used for the a) $\frac{a}{2}\langle 111 \rangle\{110\}$ and b) $\frac{a}{2}\langle 111 \rangle\{112\}$ edge dislocations, they are of radius 25Å and 30Å respectively, cut from larger cells. The dislocation cores are marked with a bright green line; the defected atoms around the cores are light grey, the frozen atoms at the boundary dark blue and the rest are active atoms.

The structure of these dislocations can be seen more clearly by comparing the displacements of the atoms in the planes above and below the glide plane. Following *Bulatov and Cai*[169] we define $u^+(x)$ and $u^-(x)$ to be the displacement along $[11\bar{1}]$ of atoms in the upper (tensile region) and lower (compressive region) planes respectively, and define $u(x) = u^+(x) - u^-(x)$ as the disregistry across the glide plane. Also, the conditions $u^-(-r) = u^+(-r) = \frac{1}{4}b$ and $u^+(r) = -u^-(r) = \frac{1}{4}b$ are set (where r is the radius of the cylinder) to facilitate comparison with *Monnet and Terentyev*[170], who simulated the $\frac{a}{2}\langle 111 \rangle\{112\}$ dislocation in α -iron using interatomic potentials previously. The distribution of this disregistry for each dislocation can then be visualised using the disregistry density $\rho(x) = du(x)/dx$, which may be regarded as the distribution of the Burgers vector due to the planarity of the cores. The relative displacements (Δu^+ and Δu^-) were also calculated by subtracting the displacement of each atom from that of the following atom. The results for the $\frac{a}{2}\langle 111 \rangle\{112\}$ edge are shown in figure 3.11.

Similar to the findings of *Monnet and Terentyev*, the variation of $u^+(x)$ in the

upper, tensile, region was abrupt, while that of $u^-(x)$ in the compressive was much smoother; and both had relative displacements that were asymmetric across the core. This asymmetry is also apparent in the disregistry density which is clearly skewed to one side; while in the Peierls-Nabarro model it would have the symmetric distribution $b\delta(x)$ around the core. *Monnet and Terentyev* found that Δu^+ had a local minimum in the centre of the core, surrounded by two peaks, which is not apparent in the results shown here; also, the single peak of Δu^+ has a maximum $\sim 0.1b$ greater than theirs. The distribution of Δu^- also has significant differences from theirs, which had sharp increases and a flat plateau around the core; although the maximum is almost identical.

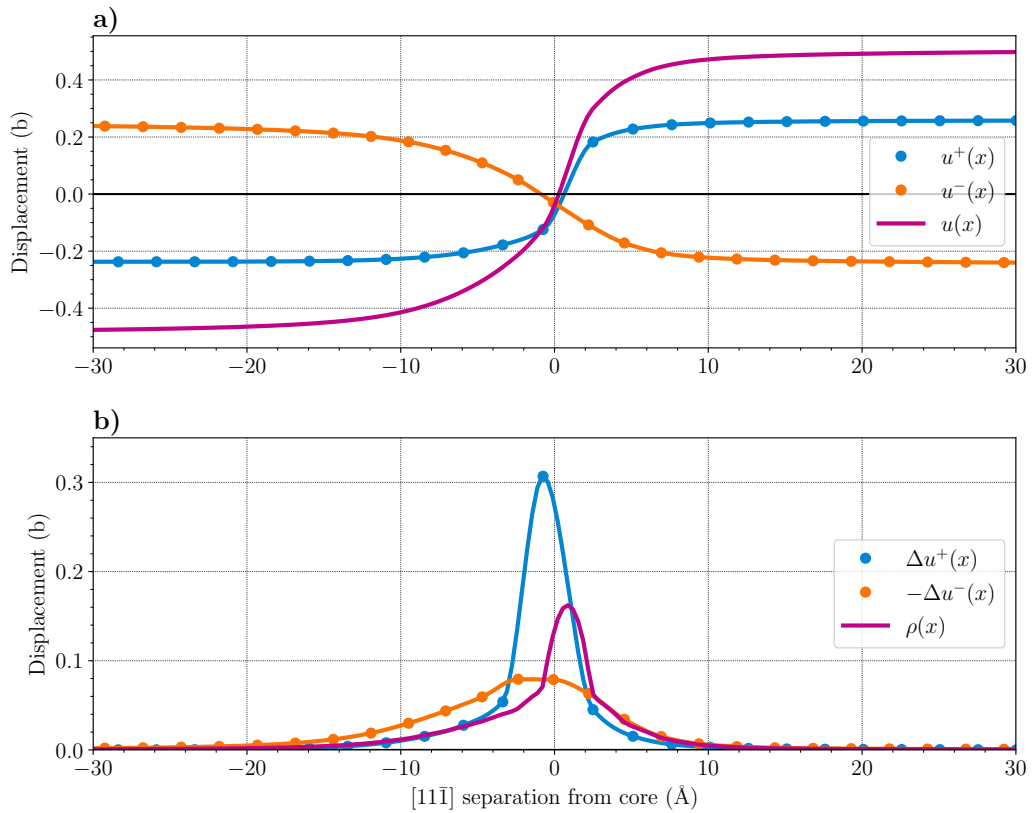


Fig. 3.11: Shown are the displacements from the perfect lattice in the Burgers vector direction for the atoms in the (112) planes above (u_u) and below (u_l) the glide plane of a $\frac{a}{2}\langle 111 \rangle \{112\}$ edge dislocation, where the tensile zone is below the dislocation. The displacements are shown in a) and the differential displacements between neighbouring atoms in b).

This dislocation was also simulated using a TB second-moment model for α -Fe

by *Masuda et al.*[171]. They found that the structure was very sensitive to the details of the model used: by changing the relative decay of the bond integrals and repulsive pairwise functions, the distribution of $\rho(x)$ could be varied between a two peaked structure that could possibly resemble that of *Monnet and Terentyev* to a single peaked structure similar to that found here, but with a greater maximum of $\sim 0.15b$. *Yamaguchi and Vitek*[172] also found that the distribution of $\rho(x)$ varied between a single and double peaked structure depending on the pair potential that was used to simulate the structure.

The distribution of the $\frac{a}{2}\langle 111 \rangle\{110\}$ dislocation is shown in figure 3.12; there is a two-fold axis of symmetry perpendicular to $\{110\}$ planes, and so this core should be symmetric, but there is a slightly asymmetry evident in the distribution of $\rho(x)$, possibly due to an issue with the simulation cell or relaxation scheme. Similar to the structures simulated by *Ingle and Crocker*[173] and *Yamaguchi and Vitek*[174] using interatomic potentials, we find that the disregistry density has a number of peaks surrounding the core; this was interpreted as the Burgers vector splitting and being localised in a number of separate positions within the dislocation core. The latter simulations only showed splitting into three peaks, however this was based on an interatomic potential only required to stabilise the BCC structure rather than a specific metal; the former simulations showed a number of peaks depending on the potential used, some with a minima in the centre. This distribution matches better with that found by *Adams et al.*[175] using interatomic potentials and flexible boundary conditions; however they found the central peak to be smaller than the two surrounding peaks.

More recently *Yan et al.* used Local Spin Density Approximation (LSDA) DFT and spin-polarised GGA-DFT to obtain generalised stacking fault energies for several slip systems, including $[1\bar{1}1](110)$, and used these results to calculate dislocation properties for these systems[176]. They do not include atomic relaxation in their simulations, but generate the disregistry from a calculation based the gradients of the generalised stacking fault energies; the features of the distributions cannot then be compared directly, but some properties may be. They define the half-width of the dislocation as the atomic distance over which the disregistry changes by half a Burgers vector, centred on the dislocation core; the value for the distribution in figure 3.12 is $2.89b$, which compares very well with their value of $3.02b$ for the SGGA and $2.25b$ for the LSDA. The maximum of the disregistry density distribution from the SGGA is $\sim 0.08b$ while that of the LSDA is $\sim 0.1b$ and the value calculated here again falls between

them at $0.091b$.

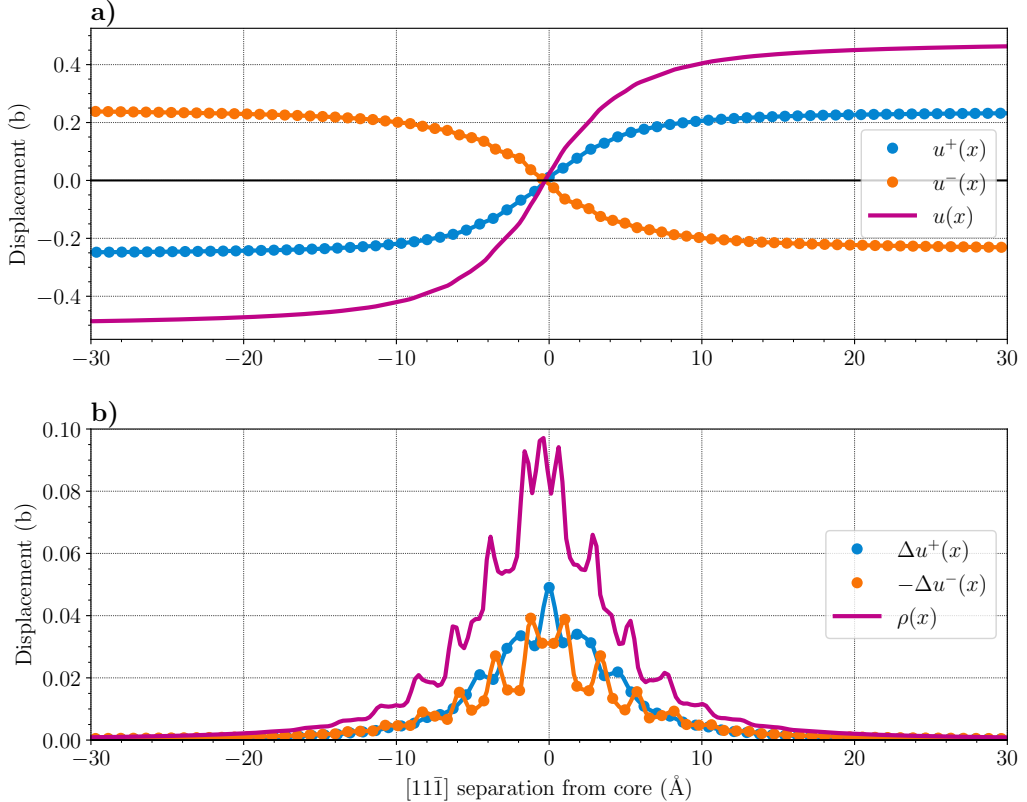


Fig. 3.12: Shown are the displacements from the perfect lattice in the Burgers vector direction for the atoms in the (110) planes above (u_u) and below (u_l) the glide plane of a $\frac{a}{2}\langle 111 \rangle\{110\}$ edge dislocation, where the tensile zone is below the dislocation. The displacements are shown in **a)** and the differential displacements between neighbouring atoms in **b)**.

In summary, we find that the $\frac{a}{2}\langle 111 \rangle\{112\}$ edge dislocation has an asymmetric core with non-equivalent displacements in the upper and lower planes. The $\frac{a}{2}\langle 111 \rangle\{110\}$ dislocation is close to being symmetric, with some minor variations, and the displacements in the upper and lower planes have a much more similar structure; we also see the splitting of the Burgers vector into a number of peaks surrounding the core. Taking the arbitrary limit $\rho(x) < 0.1b$ as the extent of the core, we find that the $\{110\}$ edge has a wider spread of $\sim 22\text{\AA}$ compared to $\sim 19\text{\AA}$ for the $\{112\}$. This is also reflected in the half-widths of the cores: the $\{110\}$ has a value of $2.89b$ while the $\{112\}$ is only $2.03b$.

Vacancy Interactions

Simulations were then carried out to estimate the interaction energy between both types of edge dislocation and vacancies in the lattice. The required cell length to minimise the interactions between vacancy images may be found by estimating the interaction between vacancies at a range of separations. Two large cuboidal cells were used, that had dimensions of $\sim 60 \times \sim 30 \times \sim 30 \text{\AA}$; they have the long axis along either [112] or [$\bar{1}10$] and are surrounded by inert atoms. The two vacancies were then placed at various points and their interaction energies calculated using equation 3.6 below, the results are shown in figure 3.13.

$$E_I^V = E^{2V} + E^P - 2E^V \quad (3.31)$$

where E^{2V} represents the energy of the cell with both vacancies, E^V that with one and E^P that of a perfect lattice. All the energies shown here that would involve a differing number of atoms (such as that of the cell containing a vacancy) will be scaled to that of the energy they are being subtracted from.

Note that the interaction energy becomes fairly meaningless beyond separations of $\sim 15 \text{\AA}$ as at these points the vacancies are closer to the inert boundaries than each other, but the interaction was already reduced to negligible values beyond $\sim 11 \text{\AA}$. These values will also not entirely represent those within the edge cells as the periodic images would involve an infinite line of vacancies rather than just two. The edge cells are then longer than may seem necessary from these results: giving separations of 20.29\AA along [$\bar{1}10$] for the {112} edge and 35.15\AA along [112] for the { $\bar{1}10$ } edge.

The variation in interaction for the most closely spaced vacancies is interesting: the two closest separations, along [111] and [100], have large attractive interactions of -0.26eV and -0.14eV respectively, while the next closest, along [$\bar{1}10$], has a repulsive interaction of 0.03eV and the next point, along [113], is only 0.7\AA more distant but has an opposite interaction of -0.03eV . So, divacancies made up of first and second nearest-neighbours are attractive, but third nearest-neighbours are repulsive. In general, it seems that those along [$\bar{1}10$] or close to it (the angle between it and [$\bar{3}31$] is only $\sim 13^\circ$) are slightly repulsive, while those along [112] and similar directions ([113] and [335] are only $\sim 10^\circ$ and $\sim 5^\circ$ distant respectively) are slightly attractive. Previous estimates from DFT based *ab-initio* models for the $\langle 111 \rangle / \langle 100 \rangle$ divacancy binding energies have been $-0.22 / -0.29 \text{eV}$ [177], $-0.19 / -0.21 \text{eV}$ [178] and $-0.17 / -0.23 \text{eV}$ [179]. All of these results find the second nearest-neighbour structure to be of lower energy,

which is not what is found here, although the energy of the first nearest-neighbour divacancy is quite close. *Masuda*[180] used a TB second-moment approximation to calculate energies for various divacancy structures, and found that the divacancies along $\langle 111 \rangle$ and $\langle 100 \rangle$ were attractive while that along $\langle 110 \rangle$ was repulsive. Interestingly, the binding energies they calculated were much closer to the results presented here before relaxation than after, both in value and ordering: before relaxation they found values of -0.22eV for $\langle 111 \rangle$, -0.15eV for $\langle 100 \rangle$ and 0.03eV for $\langle 110 \rangle$, but after relaxation these became -0.04eV , -0.05eV and 0.18eV respectively. Finally, this variation between attraction and repulsion was also found by *Johnson and Wilson*[181] using a central-force pair potential for iron, who found a binding energy of -0.14eV for the $\langle 111 \rangle$ case and 0.04eV for the $\langle 110 \rangle$ one, but they also found a much stronger binding of -0.28eV for the $\langle 100 \rangle$ case.

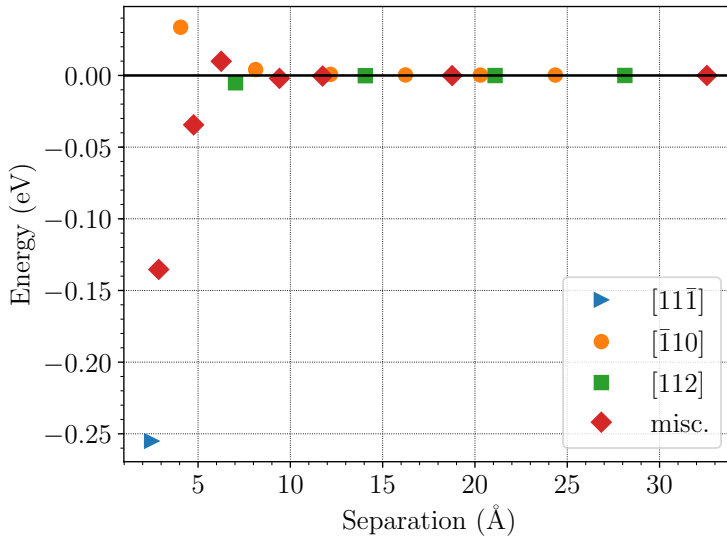


Fig. 3.13: Shown is the interaction energy between two vacancies with varying separations along the axes shown; the miscellaneous axes are, starting from the closest, $[100]$, $[113]$, $[\bar{3}31]$, $[335]$, $[337]$, $[5, 5, 11]$ and $[15, 1\bar{7}, \bar{1}]$

The chosen edge cells had radii of 30\AA and 25\AA for the $\frac{a}{2}\langle 111 \rangle\{112\}$ and $\frac{a}{2}\langle 111 \rangle\{110\}$ dislocations respectively. The validity of these cells, along with the validity of this parameter set to describe vacancies, may be further checked by calculating the vacancy formation energy with each cell, which is:

$$E_f^V = E^V - E^P \quad (3.32)$$

Preliminary Dislocation Calculations

This gives a result of 1.55eV for both cells, which is slightly low but close to the range set by previous DFT calculations of 1.61 – 2.02eV[178, 182, 183], within that of predictions from experiment which range between 1.53 – 2eV[184, 185], and very similar to the result of 1.53eV from a recent EAM simulation[186].

The interaction between the vacancy and dislocation can then be estimated as[173]:

$$E_I^{DV} = E^{D+V} + E^P - E^D - E^V \quad (3.33)$$

E^{D+V} represents the energy of the cell containing both the dislocation and vacancy and E^D is the cell containing only the dislocation. Atoms were removed from various sites surrounding the dislocation, above and below the glide plane, to observe the variation of this interaction energy with separation. Note that, due to the small Peierls barrier for edge dislocation motion in BCC metals, the core was expected to shift for some of the smaller separations and so the new separation after relaxation had to be calculated. This was done using the dislocation analysis tool within the visualisation software OVITO[187]: areas of defected material are identified by comparing the Delaunay tessellation and common neighbour analysis with that of a perfect reference crystal. Dislocation cores are then identified by carrying out Burgers circuits of increasing length around these defected areas until a non zero Burgers vector is encountered, the dislocation core is then designated as the centre of mass of this circuit. The vacant site was filled with an atom before this analysis to prevent the extra defected material from skewing the core position; however, this method is flawed for sites close to the core. The displacements of the atoms surrounding the vacant site will still extend the defected region and so the position in these cases should be considered a rough estimate.

The results of these simulations are shown in figure 3.14. Both dislocations show much stronger binding energies in the compressive region below the core than the tensile region above, this is due to the vacancy relieving the stress field of the dislocation; although, as noted by *Ingle and Crocker*[173], if this were the only effect then the sign should change across the slip plane, and so the interactions likely have a certain degree of second order inhomogeneity character as well[188]. The peak binding energies of the {112} dislocation in the atomic planes immediately above and below the core are almost double those of the {110} case: where it has -1.46eV below and -0.63eV above compared to -0.80eV below and -0.34eV above. However by $\sim 3\text{\AA}$ below the core the peak binding energies are almost identical, above the core the {112} is still slightly greater. Note that $\sim 3\text{\AA}$ above or below the core is the second atomic plane

Preliminary Dislocation Calculations

from the glide plane for the $\{110\}$ edge, but the third from the $\{112\}$ edge. The $\{112\}$ core also shows a slight repulsion in the tensile region for one of the sites, which was not found anywhere for the $\{110\}$ case.

The asymmetry of the $\{112\}$ edge core is reflected clearly in the pattern of binding energies in the plane immediately above the core, which have a much slower decline on one side than the other. The issues with the method of core determination become clear for the four strongest binding sites around the core, for which the core seems to have moved such that each is in the same site. Note that this inaccuracy in core position is further exacerbated by the fact that the core position is averaged down the cylinder: the kink structure in the edge is very low energy and so it can be energetically viable for part of the dislocation line to bend toward the vacancy such that it was more strongly bound[189]. Judging from the variation in binding energies, the $\{110\}$ edge does not seem to have shifted during the simulations for vacancy positions near the core, this could be because of the weaker binding energies associated with this edge or possibly indicate a larger Peierls barrier. In any case, the symmetry of this core is also reflected in the pattern of binding energies.

It is difficult to find any results in the literature for the the vacancy interaction with a $\{112\}$ edge, although there are several previous results for the $\{110\}$ type. Surprisingly, the results of *Ingle and Crocker*[173] using a simple interatomic potential[190] were quite close: for the $\{110\}$ type the peak binding energies above and below the core were only 0.1eV smaller,. For the $\{112\}$ type, although the peak binding they predicted was smaller by 0.34eV, they did predict that some positions in the tensile region would be repulsive. These universally lowered binding energies are likely due to the lower vacancy formation energy of 1.37eV predicted by this potential. Strangely, *Kirisanov et al.* used the same potential to describe the vacancy interaction with the $\{110\}$ dislocation and found that that peak binding energy had a greater value of 1.07eV and that the majority of sites in the tensile region below were repulsive, but they did not include periodic boundary conditions along the dislocation line. Other predictions of this peak binding energy for the $\{110\}$ case have been 0.82eV[191], 1eV[192] and 0.92eV[193], from an EAM potential, interatomic potential and a FS potential respectively.

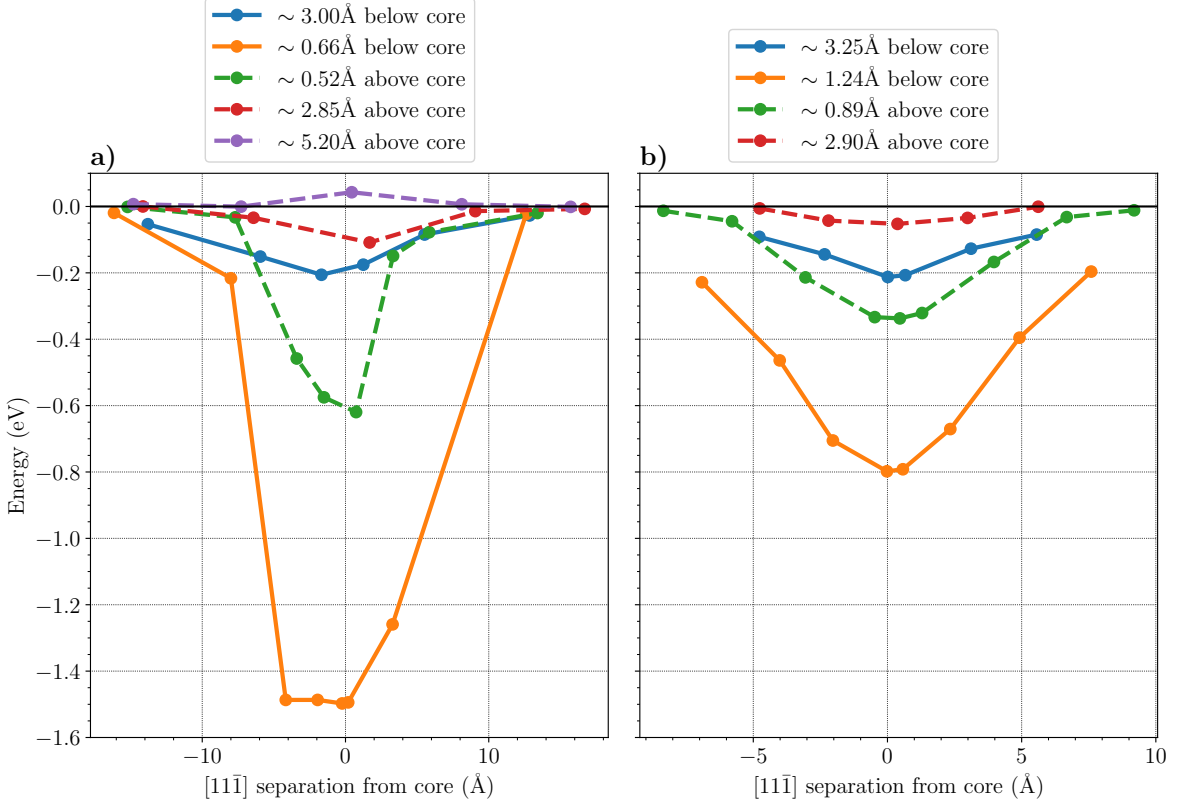


Fig. 3.14: The interaction energy between a vacancy and **a)** a $\frac{a}{2}\langle 111 \rangle\{112\}$ or **b)** $\frac{a}{2}\langle 111 \rangle\{110\}$ edge dislocations as a function of the separation between the vacant site and the dislocation core along the glide direction of the dislocation (i.e. $[11\bar{1}]$), sites in the tensile region are marked with a dashed line and those in the compressive with a solid one. The dislocation core position was recalculated for each case.

Simulating Climb

When the vacancy is located in the strongest binding site at the core of the edge dislocation, in the compressive region, the structure is equivalent to the dislocation having a double-jog present. The interaction energy between the vacancy and dislocation at this point could then be interpreted as the energy required to form the two jogs added to the energy of their mutual interaction[173]. Although the formation energies were not extracted, due to the size of the cell that would be required to minimise these interactions, it is still of interest to examine the intermediate structures involved in climb. Due to the six-layer structure of the $\frac{a}{2}\langle 111 \rangle\{110\}$ edge core, it was decided that it would be easier to interpret the climb simulations for the $\frac{a}{2}\langle 111 \rangle\{112\}$ edge,

the asymmetry of its core notwithstanding.

Pairs of positive or negative jogs were produced by cutting smaller disks from the relaxed edge structure and stacking them such that the edge changed glide planes twice along the length of the cylinder. The relaxed edge dislocation in the upper glide plane was produced by taking the large relaxed cell and adding vectors of $\frac{a}{6}[11\bar{1}]$, $\frac{a}{6}[112]$ and $\frac{a}{2}[\bar{1}10]$ to the coordinates of the atoms, where a represents the lattice parameter, and then folding the $[\bar{1}10]$ coordinate back if it went beyond the bounds of the layer, or $a[\bar{1}10]$. The equivalent structure in the lower glide plane was produced by taking these vectors away instead of adding them, and shifting the $[\bar{1}10]$ coordinate up by $a[\bar{1}10]$ if it went below zero.

The required cell size to converge these structures may be estimated by considering an edge with a pair of negative jogs separated by one layer to be a straight dislocation with an interstitial bound to it, or that with positive jogs to have a vacancy bound, and then calculating the variation in binding energy with cell radius and cell length; results are shown in figures 3.15 and 3.16. The binding energies both seem fairly well converged with radii by 25Å, although the interstitial case has a slight jump at 30Å this is only by 30meV, and the change from this value to the value at 45Å is only 46meV. The variation with cell length also seems to converge beyond values of 16.24Å, changing by only 28meV by a length of 113.65Å; note that this variation seems to be linear, possibly an issue with the relaxation or a slight difference in the cells that increases with the number of layers. Note also that the formation energy for this $\langle 111 \rangle$ interstitial dumbbell only varies by 9meV across this range, giving a value of 3.97eV which agrees fairly well with a previous DFT prediction of 4.11eV[183].

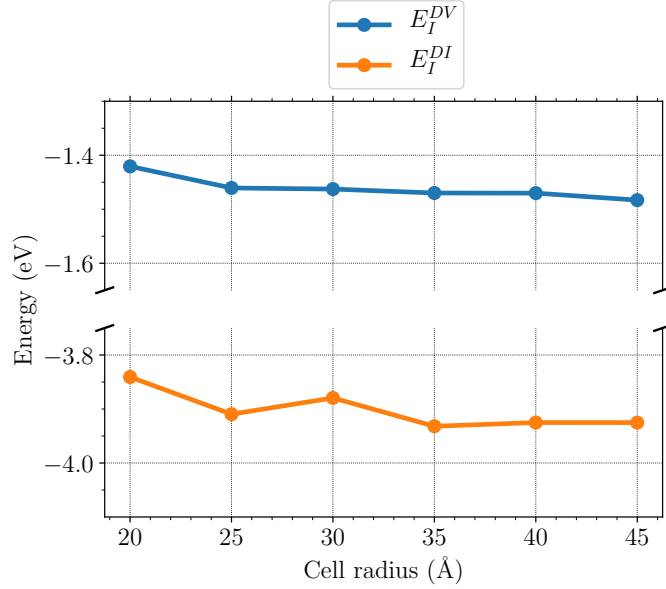


Fig. 3.15: An edge with a pair of negative/positive jogs is considered to have an interstitial/vacancy bound to it, the binding energies are then calculated at a range of cell radii; the cell length is 20.29Å.

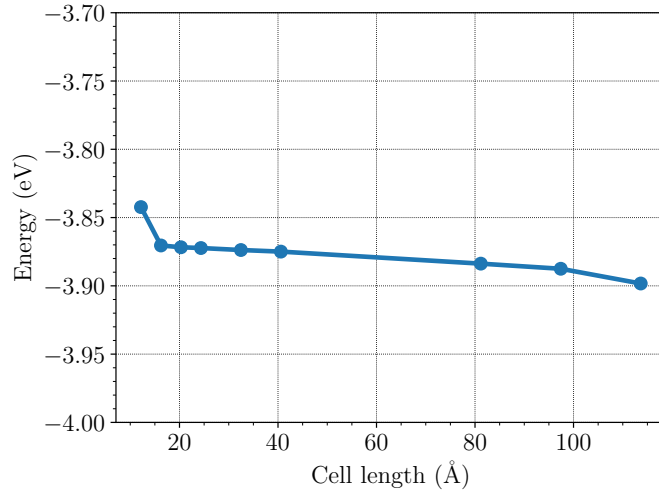


Fig. 3.16: The variation in binding energy with cell length between an edge dislocation and an interstitial; cell radius is taken as 30Å.

Lau et al.[194] used a FS potential to model the climb of a $\frac{a}{2}\langle 111 \rangle\{110\}$ 71° mixed dislocation by vacancies binding to the core, they stated that the climb process could be separated into three events: the creation of a jog-pair by the binding of a vacancy

to the edge core, the extension of this jog-pair with additional vacancies and finally the union of two jogs. They calculated the sequential binding energies of vacancies to the dislocation line and explained the trend found in the context of dislocation line length change: the binding energy of the first vacancy was the lowest, because it involved the creation of extra line length. The binding energy of the last vacancy, which unified the jogs so the entire line moved to the next glide plane, had the highest value because it removed the extra length. Finally, the intermediate vacancies all had binding energies close to halfway between these two values because they didn't involve any change in length. In order to simulate this process an edge dislocation cell was constructed with a radius of 40Å and a length of 10 lattice layers, or 40.6Å; 11 replicas of this cell were produced, the first with a straight edge dislocation and each subsequent cell with a positive jog pair of increasing width until the entire edge was moved to the next glide plane. The binding energy of each subsequent vacancy may be calculated with equation 3.33, where E_D now represents the energy of the cell with the dislocation and N_V vacancies, and E_{D+V} that with $N_V + 1$; the results are shown in table 3.1.

The pattern is the same as that found by *Lau et al.* in that the first vacancy has the lowest energy and the last the highest, while the others are intermediate. However they found greater jumps in energy: between $N_V = 0$ and $N_V = 1$ their binding increased by 78% and between $N_V = 8$ to $N_V = 9$ it increased by 23%, while the results here had increases of 4% and 0.6% respectively, and a fairly smooth increase of the intermediate values. Also, the binding energy of the last vacancy in their case was almost double that of the first; these large, sharp, differences could imply the dislocation considered here has a lower line energy than the mixed dislocation they considered, so that changes in length did not change the energy so greatly.

The gradual shift in intermediate values may be rationalised by the gradual shift in the dislocation line: the position of the line is determined by the strain it produces rather than the exact positions of the line of atoms along its edge. The binding of the first vacancy would not create a sharp jump to the next glide plane but rather a curve in the line in that direction, which would be accentuated with the binding of each subsequent vacancy. This may also be visualised as the interaction between the jogs in the pair, which would gradually decrease as they separate and then begin to increase again as the jog images approach each other, which may be seen by how the binding energies become almost constant for $N_V = 4$ and $N_V = 5$. The constancy in the intermediate values found by *Lau et al.* may indicate a shorter interaction range for jogs along that dislocation line, or a limitation of the potential used. Note that

this is not the same interaction as was plotted in figure 3.16, which demonstrated the interaction between images of a single-layer jog pair.

N_V	E_I^{DV} (eV)	N_V	E_I^{DV} (eV)
0	-1.460	5	-1.537
1	-1.514	6	-1.540
2	-1.530	7	-1.551
3	-1.534	8	-1.560
4	-1.536	9	-1.570

Table 3.1: Binding energies of vacancies to the core of a $\frac{a}{2}\langle 111 \rangle\{112\}$ edge dislocation with N_V vacancies already bound to it. The vacancies bind in a continuous line such that each subsequent vacancy is equivalent to the climb of another section of the edge, and the cell has 10 layers so that the binding of the 10th vacancy completes the climb event.

The NEB method was then employed to calculate the barriers for vacancy migration to the edge core, both for the initiation of a climb event by the production of a positive jog pair on a straight dislocation and the completion of a climb event by the union of two jogs. Due to the memory limitations associated with NEB these cells were limited to a radius of 30Å and a length of 20.29Å. Three paths were simulated for each transition: the vacancy moving between 1st nearest-neighbour sites from the tensile zone and from first and second nearest-neighbours from the compressive zone, these paths are illustrated in figure 3.17. Vacancy migrations from the glide plane were not simulated as the edge would move during the relaxation of the image.

The results are illustrated in figure 3.18, where **a)** shows the climb initiation process and **b)** the completion. As could be expected, the barrier for path III between 2nd nearest-neighbour sites from the compressive zone is much higher than the other two, between double and triple their value in both cases. In case **a)** the path from the tensile zone, or path I, has the lowest barrier at 0.29eV compared to 0.40eV for path II from the compressive zone. Interestingly the barrier for path I and III increased to 0.38eV and 0.91eV respectively for the jogged dislocation, while that for path II decreased to 0.33eV so that it becomes the lowest energy path.

Lau et al. also simulated these events, a complete match was not expected due to the differing dislocation type. For the case of the vacancy migration to the straight dislocation they found that the path from the compressive region (equivalent to path II) had the lowest barrier, less than half that of the tensile path (path I). Although,

similar to these results, they found that the barrier for the compressive path decreased by $\sim 30\%$ in the case of the jogged dislocation; they did not simulate the other paths for this case. The results found here broadly agree with the conclusions of *Lau et al.*: the barriers for vacancy migration to the edge core are dependent on the jog structure at the core and the angle of the path with respect to the dislocation line, which is commonly neglected in analytic studies of climb; although this angular dependence is not as strong as found in their case.

The vacancy migration energies in the bulk were also calculated using NEB for this cell and are shown in figure 3.19: the 1st nearest-neighbour transition is equivalent to paths I and II, and the 2nd to path III. All three paths then show a great reduction in barrier from the bulk case, by a factor of at least 3. Note however that these barriers for the vacancy migration seem to be overestimated here: nearest-neighbour migration barriers from DFT-based calculations range between 0.64–0.67eV[177, 183, 195], while estimates from experiment have been as low as 0.55eV[196]. These results show some disagreement with those of *Lau et al.*: although they found that the path from the compressive zone was decreased greatly with respect to that in the bulk, they actually found a slight increase for the tensile path. This simulation was also carried out with a periodic block of 1079 atoms, of dimensions $24.85 \times 21.09 \times 24.35\text{\AA}$, and the result varied from that of the cylindrical cell by only 20meV, implying that the inert atoms in the cell do not greatly interfere with these simulations.

This process of climb, i.e. by the migration of vacancies to the core, may not be relevant in the case of an immobile jog on a screw dislocation at normal temperatures. The barrier to vacancy diffusion is quite significant, as shown above, and these segments will not be able to glide and sweep up vacancies like a normal edge dislocation. The reverse of this process may be more relevant in this case, or the emission of vacancies by jog climb. In this case **b**) represents a straight edge dislocation emitting a vacancy to become a jogged dislocation and **a**) represents a jogged dislocation emitting a vacancy to become a straight edge dislocation. Interestingly the preferred path shows the same general pattern as for vacancy absorption: in **a**) the tensile path I has the lowest barrier at 1.18eV while the compressive path II is 1.37eV, while in **b**) the barrier for path I increases to 1.51eV and that for path II decreases to 1.06eV. Path III is once again high energy in both cases: with a barrier of 1.84eV in **a**) that decreases slightly to 1.74eV in **b**). So, once again the barrier for this process is strongly dependent on the orientation of the path, and the energetically preferred path changes region between the jogged and straight dislocations.

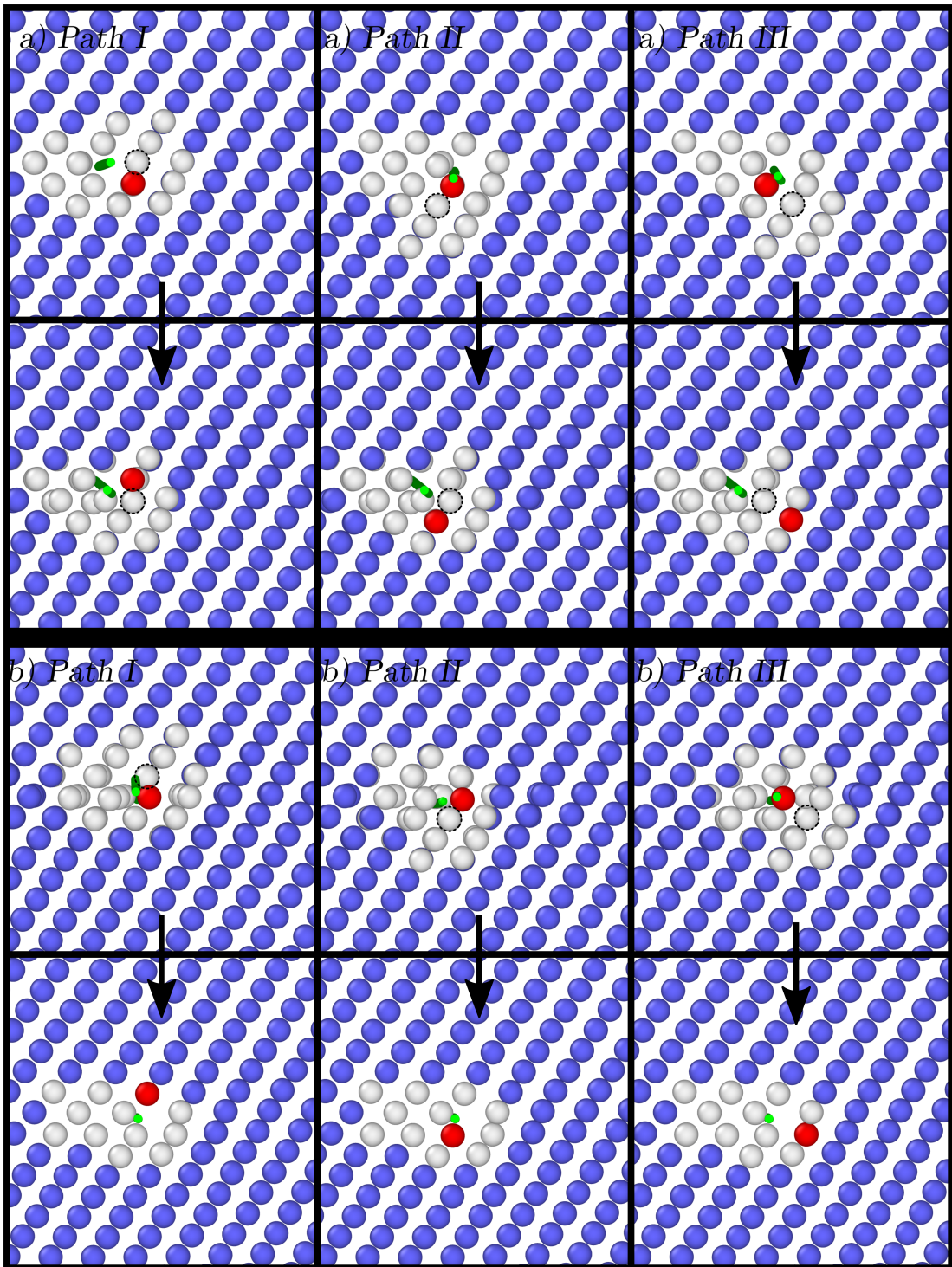


Fig. 3.17: Shown are the initial and final images for the NEB simulations of a) a vacancy binding to a straight $\frac{a}{2}\langle 111 \rangle\{112\}$ edge to create a positive jog pair and b) a vacancy binding to a jogged dislocation and leaving it straight; these processes can be considered as the initiation and completion of a climb event. The dislocation line is marked in green, the vacant site with a dashed circle and the atom that fills it is marked in red.

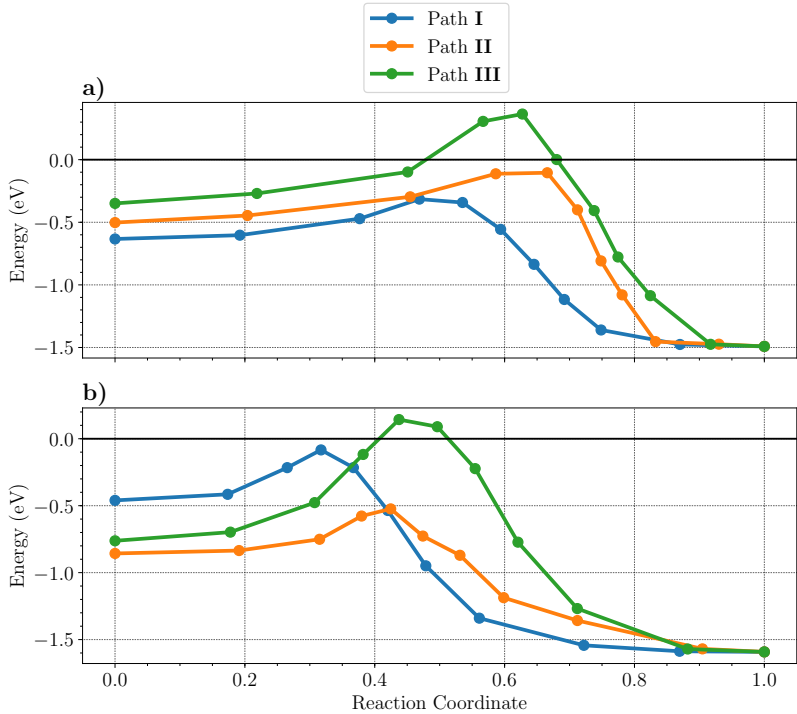


Fig. 3.18: Shown are the barriers obtained from NEB for the vacancy migrations associated with the **a)** beginning and **b)** end of a climb event, or equivalently the creation of a positive jog and destruction of a negative jog by a vacancy binding to the edge dislocation line. The energy scale is the interaction energy between the vacancy and the edge.

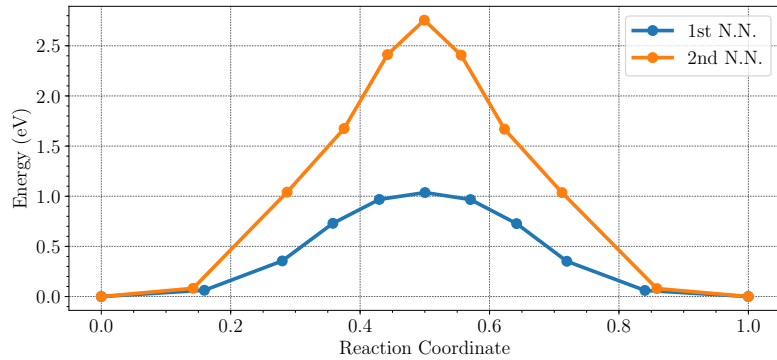


Fig. 3.19: Barriers from NEB simulations of vacancy migration in the bulk between 1st and 2nd nearest-neighbour sites.

3.5 Conclusions

A number of dislocation processes were simulated using the BOP model with two parameter sets: one fitted for used within the BOP model by *Mrovec et al.*[58] and one fit for DD-TB by *Paxton and Elsässer*[105]. The main purpose of the initial simulations, run with both sets of parameters, was to further test the and flexibility of the Paxton parameter set within BOP. This was particularly important as this Paxton parameter set was to form an integral part of the embedding model described in chapter 7; it is also employed in a number of calculations throughout this thesis. The simulations based around screw dislocations included calculating the core structure, Peierls barrier, the response to stress and the interaction with a $\Sigma 3(112)$ GB. Both parameter sets produced the non-degenerate structure that is generally accepted for screw dislocations in BCC materials, and the pattern of magnetic moments found with the Paxton set was closer to previous DFT results. However the Mrovec estimate for the Peierls barrier that was closer to the range set by *ab-initio* results, within $2\text{meV}/b$ of GGA-DFT value from a similar dislocation array, but the Paxton result was only $15\text{meV}/b$ smaller; both sets also produced acceptable Peierls transition paths.

The Peierls stress calculated from the Paxton parameters came close to the range of estimations from *ab-initio* results, while the Mrovec estimate was 0.73GPa higher. However, the main issue in this simulation was the anomalous pattern of slip found with the Paxton parameters. The Paxton screw repeatedly cross-slipped out of the MRSSP in response to pure shear stress; this pattern has been found previously with interatomic potentials in response to pure shear and more accurate models with small amounts of non-glide stresses. Due to the fact that this slip-pattern obviously occurs easily, and since screw dislocations do not move this way in the lattice but by the nucleation of kink-pairs, the Paxton parameters are still considered viable for accurate simulation within BOP.

The $\Sigma 3(112)$ GB formation energy calculated with both sets fell within the range set by previous *ab-initio* calculations, and the values of the interface atom magnetic moments matched well with DFT results. As previously observed in Tungsten[164], the Mrovec parameter screw immediately dissociated into three partial dislocations of Burgers vector $\frac{a}{6}\langle 111 \rangle$ upon entering the GB. Two of these partials separated along the GB and displaced the boundary in opposite directions above and below the dissociation site such that a step was formed. This screw was then not transmitted with increasing stress, so that the GB formed an impassable barrier, at least for the

range of stresses considered. This dissociation also seemed to occur for the Paxton parameters: the step structure was formed when the dislocation impinged on the GB, but with increasing stress the partials recombined and the screw was transmitted one glide plane above where it entered. This was confirmed by re-running the cell with free boundary conditions so that the partials could leave the cell, the Paxton screw was then not transmitted with increasing stress and the step structure remained in the GB.

The Paxton parameters were then employed to simulate the properties of edge dislocations: finding the structure of the two most common pure edge types in BCC metals, their interaction energies with vacancies and the energies associated with some of the processes involved in climb for the {112} edge. The structures found compared reasonably well with those from previous calculations. However, these results were almost entirely obtained from interatomic potentials of a similar reliability; the {110} edge did reproduce some of the structural properties estimated from DFT results very well. In estimating the required cell length to minimise vacancy interactions, the interaction energy of two vacancies was calculated at a range of separations. The interaction energy of the divacancy along $\langle 111 \rangle$ was close to previous DFT results, but that along $\langle 100 \rangle$ was underestimated by up to a factor of two. An interesting variation between repulsive and attractive interactions was also found, depending on the axis of the divacancy. The edge-vacancy interaction simulations showed very different results between the edge types: the maximum interaction energy of the {112} edge above and below the glide plane was found to be almost double that of the {110}, and had an asymmetric distribution around the core. Although, both edges converged to similar results $> 3\text{\AA}$ above or below the glide plane. It was also found that the {110} edge did not seem to shift in position for vacancy binding sites close to the core, while the {112} did, this could be due to the greater binding energy but could also imply a greater barrier to movement for the {110} edge.

The sequential binding energies of vacancies along the line of the {112} edge, such as would occur during climb, were calculated and compared to previous results found for a $\frac{a}{2}\langle 111 \rangle\{110\}$ 71° mixed dislocation by *Lau et al.*[194]. The results were found to agree qualitatively with those found for the mixed dislocation, although the differences between the first and last binding energies were not as great and the intermediate values changed smoothly rather than remaining constant. This could indicate a smaller line energy for the {112} edge and a greater level of jog interaction. The barriers calculated for the vacancy migration events associated with the initiation

and completion of climb also agreed with the conclusions of *Lau et al.* in that the value of the barrier depended both on the angle of the path with respect to the dislocation line and the jog structure at the dislocation core. However, the dependence found for the {112} edge was not as strong and the preferred path for the initiation event differed from the mixed dislocation results. The barriers for all paths were also found to be greatly reduced from their equivalent values in the bulk, although that seemed to be overestimated when compared to previous DFT results. Note also that *Lau et al.* found that the barriers to vacancy migration converged to bulk values at a separation greater than $\sim 4b$; this implies that only a small number of further simulations, including more paths paths and a greater initial separation, would be required to fully specify the energetics of this process for both edges. The energetics of the reverse of this process, that is the emission of a vacancy by edge climb, was found to follow the same general pattern, with a barrier that depended both on the path orientation and edge core structure.

The barriers obtained for vacancy emission will now form valuable input for the kMC model of *Katzarov et al.*[95], described in section 1.3. This model allowed the nucleation of kinks on any of the three {110} planes intersecting the dislocation line, and the collision of kinks to form immobile jogs, or segments of $\frac{a}{2}\langle 111 \rangle\{112\}$ edge, but not the climb of these edge segments. The of the edge by migration of vacancies to the core would generally not be relevant in this case, due to the relatively low mobility of vacancies in the lattice at normal temperatures. However, the reverse of this process, the emission of vacancies by the climb of edge segments, would be. Evidence of excess vacancies associated with plastic deformation with hydrogen have been observed in the literature[73–76], and led to the proposal of the Hydrogen Enhanced Stress Induced Vacancy mechanism of hydrogen embrittlement[70]. The effect of hydrogen on screw dislocations in the increased formation of immobile jogs on the line, and the subsequent dragging of these jogs could partially account for this excess production of vacancies and so may be able to predict the conditions of stress, hydrogen content and temperature for the HESIV mechanism to become significant. These barriers have now been included in the kMC model, and will be used for simulations in the future.

These simulations have also provided the machinery to extend this data to environments in which the effects of hydrogen are more likely to occur, such as in the high tensile stress-fields in regions around a crack tip. Due to the lower chemical potential of hydrogen in these regions, the hydrogen concentration can be orders of magnitude greater than in the bulk[197]; the high levels of stress can also make the process of jog-

drag more likely. A minimal amount of further simulation is required to incrementally apply strain to these cells and repeat the NEB simulations; furthermore, the variation of the hydrogen binding to screw dislocations in these stress fields has been calculated in chapter 6 and so the model is close to being fully specified for these regions. It may also be of interest to calculate vacancy emission on the glide plane using these cells, which could not be carried out before because the edge would move to bind the vacancy more strongly. This could perhaps be prevented by freezing the movement of a single layer of edge core atoms along [111], but a larger cell may then be required to prevent interactions with the frozen atoms skewing the results; further simulation is required to check the feasibility of this solution.

The edge structures produced within this chapter are also intended for use within future work to estimate the importance of the dislocation-assisted carbon migration mechanism. It was proposed by *Fu et al.*[198, 199] that the flow of dislocations in high carbon steels under rolling contact fatigue could aid in the flux of carbon in the system, leading to the growth of carbon precipitates and the depletion of the high-carbon martensite phase. This high-carbon phase will generally contain a large number of nano-sized carbon precipitates and so it would be thermodynamically favourable for the carbon in solid solution to migrate to and join these precipitates[199]. However, the temperatures at which these effects are observed are far too low for significant thermal diffusion of carbon. Rolling contact fatigue occurs in high-carbon steel ball-bearings put under cyclic pulses of stress; *Fu et al.* proposed that this occurs due to repeated desegregation of the Cottrell atmospheres of carbon surrounding the dislocations. During the pulse, the dislocation is supposedly unpinned from its Cottrell atmosphere and glides a short distance. In the time between pulses the carbon is drawn after the dislocation, resulting in a carbon flux.

This process of the edge dislocation unpinning from a line of carbon atoms was simulated by *Tapasa et al.*[200], employing interatomic potentials to carry out MD. At no combination of strain-rate or temperature did they observe "dynamic-drag", or the carbon atom being dragged with the edge: the distance the dislocation jumped forward by immediately after unpinning was always too great for the carbon atom to move and be recaptured. However, these conditions may not be entirely relevant to those under which rolling contact fatigue occurs, in which the key point is that the stress pulse is so short that the unpinned dislocations may still be close enough to interact with the carbon. Also, as noted by *Tapasa et al.* at the beginning of their paper, the Fe-C system is generally not well described by interatomic potentials;

Preliminary Dislocation Calculations

particularly due to the strong covalent bonds formed and the possible weakening of nearby Fe-Fe bonds in the edge core observed in *ab-initio* calculations[201].

Therefore, it would be of interest to use accurate electronic-structure methods to calculate the trapping effect of the carbon Cottrell atmosphere, how much stress would be required to unpin the dislocation and so a rough estimate of how far it might travel during the pulse. The stress field associated with these edges will be assessed at each octahedral site that could contain a carbon atom, a periodic cell within TBE will then have that local stress field applied to it to approximate each site surrounding the core. These cells may then be used to calculate an approximation to the carbon trap energies in all the sites surrounding both common edge dislocations, and then produce some approximation to the occupation of these sites. Finally, the change in the carbon binding energy with and without the edge dislocation will be used to estimate the energy required for the edge to break away from these carbon atoms, and whether or not it is likely to occur in the range of stresses observed. This project was originally intended to be carried out using the embedding schemes described in chapter 7 but would require the fitting of a new basis set, as described in that chapter. A more efficient method may be to employ a BOP model capable of describing carbon: orthogonal basis sets have been found to describe the Fe-C interaction well, particularly in the dilute limit[202]. Moreover, that parameter set was found to reproduce the carbon transition barrier in iron well and the use of the BOP would allow the simulation of a cell large enough to calculate the variation in these migration barriers in the area around the edge, allowing a more realistic description of the supposed "drag" behind the dislocation.

In conclusion, these results validate the use of the Paxton parameter set within BOP, producing results of comparable accuracy to the well-tested Mrovec parameters and comparing very well to *ab-initio* results. These parameters may then be used with confidence to describe part of the cell in the embedding method, and for further simulation with BOP. The simulations of edge dislocations in iron demonstrate the scale and accuracy achievable with BOP; these simulations will form the basis for future projects in the examination of HESIV with the kMC model of *Katzarov et al.*[95] and of edge dislocation unpinning from Cottrell atmospheres.

Chapter 4

Screw Dislocation Kink Structures

4.1 Introduction

As mentioned in chapter 2, the movement of a dislocation does not occur for each full segment at once, but rather for small, unit sections of the line. This may occur due to thermal fluctuations along the dislocation line, atomic vibrations due to thermal energy causing the line to bulge over the Peierls barrier in a given direction. The two portions of the dislocation line that lie across the barrier after this transition are known as kinks; they will have a different orientation relation between the line and the Burgers vector than the rest of the segment and so do not share its character. Propagation of these kinks along the dislocation line, provided that they separate, will move more of the line into the next Peierls valley. This process is particularly important in BCC materials: the high lattice friction for screw dislocations, along with the low barrier associated with kink propagation, means that this mechanism will determine the plasticity at lower temperatures and stresses. The dependence of this process upon temperature accounts for the steep increase in yield stresses for BCC materials as they are cooled past a certain critical temperature[32].

As well as being the result of thermal fluctuations, kinks may also be geometrically necessary. A dislocation that appears curved in experimental observations, such as Transmission Electron Microscope images, will actually be made up of a large density of these kinks between sections of straight line along the Peierls valleys. The potential energy of a dislocation is lowered by having a greater proportion of the line lying along the bottom of Peierls valleys, and so in straight sections, but the energy is also reduced by having a shorter dislocation line. The dislocation shape at a given stress will be determined by a balance between these two effects, with a greater Peierls potential

resulting in greater lengths of straight dislocation and narrower kinks. At low levels of applied stress there will be a small amount of plastic strain due to these pre-existing kinks moving to the ends of the dislocation segments[37].

The plasticity of BCC crystals is dominated by $\frac{a}{2}\langle 111 \rangle$ screw dislocations and the normal glide planes of these dislocations, i.e. the $\{110\}$ planes of the $\langle 111 \rangle$ zone, do not display mirror symmetry in this direction. Therefore, the kinks on either side of the pair for these dislocations are structurally distinct; they are generally known as vacancy or interstitial type, or sometimes right and left kinks respectively. The number of atoms involved is the same but the difference in core structure results in an increase in length for the core atoms bonds along the screw line direction for the vacancy type or a decrease for interstitial. Previous atomistic simulation has also found that these kinks differ in formation energy and, for magnetic simulations, in the pattern of magnetic moments around the core[24, 58, 203]. Both kinks have the same Burgers vector as the dislocation but their line sense is approximately opposite, and so they will tend to attract each other; many embryonic kink-pairs will then come together and annihilate immediately after formation[204]. A stable kink-pair may be defined as one with a great enough separation between the kinks that the elastic interaction is too weak to move them back together. The effective stress can also tend to move the kinks apart or together, and so the minimum stable separation will be determined by a superposition of the effects of the applied stress and the elastic attraction between the kinks.

Some description of all these structures and events, and their variation with stress and temperature, is required for an accurate simulation of screw dislocation dynamics. This is further complicated in BCC materials by the ill-defined slip plane: kinks may nucleate on any of the three $\{110\}$ planes in the $\langle 111 \rangle$ zone, and collision of kinks on different planes will result in the formation of immobile jogs. Molecular Dynamics may be employed for this purpose and has the advantage that these structures and processes are included intrinsically, provided that the description of the atomic interactions is sufficiently correct. However, current MD simulations are limited in the time-scale that they can accurately describe, typically on the order of tens of nanoseconds. The thermally-activated nucleation of kink-pairs is a rare event and so a sample in this time-scale will not provide meaningful information unless the processes are driven in some way. In the past this has meant applying exceptionally high strain-rates, which can result in artificially high dislocation velocities that are not relevant to the thermally-activated motion at lower stresses[205].

These issues may be circumvented with the kinetic Monte Carlo method: the evolution of the system is still simulated, but by a stochastic sampling of processes rather than explicit consideration of atomic interactions. This sampling occurs based on the process rates, which may be calculated from the associated barriers by employing transition state theory[38]. Atomistic calculations may then be employed to calculate these barriers, enabling a connection between accurate descriptions of small-scale processes with that of the evolution of large dislocation structures. This coarse-graining of the processes means that large volumes of the lattice may be simulated for long time-scales, with a reliability determined by that of the rates provided. Kinetic Monte Carlo models have been successfully applied a number of times in the past for descriptions of the movement of a BCC screw dislocations[204, 206, 207]; they have allowed qualitative interpretation of experimental results and the "observation" of hardening by the formation of immobile jogs on screw dislocations, previously only proposed as one of a number of potential mechanisms[208]. More recently, *Katzarov et al.*[95] have adapted one of these models to include the effect of hydrogen on this mobility.

The purpose of the calculations carried out in this chapter was to provide input for the model of *Katzarov et al.*, which was previously based on data from the literature. The kink-pair nucleation enthalpy as a function of the applied stress and the embryonic and stable kink-pair widths were taken from DFT-parameterised line tension model calculations[48, 94]. It was hoped that direct calculation of these structures would allow an estimation of these terms with fewer approximations applied and in a wider range of stresses which, due to the non-Schmid character of screw dislocations in BCC materials, could have great effect on the process[23]. This could possibly allow an estimation of the variation in these processes in the regions of high tensile and compressive stress surrounding a crack-tip.

Atomistic simulation of kink structures generally require large cells involving tens of thousands of atoms, and so interatomic potentials have been employed in the past. However, over-simplified descriptions of the atomic interactions have sometimes resulted in screw dislocations with a degenerate core structure in iron. The resulting kinks then have six different forms depending on which type of the core they are connecting and the sense of the dislocation line; each of these forms have different formation energies and so can obscure the physical results of the simulation[24, 145, 209]. The BOP model is able to simulate tens of thousands of atoms, and, as shown in chapter 3, both obtains the widely accepted non-degenerate screw dislocation core structure. Furthermore, the BOP was found to produce a similar shape and height of

Peierls barrier to previous DFT results (also within that chapter), which more simple models commonly misrepresent with a metastable state midway in the transition[46]. This also leads to erroneous descriptions of the kink structure: leading to the splitting of each kink into "half-height" kinks between the metastable state and adjacent Peierls valleys, which can both result in the separation of each kink and the nucleation of only "half-height" kink-pairs[24, 210]. This chapter details attempts to use the BOP model, with the *d*-orthogonal iron parameters of *Paxton and Elsässer*[105], to simulate both types of kink on a screw dislocation in α -iron.

4.2 Results and Discussion

Shown in figure 4.1 is the core structure of each kink, clearly illustrating the change in bond length for the core atoms that differentiates the two types. Figure 4.2 below that shows the variation in the kink formation energies with radius and cell length; this is calculated as the difference in energy between the kink cell and a screw cell, of the same radius, scaled up to the kink cell's atom number. These results show that convergence in energy was not quite reached, and there is still some variation in the formation energies for the highest cell lengths and radii simulated..

The formation energy of both types do not converge directly with radius: the energies for the 35Å cells have a lower formation energy than the equivalent 25Å and 40Å cells in both cases, and the 20Å cell is lower than the 25Å case for the interstitial type. A similar pattern occurred for *Ventelon et al.*[203], who simulated the kinks in a quadrupolar array of screw dislocations with the Ackland-Mendelev empirical potential; however the variation in their case only occurred for the vacancy type. Both types seem close to convergence in radius, showing a difference of 0.03eV and 0.04eV between the 35Å and 40Å energies in the longest cells for the interstitial and vacancy type respectively. The convergence of the formation energy with cell length indicates the level of interaction between the periodic images of each kink, and the lower radii cells seem fairly well converged for lengths $> 32b$ but this convergence gets worse with increasing radius. For a radius of 25Å the energy changes by 0.02eV between the cell lengths of $32\frac{1}{3}b/32\frac{2}{3}b$ and $44\frac{1}{3}b/44\frac{2}{3}b$ for the interstitial/vacancy types respectively, whereas at a radius of 40Å this is increased to 0.08eV. Therefore it is difficult to judge the required cell length to minimise these interactions, the 40Å still shows a variation of 0.03eV between the longest two cells for both types.

For the radii and lengths considered, the ordering in formation energy of the kink

types is the same that as generally predicted by interatomic potentials: *Ventelon et al.*[203] found an energy of 0.08eV for the vacancy type and 0.57eV for interstitial, while *Chaussidon et al.*[24] predict 0.67eV for vacancy and 1.02eV for interstitial with the Mendelev empirical potential. This is the reverse of that predicted by *Mrovec et al.*[58], who found an energy of 0.53eV for the interstitial type and 0.62eV for the vacancy with a magnetic BOP model. *Mrovec et al.* theorised that the interstitial type was lower in energy because two core atoms flip their magnetic moments to an antiferromagnetic state, while there are only marginal changes to the local magnetic moments of the vacancy type. This moment flipping was also observed in these simulations, more specifically the two core atoms of the interstitial kink marked in figure 4.1 **a)** were flipped to a magnetic moment of $\sim -2.03\mu_B$ (compared to local moments of $\sim 2.98\mu_B$) for every radius and length considered. The moments around the vacancy type core showed small changes of $\sim 0.01\mu_B$.

Due to this variation in formation energy with both length and radius it is impossible to give a precise estimate of what the converged energies would be; however they seem close to convergence at a radius of 40Å which would give formation energies of $\sim 0.54\text{eV}$ and $\sim 0.36\text{eV}$ for the interstitial and vacancy types respectively. The formation energy of the kink-pair would then be $\sim 0.90\text{eV}$, which is close to previous estimates: *Mrovec et al.* predicted a value of 1.15eV, line tension models incorporating DFT results gave results of 0.73eV[94] and 0.86eV[211], interatomic potentials range between 0.55 – 1.69eV[24, 94, 203, 211] and finally estimations based on low-temperature experimental measurements in high-purity iron have been 0.6eV[212] and 0.83eV[145].

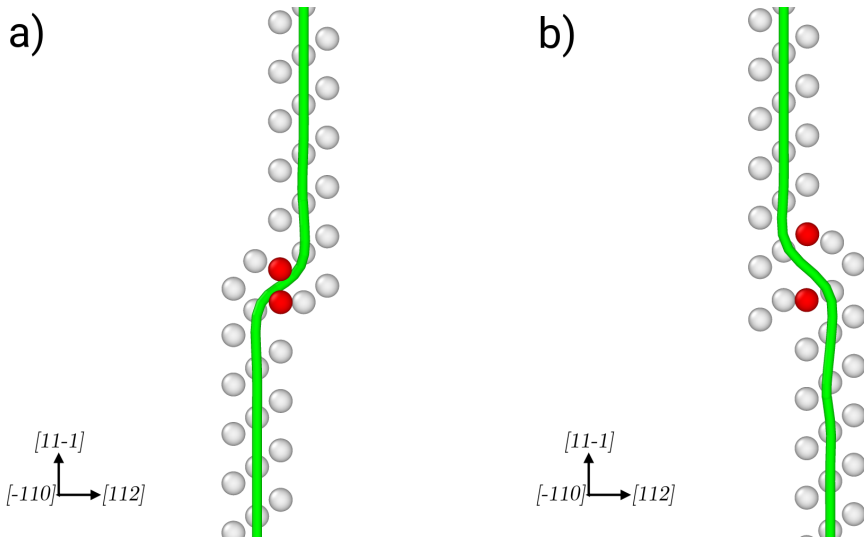


Fig. 4.1: The core structure for **a)** interstitial type and **b)** vacancy type kinks. The grey atoms are the triangle of $[11\bar{1}]$ atomic columns surrounding the core and the two atoms immediately above and below the kink are marked in red to illustrate how the $\langle 111 \rangle$ displacement of these atoms lead their difference in structure. The dislocation line is marked in green.

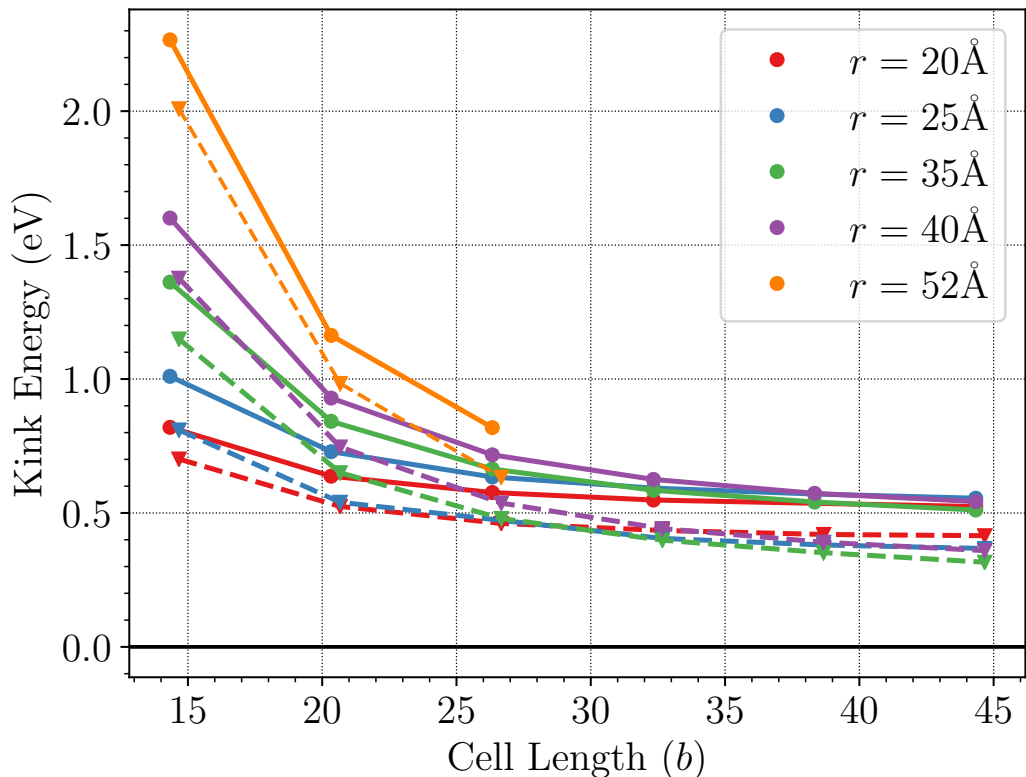


Fig. 4.2: The formation energy for both types of kink for a range of cell length and radii; the interstitial values are plotted with solid lines and circular markers while the vacancy values have dashed lines and triangular markers.

The kink core width was estimated from the $[11\bar{1}]$ displacement of the triangle of atoms between the screw core positions at each layer of the cell, these atoms are indicated in figure 4.3. The $[11\bar{1}]$ coordinate of these atoms was compared to the coordinate of the equivalent atoms beside an infinite straight screw dislocation in either position, similar to the method used by *Katzarov and Paxton*[213]. The relative displacement of each of these atoms was used to produce a dimensionless parameter that varied between zero and one depending on whether the positions of these atoms were closer to those on the left or right side of the infinite screw respectively, as shown in figure 4.4 for the 40\AA case. This parameter did not seem to be affected greatly by the variation with radius: for the interstitial type the cell length of $26\frac{1}{3}b$ had a maximum variation of 0.0037 for any layer between the radii of 20\AA and 52\AA , and for the length of $44\frac{1}{3}b$ the maximum was 0.0032 between the radii of 20\AA and 40\AA ; therefore the results for the 40\AA case may be used with some confidence. Also, as can be seen from the figures, the layers around the core overlap for the full range of cell lengths.

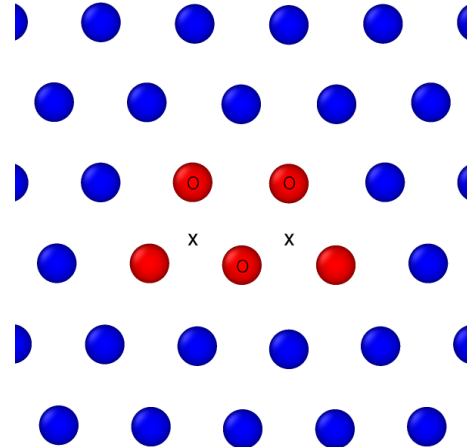


Fig. 4.3: Shown are the core positions of the two neighbouring screw dislocations used to produce the kinks (marked with an x); also marked with an O are the $[11\bar{1}]$ atomic columns used to estimate the kink core width with the method indicated in the text.

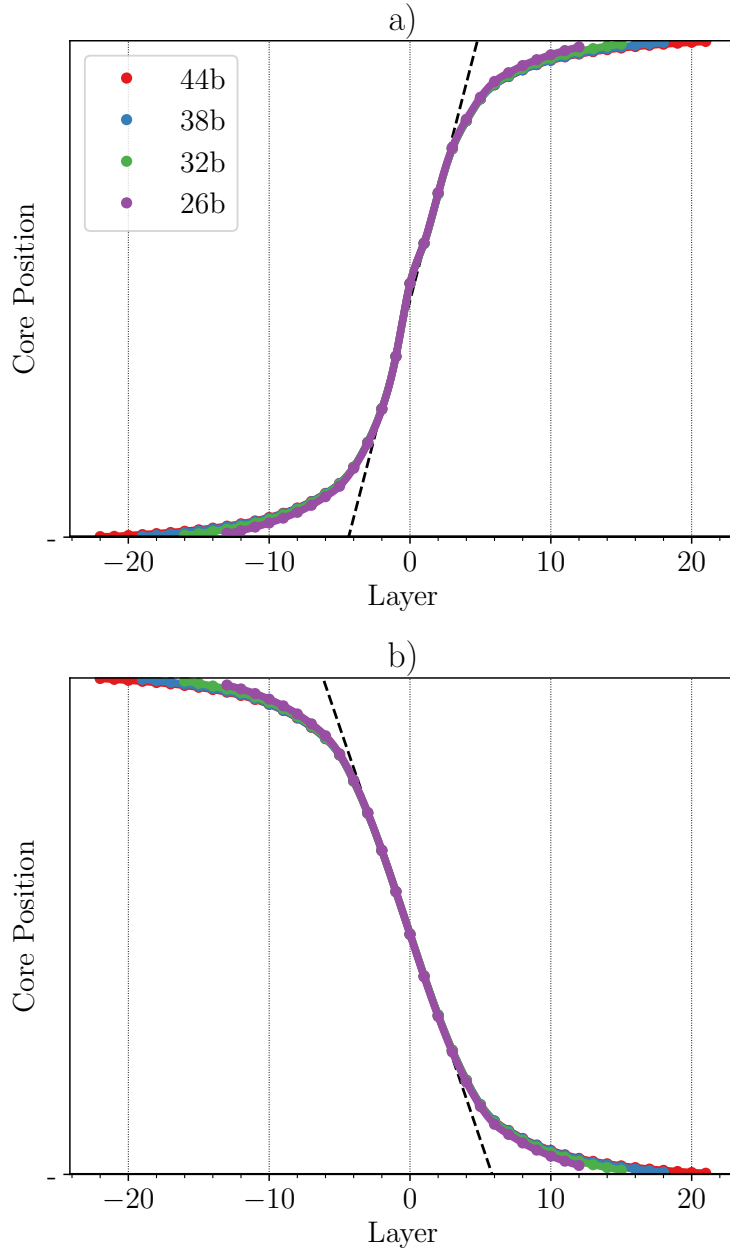


Fig. 4.4: Shown is a graphical representation of the dislocation line's transition between neighbouring Peierls valleys for the a) interstitial and b) vacancy kinks in the 40 Å cells. The core position was determined by comparing the $\bar{[1}11]$ coordinates of the triangle of atoms between the dislocation core positions for each layer to the equivalent atoms beside a straight dislocation in both positions.

The same construction as that used by *Ventelon et al.*[203] and *Itakura et al.*[94] was employed to estimate the kink width: by finding the gradient of the transition around the core planes, as shown by the dashed line in the figure, and taking the difference

in intercepts as the width. This figure, estimating from the values at a cell length of $44\frac{1}{3}b$ and a radius of 40Å, gives a width of the vacancy type kink of $\sim 12b$ and the interstitial type of $\sim 9b$. Both of these widths are much lower than the $20b$ estimated by *Ventelon et al.*; however, the potential they used produces a Peierls barrier that is both significantly lower than that found with these BOP parameters and had a metastable state midway in the transition (it predicted $\sim 12\text{meV}/b$ [45], while this BOP gives values of $\sim 25\text{meV}/b$ as seen in chapter 3), and so they likely overestimate the width. The results are in much better agreement with those from the BOP model of *Mrovec et al.*[58] which gave a width of $\sim 7 - 8b$, with the vacancy type being slightly wider; this is also quite close to the DFT parameterised line tension model of *Itakura et al.*[94] which predicted that both had a width of $10b$. The interstitial type appears to have a very slight hump midway in the transition; this was also observed for both kinks with the EAM-parameterised line tension model of *Itakura et al.*[94], based on an EAM which predicts a metastable state in the Peierls transition. However, the hump in that case was much more exaggerated and both kinks were found to have widths of $\sim 20b$.

The difference in kink structure can be seen clearly by comparing the change in bond length along the [11̄1] column of atoms between the screw core positions, shown in figure 4.5 for the $\sim 44b$ 40Å case, which had peaks within 0.02% and 0.1% of the $\sim 26b$ 52Å interstitial and vacancy types respectively. The distribution for the vacancy type are very similar to those found by *Mrovec et al.*: both have a smooth hump with two points of similar value at the peak, however the peak increase for their kinks was larger with an extension of $\sim 5\%$ compared to the value here of 2.8%. *Mrovec et al.* found a slightly greater peak decrease for the interstitial type as well, estimating 10% while the value here is only 7%. The distribution of bond length change is also slightly different in that, although both have a sharp peak at the centre, theirs was surrounded by two local minima on either side while the results here just show a fairly smooth decrease in magnitude. These values are much lower than those predicted by *Ventelon et al.*, who stated that the bond length would change by $\pm 30\%$.

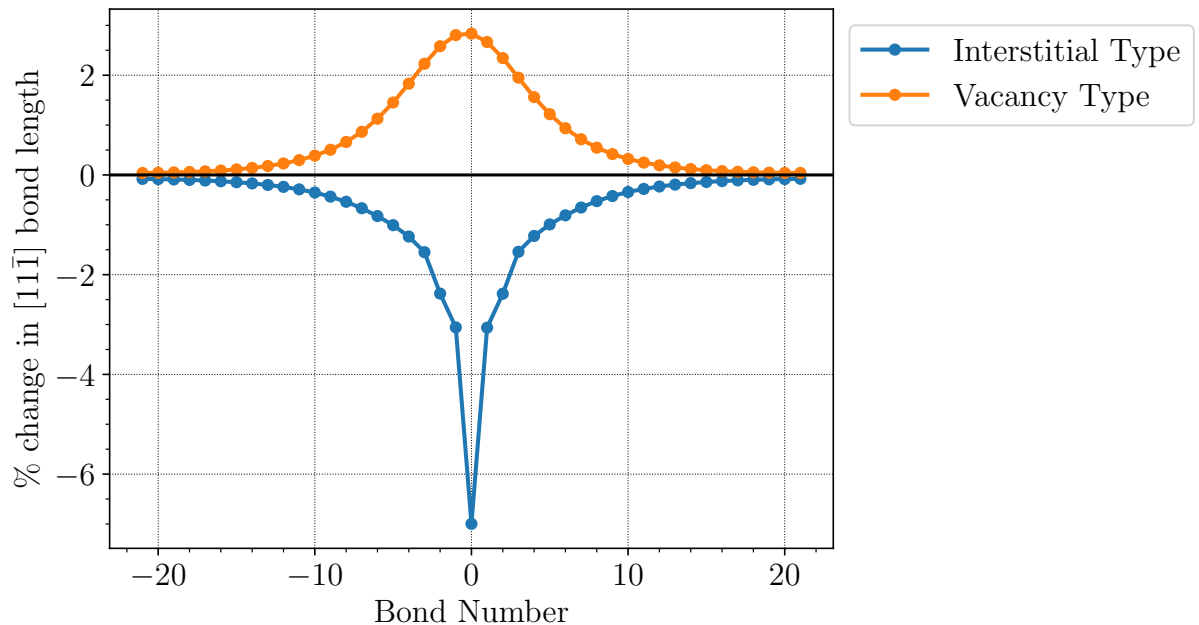


Fig. 4.5: The percentage change in the length of bonds along $[11\bar{1}]$ for the $[11\bar{1}]$ column of atoms between the screw positions, results are taken for both kinks from the cell with a length of $44b$ and a radius of 40\AA . The scale is set such that the bond at 0 is between the two red atoms in figure 4.1.

4.3 Conclusion

Isolated kinks were simulated by producing a long cylinder of atoms containing a screw dislocation that transitioned between Peierls valleys halfway along its length. This was carried out for a range of cell lengths, in an attempt to find the interaction range of the kinks, and for a range of cell radii, to find the minimum size required for the convergence of the kink formation energies. It was found that the size required to converge the formation energies would involve more atoms than could be feasibly simulated with BOP at this point. The maximum radius that could be attained, for an acceptable cell length of ~ 26 Burgers vectors, was 52\AA and involved at least 47,000 atoms. *Mrovec et al.* produced a similar configuration of kink cell and found that it took at least 70,000 atoms with a cell length of 26 Burgers vectors to converge, which equates to a radius of $\sim 63\text{\AA}$ with their lattice parameters. However, judging from the pattern of formation energies the kinks simulated here would clearly require a longer cell. Conversely, the core structures along $[11\bar{1}]$ seemed fairly unaffected by the radius: they showed only minor changes between 20\AA and 52\AA , and matched well in width

and structure with previous simulations employing the BOP and line tension models with parameters from DFT.

These results were intended as input for the kMC model of *Katzarov et al.*[95]; this would have involved calculation of the kink-pair structure. Like most kMC simulations of screw dislocation movement, this model did not consider the nucleation of all kink-pairs, the majority of which immediately come together and annihilate. This would waste a large amount of simulation time in computing fast but inconsequential processes; instead, they took a rate for stable kink-pair nucleation that was estimated from experiment. A more direct way of obtaining this rate may be to calculate the energy of each metastable state involved in the "bulge out" of the dislocation line during stable kink-pair nucleation, by relaxing cells containing an idealised kink-pair separated by an increasing distance, and then employing the methods used by *Cai et al.*[214] to calculate stable kink-pair formation rates in silicon. This consisted of calculating the formation rate of the smallest metastable state, or the kink-pair embryo, and then modifying it with the probability of the pair reaching the critical separation for survival. The probability was obtained by treating the expansion process as a 1D Markov chain, and so the probability to reach the critical width is taken as the product of the jump probabilities between neighbouring metastable states, including the backward jumps; the energy barrier for these transitions is taken as half the energy difference between states added to the secondary Peierls barrier and the effects of stress. This would allow the calculation of the rate of stable kink-pair formation as a function of the stress and temperature; however, these simulations show that a separation of at least $38b$ between images is required to minimise the interaction to an acceptable level which, along with the kink separation required to produce a stable kink-pair (found to be $\sim 16b$ from a DFT parameterised line tension model [211]), puts this structure far beyond the attainable cell size.

This issue could perhaps be addressed with a different cell configuration, such as the quadrupolar dislocation array employed by *Ventelon et al.*; however, it was considered that the interaction between the lateral strain fields of the edge components of the kinks would interfere with the structural relaxation. Furthermore, it was intended to calculate the variation of this rate with applied tensile and compressive strains, to approximate the areas surrounding a crack tip, and so it would be difficult to separate the effects of these strains from the changing interactions between cores. A more suitable method may be employing the Green function boundary conditions of *Sinclair et al.*[215], updated to three-dimensional systems by *Rao et al.*[216], which

would allow the coordinates of the inert atoms to be updated in such a way that reflects the elastic response of the lattice. It was found by *Rao et al.* that, for the simulation of kinks in α -iron, the cell with GFBC could be reduced to a radius of 40Å and still produce converged formation energies and structures. However, the region that was actually relaxed atomistically only had a radius of 20Å, the rest of the cell was frozen during this relaxation. The forces that build up in the frozen region are periodically reduced by updating the coordinates of the entire cell according to the Lattice Green Function. If these simulations could be carried out at a similar radius then they would be certainly attainable; also, the features for calculation of the Lattice Green Function and the use of Green function boundary conditions are already implemented within the BOP software and have been used for previous work[213]. The calculations of these structures as a function of the strain will form the basis of a future project.

Chapter 5

Including Broyden Mixing

5.1 Introduction

As described in chapter 2, each iteration of a self-consistent TB simulation involves constructing a Hamiltonian, which includes contributions determined by the charge densities, and then solving the associated generalised eigenproblem. A new set of charge densities will be obtained from the resultant eigenvectors of this problem, and are then used to determine the new contributions to the Hamiltonian. Self-consistency is reached when the new, output charges are sufficiently close to the inputs; in other words, when the induced charges match with the potential. Reaching self-consistency is equivalent to solving a system of highly non-linear equations, carried out numerically by iteratively adjusting the inputs. Each iteration of this procedure can be quite computationally expensive, and so it is of great interest to minimise the number required. The purpose of a mixing procedure is to accelerate this process in some way, taking into consideration a number of the previous iterations in order to produce an estimate closer to the converged result than the previous output.

Calculations in α -iron are further complicated by the requirement to accurately describe the magnetic moments: the spin-polarised charge densities must now be calculated, and so two eigenproblems must be solved for each iteration. Furthermore, the magnetic moments represent another variable that must be made self-consistent and their variation between iterations, if they are not held frozen, will slow the convergence of the charge densities. These factors can increase the computation time by such a degree as to make some problems effectively intractable, particularly in simulations that are complicated further by hydrogen interactions. It was decided then to make some attempt to accelerate the mixing within the TBE program: the Anderson

mixing scheme[217] was already implemented but the Broyden scheme[96] is generally found to have faster convergence[218], which could prove essential for the large number of magnetic α -Fe simulations intended. My contribution consists of adapting the TBE mixing procedures to use the Broyden mixing scheme implemented in the LMTO software, so that it could mix charges, magnetic moments and elements of the Hamiltonian, and to implement the "clock mixing" procedure described below. This chapter first details the structure of the Anderson and Broyden mixing schemes, and then shows the results of some simple convergence tests employed to compare their associated acceleration.

5.2 Schemes

The schemes below are illustrated with the example of charges, but may be employed in an equivalent way with any other parameter that can be altered for the self-consistency. Spin-polarised calculations may be carried out by either splitting the charge densities into minority and majority densities and mixing them separately or mixing the charges and magnetic moments separately.

Simple Mixing

The most straightforward method of obtaining new input values would be to use the previous output, however this would result in oscillations and instability for many problems. This issue can be alleviated by defining a mixing parameter, β , that determines the influence of the previous output value on the new input.

$$q_{i,in}^{n+1} = \beta q_{i,out}^n + (1 - \beta)q_{i,in}^n \quad (5.1)$$

Setting β to a lower value will then result in increased stability but with a slower convergence, but even with a large value of β this scheme will converge very slowly.

Anderson Scheme

The convergence can be greatly improved by using accelerated schemes to improve the estimate for the new input; one of the simplest of these is the Anderson scheme[217]. First, the input and output values for this iteration are mixed with the previous iteration's values.

$$\tilde{q}_{i,in}^n = \alpha q_{i,in}^n + (1 - \alpha) q_{i,in}^{n-1} \quad (5.2)$$

$$\tilde{q}_{i,out}^n = \alpha q_{i,out}^n + (1 - \alpha) q_{i,out}^{n-1} \quad (5.3)$$

An estimate for the new input charges may then be obtained from these mixed values in the same way as simple mixing.

$$q_{i,in}^{n+1} = \beta \tilde{q}_{i,out}^n + (1 - \beta) \tilde{q}_{i,in}^n \quad (5.4)$$

The convergence is accelerated by choosing a value of α such that it minimises $\sum_i^{N_{at}} (\tilde{q}_{i,out}^n - \tilde{q}_{i,in}^n)^2$. This results in the following expression for α :

$$\alpha = \frac{\sum_i^{N_{at}} \Delta q_i^n (\Delta q_i^n - \Delta q_i^{n-1})}{\|\Delta q^n - \Delta q^{n-1}\|^2} \quad (5.5)$$

Where $\Delta q_i^n = q_{i,out}^n - q_{i,in}^n$. The stability of this scheme is easily improved by including multiple iterations, this results in a system of linear equations for the optimal α which may be solved as a matrix equation. The value of β is a parameter to be set; again, a large β will result in faster convergence and reduced stability and vice versa.

Broyden Scheme

Broyden's scheme is based upon Newton's method of solving non-linear equations, which uses the Jacobian matrix of partial derivatives to calculate the new input[96]. The Jacobian is defined here as:

$$\mathbf{J} = \frac{\delta \Delta q}{\delta q} \quad (5.6)$$

The new input value that would result in convergence would then be:

$$q^{n+1} = q^n - \mathbf{J}^{-1} \Delta q^n \quad (5.7)$$

This is Newton's method, however computing and inverting the Jacobian for even a system that is simple enough to obtain the partial derivatives analytically would be prohibitively expensive. Broyden's scheme avoids this by approximating the inverse of the Jacobian matrix and then iteratively improving the estimate, this is referred to as the second method in the original paper, where the first involves approximating and updating the Jacobian. The initial estimate of the inverse Jacobian may be obtained

by carrying out a single iteration of linear mixing and approximating the derivatives with the finite differences. The estimate can then be iteratively improved by requiring that the new inverse Jacobian minimises 5.8 and 5.9 below.

$$|\mathbf{J}_n^{-1} - \mathbf{J}_{n-1}^{-1}| \quad (5.8)$$

$$|\delta q^n - \mathbf{J}_n^{-1}(\Delta q^n - \Delta q^{n-1})| \quad (5.9)$$

This is equivalent to minimising the change in the inverse Jacobian and the change in result from the previous iteration.

There have been a number of modified implementations that improve the flexibility of the scheme and remove the need to store the full Jacobian[218, 219].

Clock Mixing

Clock mixing may be carried out with both the Broyden and Anderson scheme; it is simply a shuffle of the mixing procedure rather than an actual scheme. The charges and magnetic moments are mixed separately but between every single iteration of the magnetic moments mixing the charges are mixed to self-consistency. The magnetic moments are held frozen while the charges are mixed, it was thought that this would increase the stability of the charges while accelerating the convergence of the moments. Separate mixing parameters and weights may be chosen for each to suit their stability. The purpose of this procedure is to increase the stability of particularly complex simulations, in which charge oscillation and slow convergence of magnetic moments could be a problem.

5.3 Results & Discussion

The first two columns of table 5.1 shows the results of several different simulation configurations run with both Broyden and Anderson mixing; only the spin-polarised charge densities were mixed and optimal β parameters were found by running simulations with a range of values and tightening the spread around those that converged the fastest, down to a resolution of 0.01. Broyden outperformed Anderson mixing in every configuration that was examined, and to a greater degree as the complexity was increased; however, it also showed large oscillations in its results between iterations.

The configurations shown here were all simple enough that these oscillations did not interfere with the convergence, but for those of greater complexity and scale there could be advantage to the stability of the Anderson scheme.

The last column shows the results for the clock mixing procedure using the Broyden scheme. The mixing parameters were optimised in the same way as they were before; however, because those for both the charges and the magnetic moments had to be optimised simultaneously it was difficult to know that the best values were chosen. For the first three simulations the clock mixing is a good deal slower than the other two schemes, but its purpose was to increase the stability of complex configurations and this can be seen in simulation D. In simpler simulations this stability is not required, and the requirement to repeatedly converge the charges actually slows the simulation; however, in the more complex simulations this added stability allows the use of higher β parameters and so increases the speed. It is also important to note that the tolerance for convergence of the magnetic moments in clock mixing was set to the same value as that for charges; this is rarely necessary in practice and so a looser magnetic tolerance would have given lower iteration counts.

Simulation	Broyden	Anderson	clock (Broyden)
A	9	10	16
B	48	115	142
C	65	86	84
D	142	667	107

Table 5.1: Number of iterations required for convergence with the Broyden and Anderson charge mixing schemes and Broyden mixing with the clock procedure for cells containing: A) block of 80 atoms in perfect BCC lattice; B) 53 atom BCC supercell with 4 H in octahedral sites around vacancy; C) 2 H segregated to (100) BCC surface, $2 \times 2 \times 5$ cell, 3 layers of vacuum; D) 270 atom supercell containing quadrupolar array of screw dislocations.

5.4 Conclusion

Within this chapter the Broyden mixing scheme is found to be a valuable addition to the TBE software, showing much faster convergence for all observed cases. However, this scheme also showed large oscillations in charge before convergence was reached; the Anderson scheme on the other hand showed a steady trajectory toward the converged values. Therefore, it is believed that all of the simulations shown here may have been

Including Broyden Mixing

too simple to show the benefits of the Anderson scheme, but that there could be advantage in using it for cases in which this oscillation becomes an issue. Similarly, the clock mixing procedure was also found to be useful but had specific applications, in that it is not appropriate for smaller, more simple simulations but can confer great benefits in the case of large, complex structures. In any case, there is certainly great advantage in using the Broyden scheme for cases of sufficient stability, decreasing the simulation time greatly, and it shall be employed in all the TBE simulations to follow. It was also decided to implement the Broyden mixing scheme with the clock procedure in the embedding method described in chapter 7, as it was believed that the increased stability could be of use.

Chapter 6

Hydrogen Interactions With Screw Dislocations

6.1 Introduction

A great deal of effort has been directed toward the study of hydrogen embrittlement (HE) but a full understanding of the underlying mechanism is still lacking; this is due to the complexity of the problem, involving multiple time and length scales. Two of the primary mechanisms generally discussed are hydrogen induced decohesion (HID) and hydrogen enhanced localised plasticity (HELP), although there are several others that could contribute to a different degree depending on the material, temperature, hydrogen content, stress and so on.

HID is based on the idea that hydrogen reduces the strength of bonds in the lattice, leading to decohesion at lower stresses. An issue with this model is that there has never been direct experimental evidence of hydrogen weakening interatomic bonds or altering elastic properties. This is impossible to measure as the amount of hydrogen that can be dissolved in a specimen for bulk property measurement is much less than that theorised to accumulate in the regions where HID occurs[220]. The theory of HID originally arose from a consideration of the reduction of the surface free energy by hydrogen and the relationship between that and the cohesive energy of the lattice[63]. Hydrogen follows the stress gradient and will accumulate in areas of high tensile stress, where the weakening of strained bonds could result in brittle failure; crack tips and grain boundaries are then possible sites for HID.

The theory of HELP is based around hydrogen enhancing the mobility of dislocations, resulting in localised plasticity. Again the increased hydrogen concentrations

in the tensile zone of a crack tip will increase the effect, and the increased localised plasticity is supposed to allow the crack to advance at lower levels of stress. This enhanced mobility was theorised to occur due to an atmosphere of hydrogen forming around defects: the interactions between these defects could then be reduced by the hydrogen moving to accommodate the stress[81]. Evidence for this theory originally came from the observation of ductile features on fracture surfaces, and later from an observation of the resumed motion of stationary dislocations at a constant applied stress with the introduction of hydrogen[77, 221]. Failure is then supposed to occur as a highly localised plastic process, happening where the local concentration is high near the fracture surface; therefore it is proposed that localised plasticity results in a reduction of macroscopic ductility[81]. An issue with this mechanism, at least in BCC iron, is that the shielding effect is generally found to require either unphysically large lattice concentrations of hydrogen or not to exist at all[86, 87].

A related idea is the defactant concept; it is based on a thermodynamic consideration of the segregation of solutes to defects, resulting in a reduction of the defect formation energy[88]. This is particularly important when considering the motion of screw dislocations in BCC metals, which will determine the mobility of dislocations due to the relatively low Peierls barrier of edge dislocations. As mentioned in chapter 4, the rate determining step for screw dislocation motion at low temperature will either be the formation or motion of kink-pairs; in the first case hydrogen will result in softening due to a decreased kink-pair formation energy, while in the second solute drag on the kinks will result in a hardening effect[91]. This model could then explain both the localised plasticity and the hardening effects observed with increasing hydrogen concentrations; as seen experimentally in the paper of *Wang et al.*[222], where the activation volume for dislocation motion initially shows a sharp decrease with increased hydrogen concentration but then plateaus and starts to increase until very high concentrations are reached.

As mentioned, crack-tips are considered to be particularly likely sites for these mechanisms to be active, partially due to the high local concentration of hydrogen. The driving force for hydrogen diffusion is the strain gradient: in regions of high tensile stress hydrogen has a low chemical potential, and the opposite in regions of compression[197]. Hydrogen diffusion will then tend to deplete regions of compression to enhance the concentration in regions of tension; when a load is applied and a crack begins to open this will result in a redistribution of hydrogen toward the high local strain fields surrounding a crack-tip. The plastic deformation associated with this

region will also result in a high density of dislocations, and so there will be a great number of trap sites available. In general, hydrogen seems to assist the microscopic processes that lead to crack-tip advance, whether this occurs by decohesion or by enhanced localised plasticity or some other mechanism there is certainly great advantage in examining either process and determining when it is dominant.

Katzarov et al.[95] employed a kMC model to simulate the effect of hydrogen on the screw dislocation velocity in iron; this model requires energies for the effects of hydrogen on kink-trapping and kink-pair nucleation, so the rates of escape and nucleation can be calculated from transition state theory and used as input. If the variation of these effects with strain could be produced then this model could be applied to the regions where hydrogen embrittlement is most likely to occur, i.e. the regions of high strain around a crack-tip. Estimates of the dislocation mobility variation between these local areas of tension and compression surrounding a crack tip could be invaluable to predict the conditions under which shear localisation is likely to occur. The work carried out within this chapter was then primarily to provide input for this model.

The Tight Binding model is employed to calculate the variation of the interaction between screw dislocations and hydrogen with strain. First the binding energy of several types of trap site surrounding the screw core are calculated and compared to previous DFT results. Bi-axial tension or compression is then incrementally applied in the plane normal to the dislocation line and the binding energies recalculated at each step; these results are used to carry out several rough estimates of the possible effect of hydrogen. Finally the cell is used to calculate the transition barriers for hydrogen between some of the strongest traps surrounding the screw core, the importance of pipe diffusion is also assessed. An *sd*-nonorthogonal Tight Binding parameter set, that enables the description of hydrogen/iron interactions, is used throughout this chapter[105].

6.2 Methods

Producing the Simulation Cell

A disk of radius 20 Å and containing 388 atoms was generated so that it was normal to the [11̄1] direction (taken to be the *z*-axis), and had a periodicity along this direction of a single Burgers vector. The atoms were then displaced according to the solutions of

the anisotropic linear elasticity equations in order to introduce a screw dislocation in the centre, which could be given either the hard core (HCC) or easy core configuration (ECC) by changing the sign of the Burger's vector. The atoms around the rim of the disk were frozen in these positions, in order to negate the large forces associated with the vacuum surrounding the cell, while the rest were relaxed within TBE, with *sd*-nonorthogonal Hamiltonian matrix elements for iron[105], using the Fletcher-Powell algorithm until the maximum force was less than $10^{-4}\text{eV}\text{\AA}^{-1}$ [223]. A disk of radius 8 Å was then cut out from the centre of this cell and stacked three times, allowing hydrogen to be included without significant interaction between its periodic images. The bottom three atoms of each screw core in the triple layer cell were frozen along z in order to prevent the screw moving with the introduction of hydrogen, which was placed in several of the binding sites found by *Itakura et al.*[48] (figure 6.1). The Methfessel-Paxton sampling method was used for the Brillouin zone integration, using $1 \times 1 \times 24$ and $1 \times 1 \times 16$ k -point divisions for the large, single-layer cell and the small, three-layer cell respectively[116].

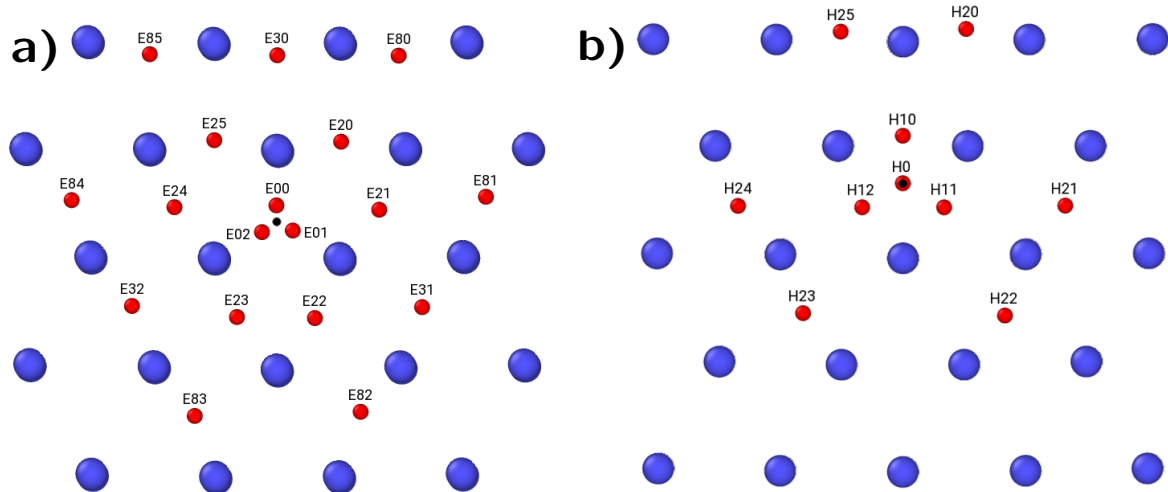


Fig. 6.1: The binding sites for hydrogen around an (a) easy core or (b) hard core screw dislocation, where the binding sites are represented by red circles and the core positions by black. The sites are labelled by the letter of the core they surround and two numbers; the first defining the sites with the labels chosen by *Itakura et al.*[48] (E0, E2, H0, etc.); the second number labels equivalent sites' position around the core, starting from the top and counting clockwise (E20, E21, E22, etc.).

Calculating the Hydrogen-Screw Binding Energy

The dissolution energy was calculated with equation 6.1 below.

$$E_s = E_{d+nH} - E_d - \frac{n}{2} E_{H_2} \quad (6.1)$$

where E_{d+nH} is the energy of the cell containing the dislocation and n hydrogen in binding sites around it, E_d is the energy of the cell containing just the dislocation and E_{H_2} is the energy of molecular hydrogen, taken to be -4.75eV . The binding energy is then taken as the difference between this energy and n times the dissolution energy of hydrogen in a bulk tetrahedral site, so that a more positive value indicates stronger binding; note that the value of E_{H_2} is fairly arbitrary for the binding energy as it cancels out.

Due to the small mass of hydrogen it is important to include quantum effects; the correction arising from zero-point vibrations was calculated for each binding site. Again following *Itakura et al.*, it was assumed that the zero-point energy (ZPE) correction could be approximated with the motion of the hydrogen atom only, assuming that the localised hydrogen vibrational modes would be decoupled from the lattice vibrations due to the large difference in mass. The hydrogen atom was displaced 0.015\AA in the $\pm x$, $\pm y$ and $\pm z$ directions and the change in forces used to construct the Hessian matrix as the 1st order central finite difference. The normal mode frequencies can then be obtained from the mass-weighted eigenvalues of the 3×3 Hessian matrix:

$$\nu_i = \frac{1}{2\pi} \sqrt{\frac{k_i}{m_H}} \quad (6.2)$$

where m_H is the mass of the hydrogen atom and k_i are the eigenvalues of the Hessian matrix. These frequencies can then be used to calculate the ZPE correction:

$$E_z = \frac{1}{2} \sum_{i=1}^3 h\nu_i \quad (6.3)$$

h represents the Planck constant. The ZPE corrected dissolution energy can then be calculated as $E_s^Z = E_s + E_z - E_{H_2}^Z$, where $E_{H_2}^Z$ is the ZPE of a hydrogen molecule and is taken as 266meV [224].

Imposing Strain

In order to observe the variation of binding energy with strain, biaxial tension and compression was applied in the xy -plane (normal to the dislocation line). The strain was imposed on the single layer cell incrementally in units of 0.1%; the cell was then relaxed, stacked again and re-relaxed with hydrogen. The values for the bulk tetrahedral site dissolution and the ZPE correction for each site were also recalculated at each value of the strain.

Obtaining Diffusion Barriers

In order to obtain the 0 K barrier for diffusion of hydrogen, both between the strongest trap sites around the ECC screw and along the line of the screws by pipe diffusion, the climbing image nudged elastic band method (CI-NEB) with variable spring strength was used[225]. The CI-NEB simulations were continued using a Fletcher-Powell relaxation scheme until the maximum gradient was less than 3.5×10^{-4} eVÅ $^{-1}$.

The attempt frequency for each of the transitions, or the frequency of vibration of the hydrogen in the direction of the saddle point, was then calculated using harmonic transition state theory. The Hessian was again constructed with the 1st order central finite differences at the initial and saddle points for each transition, then mass weighted and diagonalised for the normal mode frequencies[38]. These can then be used to calculate the attempt frequency:

$$\Gamma_0 = \frac{\prod_i^{3N} \nu_i^A}{\prod_i^{3N-1} \nu_i^S} \quad (6.4)$$

where ν_i^A are the 3N normal mode frequencies at the starting point and ν_i^S the 3N-1 normal mode frequencies when the hydrogen is constrained in the saddle point configuration (neglecting the imaginary frequency along the transition path). Again, it is assumed that the Hessian can be calculated solely with the motion of the hydrogen atom and so N is equal to 1.

The attempt frequency was then used to calculate the temperature-dependent jump frequency for each transition:

$$\Gamma = \Gamma_0 \exp[-(\Delta E + \Delta E_z)/k_b T] \quad (6.5)$$

In this equation ΔE is the difference in energies between the initial and saddle points, or the activation energy, ΔE_z is the difference in ZPE between both points, k_B is the

Boltzmann constant and T the absolute temperature. The imaginary frequency was again neglected in the calculation of the saddle point ZPE.

6.3 Results and Discussion

6.3.1 Unstrained Case

The binding sites for the hydrogen were found to be in the same positions as those found by *Itakura et al.* The E2 site was also found to match with that defined in *Zhao and Lu*[49], who used a quantum-mechanics/molecular-mechanics (QM/MM) approach with a core of DFT to simulate hydrogen around a screw dislocation. As shown in table 6.1, all of the results from TBE are found to be in excellent agreement with the DFT results, every one within the estimated error stated by *Itakura et al.* apart from E2, which was beyond the error range by 6meV, but still close to the value of 270meV found by *Zhao and Lu*. The ZPE correction is also shown to be essential in this case as it is required to correct the ordering of the H0/H1 binding strengths. It is interesting to note that *Ramasubramaniam et al.*[226] were able to obtain the correct position for the E2 site, and a similar binding energy of 240/270meV, using two interatomic potentials fitted to DFT results and experimental data; however they also found a fictitious stronger binding site for the ECC located between each of the three core atoms, where H1 would be located if the screw was HCC. Also, the ZPE-corrected dissolution energy of hydrogen in a tetrahedral site would be 319meV, in excellent agreement with previous DFT estimates of 301meV[224] and 330meV[227], and an experimental estimate of 296meV[228].

Site	E_s	E_b	E_z	E_b^z
Tet.	233 (241)	0 (0)	219 (238)	0 (0)
E0	114 (156)	119 (85)	213 (224)	126(99)
E2	7 (30)	227 (185)	152 (167)	294 (256)
E3	99 (103)	134 (138)	153 (175)	200 (201)
E8	203 (195)	30 (46)	163 (207)	86 (77)
H0	-29 (-71)	263 (286)	94 (134)	388 (390)
H1	-43 (-56)	276 (271)	161 (187)	335 (322)
H2	73 (116)	160 (125)	149 (174)	230 (189)

Table 6.1: Shown (in meV) are the dissolution energies (E_s), binding energies (E_b), ZPE corrections (E_z) and the corrected binding energies (E_b^z) for hydrogen in the bulk tetrahedral site and several sites around the ECC and HCC screw dislocation. Figures in brackets are the equivalent results from *Itakura et al.* [48].

Some cases were then attempted in including multiple hydrogen around the screw core; the results for 2 hydrogen atoms are shown in table 6.2 and those for 3 in table 6.3. Each of the equivalent sites are labelled so that they count from the top-right site clockwise from zero, as shown in figure 6.1; the screws have sixfold symmetry so there will either be 1, 3 or 6 equivalent positions for each site. $E_{b1} + E_{b2}$ (or $\sum E_b$ in the 3H case) gives the total binding energy for all the hydrogen atoms to the screw, ΔE_b is then the difference between this energy and the sum of the binding energies of the isolated hydrogen in those sites and \vec{r} is the separation between the hydrogen atoms after relaxation. The ZPE corrections were not calculated in this case as this was intended simply as a rough calculation and the number of calculations for the ZPE correction scales quadratically with number of hydrogen.

ΔE_b then shows the reduction in binding energy due to the interaction between hydrogen atoms and, as shown in the tables, this can get quite small for the sites on either side of the core. The bottom four entries of table 6.2 in particular have insignificant interaction energies, and comprise some of the strongest binding sites of both cores. It is interesting to note that the E20 E24 interaction is less than the E20 E23 by 14meV, although the second pair of hydrogen atoms are more distant by 0.59Å; however this is a small difference and so is possibly an artefact of the relaxation. Some of the interaction energies in table 6.3 are misleading in that the bulk of the interaction energy will be the result of the two closest hydrogen atoms, as can be seen by summing the interaction energies of each pair in table 6.2. For the case of E20 E21

Hydrogen Interactions With Screw Dislocations

E24, for example, almost the entirety of ΔE_b will come from the interactions between E20 and E21.

Sites	$E_{b1} + E_{b2}$	ΔE_b	\mathbf{r} (Å)
E20 E21	231	-223	1.95
H10 H11	315	-237	1.89
E23 E24	349	-104	2.60
H23 H24	227	-93	2.68
E20 E24	451	-3	3.54
H10 H24	426	-10	3.52
E20 E23	437	-17	4.13
H10 H23	429	-7	4.19

Table 6.2: Table containing the total binding energy of two hydrogen atoms to a screw dislocation ($E_{b1}+E_{b2}$), the difference between this value and the binding energies of the individual sites (ΔE_b) and the separation between the hydrogen atoms after relaxation (\mathbf{r}). Energies are given in meV.

Sites	$\sum E_b$	ΔE_b	\mathbf{r} (Å)
E20 E21 E24	445	-225	1.94, 4.24, 3.53
H10 H11 H24	457	-256	1.88, 4.03, 3.52
E20 E24 E23	562	-114	3.55, 2.61, 4.21
H10 H24 H23	486	-110	3.53, 2.69, 4.28
E20 E22 E24	659	-22	3.29, 3.29, 3.29
H20 H0 H23	547	-36	3.29, 3.29, 6.53

Table 6.3: Table containing the total binding energy of three hydrogen atoms to a screw dislocation (ΣE_b), the difference between this value and the binding energies of the individual sites (ΔE_b) and the separation between the hydrogen atoms after relaxation (\mathbf{r}). Energies are given in meV.

The E20 E22 E24 hydrogen atoms have a range of 1.65Å in their z -coordinates and show a negligible reduction in binding energy of ~ 7 meV per atom; while the H20 H0 H23 hydrogen atoms form a kind of diagonal line through the core with a z -range of 1.95Å and again show a negligible reduction in binding. These results show that it is entirely feasible for a single Burgers vector of screw core to be multiply occupied by up to three hydrogen atoms; the maximum separation in the z -coordinate of these hydrogen atoms was 2.03Å. Although the results would be of interest, the interaction

of hydrogen atoms in the same site separated in z was not examined due to the size of cell that would be required.

6.3.2 Effects of Strain

Shown in figure 6.2 (a), (b) and (c), as a function of compressive and tensile biaxial strain in the plane normal to the dislocation line, are the dissolution energies, ZPE corrected binding energies relative to a strained tetrahedral site and ZPE corrected binding energies relative to an unstrained tetrahedral site respectively. The variation of dissolution energy for each site with strain is shown to be fairly linear with some minor variation, increasing with compression and decreasing with tension as found by *Ramasubramaniam et al.*[227] using GGA-DFT for a tetrahedral site under hydrostatic strain.

It is interesting to note that the binding energy of the sites relative to the strained tetrahedral site (graph b) has the opposite pattern to those relative to the unstrained site (graph c). This is due to the fact that the gradient of the tetrahedral site dissolution energy and ZPE correction was much greater than the other sites', and so the tetrahedral dissolution energy approaches the other binding sites with tension and diverges from them with compression. This could then have the effect at equilibrium that a slightly greater proportion of the local concentration of hydrogen would be segregated to screw dislocations in compressive regions than tensile; however there would be a greater local concentration in tensile regions as the binding to tetrahedral sites is greater. The actual effect of this variation is difficult to say, and may depend on how long the system has to equilibrate between kink nucleation or movement events, but only the case of a system in full equilibrium will be considered here.

In the case of the binding energy relative to the unstrained tetrahedral site the binding for every site increases with tension as would be expected. The gradient of the binding energy for each site was found to be roughly proportional to the inverse of their binding strengths; so H0 has the strongest binding and the smallest gradient with a variation of 41meV between 1% tension and compression, while E0 is the second most weakly bound has a variation of 101meV. The magnitude of the gradient for each of the sites is then ordered oppositely to their binding strength, apart from the weakest site, E8, which has a variation of 76meV and so is less than E0 but still greater than E3 at 63meV. This is a fairly weak effect but would mean that the energy landscape for hydrogen around the screw core would become slightly more or less rugged with compression and tension respectively, which may slightly alter the effect that the

Hydrogen Interactions With Screw Dislocations

presence of hydrogen has on the energetics of screw processes.

Itakura et al. calculate the change in enthalpy for the kink-nucleation process by considering the hydrogen to remain stationary during the transition, a fair assumption for the E2 site in front of the dislocation line as it is strongly bound throughout. The hydrogen in this site moves relative to the dislocation core through the sites E2-H0-E2 during the transition, showing an increase in binding energy from E2 to H0 of 94meV at 0% strain and so reducing the enthalpy for the process; this binding energy change shows a very slight variation with strain, increasing by only 3meV with 1% compression and decreasing by 7meV at 1% tension.

Strain will also have a slight effect on the kink trapping by hydrogen: as the time scale for kink migration is much shorter than hydrogen diffusion the hydrogen will remain essentially stationary as the kink sweeps past and moves the dislocation line one Peierls valley relative to the hydrogen atom, therefore a decrease in binding energy will act to trap the kink. The largest kink trap energy for hydrogen behind the dislocation line would come from hydrogen that follows the path of E2-H2-E8 relative to the screw core as the kink sweeps past, which would have a total decrease in binding energy, or kink trapping energy, of 207meV at 0% strain. This shows an increase of 14meV at 1% compression and a decrease of 11meV at 1% tension. Finally the other kink trapping energy would come from the path E2-H2-E3 which shows a weaker trapping effect of 94meV at 0% and changes of ± 6 meV at 1% compression and tension respectively. The weaker binding energies of the E3 and E8 sites would result in lower occupancy and so any transition with the hydrogen initially in these sites is unlikely to have a large effect.

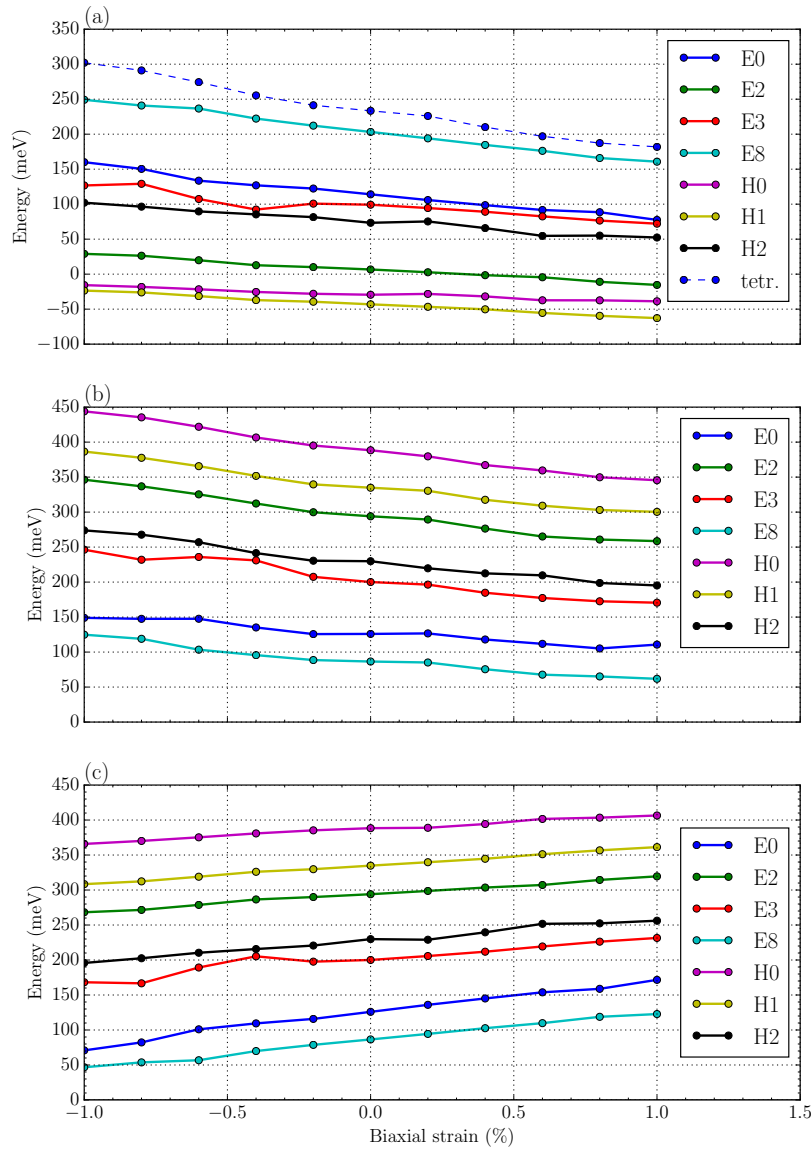


Fig. 6.2: Graphs of the variation of (a) dissolution energy, (b) ZPE corrected binding energy relative to a strained tetrahedral site and (c) ZPE corrected binding energy relative to a unstrained tetrahedral site for the hydrogen trap sites around ECC and HCC screw cores with biaxial tensile and compressive strain in the plane normal to the dislocation.

Itakura et al. used their results to calculate the conditions required for significant hydrogen softening. They used McLean's equation to estimate the concentration (C_B) of hydrogen in a binding site of strength E_b^z with a hydrogen lattice concentration C_0

at temperature T :

$$C_b = \frac{C_0^s \exp(E_b^z/k_B T)}{1 + C_0^s \exp(E_b^z/k_B T)} \quad (6.6)$$

where k_B represents the Boltzmann constant and C_0^s is the number of solutes per site, or a third of the concentration in atomic parts per million as there are three tetrahedral sites per iron atom. Hydrogen in the E2 sites in front of the dislocation will enhance the kink nucleation rate by $1 + C_b W_k \{\exp(\Delta E_k/k_B T) - 1\}$; W_k here is the width of the embryonic kink-pair (taken to be 10 Burgers vectors) and ΔE_k is the change in kink nucleation enthalpy with hydrogen in the E2 site. This factor may be arrived at by considering that a proportion of the line, given by $C_b W_k$, will have a hydrogen atom in front of the embryonic kink-pair as it is nucleated, and so will have the barrier lowered by ΔE_k . *Itakura et al.* calculated this enthalpy change to be 110meV using a line tension model and the string method[229]. A line tension model for a dislocation line consists of considering the dislocation as a large number of segments with a length of a Burgers vector along $\langle 111 \rangle$, or the axis that the pure screw would have its dislocation line along, and calculating the dislocation energy as the sum of the energies of these segments. The energy of each segment will be made up of the dislocation line energy multiplied by the length of that segment, the energy of the Peierls surface at the point that the segment intersects it, and the energy due to the interaction with the stress field. The shape of the line will have certain constrictions on the maximum angle allowed between segments, but is otherwise allowed to relax and can provide a good approximation to the line shape, provided that the segment energies are well specified. This group previously employed this formulation to calculate the kink-pair activation energy and found good agreement with previous MD results, and now simply included a term to account for the interaction with hydrogen as the kink-pair is formed[94].

I will use this value here since, as mentioned, the variation in energy of the E2-H0-E2 pathway is only 10meV between 1% tension and compression and the values of the binding energies presented here are of sufficient similarity to theirs. *Itakura et al.* defined the condition for significant increase of the kink-pair nucleation rate as when the hydrogen concentration in the E2 site is greater than C_b^E , which is given by:

$$C_b^E = \frac{1}{W_k \{\exp(\Delta E_k/k_B T) - 1\}} \quad (6.7)$$

This results in a critical temperature, T_u , for each hydrogen lattice concentration above which C_b^E exceeds C_b and kink nucleation enhancement is not significantly

large. The definition of C_b^E is slightly arbitrary, as the concentration required for the $C_b W_k \{ \exp(\Delta E_k / K_B T) - 1 \}$ term in the nucleation enhancement factor to be equal to one, however the exponential dependence on temperature means that the enhancement becomes significant very quickly as the temperature decreases below T_u . The value for T_u is shown in figure 6.3 for all the strains considered here; it shows a general trend of increasing with tension and decreasing with compression, as might be expected.

A realistic hydrogen lattice concentration would be < 1appm, while values up to 10appm are only really achievable with charging, and so it is the bottom three lines that will be of most relevance to industrial environments. As mentioned, these lines are not a sharp distinction: the degree of nucleation enhancement will decrease smoothly as the temperature approaches T_u , but the exponential dependence means that the range of each line can still define regions of temperature where significant enhancement is occurring in tensile zones but not in compressive. At a concentration of 0.001appm kink nucleation enhancement would only occur in regions of high tension ($> 1\%$) at room temperature, while at $C_0 = 0.1$ appm the effect will be significant in all regions except those under high compression. These lines also demonstrate generally how, in an isothermal solid with $T < T_u$, the degree of nucleation enhancement will be much greater in regions of tension.

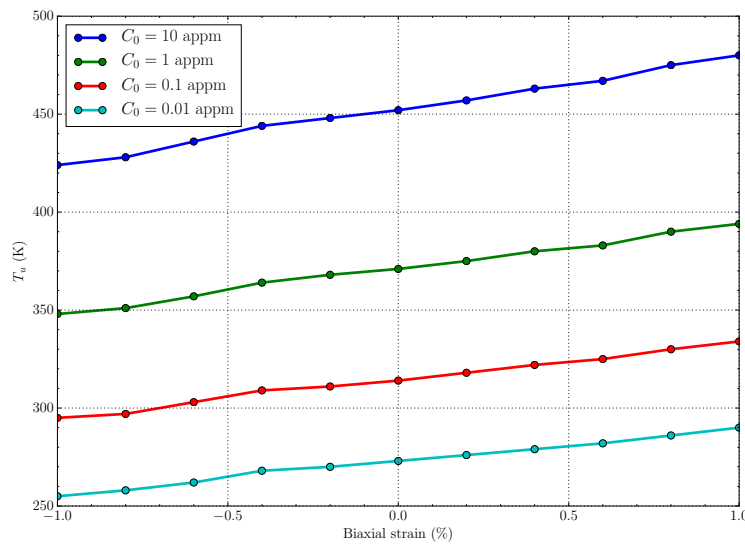


Fig. 6.3: Shown are the critical temperatures T_u , above which the hydrogen will not produce a significant enhancement of the kink nucleation, across the range of biaxial strains studied for several hydrogen lattice concentrations C_0 .

Itakura et al. used the result calculated for the kink trapping energy to estimate a

Hydrogen Interactions With Screw Dislocations

lower critical stress, below which the enthalpy increase per unit length of kink motion due to hydrogen detrapping, ($C_b E_t^0 / b$), is greater than the decrease in enthalpy for the same movement, ($-\sigma b h$). C_b represents the concentration of hydrogen in the E2 site behind the screw line and E_t^0 the kink trapping energy at zero effective stress, arising from the hydrogen changing from the E2 to E8 site as the kink sweeps past, b represents the Burgers vector, σ is the effective shear stress on the dislocation (which will include the applied stress and the stress fields resulting from other defects in the area) and h is the kink height, or $\frac{2}{\sqrt{6}}a$.

They then consider that if the enthalpy increase from kink trapping is greater than the reduction from kink motion then the kinks will be locked and the screw dislocation cannot move; this results in a relation for the lower critical stress:

$$\sigma_l = \frac{C_b E_t^0}{h b^2} \quad (6.8)$$

In reality this limit is not absolute: the kinks will still escape these traps by thermal fluctuations, this is really just a measure of how much kink-drag is occurring. It is also important to note that kink-drag will still occur at effective stresses above σ_l , until a much higher stress when the barrier is reduced to zero; σ_l simply defines a limit below which movement of the screw dislocation becomes energetically unfavourable. The variation of this lower critical stress with temperature for several hydrogen lattice concentrations is shown in figure 6.4. And so, as the temperature is increased a higher C_0 is required for a significant trapping effect.

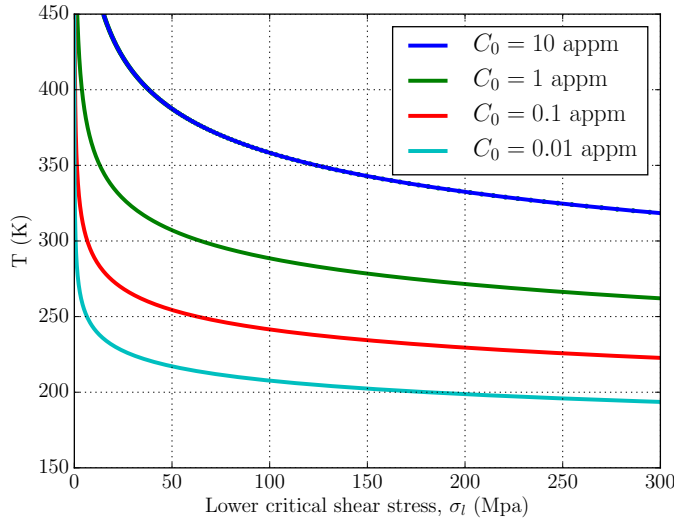


Fig. 6.4: The variation with temperature of the lower critical shear stress (σ_l) required for screw dislocations to escape the hydrogen kink trapping effect at several hydrogen lattice concentrations.

Equation 6.8 was then used to calculate the variation of the lower critical stress with biaxial strain for several temperatures and lattice concentrations, shown in figure 6.5. At lower temperatures σ_l is large even for the low hydrogen concentrations and has a large variation with strain: at $T=200\text{K}$ the σ_l of $C_0 = 0.01\text{appm}$ increases from 46MPa to 595MPa from 1% compression to tension; while $T=250\text{K}$ the σ_l of $C_0 = 0.1\text{appm}$ varies from 21MPa to 184MPa. This implies that at low temperatures the slip of screw dislocations may actually be localised to regions of high compression rather than tension, although it is difficult to estimate the overall effect with the increased kink-pair nucleation in tensile areas.

As mentioned, this effect is reduced with temperature and so higher concentrations will be required at higher temperatures for a significant effect; at 300K and $C_0 = 1\text{appm}$, σ_l has a range from 26MPa to 157MPa, while at 350K this is reduced to between 6MPa to 29MPa. In the case of $C_0 = 0.01\text{appm}$ at 300K the maximum σ_l is only 2MPa and the maximum T_u is $\sim 290\text{K}$, implying that the total effect of hydrogen will not be significant. For $C_0 = 0.1\text{appm}$ the σ_l at 300K is also very small, with a maximum of 17MPa, but it will show significant kink nucleation enhancement for strains less than 0.09% compression; this is a similar pattern to $C_0 = 1\text{appm}$ at 350K . $C_0 = 10\text{appm}$, on the other hand, will show significant kink trapping and nucleation enhancement at all the temperatures considered here.

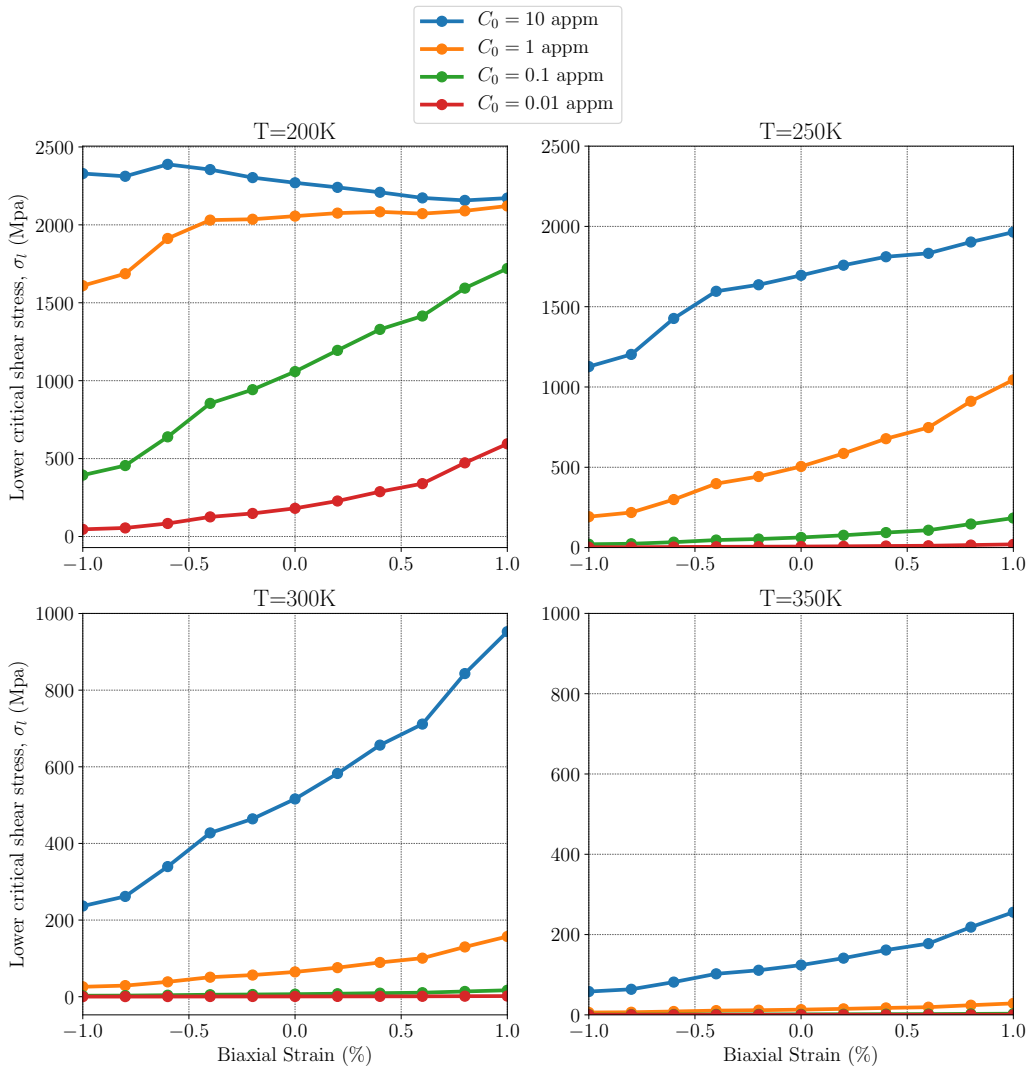


Fig. 6.5: Shown for the temperatures 200K, 250K, 300K and 350K is the variation of lower critical shear stress (σ_l) required for screw dislocations to escape the hydrogen kink trapping effect with applied biaxial strain for several hydrogen lattice concentrations.

The variation of kink trapping energy with strain has been included here; generally having the effect of slightly increasing σ_l in the compressive regime and reducing it in the tensile, reducing the range by a small amount. This effect is $\sim \pm 5\%$ of the kink trapping energy and so only really has a significant effect at high values of σ_l : at T=250K for $C_0 = 1$ appm it increases σ_l at 1% compression by 12MPa from 180 to 192MPa, and decreases it at 1% tension by 57MPa from 1101MPa to 1044MPa; while at T=300K for the same concentration it only increases σ_l from 24MPa to 26MPa at

1% compression and decreases it from 166MPa to 157MPa at 1% tension.

It may be easier to see the effect of hydrogen on screw dislocation mobility by considering the variation in average kink velocity with hydrogen bulk concentration. *Katzarov et al.*[95] estimated the velocity at which a kink would travel past a hydrogen atom in their kMC model from the transition state theory expression for the rate at which the kink could escape each hydrogen trap:

$$P_H = f_k \exp \left(-\frac{E_t(\sigma)}{k_B T} \right) \quad (6.9)$$

$E_t(\sigma)$ in this case represents the stress-reduced hydrogen kink trapping energy, *Itakura et al.* estimated it using the string method at various values of applied shear; the $E_t(\sigma)$ used here was obtained by fitting a cubic spline to their results and then scaling it such that it matched the value for each strain calculated here at zero effective shear stress (E_t^0), as shown in figure 6.6. The attempt frequency f_k is taken to be the Debye frequency for iron ($f_k = 1.34 \times 10^{13} \text{s}^{-1}$). However, this would not include the chance that kinks could jump back into the hydrogen trap immediately after escaping; *Katzarov et al.* calculate this chance from the forward and backward jump frequencies from the kink position directly after the trap, or J_k^+ and J_k^- respectively.

$$J_k^+ = f_k \exp \left(-\frac{\Delta E - \sigma b^2 h}{k_B T} \right) \quad (6.10)$$

$$J_k^- = f_k \exp \left(\frac{E_t(\sigma) - \sigma b^2 h}{k_B T} \right) \quad (6.11)$$

ΔE represents the the energy change as the kink moves forward, from elastic interactions with other kinks and so on; in the simplified estimates made here this contribution will be approximated to be zero, so the kinks do not interact with any surrounding defects. The modified escape-rate is then:

$$P_H^+ = P_H \frac{J_k^+}{J_k^+ + J_k^-} \quad (6.12)$$

which may then be employed to estimate the velocity with which a kink would pass a hydrogen atom:

$$v_k^H = \frac{\sigma b h}{k_B T} b^2 P_H^+ \quad (6.13)$$

The Burgers vectors are kept separate in this expression because one arises from the

expression for the kink mobility ($\frac{b^2}{k_B T} P_H^+$) and the other from the lateral force due to stress ($\sigma b h$)[230].

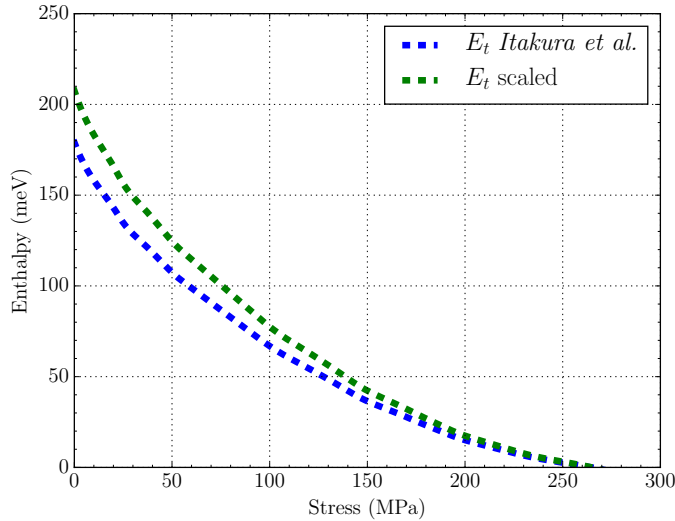


Fig. 6.6: The value of the hydrogen kink trapping energy against applied stress; a function was fitted to the results presented in *Itakura et al.*[48] and then scaled to match the trapping energy at zero stress calculated here.

The barrier to kink motion without solute drag is so low in iron that it does not require thermal fluctuations to overcome it, even at low applied stresses (estimated to be 5×10^{-5} eV or 9×10^{-5} eV)[203]. Therefore, if it does not encounter hydrogen or other defects, its velocity will only be limited by phonon drag, or lattice damping resistance, which is characterised by the coefficient B_k [231]. In this case the kink velocity will be proportional to this phonon drag coefficient and the effective stress on the dislocation:

$$v_k = \frac{\sigma b}{B_k} \quad (6.14)$$

The most reliable way to estimate the phonon drag coefficient is to observe the mobility of individual dislocations with applied stress; B_k will then be proportional to the gradient of the steady state velocity of the dislocation. *Kuksin and Yanilkin*[232] used MD simulations with an interatomic potential for iron to obtain values for B_k at a range of temperatures, observing a fairly linear dependence characterised by the

relation shown below.

$$B_k = (2.7 + 0.008T) \times 10^{-5} \text{ Pas} \quad (6.15)$$

This relation for the phonon drag coefficient will be used here; although *Kuksin and Yanilkin* also found that B_k increased with hydrostatic compression the change was by < 2% at 1% compression and so this variation will not be included. The reduced velocity of the kinks due to the presence of hydrogen can then be estimated from these two velocities:

$$v'_k = C_b v_k^H + (1 - C_b) v_k \quad (6.16)$$

Results for several values of effective shear at a temperature of 300K are shown in figure 6.7; however, these values should be considered an upper limit as they do not include the interaction between kinks or with other obstacles. Due to the small secondary Peierls barrier, normal kink motion is very fast and even the lowest concentration of hydrogen reduces the kink velocity to a small proportion of its original value at $\sigma = 30\text{MPa}$. However, even the lowest reduced velocity calculated here is still $2 \times 10^{-2}\text{ms}^{-1}$ (for $C_0 = 10\text{appm}$ at $\sigma = 30\text{MPa}$), a large value relative to the length of dislocations, which would be on the order of micrometers. This velocity is only decreased to $6 \times 10^{-6}\text{ms}^{-1}$ at a lower stress of $\sigma = 1\text{MPa}$. As the effective shear is increased the kink trapping becomes less effective, and so the velocity at all applied strains and hydrogen concentrations increases as a proportion of v_0 . In general, it can be seen that this drag is much more effective in regions of tension, but if the strain is sufficient to free the kinks from hydrogen trapping then the effect is reduced and the velocity is almost constant across the applied strains.

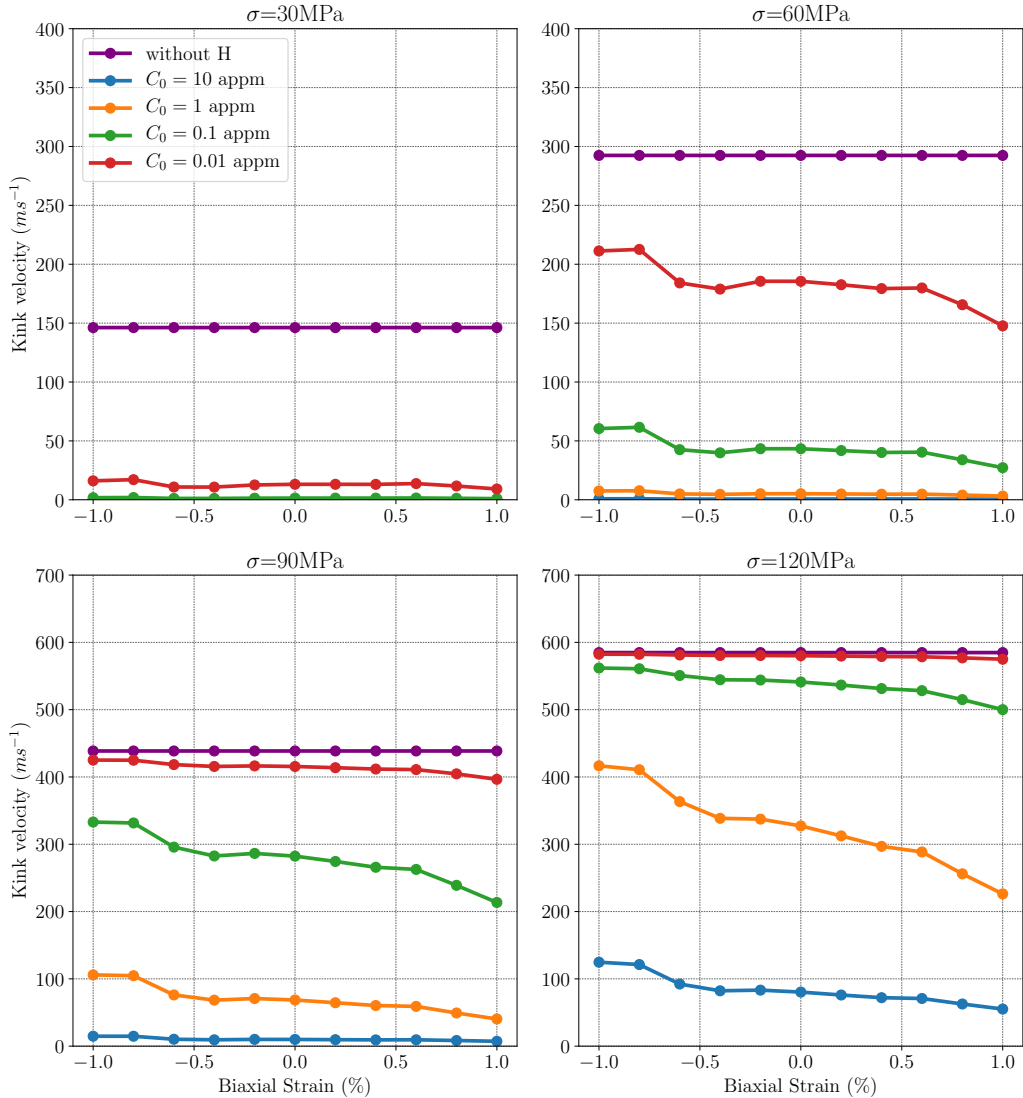


Fig. 6.7: The average kink velocity against the biaxial strain at several effective shear stresses and hydrogen lattice concentrations at a temperature of 300K.

It should be noted that the kink velocity will not directly determine the degree of hardening unless the movement and annihilation of kinks is the rate limiting step in dislocation motion. Kink-pair nucleation is a rare event with a high activation energy and, as mentioned in chapter 4, if the embryonic kink-pair does not quickly separate beyond the critical width then the new kinks will frequently annihilate with each other. The temperature and strains shown here were chosen to illustrate the variation in magnitude of hydrogen's effect on the kink velocity with biaxial strain; it is unlikely for the kink motion to be the rate limiting step in these regimes, which

may be seen by considering an example. *Itakura et al.* calculate the stable kink-pair nucleation rate using the Arrhenius law:

$$R_N = D_d N_d \exp\left(-\frac{E_k}{k_B T}\right) \quad (6.17)$$

where N_d is the dislocation length in units of b and E_k is the kink nucleation enthalpy. This attempt frequency D_d was estimated from experimental measurements of the dislocation velocity at room temperature by *Caillard*[149], and so this rate would only refer to the nucleation of stable kink-pairs, not those that immediately annihilate after nucleation.

For a dislocation of length $2\mu m$ at 300K with an applied stress of 33MPa they estimate this rate to be $81s^{-1}$; as mentioned they estimate that this rate will be enhanced by hydrogen by a factor of $1+C_b W_k \{\exp(\Delta E_k/K_b T)-1\}$. At a concentration of $C_0 = 10appm$ this rate will be enhanced to $2.1 \times 10^3 s^{-1}$ at 1% compression and $9.2 \times 10^3 s^{-1}$ at 1% tension. The rate of kink annihilation (R_A) can be estimated by calculating the rate at which kinks could travel the length of the dislocation, or slightly greater than the maximum possible distance travelled before annihilation, assuming only forward motion. This results in a rate of $1.5 \times 10^4 s^{-1}$ at 1% compression and $1.2 \times 10^4 s^{-1}$ at 1% tension. Therefore, at no point is the kink-annihilation the rate-limiting step; a concentration of at least 22appm would be required in this case for kink annihilation to be the rate limiting step at zero applied strain, although it is only 14appm at 1% tension. The effect of hydrogen will increase at lower temperatures, but the base rate of kink-pair nucleation will decrease; for a concentration of 1appm the annihilation never becomes the rate limiting step, but for 10appm it does at 250K.

Again, this is a very simplified calculation, assuming that the kinks encounter no obstacles except for hydrogen, and so the kink velocities are certainly overestimated. The nucleation estimation also includes the assumption that concentration of hydrogen in front of the screw dislocation is always sufficient for kink-pair nucleation enhancement but these calculations simply serve to illustrate the trend. This is the pattern predicted by *Kirchheim*[91] in the defactant model: the time taken for kinks to travel along the line increases with the hydrogen concentration, while that required for kink-pair generation decreases. They predict that at some point these rates will pass each other, and the regime will pass from softening, by enhanced kink-pair nucleation, to hardening, by solute drag. The concentration required in this example was very high, but this could perhaps be reduced somewhat with a more realistic description of the kink movement.

Hardening does not only occur directly from the reduction in kink velocity, but also in some situations indirectly: as the kink-pair nucleation rate is enhanced and the average kink velocity is decreased it becomes more likely that the dislocation will still have kinks travelling along it when it nucleates a new kink-pair, possibly on another slip plane[95]. The collision of kinks on different slip planes will result in the generation of jogs: short sections of edge dislocation on a different glide plane from the rest of the dislocation. These often form strong pinning points for the dislocation, requiring climb of the jog segment for the dislocation to move in its glide plane and so reducing the dislocation's mobility. This form of hardening would be more likely to have an effect at lower concentrations because it does not require the kink-annihilation to be the rate limiting step to be active, but smoothly increases in likelihood as the annihilation rate approaches the nucleation rate.

As the temperature is decreased so is the phonon drag, and so the normal kink velocity will increase slightly: at $\sigma = 100\text{MPa}$ and $T = 300\text{K}$ $v_0 = 487\text{ms}^{-1}$, while at $T = 250\text{K}$ $v_0 = 529\text{ms}^{-1}$. However, the kink trapping also becomes more effective as thermal fluctuation is less likely to free kinks and the concentration in the E2 site increases. At the same time the decrease in temperature decreases the rate of kink-pair nucleation, but increases the factor by which hydrogen enhances that rate. It is then difficult to say how a changing temperature will change the effect of hydrogen on screw dislocations, which will be demonstrated below.

Using the dislocation from *Itakura et al.*'s paper mentioned above (with a length of $2\mu\text{m}$, an effective stress of 33MPa and a kink nucleation enthalpy of 595meV) the variation of kink velocity and kink-pair nucleation rate may be calculated at a range of biaxial strains, hydrogen bulk concentrations and temperatures. The rate of kink annihilation can be estimated in the same way as above, then taking the kink-pair nucleation rate over the rate of kink annihilation will give an estimate of the number of kink-pairs formed while each kink travels along the dislocation line, or the chance for crossed-kinks to collide and form pinning points. Of course this is a very simplified calculation, making the same assumptions as before and the further assumptions that the kink-pairs are nucleated both in front of and on a different glide plane to the travelling kink, but again this calculation serves only to illustrate a general trend. Results for the range of concentrations, temperatures and strains are shown in figure 6.8.

Almost all of the graphs illustrate that the chance of pinning-point formation is much greater in areas of tension, apart from that for $C_0 = 10\text{appm}$ for which

the lower-temperature lines begin to show the reverse trend. This occurs because of the variation in trap energy with strain and the concentration saturation at high bulk concentrations. As mentioned, due to the variation in the trap site's binding energy gradient with strain, E_t is greater at 1% compression than 1% tension by $\sim 10\%$; also, as the bulk concentration is increased, the proportional difference in the occupation of these sites between regions of tension and compression is decreased. The exponential dependence on the trap energy means that this small variation becomes more important than the concentration difference between regions after a certain point. Solute drag is then more effective in compressive zones but the nucleation enhancement is similar, so pinning point formation becomes more likely in the compressive zone. However, this effect likely only becomes active at very low temperatures and high hydrogen concentrations.

For $C_0 > 0.01\text{appm}$, every graph generally shows an increase in pinning-point formation chance as the temperature is lowered, and an increase in the gradient of the lines so that the discrepancy between tensile and compressive regions is intensified. At $C_0 = 0.01\text{appm}$, however, this trend seems to be reversed for the highest temperatures, which show a steady increase in chance and little dependence on strain. This occurs because the effects of temperature on these processes become dominant over those of hydrogen: the low concentration and high temperature means that the kink velocity is determined more by the phonon drag than solute drag, and the increased temperature also results in an increase of the kink-pair formation rate. This is why the lines for $T \geq 300\text{K}$ are close to level across the strains. *Katzarov et al.*[95] also observed this trend with their kMC model: at low applied stresses ($\sigma \approx 50\text{MPa}$) pinning-point formations at 300K were unlikely and required concentrations of $C_0 > 0.5\text{appm}$, but the chance increased greatly at 400K, with no hydrogen, because the nucleation of kink-pairs on different glide planes became more likely. However, if the elastic interactions between the kinks and other defects were included, the kinks would be more likely to transition back into hydrogen traps and so increase the drag effect; the effect of hydrogen in these cases is then likely underestimated. This could at least increase the chance at lower temperatures; *Katzarov et al.* found that concentrations of only 0.001appm were required for significant pinning at 150K for these low stresses.

The strong temperature dependence of the other graphs matches the general trend seen experimentally by *Kimura and Matsui*[85, 233] in a series of tensile tests on high purity iron: they observed a softening effect in the flow stress between 200-300K and hardening below 200K; they also found that for lower concentrations this transition

Hydrogen Interactions With Screw Dislocations

temperature would be lowered. There is some evidence, however, that in pure iron below 200K the mechanism for screw dislocation movement ceases to be based on kink nucleation and annihilation, and so results based on these processes may not be relevant to low-temperature hardening[234].

These graphs generally illustrate that the chance of pinning-point formation is much greater in tensile zones, particularly for the concentrations of 1appm and 0.1appm (which would be relevant to industrial environments[95]). They also illustrate that the effect is dominated by the increased binding energy of hydrogen trap-sites with tension at low temperatures and concentrations, but by the increased energy of the kink-trapping effect by hydrogen with compression at high concentrations. Although, this second effect is likely to require very high hydrogen concentrations. The description used here is greatly simplified and really approximates a snapshot of a straight dislocation with no surrounding microstructure, which could affect the results greatly.

It is difficult to make predictions without the full kMC model based on these results, but the data presented here indicates that screw dislocations in tensile areas will generally undergo the effects of hydrogen to a greater degree than those in compressive areas. With an increasing lattice concentration of hydrogen the screw dislocations will first have their mobility enhanced as the kink nucleation rate is enhanced. This effect will then be reversed as both the kink-pair nucleation enhancement and the kink-drag reach the point that the nucleation rate becomes comparable with that for annihilation, so that crossed-kink collision is more likely. Depending on the lattice concentration, effective stress and temperature there could then be regimes that have significant softening only in tensile zones or even softening in compressive zones and significant hardening in tensile zones.

Hydrogen Interactions With Screw Dislocations

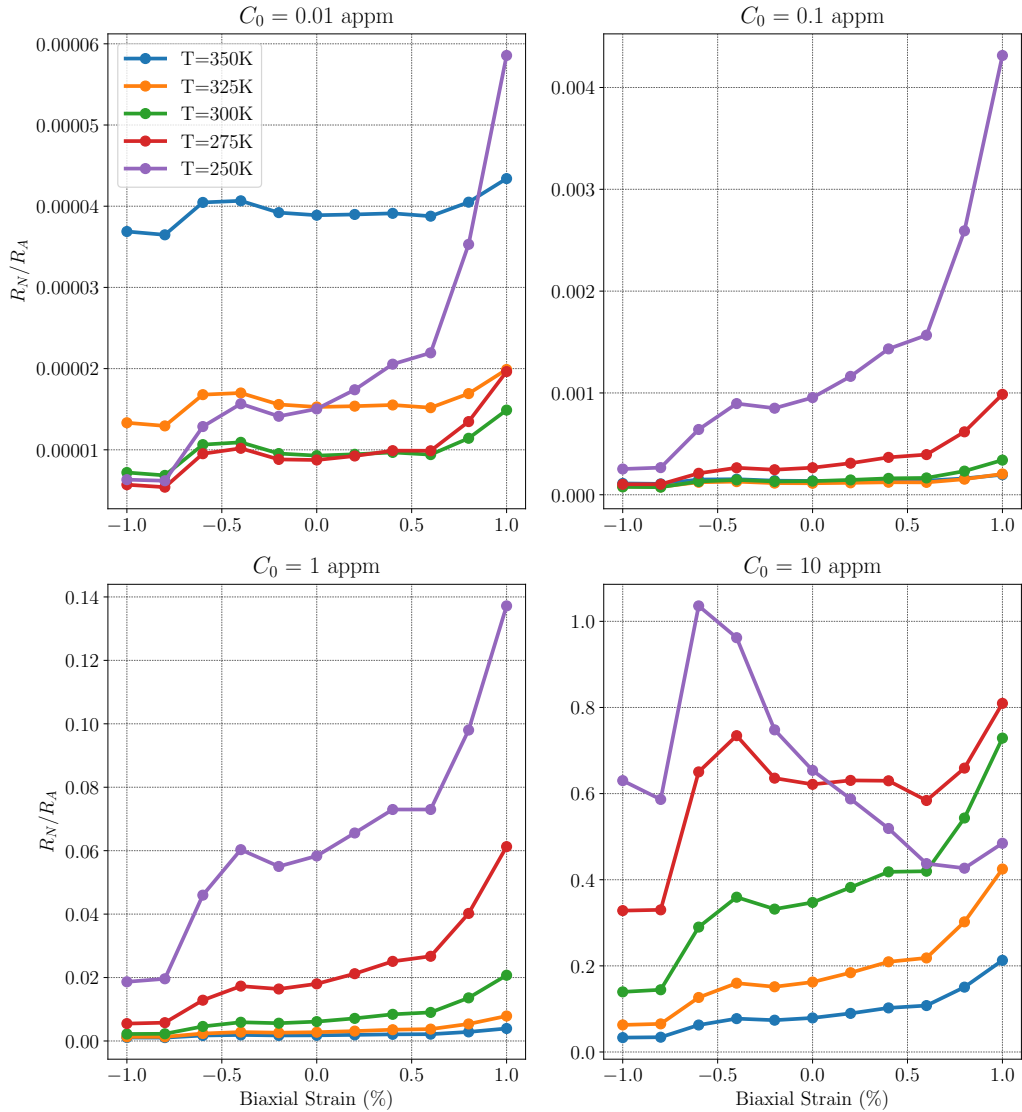


Fig. 6.8: Shown for several hydrogen lattice concentrations (C_0) and temperatures (T) is the kink-pair nucleation rate (R_N) over the kink annihilation rate (R_A), which is taken as the time taken for the kink to travel the length of the dislocation. This provides a rough estimation of the chance of pinning-point formation for each kink-pair nucleated. The dislocation length is $2\mu m$ and the applied stress is 33MPa.

The effect of these biaxial strains on the Peierls barrier for a quadrupole of dislocations simulated using the BOP is shown in figure 6.9. These Peierls barriers were calculated for each strain in the same way as in chapter 3: anisotropic linear elasticity theory was used to introduce a quadrupole of dislocations into a square section of a

(11̄1) plane containing 576 atoms, that is periodic in every direction. Biaxial tension or compression was then applied increments of 0.1% and the cell was relaxed until the maximum force on an atom was less than $10^{-4}\text{eV}\text{\AA}^{-1}$. Finally the NEB method was used to calculate the minimum energy path for all the screw dislocations to move to the next Peierls valley simultaneously. The barrier increases with 1% compression by $\sim 5\text{meV}$ and decreases with 1% tension by $\sim 8\text{meV}$; however these values cannot be taken as exact as the biaxial strain may affect the interaction between the screw cores in the array, which could alter the energetics of the process. The trend shown in figure 6.9 can be validated by comparing the core energies of the HCC and ECC; although the saddle-point of the transition does not pass directly through the HCC (as shown in chapter 3), the energy of the saddle-point should be similar to that of the HCC and so the energy difference between cores will have a similar trend to that of the Peierls barrier[94]. The difference in energy between a 60 Å radius single-layer cell containing the HCC screw or the ECC screw, strained incrementally and relaxed within the BOP method, is shown in figure 6.10. The dependence of the Peierls barrier on strain indicates that the kink-pair nucleation enthalpy will also have a strong dependence. Therefore, these results for the hydrogen binding cannot be employed in the kMC model until the variation in kink-pair formation rate has also been calculated.

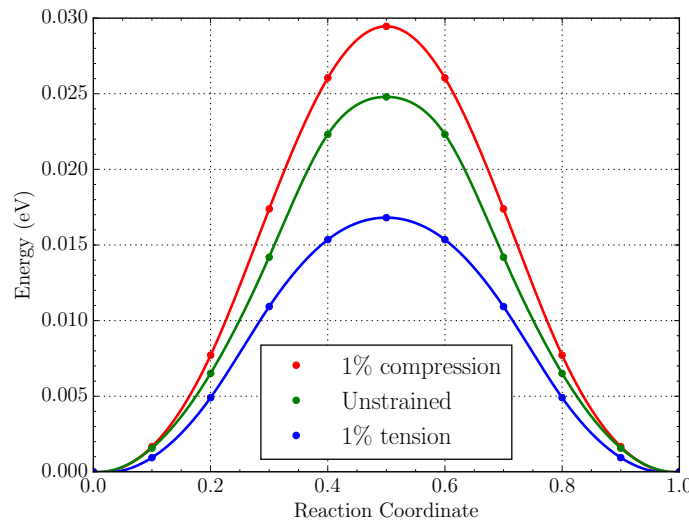


Fig. 6.9: Graph of the variations of screw Peierls barrier with applied biaxial strain. These barriers were obtained by using NEB to move a quadrupolar array simultaneously one Peierls valley over.

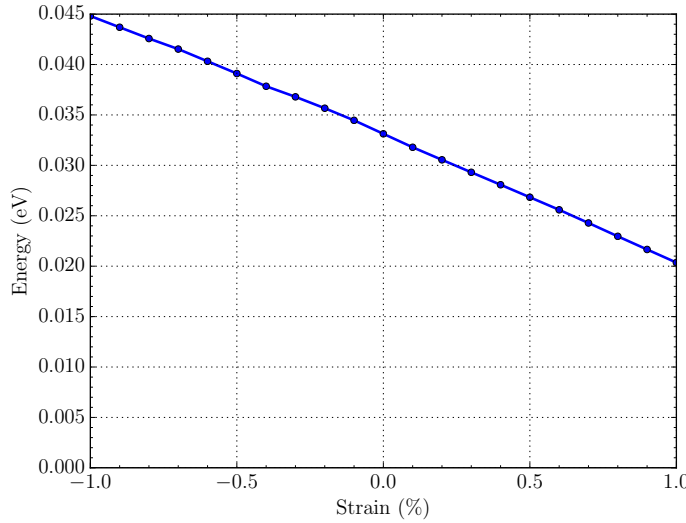


Fig. 6.10: Energy difference between a 60Å radius cell relaxed with BOP containing either an ECC or HCC screw dislocation with applied biaxial strain.

6.3.3 Hydrogen Diffusion Around a Screw Core

Shown in figure 6.11 are the barriers for the hydrogen migration from E3 to E2 and E2 to E0 characterised by CI-NEB at different values of the biaxial strain, and below in table 6.4 are the activation barriers, ZPE corrected barriers, attempt frequency and jump frequency at 300k calculated from the CI-NEB results. The calculated ZPE correction caused slight increases to the barriers for the E3 to E2 transitions, but the reduction for the E0 to E2 transition barrier was sizable, reducing it to a value comparable to the barrier for hydrogen transitions between tetrahedral sites in the bulk[224, 226, 235, 236].

Kimizuka and Ogata[237] used path-integral molecular dynamics modelling based on an EAM interatomic potential, with iron parameters taken from *Mendelev et al.*[238] and hydrogen parameters fitted to reproduce hydrogen transition states in the perfect lattice and around a vacancy, to study the diffusion of hydrogen around a screw ECC. The binding value they obtained for the E2 and E8 sites at 300K were quite close to our ZPE corrected values at 290meV and ~100 meV (this value is estimated from figure 2 in their paper) respectively, however they found close to zero for the binding at E0, ~100 meV distant from the result presented here and that of *Itakura et al.*. The migration barrier they obtain for the transition from E0 to E2 at 300K (~ 10 meV) is of a similar magnitude to the ZPE corrected value in table 6.4,

Hydrogen Interactions With Screw Dislocations

however their barrier from E2 to E0 is 154 meV greater at 360 meV.

The migration barriers between the E3 and E2 sites show a fairly strong dependence on strain, with both barriers decreasing by ~ 40 meV between 0 % and 1 % tension. The barrier between the E2 and E0 is much more insensitive, showing very little variation; however, the relative depth of the E0 trap increases by ~ 10 meV with 1% tension and decreases by ~ 20 meV with 1% compression, and so the barrier to escape the core actually increases slightly with tension. The attempt frequencies are also found to be quite insensitive to the strain, similar to the results for hydrogen transitions between tetrahedral sites found using DFT by *Ramasubramaniam et al.*[227], however the exponential dependence of the jump frequency on activation barrier means that the occurrence of these processes will show the same dependence as their barriers.

Altogether, these results indicate that hydrogen diffusion between these sites is much slower than in the bulk: the transition barrier between tetrahedral sites in the unstrained lattice was found to be 42 meV and 45 meV by *Jiang and Carter*[224] and *Ramasubramaniam et al.*[227] respectively with *ab-initio* models, the barriers shown here are between 5 – 10 times these values. This implies that hydrogen diffusion around the screw core is much slower than in the bulk; this was also the conclusion of *Kimizuka and Ogata*[237], finding that the hydrogen diffusivity was much lower in the area around the core, and that the activation free energy for hydrogen diffusion in these areas was 11 – 13 times higher than in the regular lattice. The jump-rates shown for each transition at 300K are also at least 4 orders of magnitude less than that inferred for bulk diffusion from experiment in the temperature range 283 – 348K, or that found in *ab-initio* calculations, which would be of the order of 10^{13}s^{-1} [227, 239]. This may mean that screw dislocations could leave behind their hydrogen atmospheres relatively easily, although more simulations are required to explore all possibly hydrogen pathways.

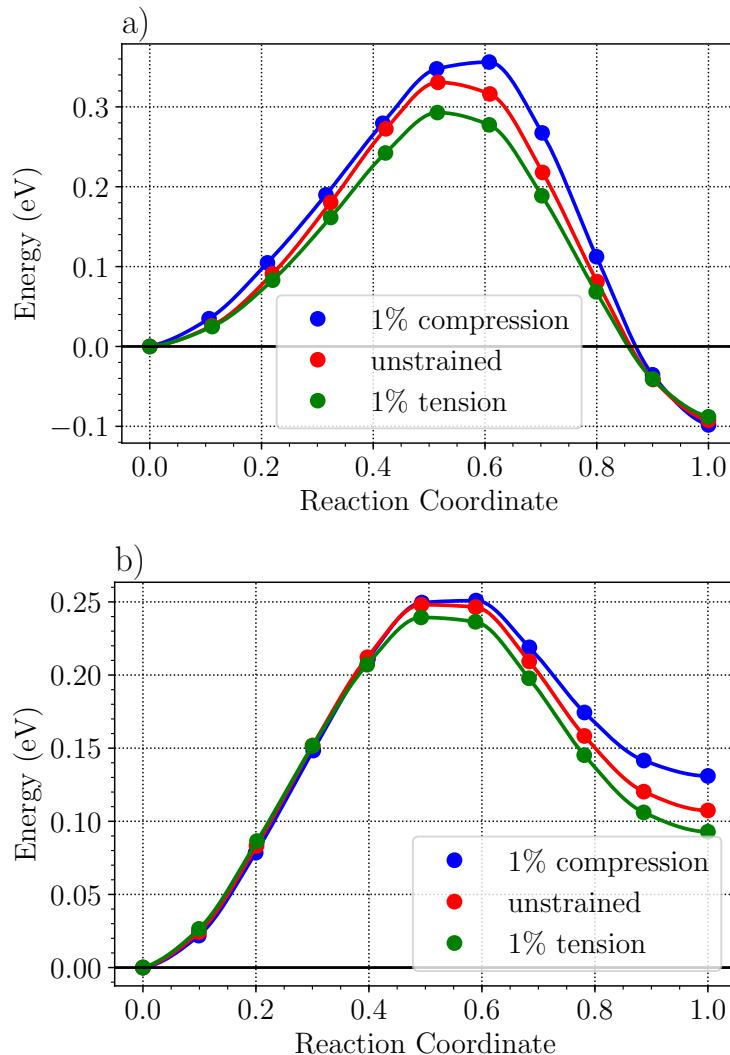


Fig. 6.11: Graphs of the variation of activation barriers with biaxial tensile and compressive strain for the transition between a) E3 to E2 and b) E2 to E0..

Path	Strain	ΔE	$\Delta E + \Delta E_z$	Γ_0	Γ (300K)
E3 - E2	-1%	356	360	1.452E+13	1.307E+7
	0%	330	344	1.000E+13	1.677E+7
	1%	293	301	1.157E+13	1.028E+8
E2 - E3	-1%	454	460	1.590E+13	2.927E+5
	0%	423	432	1.404E+13	7.677E+5
	1%	381	389	1.386E+13	4.008E+6
E2 - E0	-1%	251	231	2.635E+13	3.404E+9
	0%	248	221	3.411E+13	6.556E+9
	1%	239	214	3.210E+13	8.100E+9
E0 - E2	-1%	120	34	8.535E+13	2.280E+13
	0%	141	54	9.321E+13	1.138E+13
	1%	147	66	8.105E+13	6.237E+12

Table 6.4: Table containing the energy barrier (ΔE), ZPE corrected energy barrier ($\Delta E + \Delta E_z$), attempt frequency (Γ_0) and the jump frequency (Γ) at a temperature of 300K for the diffusion of hydrogen between the strongest binding sites around the screw ECC. Energies are in meV and frequencies in s^{-1} .

In the ECC screw the three core atoms form a helix of opposite chirality to the surrounding lattice, and so the path for diffusion along the dislocation line will form a kind of spiral around the core between neighbouring E0 sites, as illustrated in figure 6.12. As the sites have a greater binding energy than bulk tetrahedral sites and there is an increased atomic volume in the screw core it was believed that dislocation lines could act as an accelerated pathways through the lattice for hydrogen atoms in a mechanism known as pipe diffusion[240].

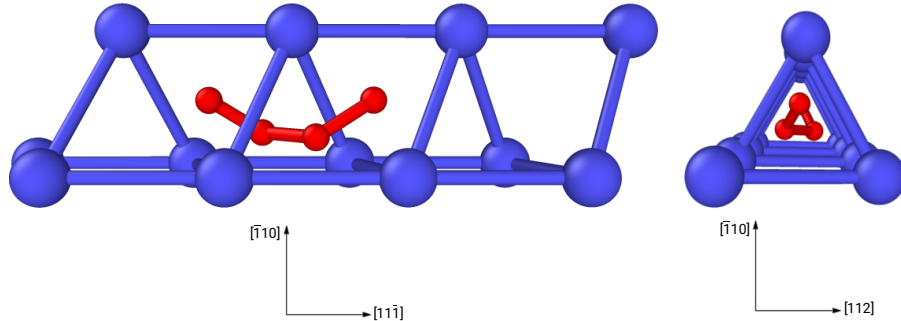


Fig. 6.12: Shown is the path hydrogen would take to move one Burgers vector along the ECC from a viewpoint perpendicular to and along the dislocation line respectively; the red atoms are the hydrogen binding sites and the blue are the iron atoms of the three $[11\bar{1}]$ columns surrounding the core.

In order to estimate the importance of this effect CI-NEB was used to calculate the barriers between the four E0 sites the hydrogen moves through to move one Burgers vector along the dislocation line. The cell in this case was the same size as that used for the previous binding and diffusion calculations except that it was stacked four times instead of three; this was done to prevent the interaction between the hydrogen atom and the three frozen core atoms altering the energy for one of the E0 sites. The barrier was found to increase with 1% compression by 14meV, however tension had very little effect and only reduced the barrier by 1meV, as shown in figure 6.13.

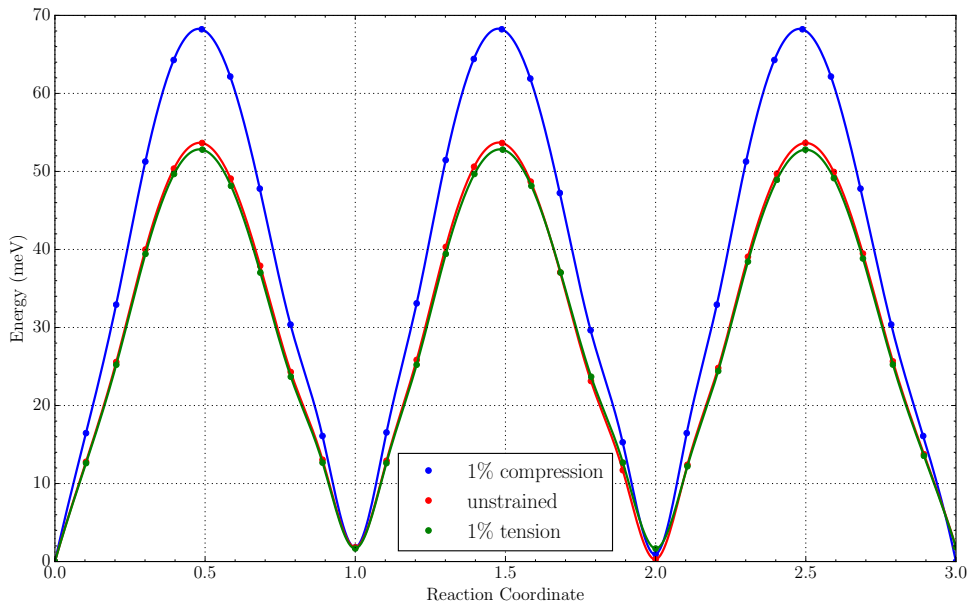


Fig. 6.13: Graph showing the variation in energy barrier for a hydrogen atom to move one Burgers vector along an ECC screw dislocation line with applied biaxial strain.

These results were again used to calculate the ZPE-corrected barriers and jump frequencies, as shown in table 6.5. The result at zero strain is found to match very well with that of *Kimizuka and Ogata*[237] who predicted an almost identical barrier of 22 meV, and also quite similar to the result of 35 meV from QM/MM calculations by *Zhao and Lu*[49]. This is around half the barrier for bulk diffusion at zero strain found with *ab-initio* methods[224, 227]. These results would support the idea of pipe diffusion except that the jump frequency for the E0-E2 transition is greater than that for E0-E0 and so the hydrogen is unlikely to spend long enough in the E0 sites for significant diffusion along [11̄1]. Again, this agrees with the conclusions of *Kimizuka*

and Ogata: they employed Path-Integral Molecular-Dynamics with the EAM potential they were using and found that the hydrogen did not spend long enough in the core for significant diffusion along the dislocation line.

This instability only increases with compression, with the E0-E2 jump frequency reaching $\sim 5\times$ the value for E0-E0 at 1% compression. At 1% tension, however, the E0-E2 barrier has increased while that for E0-E0 remains the same and so the E0-E0 jump frequency is actually greater. This pipe-diffusion may then become slightly more likely with increasing tension, although not to a significant degree as the jump frequencies are still at a similar magnitude at 1% tension and the transition into E0 is relatively unlikely in the first place.

Strain	ΔE	$\Delta E + \Delta E_z$	Γ_0	$\Gamma(300K)$
-1%	68	36	2.012E+13	5.005E+12
0%	54	20	2.012E+13	9.424E+12
1%	53	21	1.912E+13	8.518E+12

Table 6.5: Table containing the energy barrier (ΔE), ZPE corrected energy barrier ($\Delta E + \Delta E_z$), attempt frequency (Γ_0) and the jump frequency (Γ) at a temperature of 300K for the pipe diffusion of hydrogen along an ECC screw dislocation line. Energies are in meV and frequencies in s^{-1} .

6.4 Conclusion

A cylindrical cell containing an isolated screw dislocation was used to calculate the binding energy for hydrogen to several of the strongest sites surrounding the dislocation. The advantage of using Tight Binding for these calculations was that it could provide both the quantum-mechanical accuracy required to give a valid description of hydrogen and the scale required to approximate the structural variation of the core with strain. These binding energies were found to have a similar accuracy to previous DFT simulations: almost every value was within the error bounds set by *Itakura et al.*[48] for their DFT results, apart from that for the E2 site which exceeded them by 6meV. This cell was then used to estimate the interaction between multiple hydrogen segregated to the dislocation; it was found that, for both types of dislocation core, up to 3 hydrogen atoms could occupy the strongest binding sites within the same {111} plane with minimal interaction. This could result in a greater value for the kink trapping at very high hydrogen concentrations.

Hydrogen Interactions With Screw Dislocations

These cells were then used to assess the variation in screw-hydrogen binding energy in regions of high compressive and tensile strain, as might be found around a crack tip. The binding energy of the sites relative to a tetrahedral site under the same strain were found to increase with compression; the opposite trend for the binding energies relative to an unstrained tetrahedral site. This could possibly result in a greater proportion of the local hydrogen concentration being segregated to screw dislocations in regions of compression; although the local hydrogen concentration would be greater in regions of tension. It was also found that the relative depths of the binding sites around the screw dislocation should converge slightly with tension; this would result in a slight decrease in the effect of a hydrogen atom on screw dislocation motion, whether by kink-trapping or reducing the energy for kink-pair formation enthalpy. The variation was found to be around $\pm 5\%$ of the energy difference between binding sites, that would result in kink trapping or kink-pair formation enthalpy reduction, with $\mp 1\%$ biaxial strain respectively.

These results were then used to carry out several calculations to give an indication of the variation in hydrogen effect on screw dislocation mobility between regions of tension and compression. As defined by *Itakura et al.*, the upper critical temperature, T_u , and the lower critical stress, σ_l , were calculated for each applied strain. These properties give an idea of the hydrogen effect: T_u is defined as the maximum temperature at which the hydrogen concentration in front of the line is sufficient to enhance the kink-pair nucleation rate significantly. Although this is simply defined as when the concentration-dependent term in the kink-pair rate enhancement is equal to one, the exponential dependence on temperature means that this term increases quickly with further cooling. T_u was found to increase linearly with tension, and so the degree of kink nucleation enhancement should generally be much more significant in tensile zones. σ_l is the lower bound of the stress at which the enthalpy increase from kinks escaping hydrogen traps along the dislocation line becomes greater than the decrease due to the stress relaxation associated with their movement, giving an idea of the hardening. This stress increased with bulk hydrogen concentrations and as the temperature was decreased; it followed the same pattern as T_u , increasing with tension, although it began to plateau at the highest concentrations and lowest temperatures so that it was the same everywhere. In general, these calculations indicated that the effect of hydrogen, whether it be softening or hardening, would be much more significant in tensile regions.

The average kink velocity was then estimated from the velocity with which kinks

Hydrogen Interactions With Screw Dislocations

would pass a hydrogen atom, estimated with the escape rate from hydrogen-traps, and the unimpeded velocity for a range of effective shear stresses and hydrogen concentrations. The velocity was found to be reduced by a great deal even for low hydrogen concentrations and again showed a large difference between regions of tension and compression; however, even the lowest values calculated were still large in terms of the length of a dislocation. An estimate was then made for an example dislocation, of length $1000b$ at 300K and under an effective stress of $\sigma = 33\text{MPa}$, to find the hydrogen concentration at which that the kink annihilation becomes the rate-limiting step for dislocation movement rather than kink-pair nucleation. This would indicate the hydrogen concentration required for macroscopic hardening by solute drag on kinks; in this case it was found that very large concentrations were required for this effect ($C_0 > 22\text{appm}$ in the unstrained case). In general, it was also found that the difference between regions of tension and compression was decreased under higher effective stresses, as the kinks could escape the hydrogen traps more easily.

This same dislocation was then used to estimate the number of kink-pair nucleation events that could occur while kinks are still travelling along the dislocation line, or the number of potential pinning points that could be formed from kinks on different glide planes colliding per kink-pair nucleation. This was found to be a complex, multivariate problem dependent on both the degree of kink trapping and kink-pair nucleation enhancement from hydrogen. The calculation was also very simplified, involving many approximations, but it indicated that this pinning point formation chance would increase greatly with tension for most concentrations and temperatures, and that this strain dependence increased for lower temperatures. There was some variation at the highest concentration, when the concentration difference between strained regions became small; this meant that the increased kink-trapping energy of hydrogen in compressive areas became dominant in determining the effect, so that the trend was reversed. The lowest concentration calculated also showed some variation in that the effect of hydrogen was so low that the effects of temperature became dominant: the pinning-point chance was then determined by the increased phonon-drag and thermally activated kink-pair nucleation. In this case the effects of hydrogen across the strains became fairly constant.

Altogether these results indicate that the effect of the same bulk concentration of hydrogen could be very different between regions of tension and compression: the required bulk concentration for significant kink-pair nucleation enhancement would be much lower in regions of tension, and so softening could be entirely localised to

those regions. The required bulk concentration for significant pinning-point formation would also be much lower in regions of tension, and so there may be concentrations at which there is significant hardening in tensile regions but significant softening in unstrained or compression regions; this implies that the area of likely shear-localisation will change completely with hydrogen concentration and temperature.

The variation of the Peierls barrier with applied strain was also calculated and found to decrease with tension. This calculation was a very rough estimate as it was carried out with a quadrupolar array of dislocations and the variation in their interaction was not accounted for. However, the trend itself was validated by observing the energy difference between cells containing a HCC or ECC screw at each strain. The difference between the ECC and HCC decreased linearly with tension and it has been found before that the HCC will have a similar energy to the transition saddle-point[94]. The predictions made above then likely underestimate the increase of kink-pair nucleation with tension, so that the effect of tension would be even greater.

The main purpose for these simulations was to provide input for the kMC model used by *Katzarov et al.*[95] to predict the effect of hydrogen on the screw dislocation velocity. The predictions produced at the end of this chapter involve many approximations and also are based on a snapshot of a straight dislocation with no surrounding microstructure. The kMC model would instead allow a realistic description of how the dislocation would evolve, which could alter these effects greatly, and produce much more quantitative results. The rates of the kink-pair nucleation, the movement of the kinks and their escape from hydrogen-traps as a function of the stress and temperature were inputs to the model; kinks were allowed to nucleate on any of the three {110} glide planes intersecting the screw ⟨111⟩ slip direction. The collision of crossed-kinks to form immobile jogs was also included in the model, forming strong pinning points on the line. This model was limited by its input: data from the literature was required to produce these rates and so the model could not be applied to environments for which these hydrogen interactions had already been calculated.

The results produced here represent almost all of the data required to extend this model to describe the effects of hydrogen on screw dislocation mobility in the strained areas surrounding a crack-tip. However, these results cannot be used until the effect of strain on the kink-pair nucleation rate has been calculated. The enthalpy change for this process due to hydrogen in front of the kink-embryo was judged to be fairly insensitive to strain: the energy change as hydrogen moved through the sites E2-H0-E2 only varied by 10meV across the range of strains. On the other hand, the

large variation of the Peierls barrier with strain implies the energetics of the process itself have a much stronger dependence. These calculations could be carried out with the methods described in chapter 4: employing Green function boundary conditions (GFBC)[216] to relax the kink-pair structures within BOP across the range of strains and estimate the rate variation. The functions to calculate the Lattice Green Function and include GFBC have already been implemented within the BOP software, and were employed for a previous paper[213]. Another method would be to use a line tension model, as described above and used by *Itakura et al.*[48, 94] in their papers. The parameterisation of this model would require the calculation of the Peierls surface and line energy of the screw dislocation at each applied strain. As shown in chapter 3, the BOP model reproduces the results of DFT well, and so it could be employed in these calculations. The use of the BOP would also allow the simulation of a cell large enough to calculate these results for an isolated screw without the risk of interactions with the inert boundaries skewing the results.

Finally the cells were used in CI-NEB simulations to observe how strain affects hydrogen diffusion between the strongest binding sites around the ECC screw dislocation. The diffusion barriers, attempt frequencies and jump frequencies at a temperature of 300K were calculated for the transitions between the E3, E2 and E0 sites at 1% compression, no strain and 1% tension. The attempt frequencies for all transitions were found to be fairly insensitive to the strain, but the barrier between the E3 and E2 sites had a fairly strong dependence, decreasing by around 60 meV from 1% compression to tension; the jump frequency for this transition then increased greatly with tension. The strain dependence of the E2 to E0 transition was not as strong, showing only a variation of 15meV across the range of strains; however, the depth of the E0 site relative to the barrier did increase and so made the transition out of the E0 site less likely with tension. The transition of hydrogen along the line of the dislocation between E0 sites, known as pipe diffusion, was then simulated. The barrier was found to be lower than that for bulk diffusion, and it would support the theory of dislocation lines as viable pathways if the transition to the E2 site were not more likely. Hydrogen is then too unstable in the core site for pipe diffusion to have a large effect on hydrogen transport, although it did become slightly more stable with tension. The barriers for all of these transitions, apart from those from the E0 site, were surprisingly high, generally 5 – 10 times the values of the bulk diffusion barriers. This implies that diffusion around the screw core is much slower than in the bulk, although more calculations are needed to assess the other barriers to leave each trap site.

Hydrogen Interactions With Screw Dislocations

It would be interesting to include these barriers in a kMC model to study coupled hydrogen diffusion and screw dislocation motion, which could possibly give predictions on the stresses at which screw dislocations begin to break away from their hydrogen atmospheres. However, many more calculations would be required in order to fully specify this model, requiring all of the pathways surrounding the screw dislocation. It would have been particularly interesting to calculate the barrier between the E8 and E2 sites: after a kink sweeps past a hydrogen atom in the E2 site behind the line, the hydrogen will be left in an E8 site. This barrier was not calculated due to oversight, but all the structures involved in these calculations have already been relaxed and so these barriers would not be difficult to obtain in the future.

Chapter 7

Embedding a Self-Consistent Tight Binding Cluster Within Bond Order Potential

7.1 Introduction

The simulation of many defect processes in solids, such as dislocation movement or interstitial diffusion, involve an inherent coupling of length scales: they require both an accurate description of bond breaking and formation at the site of the process and a large surrounding area to dissipate long-range stresses, which can have great effects on the energetics and atomic behaviour throughout. Accurate models such as DFT can produce a good description of the entire cell but computational expense limits the attainable size. Also, the atoms in the area surrounding a defect will only be slightly perturbed from equilibrium and so don't necessarily need an accurate quantum-mechanical description to produce good results. One method of overcoming this limitation for dislocation simulations has been arranging the dislocation cores in such a way that their stress fields cancel, greatly reducing the required cell size while still accurately describing core processes. However, this may have effects on the structure of the dislocation core and simulations are limited to those processes for which the dislocations remain in a stable array throughout[45, 241].

There have then been frequent attempts to include multiple levels of complexity in simulation, and there are two general formulations for doing so: concurrent, whereby the entire system is treated at the same time, building some description of the config-

Embedding a Self-Consistent Tight Binding Cluster Within Bond Order Potential

uration that can include multiple techniques; or hierarchical, in which the parameters obtained by accurate simulation at a small scale may be used to inform a model at a much larger scale, such as the rate of processes for kinetic Monte Carlo[242]. Concurrent simulation is the more difficult of the two techniques but has still been a subject of interest for some time; the range of accurate simulations that could be carried out is an attractive prospect, previously only possible with a great deal of approximation.

Typically these simulations will involve the cell being separated into the region that requires a quantum-mechanical description and the large surrounding area that can be coarse grained. The issue then is in producing a smooth transition between these regions. If the electronic interactions across the boundary are not included correctly then the distribution of charge within the quantum-mechanical region can be affected, which will change the behaviour within that region. Attempts to preserve these interactions have included precalculating and freezing the bonds across the boundary or saturating bonds with additional hydrogen atoms, both of which can obscure the physical results of the model[243–245]. Dealing with the forces across the boundary is also an important issue: mismatch at the border can cause stress across the quantum region and change the results of the simulation. One attempt at dealing with this is to set a buffer region of finite width that is calculated with both models and then either have the atoms in each region only see the forces from their own model (although this can result in non-conservation of momentum) or have some smooth interpolating function to vary the forces between atoms depending on their position in the buffer region[246, 247].

The issues associated with the interfaces between models may also be avoided by using the same model throughout but treating the forces in the outer region differently. Green function boundary conditions essentially allow the simulation of isolated defects by coupling the simulation cell to an infinite harmonic lattice through the lattice Green function[215, 216]. The cell is split into three regions: region 1 is the small area surrounding the defect that requires accurate simulation, region 2 is a shell surrounding that with the thickness required to saturate the interactions from region 1 and isolate it from region 3. This final region simply serves to isolate the inner two from the area outside the cell. The calculation proceeds by first freezing the outer two regions and relaxing region 1 according to the forces calculated from the accurate model, which will induce forces in region 2. Displacements for the entire cell are then generated by the lattice Green function in response to the forces in region 2, which will reduce the built-up forces in this region but generate forces in region 1. These two steps are

Embedding a Self-Consistent Tight Binding Cluster Within Bond Order Potential

repeated alternately until the forces in the inner two regions are minimised.

An issue with this method can be the limitation to small system sizes: if the model is an electronic structure method, like DFT or TB, then all three regions must be included within the Hamiltonian to avoid non-physical surfaces on regions 1 and 2. The alternating steps in the relaxation can also lead to long simulation times, requiring repeated relaxation of the forces generated in the inner region. Furthermore, *Fellinger et al.*[50] employed this method with DFT and found that the bulk lattice Green function was not appropriate to describe all the dislocation structures they considered. The lattice Green function is obtained as the inverse of the force constant matrix, which is built by approximating the force constants each pair of atoms with that of a similar pair in the bulk; this failure was theorised to occur because pairs of atoms surrounding the dislocation core were too dissimilar from the bulk. They then had to generate a force constant matrix specifically for this cell, simulated with a more economical method. This lack of flexibility may imply that this method is not appropriate for the simulation of some processes, such as those involving structural changes at a dislocation core.

Another way to mitigate these interface issues, while still retaining the speed and flexibility of simulation, is to employ models of sufficient similarity as to minimise the change across the interface. The direct diagonalisation (DD) of the TB Hamiltonian and the Bond Order Potential (BOP) approximation are ideal methods for this purpose: they can share the same Hamiltonian and energy structure, so the bonds across the surface are not terminated in an non-physical way, and the forces will be similar on both sides of the interface. The limitation of the BOP model to LCN self-consistency (and generally a single basis orbital) will have no issue with describing the near-equilibrium atoms surrounding a defect, and the fact that the computation time scales linearly with system size could enable the inclusion of a large surrounding area. Both models may also be naturally couched in Green functions and so interactions with another region may be included as a perturbation, and indeed there is a large amount of literature dedicated to the subject[248].

This chapter details the attempts to produce this TB embedding scheme, which was intended to be employed in simulations of hydrogen in iron at a previously unattainable scale. The motivation behind these simulations was to provide input data for the kMC model of *Katzarov et al.*[95], which gave a good estimation of the effect of hydrogen on dislocation mobility but requires input from accurate atomistic methods. This model was then limited by the structures that could be simulated, particularly

with the inclusion of hydrogen. However, this scheme could possibly be used to accurately simulate a wide range of defect/impurity interactions. The start of this chapter describes the implementations of this method, giving the structure of the terms and the approximations applied, and then details of the simulation mechanics. A number of tests are then carried out to estimate the validity of these implementations, particularly with respect to the description of hydrogen in α -iron. These simulations were carried out with the d -orthogonal set parameter set tested in chapter 3 and a sd -nonorthogonal set that enables description of iron/hydrogen interactions, as used in chapter 6[105].

7.2 Implementations

Two implementations of the embedding scheme were created, differing in the degree of approximation applied. It was important to create both as comparison between them would allow the determination of the effect of the approximations applied and the situations where they become important. This also enables verification of issues in the implementations, to demonstrate that they were not a result of these approximations.

Green Function Matching

This method was described by Ivaylo Katzarov in private communications[249]. The interactions between the DD and BOP regions are included using a formulation based upon the Dyson equation below.

$$\mathbf{G}(\epsilon) = \mathbf{G}^0(\epsilon) + \mathbf{G}^0(\epsilon)\Delta\mathbf{H}\mathbf{G}(\epsilon) \quad (7.1)$$

$\Delta\mathbf{H}$ represents the difference in the Hamiltonian matrix between the interacting and non-interacting system, and so contains all of the bonds that cross the DD/BOP interface;. $\mathbf{G}^0(\epsilon)$ represents the Green matrix for the system without interactions between the DD and BOP regions; finally $\mathbf{G}(\epsilon)$ represents the Green matrix for the full, interacting system. This equation is then essentially used to modify the Green matrix for the non-interacting system such that it includes the bonds between regions. The non-interacting Green function for the system would have the structure:

$$\mathbf{G}^0 = \begin{pmatrix} \mathbf{G}_B^0 & \cdot \\ \cdot & \mathbf{G}_D^0 \end{pmatrix} \quad (7.2)$$

Embedding a Self-Consistent Tight Binding Cluster Within Bond Order Potential

Where the "·" represent blocks of zeroes and \mathbf{G}_B^0 and \mathbf{G}_D^0 represent the isolated BOP and DD blocks respectively. Then the correlating blocks, holding the interactions, are:

$$\Delta\mathbf{H} = \begin{pmatrix} \cdot & \mathbf{H}_{BD} \\ \mathbf{H}_{DB} & \cdot \end{pmatrix} \quad (7.3)$$

The calculation is carried out in real space and so \mathbf{H}_{DB} is the transpose of \mathbf{H}_{BD} . With these terms the Dyson equation would result in the structure:

$$\mathbf{G} = \begin{pmatrix} \mathbf{G}_B^0 + \mathbf{G}_B^0 \mathbf{H}_{BD} \mathbf{G}_{21} & \mathbf{G}_B^0 \mathbf{H}_{BD} \mathbf{G}_{22} \\ \mathbf{G}_D^0 \mathbf{H}_{DB} \mathbf{G}_{11} & \mathbf{G}_D^0 + \mathbf{G}_D^0 \mathbf{H}_{DB} \mathbf{G}_{12} \end{pmatrix} \quad (7.4)$$

The dependence of the Green matrices upon ϵ has been suppressed in these equations for brevity.

An approximation is applied here: that there is no significant difference in the Green function for the BOP region between a cell that is described entirely with BOP and one that describes the central, embedded cluster with a full DD SCTB model. The initial step then is to calculate the entire cell to self consistency with LCN BOP but excluding any atoms in the DD region that the BOP would have difficulty describing, such as hydrogen impurities. The Green function matrix for the BOP region is then frozen and the inner region of DD is run to self-consistency, including the interactions with the surrounding BOP atoms on each iteration using the pattern provided by the Dyson equation, so that the matrix for the full system has the structure:

$$\mathbf{G} \simeq \begin{pmatrix} \mathbf{G}_{11} & \mathbf{G}_{12} \\ \mathbf{G}_{21} & \mathbf{G}_D^0 + \mathbf{G}_D^0 \mathbf{H}_{DB} \mathbf{G}_{12} \end{pmatrix} \quad (7.5)$$

Where \mathbf{G}_{11} , \mathbf{G}_{12} and \mathbf{G}_{21} now represent the blocks of the Green matrix that are obtained using the BOP method and frozen.

The advantage of this method is that it is fast; the initial BOP calculation proceeds quickly and, unlike the second implementation, the DD Green matrix is produced before the interactions are included, and so it may be produced from the eigenvectors of the Hamiltonian:

$$G^{RLR'L'}(\epsilon) = \sum_n^{\infty} \frac{C_{RL}^n C_{R'L'}^{n*}}{\epsilon - \epsilon_n} \quad (7.6)$$

This is especially useful as the Green function must be produced at every point of the energy integration, which is carried out with the modified Matsubara scheme, as

Embedding a Self-Consistent Tight Binding Cluster Within Bond Order Potential

described at the end of section 2.2.2. Therefore, with equation 7.6, the Hamiltonian may be diagonalised once, the product $C_{RL}^n C_{R'L'}^{n*}$ produced and so only the inversion of the diagonal matrix $(\epsilon - \epsilon_n)$ and the matrix multiplications must be carried out at each integration point.

This method also enables the BOP region of the cell to be extended indefinitely without significant increase in computation time. Only the BOP atoms that have DD neighbours (which should already be saturated even with the smallest possible cell) will be involved in the second, slower, part of the calculation and so increasing the BOP region size beyond this minimum size will only slow the initial BOP simulation, which makes up a negligible portion of the full calculation time.

Direct Block-Matrix Inversion

This method was first described in the thesis of Dimitar Pashov[250]. The idea for this implementation began with producing the Green matrices for the non-interacting system and introducing the interactions perturbatively using the Dyson equation. However, it was found that proceeding from the inversion for the interacting Green matrix in the first place would require less memory and fewer write operations.

The Green function matrix of the interacting system would have the structure:

$$\begin{aligned}\mathbf{G}(\epsilon) &= (\epsilon \mathbf{S} - \mathbf{H}^0 - \Delta \mathbf{H})^{-1} \\ &= \begin{pmatrix} (\epsilon \mathbf{I} - \mathbf{H}_B) & -\mathbf{H}_{BD} \\ -\mathbf{H}_{DB} & (\epsilon \mathbf{S} - \mathbf{H}_D) \end{pmatrix}^{-1}\end{aligned}\quad (7.7)$$

\mathbf{H}^0 here represents the non-interacting Hamiltonian; made up of the blocks \mathbf{H}_B and \mathbf{H}_D which correspond to the BOP and DD regions respectively. The inversion of a 2×2 block matrix can be written analytically, and results in the pattern:

$$\mathbf{G}(\epsilon) = \begin{pmatrix} \mathbf{G}_B^0 + \mathbf{A} \mathbf{C} \mathbf{A}^T & -\mathbf{A} \mathbf{C} \\ -(\mathbf{A} \mathbf{C})^T & \mathbf{C} \end{pmatrix}\quad (7.8)$$

Where \mathbf{G}_B^0 replaces $(\epsilon \mathbf{I} - \mathbf{H}_B)^{-1}$ in this formulation, but is obtained using the BOP method for the non-interacting BOP region. \mathbf{A} is a shorthand substitution for:

$$\mathbf{A} = -\mathbf{G}_B^0 \mathbf{H}_{BD}\quad (7.9)$$

Embedding a Self-Consistent Tight Binding Cluster Within Bond Order Potential

The \mathbf{C} -matrix, which represents the interacting DD Green matrix, is then:

$$\mathbf{C} : \mathbf{G}_D(\epsilon) = ((\epsilon \mathbf{S} - \mathbf{H}_D) - \mathbf{H}_{DB} \mathbf{G}_B^0 \mathbf{H}_{BD})^{-1} \quad (7.10)$$

This method would then be formally exact if the BOP were not used to approximate part of the Green matrix. The calculation of the interacting DD matrix is equivalent to the perturbed-cluster formulation of Baraff and Schlüter, whereby the effect of the surrounding lattice on a cluster may be included during the calculation of the Green matrix for the cluster alone; this is done by adding an additional energy-dependent embedding potential ($-\mathbf{H}_{DB} \mathbf{G}_B^0 \mathbf{H}_{BD}$) to the Hamiltonian before the inversion[248, 251]. The BOP is used to calculate the majority of the Green matrix and the sparsity of \mathbf{H}_{DB} may be exploited to speed up the calculation of \mathbf{A} significantly, which can be stored for the calculation of \mathbf{C} , so the majority of this calculation proceeds quite rapidly. The inversion of this dense matrix for the DD portion is then the slowest part of this model but the idea is to keep the DD region as small as possible.

The transition between regions will occur much more smoothly in this implementation than in the first, due to the fact that it allows both regions to reach self-consistency together; however, the variation in the BOP region during the self consistency cycle will slow the convergence of the DD region. This, along with the computationally intensive dense-matrix inversion that must be carried out at every integration point, will make this implementation much slower than the first for the calculation of the same cell. This difference is only further exacerbated by increasing the size of the BOP region: as mentioned, in the first implementation the calculation of the BOP region proceeds quickly and the intensive DD calculation only involves the BOP atoms directly interacting with DD atoms; while, for this method, increasing the BOP region beyond the range of maximum interaction with DD atoms will slow the convergence rate of the entire cell, and increase the size of the matrix multiplication operations to produce \mathbf{A} and \mathbf{AC} .

7.3 Simulation Details

The cell structure was defined with the idea of easing the transition between the SCTB DD and LCN BOP regions: every DD atom that has a BOP atom as a neighbour is restricted to LCN self-consistency and the basis set used in the BOP region, i.e. d -orthogonal for these simulations.

Periodic boundary conditions involving k -space integration have not yet been implemented, so the DD region is restricted to a molecular Hamiltonian. A limited kind of PBC were included with the BOP model: the BOP Green matrix may be extended without difficulty by including atoms in surrounding images of the cell in the recursion chains and neighbour tables, and so the cell may be surrounded with images described entirely with BOP. The central structure of each image will then be defined by the positions of DD atoms, excluding the impurity atoms that are not well described with this BOP (such as hydrogen).

Self-consistency was accelerated for the DD-SCTB atoms using the Broyden mixing scheme[96] with the clock procedure, described in chapter 5. It was thought that these atoms could benefit from the increased stability of this procedure. The LCN, DD and BOP, atoms use the susceptibilities obtained by integration of the Green function to generate energy shifts, as described in section 2.2.3.

Parallelisation of the code became necessary to simulate cells large enough to extract meaningful results. In the BOP program, the calculation is split over blocks of atoms: the BOP model generates the Green function from the local environment of each atom, allowing the calculation of each atomic block of the Green matrix to proceed fairly independently. This is not the case for the embedding as both implementations have computationally-heavy steps at each point of their integration cycle that cannot be split into blocks of atoms. It was therefore decided to split the calculation over energy integration points instead, each processor then calculates a portion of the sum in equation 2.64; this showed satisfactory acceleration, as shown in figure 7.1, although it could be improved with further optimisation. One of the attractive features of the BOP is that, due to it being naturally divisible into blocks of atoms, each processor need only store the recursion coefficients, Hamiltonian elements and so on for the block of atoms that it is dealing with. This results in vastly decreased memory usage, a feature that is unfortunately lost in embedding.

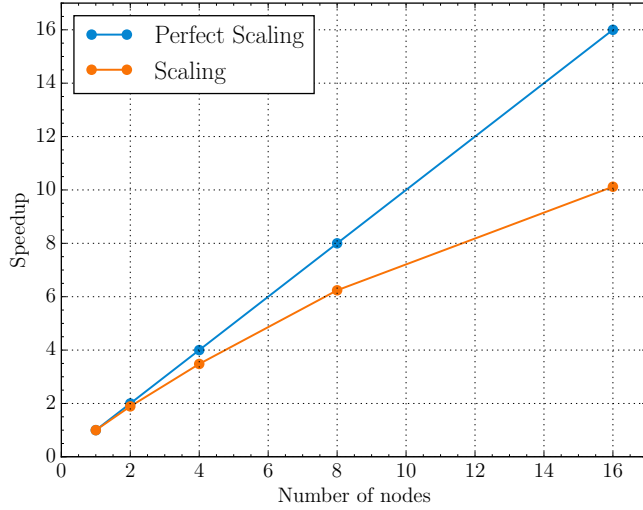


Fig. 7.1: Shown is the speed-up of an embedding calculation (marked in orange) with increased node usage on the ARCHER supercomputer[252]; each node is made up of 24 CPUs.

7.4 Results & Discussion

7.4.1 Preliminary Tests

Phonon Dispersion Curves

Phonons represent the quantised lattice vibrations of a system, and so many of the mechanical and thermal properties of the crystal, such as the elastic coefficients and thermal conduction, will be partially determined by the propagation of phonons. The energy of any arbitrary infinitesimal atomic displacement will be contained within the phonon dispersion relation. The matching of phonon spectra between models then guarantees a matching of the forces across the interface for near-equilibrium configurations, and negates the possibility of spurious boundary forces[253].

The phonon dispersion relations and density of states may be obtained by using a program called Phonopy[254]. This program takes a block of atoms in the perfect lattice and displaces them in certain symmetry-defined ways to generate the force constant matrix, which can then be used to obtain the phonon frequencies and polarisation vectors. A supercell of BCC iron was made out of $4 \times 4 \times 4$ unit cells; the direct diagonalisation SCTB simulations used a $16 \times 16 \times 16$ mesh of k -points and the BOP

Embedding a Self-Consistent Tight Binding Cluster Within Bond Order Potential

simulation used an electron temperature of $k_B T = 0.008\text{eV}$; all of the simulations had a tolerance of 10^{-6} for the atomic charge self consistency cycles. The phonon density of states were calculated with a $128 \times 128 \times 128$ q -point mesh using the tetrahedron integration method; these distributions were scaled so that their integration over energy range was normalised to one.

Results are shown below in figure 7.2; the d -orthogonal direct diagonalisation and BOP in figure **a)** match almost perfectly, with only very minor differences in the density of states. The match in figure **b)**, between the sd -nonorthogonal DD and BOP (and so also the d -orthogonal model), is not nearly so good: the maxima of the sd -model's dispersion relation are in general decreased in energy and there is an additional peak between Γ and H ; this disparity is also clear in the DOS distribution, the entire distribution of which has been shifted downward in energy and only has one secondary peak when there should be two. There is a proportionality between the slope of the phonon bands near the Γ -point and the elastic constants; the fact that the sd -model was fitted to reproduce the elastic constants can be seen clearly in the similarity of this slope. The d -model has values of 118 GPa and 48 GPa for C_{44} and C' respectively, while the sd -model has 108 GPa and 43 GPa[105].

It should be noted that it is the d -orthogonal DD and BOP that fit better with experiment: *Klotz and Braden*[255] measured the phonon dispersion of iron using inelastic neutron scattering, fitted with a Born-von Karman model, and found a very similar structure. The crossings of the bands at the high symmetry points for d -orthogonal DD and BOP are very similar to those reported by *Klotz and Braden*, with the largest difference between them being ~ 5 meV at the H -point but the other differences being ≤ 2 meV; the DOS also shared a similar three-peaked structure and the locations of the peaks were within 3 meV of the results shown here.

In summary, the BOP is shown to be an ideal model for the purposes of embedding, which shows a similarity with DD such that no fictional forces should build up in the interface between it and d -orthogonal DD. However, the disparity between the results for the d -orthogonal and sd -nonorthogonal models imply that the boundary between these models will be an issue; the mechanical properties of these models may be similar enough (as implied by the elastic coefficients) but there will still be a discontinuity in the boundary between models.

Embedding a Self-Consistent Tight Binding Cluster Within Bond Order Potential

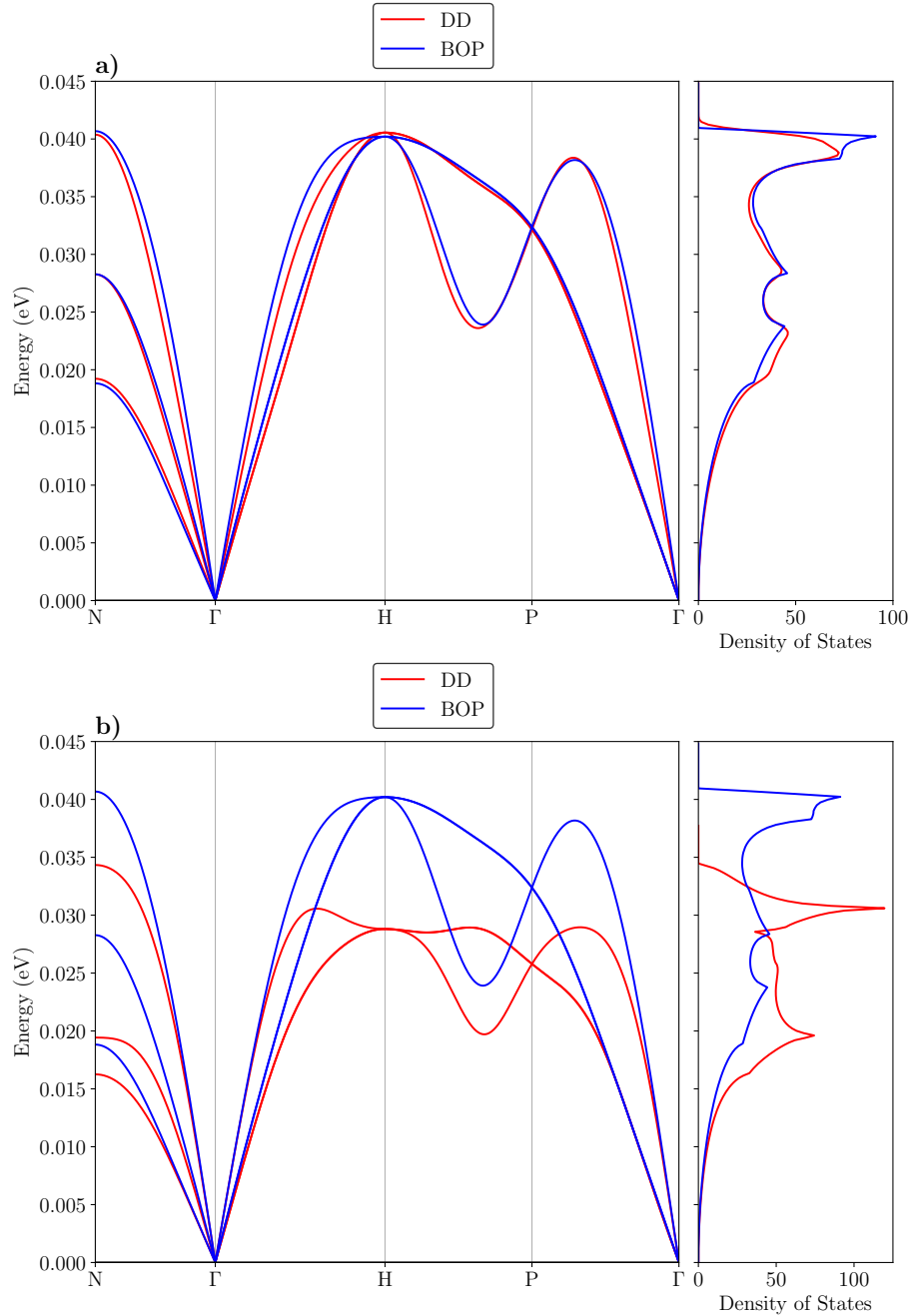


Fig. 7.2: The phonon dispersion and density of states of *d*-orthogonal iron described by the Bond Order Potential overlaid with the results from **a)** *d*-orthogonal **b)** *sd*-nonorthogonal iron described by direct diagonalisation SCTB.

Border Atom Energy Gradients

For an energy-conserving model, the forces on each atom should be exactly equal to the gradients of the total energy along those directions. Due to the approximations

Embedding a Self-Consistent Tight Binding Cluster Within Bond Order Potential

applied these models are not expected to be perfectly energy-conserving, however the relation between the forces and energy gradients are a good measure of how well the interface is treated. The binding energy gradients were obtained by taking an $8 \times 4 \times 4$ block of perfect BCC Fe atoms, split evenly such that the BOP and DD regions were made up of adjacent cubes of 64 atoms each, then displacing BOP, DD or border atoms perpendicular to the interface between regions in steps of 0.005\AA . The first derivative of the binding energy was then approximated as the fourth order central difference, shown below.

$$f'(x) \approx \frac{-f(x+2h) + 8f(x+h) - 8f(x-h) + f(x-2h)}{12h} \quad (7.11)$$

Where f represents the binding energy at each point and h is the separation between the points ($h = 0.005\text{\AA}$). Figure 7.3; **a), b)** and **c)** below show the results from both implementations for a DD border atom, a border-adjacent BOP atom and a border-adjacent DD atom respectively.

As the first implementation freezes the BOP Green function outside of the DD region, the forces and energies were not expected to be consistent for the border atom, and indeed they have a large separation in graph **a)**, with an opposite sign for the points considered, although the gradients seem to be identical. The second implementation, however, shows good consistency between the energy and forces for the border atom, as the Green functions are allowed to change together this obviously prevents any discontinuity in the interface.

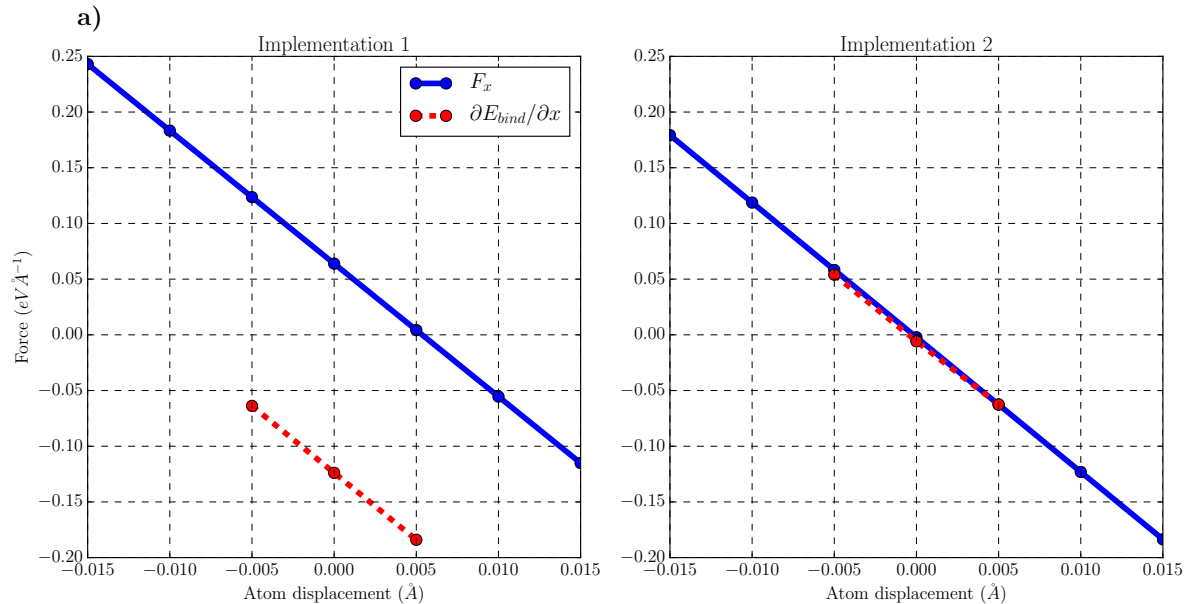
In the case of the BOP atom (**b**)), both implementations seem to give consistent energy and forces, and the first implementation is actually slightly closer than the second, although only by $\sim 0.02\text{eV\AA}^{-1}$. This is due to the fact that, within the first implementation, all the interactions with BOP atoms are treated entirely with BOP, and so the the change to the energy and forces by displacing a BOP atom would similar if the entire cell were simulated within BOP. The second implementation is slightly worse because it is described using the Green matrix for the isolated BOP region with the interactions included using the pattern from the inversion, and the BOP can have issues with describing free surfaces.

Finally in the case of the border-adjacent DD atom the second implementation again is more consistent than the first, having about half the difference between the energy gradient and force; although it too shows some discontinuity at this point with a difference of $\sim 0.07\text{eV\AA}^{-1}$. Note that in this case the undisplaced atom in both implementations has a sizeable force on it; this is due to the fact that this

Embedding a Self-Consistent Tight Binding Cluster Within Bond Order Potential

atom will form the interface between the d -orthogonal DD border atoms and the sd -nonorthogonal DD atoms, and there is some mismatch in forces between these models as demonstrated in the previous section. The second implementation actually shows a greater total force at each position by $\sim 0.1\text{eV}\text{\AA}^{-1}$, although a displacement of only 0.01\AA is required for the models to converge.

These results show that the second implementation gives a much more self-consistent description of the energy and forces across the boundary. The first implementation results in a discontinuity across the border, however it does produce forces of sufficient similarity for useful static calculations.



Embedding a Self-Consistent Tight Binding Cluster Within Bond Order Potential

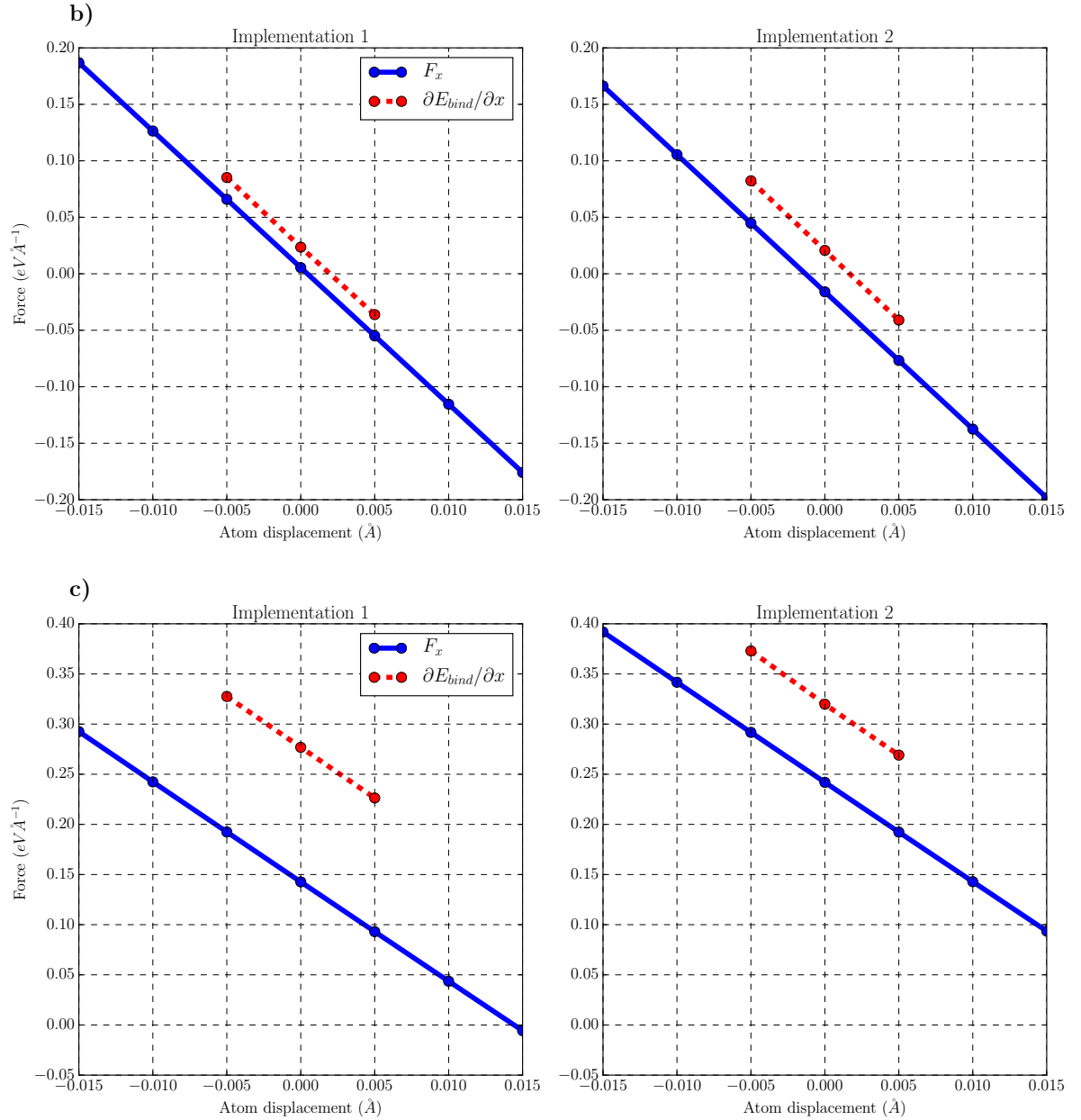


Fig. 7.3: The gradient of the total binding energy for a) interface atom, b) interface-adjacent BOP atom and c) interface-adjacent DD atom displaced along x (perpendicular to the interface) and the x -component of the total force on that atom for both implementations.

Comparisons with SCTB and BOP

The band structure forces from each implementation were then compared with BOP and DD using a $12 \times 5 \times 5$ BCC cell. This was simulated with embedding split evenly between DD and BOP (into two $6 \times 5 \times 5$ blocks), with BOP entirely and with SCTB DD entirely; the geometry of the embedding cell is shown in figure 7.4. In order to compare the development of the band structure forces with distance from the boundary, the average magnitude of the difference in atomic forces from BOP or SCTB DD was calculated for each atomic plane, as numbered in the figure. This was done by simply calculating the magnitude of the difference in forces on each atom between the embedding cells and full SCTB or full BOP, summing this value for each atomic plane and then dividing by the number of atoms in the plane. The results for the case where the embedding DD region was simulated with d -orthogonal SCTB (and the SCTB DD simulation was also carried out with a d -orthogonal basis set) are shown in figure 7.5.

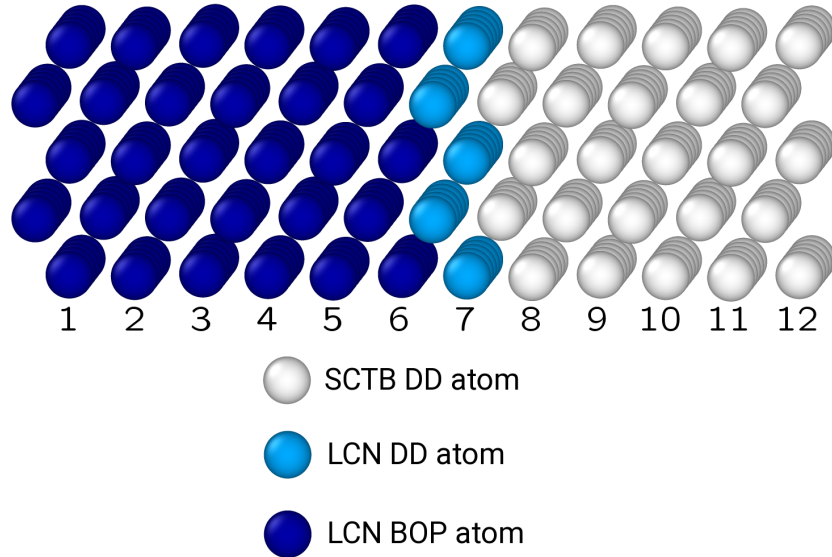


Fig. 7.4: Shown is the cell used for the force comparisons between the embedding implementations, BOP and SCTB; it is made up of 12 $\{112\}$ planes of 25 atoms each (as numbered), split for the embedding such that 6 were treated with BOP and 6 with DD.

The forces for the BOP atoms in implementation 1 are identical to those from the full BOP cell due to the frozen Green function for that region, but there is a sharp

Embedding a Self-Consistent Tight Binding Cluster Within Bond Order Potential

difference at the boundary, with similar differences from both BOP and SCTB. The first two DD planes then have sizeable differences from both BOP and SCTB, before decreasing to reasonable levels by plane 9 and continuing to come closer to SCTB toward the end. The second implementation shows a much smoother boundary, and the BOP and SCTB lines are almost mirror images of each other which both show small differences in force, even on the boundary planes. It may be noted that the phonon spectra in the previous section should imply that there will be no difference in the near-equilibrium forces between d -orthogonal DD and BOP models; however the cell simulated here is not near equilibrium, it is a small cuboid surrounded by free surfaces and so some difference in forces between the models is to be expected.

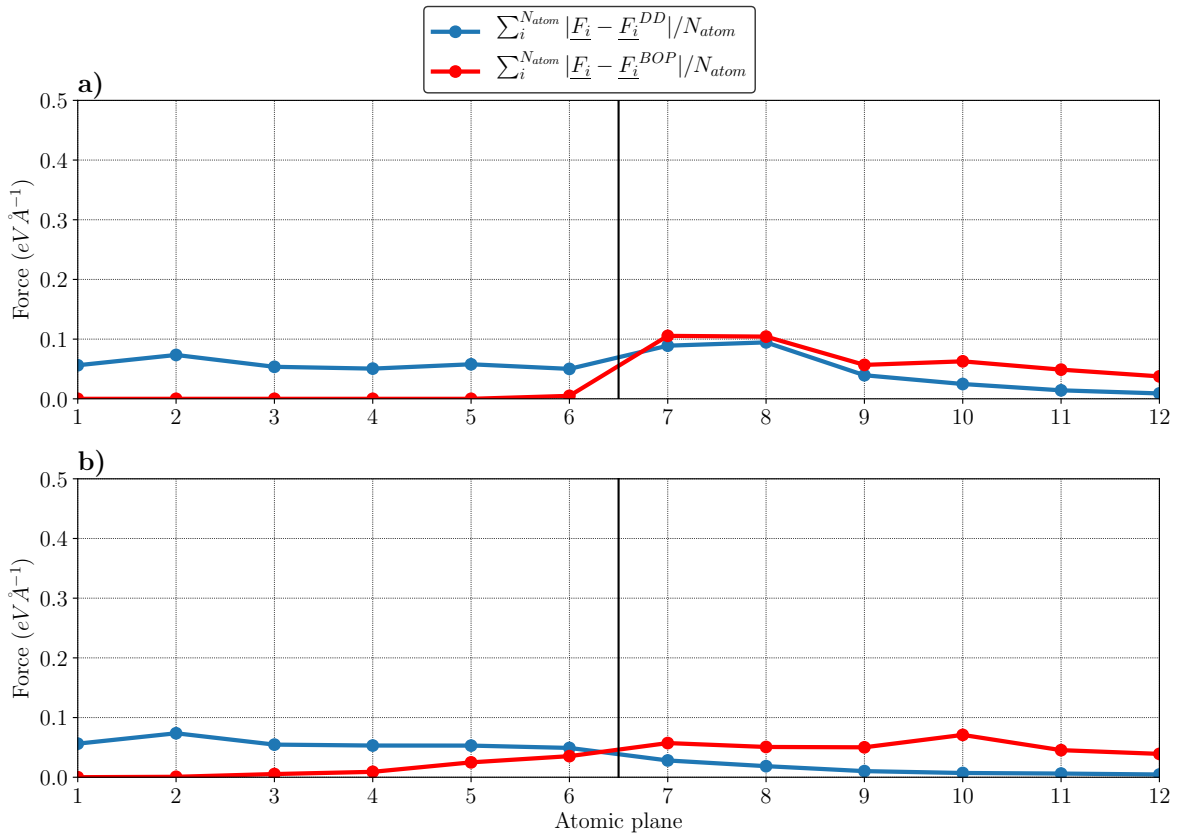


Fig. 7.5: The average norm of the difference in band structure forces on each atom between a fully d -orthogonal embedding cell, simulated by **a)** implementation 1 and **b)** implementation 2, from the same cell simulated with d -orthogonal BOP and d -orthogonal SCTB DD. The solid black line marks the border between the BOP and DD regions (where planes 1-6 make up the BOP region and 7-12 the DD) and the average difference is calculated by summing the norm of the difference in forces for each atom in each plane and dividing by the number of atoms in the plane.

Embedding a Self-Consistent Tight Binding Cluster Within Bond Order Potential

The development of the DD portion of the cell can also be visualised by comparing the charges on each site with the SCTB cell, as in figure 7.6; this figure shows the average absolute differences in charge per plane. The largest difference for both implementations is on the 7th plane, or the plane limited to LCN self-consistency but both quickly decrease, down to an average difference of ~ 0.0002 by the 8th plane, and continue to approach the SCTB result with increasing distance from the border. Both implementations then reproduce the results from SCTB well beyond the 8th plane, and it is interesting that the results from both methods are almost identical.

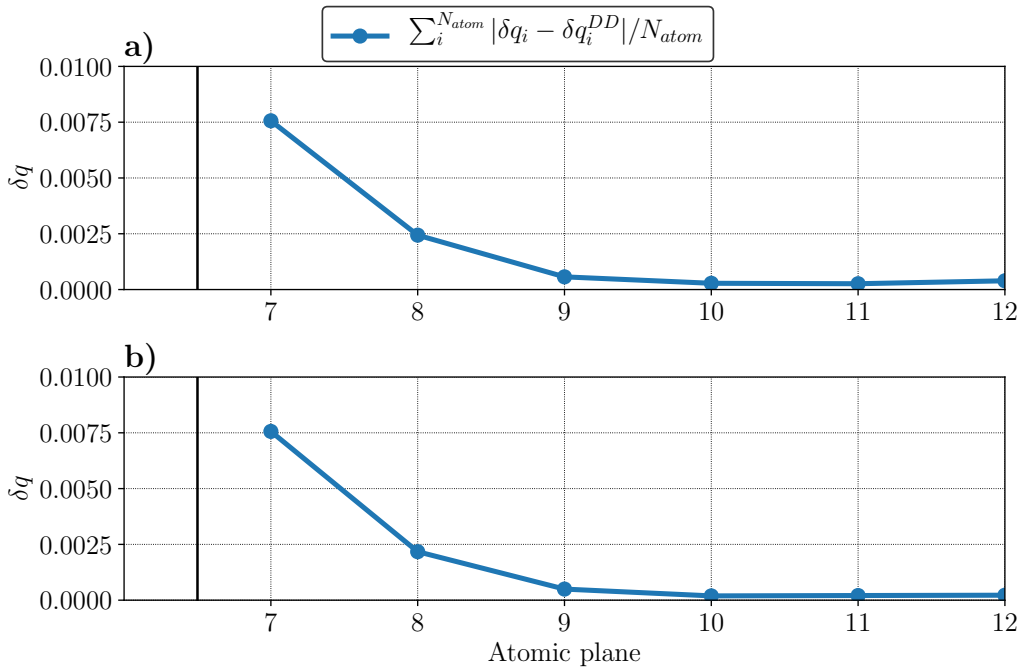


Fig. 7.6: The average absolute difference in on-site charge per atomic plane between the DD portion of a fully d -orthogonal embedding cell and the same cell calculated with d -orthogonal SCTB DD for **a)** implementation 1 and **b)** implementation 2.

Figure 7.7 shows the results for the calculation with sd -nonorthogonal atoms in the DD region; their forces are now compared to a full sd -nonorthogonal SCTB DD calculation. Again both implementations show good similarity to BOP for the first 6 planes, although of course the difference from SCTB in this region is more marked. Both graphs then show a large spike in force difference from both BOP and SCTB on plane 8: this corresponds to the interface between the DD d -orthogonal and sd -nonorthogonal atoms and so the total forces on these atoms show the imbalance in equilibrium forces from each basis set. Although the difference from both models is

Embedding a Self-Consistent Tight Binding Cluster Within Bond Order Potential

slightly smaller for implementation 2 it shows a larger spike in difference on plane 8 by $\sim 0.05\text{eV}\text{\AA}^{-1}$. After this point both implementations are fairly similar, decreasing greatly from plane 9 to 11 and showing a slight increase on plane 12.

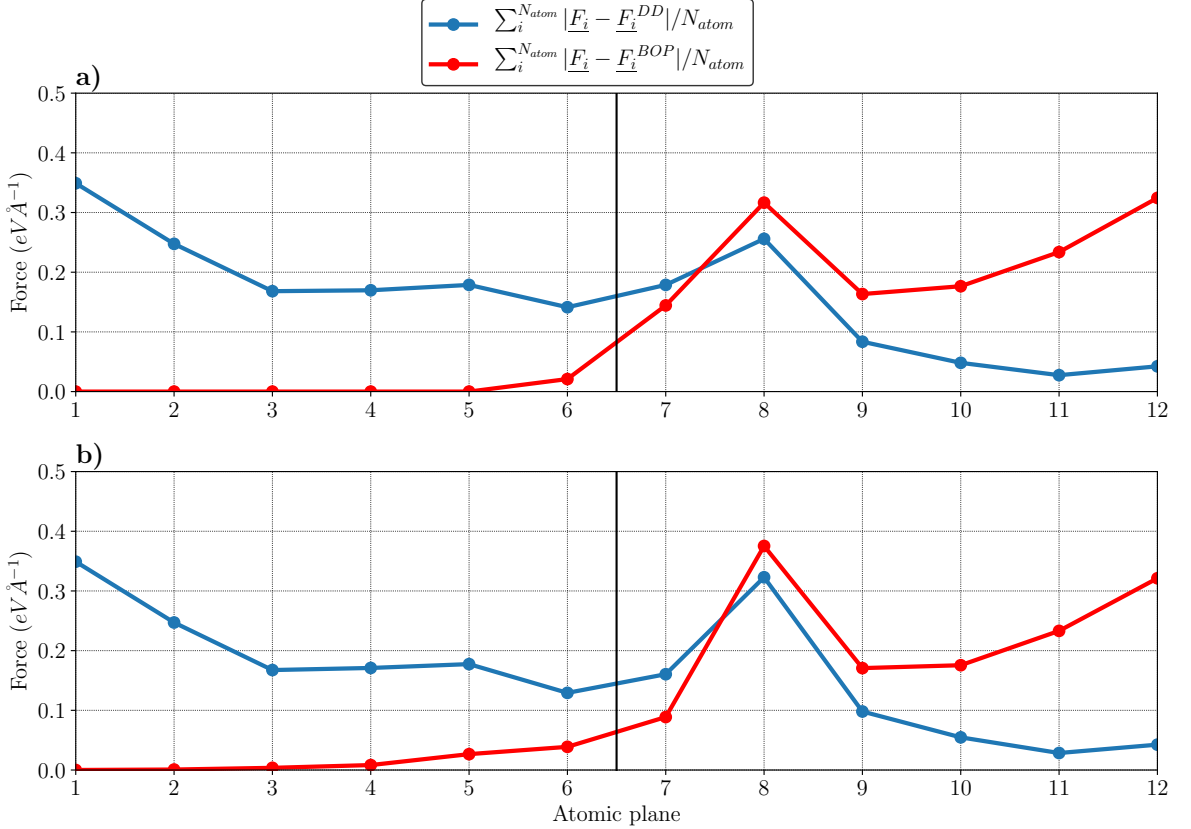


Fig. 7.7: The average norm of the difference in band structure forces on each atom between an embedding simulation with an *sd*-nonorthogonal DD region, simulated by **a)** implementation 1 and **b)** implementation 2, from the same cell simulated with *d*-orthogonal BOP and *sd*-nonorthogonal SCTB DD. The solid black line marks the border between the BOP and DD regions (where planes 1-6 make up the BOP region and 7-12 the DD) and the average difference is arrived at by summing the norm of the difference in forces for each atom in each plane and dividing by the number of atoms in the plane.

This large spike at the *d*-orthogonal to *sd*-nonorthogonal DD interface then corresponds the fictional forces predicted by the difference in phonon spectra between the two models in the previous section. The purpose of the embedding models was to create a smooth transition between the DD and BOP atoms, not the *d*-orthogonal and *sd*-nonorthogonal basis sets and so this discontinuity is not affected by the embedding procedures at all. Indeed, it would yield similar results if the entire cell were calculated

Embedding a Self-Consistent Tight Binding Cluster Within Bond Order Potential

with DD SCTB but with the blocks described with d -orthogonal and sd -nonorthogonal basis sets.

This interface between parameter sets also creates a problem with the electronic description of the cell; this can be seen in figure 7.8 which shows the average magnitude of the atomic charge differences from sd -nonorthogonal SCTB DD for each plane. In this case the first, LCN, DD plane is actually one of the closest to the SCTB results; the differences in charges only increase until the 10th plane and then linearly decrease for the last two. It then takes at least 4 planes of atoms, or a separation of $\sim 9.3\text{\AA}$, before the charges even begin to approach the SCTB values.

The development of these charges may be visualised by taking a sum of charges for each plane and comparing them to the SCTB results, as shown in figure 7.9. The sum of the charge for the first two planes is actually quite similar to SCTB for both implementations, however they both then show large oscillations in charge after the d/sd interface and only come to match the SCTB values for the last two planes which form a kind of dipole due to the free surface. It is again interesting to note that the results from the first method are almost identical to the second.

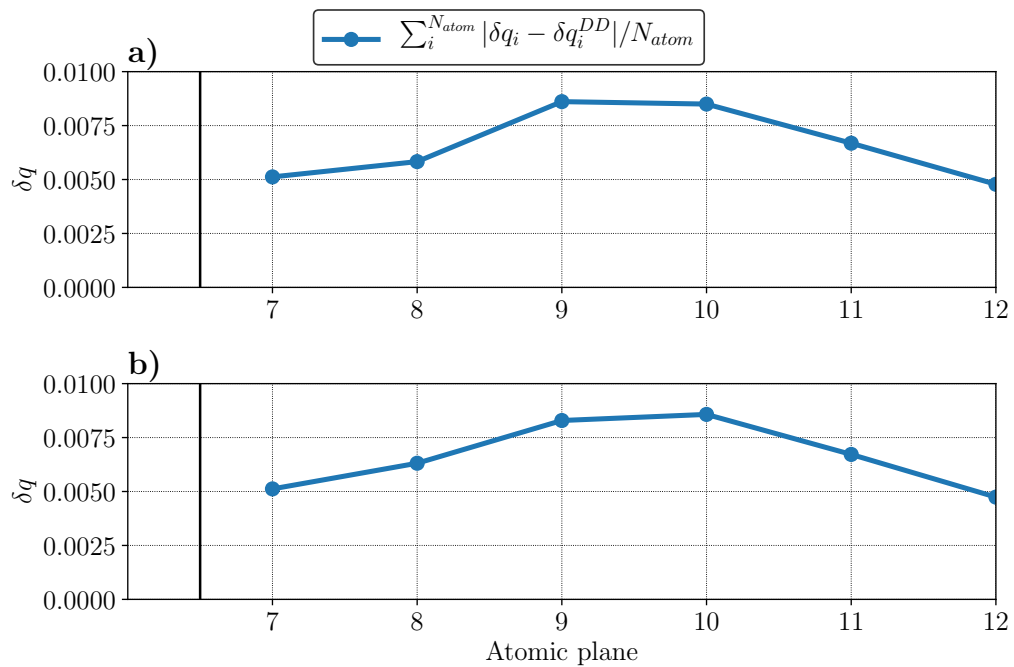


Fig. 7.8: The average absolute difference in on-site charge per atomic plane between the DD portion of an embedding cell with a sd -nonorthogonal region embedded within a d -orthogonal one and the same cell calculated with fully sd -nonorthogonal SCTB DD for **a)** implementation 1 and **b)** implementation 2.

Embedding a Self-Consistent Tight Binding Cluster Within Bond Order Potential

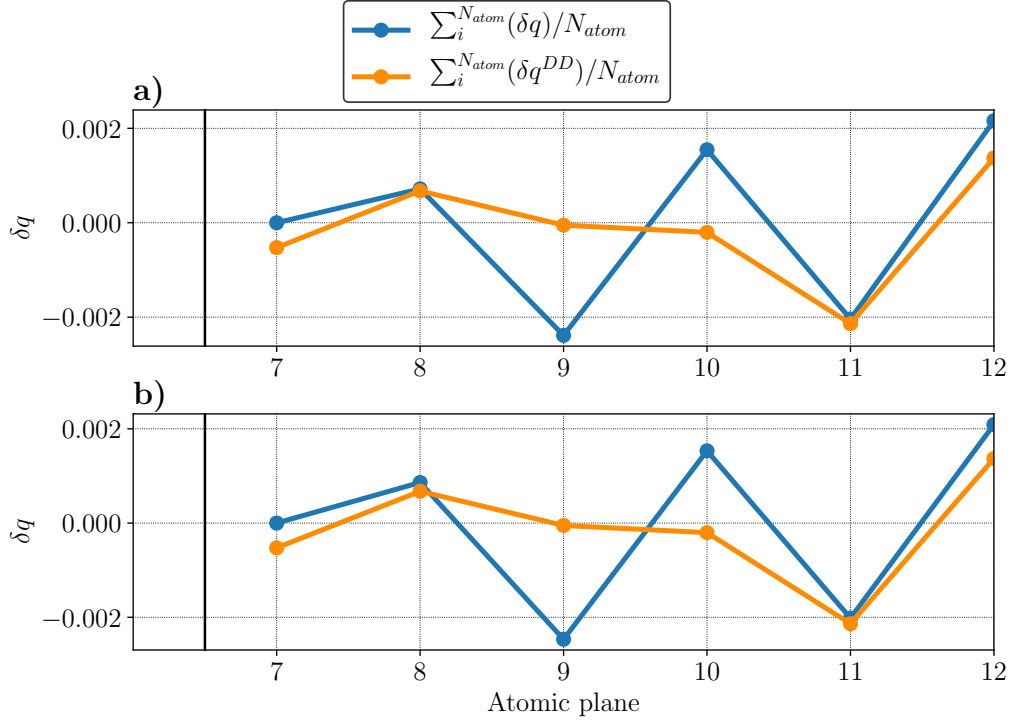


Fig. 7.9: The average charge per plane for the DD portion of an embedding cell with a *sd*-nonorthogonal region embedded within a *d*-orthogonal one and the average for the same planes from a fully *sd*-nonorthogonal SCTB DD calculation of the same cell for **a)** implementation 1 and **b)** implementation 2.

It was thought that the problem of the interface between the *d*-orthogonal and *sd*-nonorthogonal layers could possibly be ameliorated somewhat, or at least moved further from the centre of the SCTB cluster, by forgoing the *d*-orthogonal layer in the DD region altogether and having the interface layer made up of *sd*-nonorthogonal LCN atoms; the average norm force differences for this case are shown in figure 7.10. However, this solution would not improve the hydrostatic pressure that the *d/sd* interface puts the DD region under by simply moving it one plane further away.

The force difference spike is now on plane 7 for both implementations; however, for the first implementation it actually increases the spike in the differences by $\sim 0.15\text{eV}\text{\AA}^{-1}$. This is possibly due to the frozen BOP Green matrix, showing no response whatsoever to the border atoms' change in configuration. Plane 8 for this implementation only reduces in average norm difference by $\sim 0.08\text{eV}\text{\AA}^{-1}$ and the other planes are unchanged. The second implementation shows a much greater improvement: the maximum difference is slightly decreased and plane 8 shows a reduction in force difference from SCTB DD of $\sim 0.2\text{eV}\text{\AA}^{-1}$. Even planes 9 and 10 show slight

Embedding a Self-Consistent Tight Binding Cluster Within Bond Order Potential

reductions of $\sim 0.03\text{eV}\text{\AA}^{-1}$; although obviously the difference from BOP in plane 6 is also slightly increased.

Unfortunately this also has the effect of removing the force/energy consistency for the border atoms in the second implementation, as shown in figure 7.11. The difference between the force and energy gradient is much greater in this case than it was for the *sd*-nonorthogonal DD atom moving perpendicular to the *d*-orthogonal border, possibly due to the fact previously the interactions between *sd* and *d* atoms were contained in the same Hamiltonian, but now they are included by the embedding procedure.

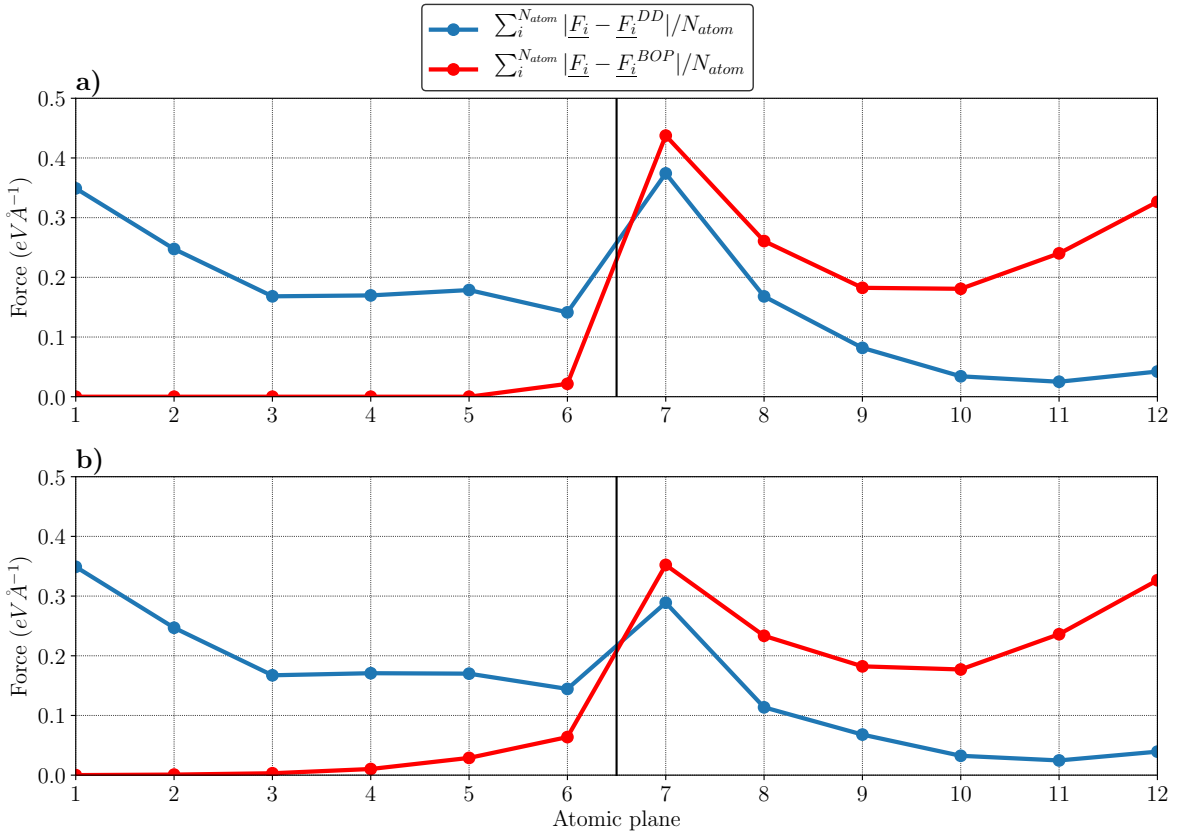


Fig. 7.10: The average norm of the difference in band structure forces on each atom between an embedding simulation with an *sd*-nonorthogonal DD region, simulated by a) implementation 1 and b) implementation 2, from the same cell simulated with *d*-orthogonal BOP and *sd*-nonorthogonal SCTB. The solid black line marks the border between the BOP and DD regions (where planes 1-6 make up the BOP region and 7-12 the DD) and the average difference is arrived at by summing the norm of the difference in forces for each atom in each plane and dividing by the number of atoms in the plane.

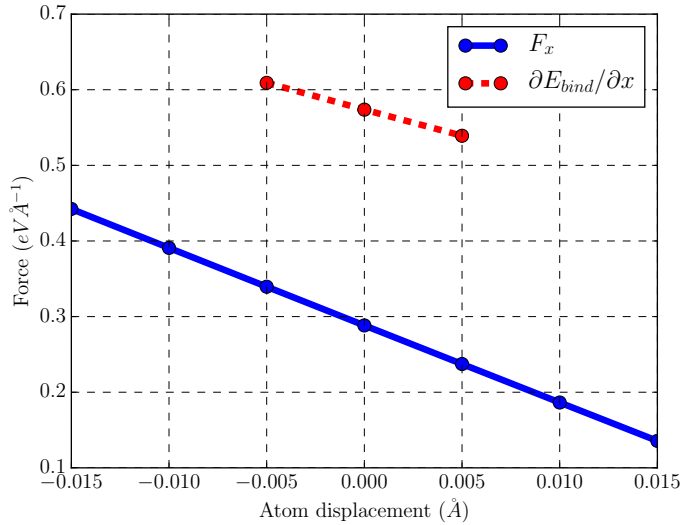


Fig. 7.11: The gradient of the total binding energy for a nonorthogonal DD border atom displaced along x (perpendicular to the interface) and the x -component of the total force on that atom simulated within the second implementation.

7.4.2 Hydrogen Solution Energy

In order to gauge the effect of the introduced electronic inaccuracy on actual simulation it was decided to observe the variation in hydrogen dissolution energy in a tetrahedral site with separation from the d/sd interface. A sphere of BCC atoms was produced with a radius of 18 Å and centred on a tetrahedral site, this was then surrounded by a 8 Å shell of inert atoms . The central region of the sphere was designated as the DD region, and the cell was calculated to self consistency for a range of DD region radii with, and without, a hydrogen atom in the central tetrahedral site. These calculations were carried out without relaxation, and so the spurious forces at the d/sd interface would have no effect here. The energy of both these cells at each DD-radius can then be used to calculate the dissolution energy of hydrogen, using equation 6.1, and observe how it changes with separation from the d/sd interface. The results are shown in figure 7.12, along with the result from a periodic block of 576 iron atoms simulated with SCTB; note that the x -axis denotes the radius of the total DD region, and so the d/sd interface would be closer by ~ 4 Å.

The results from both implementations were within 0.04eV of each other for all the radii simulated. At 6 Å both models are ~ 0.4 eV distant from the SCTB results, by 7 Å they approach to within ~ 0.09 eV and then seem to oscillate around the SCTB

Embedding a Self-Consistent Tight Binding Cluster Within Bond Order Potential

result, getting slightly closer with increased radius. Note that the atomic charges for the block calculation only began to approach the SCTB results in figure 7.8 after a separation of $\sim 9.3\text{\AA}$ from the interface, and so these calculations never approach the radii that could possibly result in accurate atomic charges in the centre of the cell. Beyond a radius of 11\AA (or 10\AA for implementation 2) the calculation begins to become impractical and so the required radius that could possibly result in accurate calculation was not found.

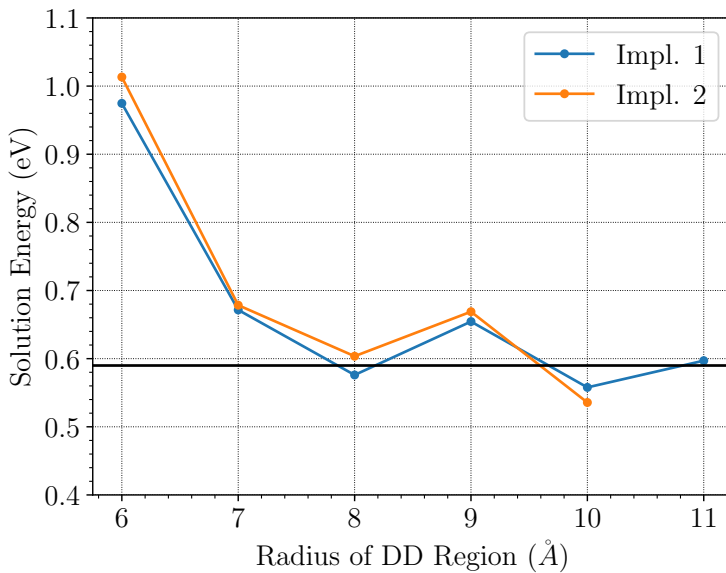


Fig. 7.12: The solution energy, without relaxation, for hydrogen in a tetrahedral site against the radius of the DD region calculated by both implementations; the value from a 576 block of periodic atoms simulated with SCTB is marked with a black line. The DD region is surrounded by a region of at least 6\AA BOP atoms which is in turn surrounded by inert atoms.

This inaccuracy in atomic charges may be seen more clearly in figure 7.13, which shows the average atomic charges from the sphere with a DD region of radius 11\AA , simulated with implementation 1, compared to the equivalent results from a periodic block of 576 iron atoms simulated with SCTB DD. The atoms were sorted by distance from the central hydrogen atom and then grouped in 1\AA shells to obtain the averages. Note that this plot is slightly misleading in that more atoms are included in each shell the further from the centre of the sphere, where $0 - 1\text{\AA}$ only includes the hydrogen atom and $1 - 2\text{\AA}$ includes the four surrounding iron atoms while $8 - 9\text{\AA}$ includes 88 iron atoms; the difference in average charges then represents a greater total difference in charge further from the centre. The SCTB atoms beyond 4\AA from the hydrogen atom

Embedding a Self-Consistent Tight Binding Cluster Within Bond Order Potential

become almost neutral, but the equivalent embedding atoms continue to have large oscillations in charge right up to the d/sd interface, which is located at $\sim 8\text{\AA}$. These oscillations result in inaccuracies in the charges of the central atoms: the hydrogen atom charge is smaller by $\sim 18\%$ while the four surrounding iron atoms are smaller by $\sim 26\%$. Note that the the charge inaccuracy for the four central iron atoms only represents a total difference of ~ 0.012 electrons, while the large peak between $5 - 6\text{\AA}$ would represent a total excess of 0.16 electrons for that 1\AA shell.

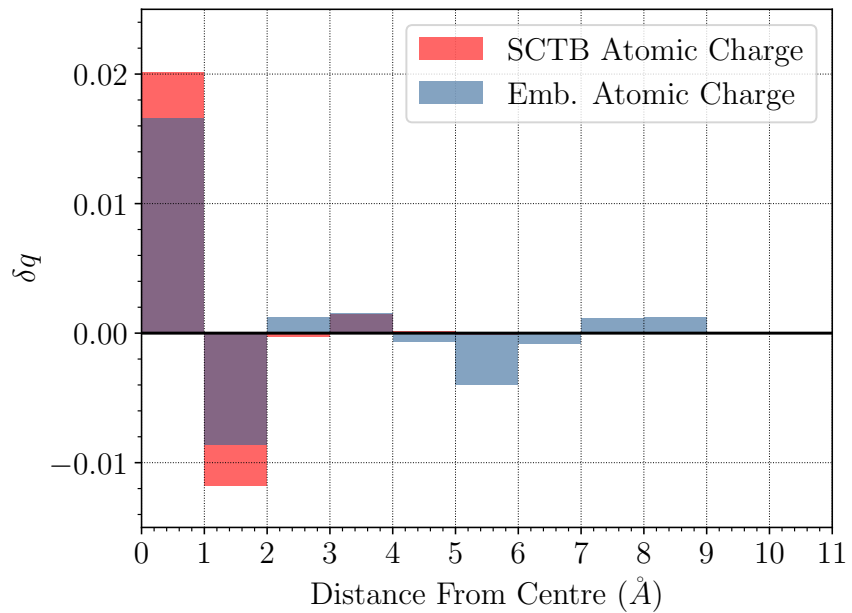


Fig. 7.13: Shown is the average atomic charge of atoms in the sphere, with a central hydrogen atom, simulated with implementation 1 and a DD region of radius 11\AA , also shown is the equivalent atomic average from a 576 atom periodic block simulated with SCTB. The atoms are sorted with distance from the hydrogen atom and averaged in 1\AA shells, such that $0 - 1\text{\AA}$ only includes the hydrogen atom and $1 - 2\text{\AA}$ includes the four surrounding iron atoms.

These results show that the problems with embedding sd -nonorthogonal atoms within a sheath of d -orthogonal do not end with the spurious forces at their interface: the dissimilarity in these basis sets also results in significant inaccuracy in the charge density for at least 11\AA into the sd -nonorthogonal region. This issue could not then be fixed by compensating for the force imbalance with a refitted pair-potential for the border atoms; the electronic properties are still inaccurate for a non-feasible separation from the interface.

7.5 Conclusions

The motivation behind these embedding methods was to employ them to simulate the interaction of hydrogen with dislocations in iron; the kMC model of *Katzarov et al.*[95] produced useful results on the effect of hydrogen on dislocation mobility, but was hampered by the inability to calculate hydrogen trapping data for all of the structures involved. These schemes are clearly not feasible for this purpose: a minimal basis set of *s*- and *d*-orbitals is required for the iron atoms to include interactions with hydrogen, and the interface between the *sd*-nonorthogonal and *d*-orthogonal atoms results in spurious boundary forces and electronic inaccuracy that penetrates deep into the DD region. However, this issue arises solely from the dissimilarity between the basis sets: as shown in figures 7.5 and 7.6, the interface between the BOP and DD models with the same, *d*-orthogonal, parameter set does not result in these issues. The solution to this problem would then consist of either finding *d*-orthogonal and *sd*-nonorthogonal basis sets of greater similarity or finding other problems that don't require such dissimilar basis sets but could still benefit from the increased cell size. The fitting of parameter sets is not a simple task however, particularly with such stringent requirements, and attempts so far have not yielded any success. On the other hand, these schemes could be useful for describing interactions in other metals: titanium has already been well described with BOP models and could retain a *d*-orthogonal parameter set throughout, while impurity atoms such as oxygen and carbon could be included with *sd*- or *pd*-interactions in the DD region[256, 257]. Also, it is important to include the effects of charge transfer when considering titanium-carbon interactions as the transfer toward the carbon can be of the order of one electron[258], or at least will have significant effects on the interaction energies[257].

It is gratifying to see that the first implementation closely reproduces the results of the second in most simulations because it was the method with the most serious approximations applied. The advantage of the second implementation was that it was close to being formally exact, where the only approximation applied is the use of BOP to produce part of the Green matrix (without including periodic boundary conditions). This can be seen in the smooth transition between regions in figure 7.5, and in the matching of the forces to the binding energy gradients of the border atoms. However, this method is so slow as to be impractical, and has similar limitations in system size to normal DD-SCTB calculations. The first implementation, on the other hand, can surpass these limitations, where the size of the BOP region is only

Embedding a Self-Consistent Tight Binding Cluster Within Bond Order Potential

limited by memory constraints and so can reach thousands of atoms. The difference in forces and energies between the methods is minor, as can be seen in figures 7.5 and 7.12 respectively, and the electronic difference is negligible even with the significant electronic disturbance from the d/sd interface, as shown in figures 7.6, 7.8 and 7.9. These differences can be seen as a demonstration of the errors introduced in the first model by the approximations applied, due to how close the second model is to being exact, and we can conclude that they are not overly significant.

If these schemes are to be used, it is necessary to implement k -space integration for the DD region; the slight inaccuracy in forces of the first implementation at the border would become less of an issue if the DD region were not an isolated cluster surrounded by BOP. The range of problems that could be treated would also be extended by the inclusion of k -space integration: one-dimensional integration would enable the treatment of dislocation lines, while two-dimensional would enable that for surfaces. The k -space modification would then consist of producing a Bloch-transformed Hamiltonian, with only one k -point division in one or two of the axes such that it becomes periodic in two or one of the axes respectively, and then carrying out an inverse Bloch transformation in order to extract the real-space Hamiltonian; this would then be used in the embedding procedures. This modification was not implemented due to time constraints, but would prove essential for effective use of this method.

Work is now under way to employ this embedding scheme on another problem: the effect of oxygen on $\langle a \rangle$ screw dislocation cores in HCP α -titanium. Small amounts of oxygen in this lattice are enough to have a significant macroscopic hardening effect; TEM images of the microstructure after deformation tests evidenced long segments of $\langle a \rangle$ screw dislocations, indicating that the hardening effect was due to some interaction with these screws[259]. Furthermore, a strong temperature dependence of the yield stress and an increased incidence of cross-slip was observed; these effects were confirmed in later observations[260]. The hardening effect cannot be explained solely by elastic interactions between the dislocation cores and impurities, which predicts a relatively weak interaction between oxygen and these dislocations[259, 261]. These interactions imply that oxygen has some effect on the $\langle a \rangle$ screw core structure; this has actually been observed in high resolution scanning TEM images, which showed that the core seems to contract in the plane normal to the dislocation line with increased oxygen content[261]. DFT simulations of these structural changes have also been carried out: finding that the oxygen lattice site is collapsed by interaction with the prismatic stacking fault associated with the dominant slip of this dislocation,

Embedding a Self-Consistent Tight Binding Cluster Within Bond Order Potential

which could account for the surprisingly large interaction energy, and that interaction with oxygen induced large changes in the core structure, depending on their relative positions[261, 262]. However, due to the computational expense associated with DFT, these simulations were carried out either in very small cells or with the dislocations in a quadrupolar array, which could affect the structures involved. Embedding then offers a method of simulating an isolated $\langle a \rangle$ screw dislocation accurately, removing any interactions with other dislocations or inert atoms, and so could possibly produce much more quantitative results on the effect of oxygen on these screw cores. The economic nature of these simulations would also allow simulations with the oxygen in a large range of surrounding interstitial sites.

Chapter 8

Conclusion

The significance of hydrogen effects on kink trapping and defect formation energies was demonstrated well with the work of *Katzarov et al.*[95]: a kMC model was produced that was able to capture both the regimes of hydrogen induced softening and hardening, and estimate under which conditions they are likely. The work carried out during this thesis was with the intention of extending this research, providing the data and machinery to increase the understanding of hydrogen embrittlement in iron in the light of the defactant model, as well as investigating the connection with other mechanisms. This primarily involved attempts to provide input to improve the functionality of this kMC model, both in the environments it could describe and the information it could produce, and to improve simulation techniques such that the simulations of hydrogen in iron could be carried out at a previously unattainable speed and scale.

Preliminary Dislocation Simulations

This work began with a range of defect simulations carried out with the Bond Order Potential Method, introducing dislocations into the simulation cells with the solutions of anisotropic linear elasticity theory. The initial simulations were carried out both to extend my understanding of large-scale defect structures and to test a set of BOP parameters for iron, initially fit for direct diagonalisation Tight Binding. These preliminary simulations primarily concerned screw dislocations, and were also carried out with another, well-established, set of BOP parameters[58] to enable direct comparison of the structures involved as well as comparing the results to the literature. The parameter set was found to reproduce defect structures and energetics well, including the atomic and magnetic structure of the screw dislocation core, the Peierls barrier

Conclusion

height and shape, the core transition path, the Peierls stress, and the formation energy of the $\Sigma 3\{112\}$ grain boundary. However, the screw dislocation was found to take an anomalous path in response to pure shear on a $\{110\}$ plane, repeatedly cross-slipping such that the average glide plane was close to a $\{112\}$ plane. This issue had been found previously with several models of greater simplicity and may be considered a failing of the parameter set; although accurate models have shown that only small amounts of non-glide stresses are required to cause this kind of glide. Therefore, these parameters are considered to give a sufficiently accurate description of iron, and were employed thereafter in a number of further simulations.

With the parameters well-tested and verified, they were then employed in the first attempt to extend the kMC model: including climb of the jog segments. This model allowed the formation of kinks on multiple glide planes and the collision of crossed-kinks to form jogs, but not the climb of these jogs. Climb is a primary source of vacancies in the lattice, and several groups have found evidence of excess vacancies after deformation in hydrogen[73–76]; this forms the basis of the Hydrogen Enhanced Stress Induced Vacancy (HESIV) model of hydrogen embrittlement[70]. Drag of these jogs during the movement of the screw dislocation could serve to partially account for this abundance of vacancies and so is a valuable extension of the model, allowing predictions of the conditions under which this jog drag is maximised.

The $\frac{a}{2}\langle 111 \rangle\{110\}$ and $\frac{a}{2}\langle 111 \rangle\{112\}$ edge dislocations were first relaxed and compared to structures from the literature before the $\frac{a}{2}\langle 111 \rangle\{112\}$ edge, i.e. the structure of the jogs, was used to assess the energetics of climb. Both the sequential binding energies of a line of vacancies to the core and the barriers for the vacancy migrations associated with climb events were calculated. The pattern of the binding energies was found to qualitatively agree with previous results for a $\frac{a}{2}\langle 111 \rangle\{110\}$ 71° mixed dislocation, with an increase of binding energy from the first to the intermediate vacancies, and from the intermediate to the last vacancy[194]. Barriers for the climb process were found to be dependent on both the orientation of the vacancy path relative to the dislocation line and the jog structure at the core, although two of the probable paths, i.e. vacancy emission on the glide plane, have not yet been calculated due to issues with the movement of the edge core. These barriers have now been included in the kMC model, and will be employed to provide information on the production of vacancies as a function of the stress, temperature and hydrogen content. Future work will include the extension of these simulations to include emission on the glide plane, the emission of a vacancy from an edge dislocation with a single jog and how these

barriers are affected by the tensile and compressive strain fields around a crack tip; all of which may be carried out within the BOP model at no great expense.

Screw Dislocation Kink Structures

Input for the kMC model had previously come from the literature: the stable kink-pair width, kink-pair embryo width and the kink-pair nucleation rates had all been taken from results calculated by *Itakura et al.*[94] with a DFT-parameterised line tension model. It was thought that if these quantities could be calculated with the BOP model it would both reduce the degree of approximation applied, as the BOP had now been shown to reproduce screw dislocation properties well, and increase the flexibility of the kMC model, allowing it to be applied to different strained regions with further BOP calculations. These simulations then began with attempts to relax single kinks within long cylinders of atoms, with the intention to extend to kink-pairs when the energy of each isolated kink was found.

However, convergence of the single kink formation energies with cell radius and length was not reached, with cells of the largest radius still showing a change of $\sim 6\%$ between the longest two lengths, and a similar variation between the largest two radii. Even so, the change of the kink core structure along the screw dislocation line direction was minor as the radius was increased. These core structures were found to compare well in width with results from previous BOP[58] and DFT-parameterised line tension[94] models; the magnetic structure at the cores also compared well to the BOP results.

The kink-pair nucleation rate estimates would involve the relaxation of all the metastable states involved in the nucleation of a stable kink-pair, and so are clearly not attainable in this configuration with BOP. However, *Rao et al.*[216] found that they could reduce the cell size required for the relaxation of single kinks greatly with the use of Green function boundary conditions in EAM simulations, by up to 90% in the central, atomistic region. Even with less significant reductions, these simulations could then be carried out with a low computational cost; this is particularly important if their variation with tensile and compressive strain is to be estimated. Calculation of the Lattice Green Function and the use of the Green function boundary conditions to relax these structures across the range of applied strains will form the basis of future work; both of these functions are implemented in the BOP software and have been employed for previous calculations[213].

Including Broyden Mixing

A difficulty in the simulation of iron is the requirement to describe magnetism; it was realised that these simulations must be accelerated if the large number required to specify the kMC model, described in the following chapter, were to be carried out. One of the most direct ways of achieving this was to improve the mixing scheme. This was also intended to accelerate the large number of configurational calculations involved in the estimation of hydrogen's decohesive effects across grain boundaries, although these simulations were not carried out. Broyden mixing of the charge densities, the magnetic moments and the Hamiltonian elements was implemented along with a variation of the mixing procedure that involved freezing the magnetic moments and mixing the charges to self-consistency between each iteration of the moments mixing. The Broyden mixing scheme was found to outperform the existing Anderson mixing scheme in all of the configurations considered; the variation to the mixing procedure was also found to have advantages for the convergence of more complex structures, and so was included in the embedding method described in chapter 7.

Hydrogen Interactions With Screw Dislocations

The central work in this thesis was based around expanding the kMC model to approximate the regions of high strain surrounding a crack-tip: the most computationally intensive part of which is to calculate the variation of the hydrogen/screw dislocation interactions with strain. These simulations would both require a quantum-mechanical treatment, for a valid description of hydrogen, and a great enough area surrounding the screw core, to approximate the structural variation with strain correctly. The direct diagonalisation Tight Binding method was employed for this purpose, first introducing a screw dislocation to a large, single-layer cell with anisotropic linear elasticity and relaxing it before cutting a smaller cell out, stacking it three times and including hydrogen. Hydrogen binding energies to several of the strongest trap-sites around both the hard and easy core configurations were found to match well with results from the literature; almost every value fell within the error range found for a set of previous DFT results[48].

Biaxial tension and compression, in the plane normal to the dislocation line, were then applied incrementally to the single layer cell, and the binding energies recalculated for a range of strains between 1% tension and compression. These values were then employed to carry out a range of estimations to demonstrate the variation in the

Conclusion

effect of hydrogen on screw dislocation mobility between regions of tension and compression, a rough demonstration of those that could be found with the kMC model. Within the Defactant model of hydrogen embrittlement[88, 90, 91], low concentrations of hydrogen in the lattice can result in an increase in the screw dislocation mobility due to the hydrogen-associated decrease in kink-pair formation energy or, at higher concentrations, decrease this mobility due to the solute drag effect of hydrogen on moving kinks. First, the upper critical temperature and the lower critical stresses were calculated across the range of strain for several hydrogen lattice concentrations; these quantities, defined by *Itakura et al.*[48], simply gave an idea of the degree of nucleation enhancement and solute drag occurring. The upper critical temperature is the temperature at which the kink-pair nucleation rate enhancement factor is equal to one; this is an arbitrary definition in some ways but, due to the exponential dependence on temperature, the enhancement increases quickly below this upper critical temperature. The lower critical stress is the stress at which the increase in enthalpy due to hydrogen detrapping per unit length of kink motion is greater than the decrease from the stress relaxation due to the same motion; giving an idea of how effectively the kinks are trapped. These measures generally demonstrated that the effect of hydrogen in an isothermal solid will be much greater in regions of tension than compression, whether by nucleation enhancement or solute drag.

The effect of hydrogen on the kink velocity was then estimated, from the average time a kink would spend trapped per Burgers vector and the untrapped velocity, when it is limited by phonon drag[232]. These velocities were used to produce rough estimates of the kink annihilation rates for an example dislocation (with a length of $2\mu m$ and under an effective stress of 33MPa) as the rate at which kinks could travel the dislocation length, and compare each to the hydrogen-enhanced kink-pair nucleation rate for that dislocation. These calculations indicated that high hydrogen concentrations would be required for the kink-drag to cause a significant hardening effect, as the annihilation of kinks must become the rate-limiting step for kink-drag to have any direct effect on the dislocation mobility.

The number of kink-pair nucleation events that could occur while kinks were travelling along the line was then estimated, or the chance of pinning-point formation from the potential collision of crossed-kinks, across the range of strains for a number of temperatures and hydrogen concentrations. This was a very rough calculation, with a great deal of approximation applied, but was used simply to illustrate the trend. For most concentrations and temperatures this chance was enhanced greatly with tensile

strain, and to a greater degree for lower temperatures. At the lowest concentration calculated, however, it was found that the chance increased with temperature, and showed a weak dependence on the strain; this was due to the fact that the effect of hydrogen was low in all regions at these concentrations and the pinning-point formation was determined more by the temperature dependent effects of phonon drag and thermally activated kink-pair nucleation. This increase in pinning-point formation at higher temperatures on the process had been previously observed with the kMC model. At the highest concentration it was also found that the trend with strain was reversed for the lowest temperature: pinning became more likely in compressive regions because the kink-trapping energy of hydrogen in these regions is greater and the variation in hydrogen concentration with strain was no longer large.

These variations aside, the calculations generally demonstrated that the effect of the same bulk concentration of hydrogen could change greatly between tension and compression: at lower concentrations, there could be significant softening due to the enhancement of kink-pair nucleation localised completely to regions of high tensile stress. As the concentration increases, this effect could change to significant hardening in these tensile regions, as the kink-pair nucleation rate increased to the point that pinning-point formation becomes likely, while there may still be softening in unstressed or compressive regions. Therefore, the region of likely shear localisation around a crack-tip could change completely depending on the hydrogen content and temperature. Again, these predictions were carried out with great approximations applied, and do not consider the evolution of the microstructure as the dislocation moves. Furthermore, calculations of the Peierls barrier indicated that the kink-pair nucleation enthalpy should decrease in regions of tension, which would further increase this disparity across the range of strains.

The kMC model would allow the evolution of the screw dislocation as it moves, including more realistic descriptions of the cross-slip and the elastic interactions between kinks and other defects that could decrease their velocity greatly. It would also allow more quantitative estimations of the effects of these strains on shear-localisation. However, if these results are to be employed in the kMC model, the variation of the kink-pair formation rate with strain must also be calculated. This will be carried out with either the methods described in chapter 4 or, if the Green function boundary conditions prove insufficient to relax the kink-pair structures, by using the BOP to carry out all the calculations required to produce a line tension model, across the range of strains.

These cells were then employed to calculate the barriers and jump frequencies for hydrogen diffusion between the strongest binding sites around the screw core in the unstressed crystal, at 1% compression and at 1% tension. The effect of the strain on these barriers changed completely depending on the sites that the hydrogen was moving between: some decreased with tension, some showed little dependence at all on the strain and the barrier to leave the core itself actually increased with tension. All of these barriers, apart from that to leave the core site, were between 5 – 10 times previously calculated barriers for bulk diffusion[224, 227]; this implied that diffusion around the screw core is relatively slow, at least for the pathways calculated. The barriers and jump frequencies for pipe diffusion of hydrogen along the dislocation line were also calculated, which had been theorised to be a possible pathway for accelerated diffusion of hydrogen through the lattice in the past. Although the barrier for this path was found to be significantly lower than that generally found for diffusion in the bulk, and hydrogen is more likely to remain in the core at higher tensile strain as the barrier to leave increases, it was still generally found that hydrogen was too unstable in these sites for this diffusion pathway to have a significant effect at any of the strains calculated. Moreover, the barrier to enter the core was quite significant, and so hydrogen is unlikely to enter in the first place. It would be interesting to include these barriers in a kMC model to simulate the coupled screw dislocation mobility and hydrogen diffusion, in order to estimate the conditions under which screws begin to break away from their hydrogen atmospheres, but all the other barriers surrounding the core would also have to be calculated to fully specify the model. However, all the structures involved have already been relaxed and so these simulations would not be difficult to carry out, just computationally expensive.

Embedding Tight Binding Within Bond Order Potential

Finally, it was understood that many of the possible simulations intended, such as the interaction between a kink-pair embryo and hydrogen, would require a scale beyond that attainable with direct diagonalisation Tight Binding. An attempt was then made to seamlessly embed a region described with direct diagonalisation Tight Binding into a much larger surrounding described with the Bond Order Potential model. It was thought that this would allow the calculation of the effect of hydrogen on dislocations with fewer approximations applied than ever before. Two variations of the method were implemented: one that was almost impractically slow and limited in scale but close to being exact, and another that was fast and could reach scales far above those

Conclusion

achievable with DD TB at little extra cost but had serious approximations applied.

A number of tests were then carried out with the models: the consistency of the interactions across the interface were assessed by displacing atoms adjacent to this border and comparing the gradients of the binding energy to the forces. The more exact model handled these interactions very well, having a good match in all cases, but the faster model did have discrepancies. This was expected, as one of the approximations involved freezing these border interactions during the calculation; however, the forces themselves were still close to correct and these models were only intended for molecular-statics simulations, so the lack of energy conservation at the border would not be an issue. These models were then used to simulate a large block of atoms, split between DD-SCTB and BOP, and the results compared to the cell described fully by DD-SCTB. In the case that the entire cell was described with a *d*-orthogonal parameter set, the results for both implementations were very good, showing forces and charges that converged to the full Tight Binding results within a short distance of the interface. When the block was split between a *d*-orthogonal region and a *sd*-nonorthogonal region, however, the results diverged quite a bit from the DD-SCTB results. The forces on interface atoms showed large imbalances due to the difference in forces between these parameter sets, which would result in large hydrostatic stresses across the embedded cluster. Also, the great electronic disturbance at the interface meant that this issue could not be resolved by refitting the pair-potential: significant charge oscillations occurred throughout the cluster for even the largest cells that could be simulated. At the same time, however, even with the greatest of these disturbances the faster model was found to reproduce the results of the other almost exactly, indicating that the approximations applied do not affect the result greatly and this implementation would work well if the issues with the interface could be dealt with.

The *d*-orthogonal simulations demonstrate that these methods work well if both regions have a similar basis set, the issue is then with the dissimilarity between the *d* and *sd* basis sets. This issue could then possibly be resolved by employing basis sets of greater similarity, possibly refitting the existing sets or employing a BOP model with approximations to non-orthogonality, or by using these methods for problems which could be well described by an orthogonal basis set throughout. No progress has been made with the first of these solutions, although attempts were restricted to refitting the *d*-orthogonal basis set and so there could be more success with a different approach. On the other hand, there are a number of problems for which these methods would

Conclusion

be appropriate, including the effect of oxygen on a dislocation core in titanium: the titanium may be described throughout with a *d*-orthogonal model, and the interactions with oxygen included solely with *sd* bond integrals[256, 257]. This, and a range of other work in titanium, will form the basis of future projects; however, an essential adaptation that must be carried out first is to enable Periodic boundary conditions in the DD-TB region with *k*-space integration. This process, which would consist of producing a Bloch-transformed Hamiltonian and carrying out an inverse Bloch transformation to recover the real-space Hamiltonian, would allow the extension of the DD-TB region to describe infinite surfaces or dislocation lines and extend the range of problems that could be treated greatly.

References

- [1] G. I. Taylor and C. F. Elam, “The plastic extension and fracture of aluminium crystals,” *Proceedings of the Royal Society A: Mathematical, Physical and Engineering Sciences*, vol. 108, pp. 28–51, may 1925.
- [2] E. Schmid and W. Boas, “Deutung der eigenschaften vielkristalliner technischer werkstücke auf grund des einkristallverhaltens,” in *Kristallplastizität*, pp. 302–335, Springer Berlin Heidelberg, 1935.
- [3] G. I. Taylor and C. F. Elam, “The distortion of iron crystals,” *Proceedings of the Royal Society A: Mathematical, Physical and Engineering Sciences*, vol. 112, pp. 337–361, sep 1926.
- [4] G. I. Taylor, “The deformation of crystals of β -brass,” *Proceedings of the Royal Society A: Mathematical, Physical and Engineering Sciences*, vol. 118, pp. 1–24, mar 1928.
- [5] T. Taoka, S. Takeuchi, and E. Furubayashi, “Slip systems and their critical shear stress in 3% silicon iron,” *Journal of the Physical Society of Japan*, vol. 19, pp. 701–711, may 1964.
- [6] B. Šesták and N. Zárubová, “Asymmetry of slip in Fe-Si alloy single crystals,” *physica status solidi (b)*, vol. 10, no. 1, pp. 239–250, 1965.
- [7] A. Argon and S. Maloof, “Plastic deformation of tungsten single crystals at low temperatures,” *Acta Metallurgica*, vol. 14, pp. 1449–1462, nov 1966.

References

- [8] D. K. Bowen, J. M. Capus, and C. E. Silverstone, “Plastic flow of martensite,” *Philosophical Magazine*, vol. 15, pp. 1041–1044, may 1967.
- [9] M. Duesbery and V. Vitek, “Plastic anisotropy in BCC transition metals,” *Acta Materialia*, vol. 46, pp. 1481–1492, mar 1998.
- [10] V. Volterra, “On the equilibrium of multiply-connected elastic bodies,” *Ann. Ec. Norm.*, vol. 3, no. 24, pp. 401–517, 1907.
- [11] E. Orowan, “Mechanical strength properties and real structure of crystals,” *Z. Kristallogr.*, vol. 89, pp. 327–343, jul.
- [12] M. Polanyi, “Lattice distortion which originates plastic flow,” *Zeitschrift für Physik*, vol. 89, pp. 660–664, sep 1934.
- [13] G. I. Taylor, “The mechanism of plastic deformation of crystals. part i. theoretical,” *Proceedings of the Royal Society A: Mathematical, Physical and Engineering Sciences*, vol. 145, pp. 362–387, jul 1934.
- [14] P. B. Hirsch, R. W. Horne, and M. J. Whelan, “LXVIII. direct observations of the arrangement and motion of dislocations in aluminium,” *Philosophical Magazine*, vol. 1, pp. 677–684, jul 1956.
- [15] F. E. Neumann and O. E. Meyer, *Vorlesungen über die Theorie der Elastizität der festen Körper und des Lichtäthers: gehalten an der Universität Königsberg*, vol. 4. BG Teubner, 1885.
- [16] P. B. Hirsch, R. W. Horne, and M. J. Whelan, “Proceedings of the fifth international conference on crystallography,” p. 139, 1960.
- [17] M. S. Duesbery and R. A. Foxall, “A detailed study of the deformation of high purity niobium single crystals,” *Philosophical Magazine*, vol. 20, pp. 719–751, oct 1969.

References

- [18] V. Vítek, R. C. Perrin, and D. K. Bowen, “The core structure of $\frac{1}{2}\langle 111 \rangle$ screw dislocations in BCC crystals,” *Philosophical Magazine*, vol. 21, pp. 1049–1073, may 1970.
- [19] Z. S. Basinski, M. S. Duesbery, and R. Taylor, “Influence of shear stress on screw dislocations in a model sodium lattice,” *Canadian Journal of Physics*, vol. 49, pp. 2160–2180, aug 1971.
- [20] S. Ismail-Beigi and T. A. Arias, “*Ab-Initio* study of screw dislocations in Mo and Ta: A new picture of plasticity in BCC transition metals,” *Physical Review Letters*, vol. 84, pp. 1499–1502, feb 2000.
- [21] S. L. Frederiksen and K. W. Jacobsen, “Density functional theory studies of screw dislocation core structures in BCC metals,” *Philosophical Magazine*, vol. 83, pp. 365–375, jan 2003.
- [22] M. Mrovec, D. Nguyen-Manh, D. G. Pettifor, and V. Vitek, “Bond-order potential for molybdenum: Application to dislocation behavior,” *Physical Review B*, vol. 69, mar 2004.
- [23] R. Gröger and V. Vitek, “Breakdown of the schmid law in BCC molybdenum related to the effect of shear stress perpendicular to the slip direction,” *Materials Science Forum*, vol. 482, pp. 123–126, apr 2005.
- [24] J. Chaussidon, M. Fivel, and D. Rodney, “The glide of screw dislocations in BCC Fe. atomistic static and dynamic simulations,” *Acta Materialia*, vol. 54, pp. 3407–3416, aug 2006.
- [25] V. Vítek, “Intrinsic stacking faults in body-centred cubic crystals,” *Philosophical Magazine*, vol. 18, pp. 773–786, oct 1968.
- [26] V. Vítek, “Multilayer stacking faults and twins on $\{211\}$ planes in BCC metals,” *Scripta Metallurgica*, vol. 4, pp. 725–732, sep 1970.

References

- [27] Z. S. Basinski, M. S. Duesbery, and R. Taylor, “Screw dislocation in a model sodium lattice,” *Philosophical Magazine*, vol. 21, pp. 1201–1221, jun 1970.
- [28] R. Peierls, “The size of a dislocation,” *Proceedings of the Physical Society*, vol. 52, pp. 34–37, jan 1940.
- [29] F. R. N. Nabarro, “Dislocations in a simple cubic lattice,” *Proceedings of the Physical Society*, vol. 59, pp. 256–272, mar 1947.
- [30] J. D. Eshelby, “Uniformly moving dislocations,” *Proceedings of the Physical Society. Section A*, vol. 62, pp. 307–314, may 1949.
- [31] W. Shockley, “Solid state physics in electronics and in metallurgy,” *JOM*, vol. 4, pp. 829–842, aug 1952.
- [32] A. Seeger, “The kink picture of dislocation mobility and dislocation-point-defect interactions,” *Le Journal de Physique Colloques*, vol. 42, pp. C5–201–C5–228, oct 1981.
- [33] T. Altshuler and J. Christian, “Low temperature twinning in pure iron,” *Acta Metallurgica*, vol. 14, pp. 903–908, jul 1966.
- [34] T. L. Altshuler and J. W. Christian, “The mechanical properties of pure iron tested in compression over the temperature range 2 to 293 degrees K,” *Philosophical Transactions of the Royal Society A: Mathematical, Physical and Engineering Sciences*, vol. 261, pp. 253–287, jun 1967.
- [35] A. H. Cottrell and R. J. Stokes, “Effects of temperature on the plastic properties of aluminium crystals,” *Proceedings of the Royal Society A: Mathematical, Physical and Engineering Sciences*, vol. 233, pp. 17–34, dec 1955.
- [36] L. Kubin, *Dislocations, mesoscale simulations and plastic flow*, vol. 5. Oxford University Press, 2013.
- [37] D. Hull and D. Bacon, “Introduction to dislocations,” 2001.

-
- [38] G. H. Vineyard, “Frequency factors and isotope effects in solid state rate processes,” *Journal of Physics and Chemistry of Solids*, vol. 3, pp. 121–127, jan 1957.
 - [39] A. Carlsson, “Beyond pair potentials in elemental transition metals and semiconductors,” in *Solid State Physics*, pp. 1–91, Elsevier, 1990.
 - [40] F. H. Stillinger and T. A. Weber, “Computer simulation of local order in condensed phases of silicon,” *Physical Review B*, vol. 31, pp. 5262–5271, apr 1985.
 - [41] M. Mrovec, R. Gröger, A. G. Bailey, D. Nguyen-Manh, C. Elsässer, and V. Vitek, “Bond-order potential for simulations of extended defects in tungsten,” *Physical Review B*, vol. 75, mar 2007.
 - [42] S. Chiesa, M. Gilbert, S. Dudarev, P. Derlet, and H. V. Swygenhoven, “The non-degenerate core structure of a $\frac{1}{2}\langle 111 \rangle$ screw dislocation in BCC transition metals modelled using finnis–sinclair potentials: The necessary and sufficient conditions,” *Philosophical Magazine*, vol. 89, pp. 3235–3243, dec 2009.
 - [43] W. Kohn and L. J. Sham, “Self-consistent equations including exchange and correlation effects,” *Physical Review*, vol. 140, pp. A1133–A1138, nov 1965.
 - [44] P. Hohenberg and W. Kohn, “Inhomogeneous electron gas,” *Physical Review*, vol. 136, pp. B864–B871, nov 1964.
 - [45] L. Ventelon and F. Willaime, “Core structure and peierls potential of screw dislocations in α -Fe from first principles: cluster versus dipole approaches,” *Journal of Computer-Aided Materials Design*, vol. 14, pp. 85–94, dec 2007.
 - [46] L. Ventelon, F. Willaime, E. Clouet, and D. Rodney, “*Ab-initio* investigation of the peierls potential of screw dislocations in BCC Fe and W,” *Acta Materialia*, vol. 61, pp. 3973–3985, jun 2013.

- [47] L. Dezerald, L. Ventelon, E. Clouet, C. Denoual, D. Rodney, and F. Willaime, “*Ab-initio* modeling of the two-dimensional energy landscape of screw dislocations in BCC transition metals,” *Physical Review B*, vol. 89, jan 2014.
- [48] M. Itakura, H. Kaburaki, M. Yamaguchi, and T. Okita, “The effect of hydrogen atoms on the screw dislocation mobility in BCC iron: A first-principles study,” *Acta Materialia*, vol. 61, pp. 6857–6867, oct 2013.
- [49] Y. Zhao and G. Lu, “QM/MM study of dislocation—hydrogen/helium interactions in α -Fe.,” *Modelling and Simulation in Materials Science and Engineering*, vol. 19, p. 065004, jul 2011.
- [50] M. R. Fellinger, A. M. Z. Tan, L. G. Hector, and D. R. Trinkle, “Geometries of edge and mixed dislocations in BCC Fe from first-principles calculations,” *Physical Review Materials*, vol. 2, nov 2018.
- [51] M. W. Finnis, A. T. Paxton, M. Methfesselt, and M. van Schilfgaarde, “Self-consistent tight-binding approximation including polarisable ions,” *MRS Proceedings*, vol. 491, jan 1997.
- [52] A. T. Paxton and M. W. Finnis, “Magnetic tight binding and the iron-chromium enthalpy anomaly,” *Physical Review B*, vol. 77, jan 2008.
- [53] A. Y. Lozovoi, T. J. Sheppard, D. L. Pashov, J. J. Kohanoff, and A. T. Paxton, “Universal tight binding model for chemical reactions in solution and at surfaces. II. water,” *The Journal of Chemical Physics*, vol. 141, p. 044504, jul 2014.
- [54] T. N. Todorov, “Tight-binding simulation of current-carrying nanostructures,” *Journal of Physics: Condensed Matter*, vol. 14, pp. 3049–3084, mar 2002.
- [55] A. P. Horsfield, A. M. Bratkovsky, D. G. Pettifor, and M. Aoki, “Bond-order potential and cluster recursion for the description of chemical bonds: Efficient real-space methods for tight-binding molecular dynamics,” *Physical Review B*, vol. 53, pp. 1656–1666, jan 1996.

References

- [56] A. P. Horsfield, A. M. Bratkovsky, M. Fearn, D. G. Pettifor, and M. Aoki, “Bond-order potentials: Theory and implementation,” *Physical Review B*, vol. 53, pp. 12694–12712, may 1996.
- [57] D. Pettifor, “New many-body potential for the bond order,” *Physical Review Letters*, vol. 63, pp. 2480–2483, nov 1989.
- [58] M. Mrovec, D. Nguyen-Manh, C. Elsässer, and P. Gumbsch, “Magnetic bond-order potential for iron,” *Physical Review Letters*, vol. 106, jun 2011.
- [59] Y.-S. Lin, M. Mrovec, and V. Vitek, “Bond-order potential for magnetic body-centered-cubic iron and its transferability,” *Physical Review B*, vol. 93, jun 2016.
- [60] G. Alefeld and J. Völkl, eds., *Hydrogen in Metals I*. Springer Berlin Heidelberg, 1978.
- [61] W. H. Johnson, “On some remarkable changes produced in iron and steel by the action of hydrogen and acids,” *Proceedings of the Royal Society of London*, vol. 23, pp. 168–179, jan 1875.
- [62] L. B. Pfeil, “The effect of occluded hydrogen on the tensile strength of iron,” *Proceedings of the Royal Society A: Mathematical, Physical and Engineering Sciences*, vol. 112, pp. 182–195, aug 1926.
- [63] R. A. Oriani, “A mechanistic theory of hydrogen embrittlement of steels,” *Berichte der Bunsengesellschaft für physikalische Chemie*, vol. 76, pp. 848–857, aug 1972.
- [64] H. Vehoff and P. Neumann, “Crack propagation and cleavage initiation in Fe 2.6%-Si single crystals under controlled plastic crack tip opening rate in various gaseous environments,” *Acta Metallurgica*, vol. 28, pp. 265–272, mar 1980.
- [65] H. Vehoff, W. Rothe, and P. Neumann, “Hydrogen assisted crack growth in high purity low pressure hydrogen gas,” in *Atomistics of Fracture*, pp. 829–834, Springer US, 1983.

References

- [66] Y. A. Du, L. Ismer, J. Rogal, T. Hickel, J. Neugebauer, and R. Drautz, “First-principles study on the interaction of H interstitials with grain boundaries in α -and γ -Fe,” *Physical Review B*, vol. 84, oct 2011.
- [67] A. A. Griffith, “The phenomena of rupture and flow in solids,” *Philosophical Transactions of the Royal Society A: Mathematical, Physical and Engineering Sciences*, vol. 221, pp. 163–198, jan 1921.
- [68] I. H. Katzarov and A. T. Paxton, “Hydrogen embrittlement II. analysis of hydrogen-enhanced decohesion across (111) planes in α -Fe.,” *Physical Review Materials*, vol. 1, aug 2017.
- [69] E. J. McEniry, T. Hickel, and J. Neugebauer, “*Ab-initio* simulation of hydrogen-induced decohesion in cementite-containing microstructures,” *Acta Materialia*, vol. 150, pp. 53–58, may 2018.
- [70] M. Nagumo, “Hydrogen related failure of steels – a new aspect,” *Materials Science and Technology*, vol. 20, pp. 940–950, aug 2004.
- [71] M. Nagumo, M. Nakamura, and K. Takai, “Hydrogen thermal desorption relevant to delayed-fracture susceptibility of high-strength steels,” *Metallurgical and Materials Transactions A*, vol. 32, pp. 339–347, feb 2001.
- [72] P. Jones, J. Schaffer, F. Cocks, F. Clinard, and G. Hurley, “A comparison of the doppler-broadened positron annihilation spectra of neutron irradiated Al_2O_3 and MgAl_2O_3 ,” *Journal of Nuclear Materials*, vol. 127, pp. 221–224, jan 1985.
- [73] K. Sakaki, T. Kawase, M. Hirato, M. Mizuno, H. Araki, Y. Shirai, and M. Nagumo, “The effect of hydrogen on vacancy generation in iron by plastic deformation,” *Scripta Materialia*, vol. 55, pp. 1031–1034, dec 2006.
- [74] K. Takai, H. Shoda, H. Suzuki, and M. Nagumo, “Lattice defects dominating hydrogen-related failure of metals,” *Acta Materialia*, vol. 56, pp. 5158–5167, oct 2008.

References

- [75] T. Doshida, H. Suzuki, K. Takai, N. Oshima, and T. Hirade, “Enhanced lattice defect formation associated with hydrogen and hydrogen embrittlement under elastic stress of a tempered martensitic steel,” *ISIJ International*, vol. 52, no. 2, pp. 198–207, 2012.
- [76] M. Hatano, M. Fujinami, K. Arai, H. Fujii, and M. Nagumo, “Hydrogen embrittlement of austenitic stainless steels revealed by deformation microstructures and strain-induced creation of vacancies,” *Acta Materialia*, vol. 67, pp. 342–353, apr 2014.
- [77] C. D. Beachem, “A new model for hydrogen-assisted cracking (hydrogen “embrittlement”),” *Metallurgical and Materials Transactions B*, vol. 3, pp. 441–455, feb 1972.
- [78] T. Tabata and H. Birnbaum, “Direct observations of the effect of hydrogen on the behavior of dislocations in iron,” *Scripta Metallurgica*, vol. 17, pp. 947–950, jul 1983.
- [79] T. Tabata and H. Birnbaum, “Direct observations of hydrogen enhanced crack propagation in iron,” *Scripta Metallurgica*, vol. 18, pp. 231–236, mar 1984.
- [80] I. Robertson and H. Birnbaum, “An HVEM study of hydrogen effects on the deformation and fracture of nickel,” *Acta Metallurgica*, vol. 34, pp. 353–366, mar 1986.
- [81] H. Birnbaum and P. Sofronis, “Hydrogen-enhanced localized plasticity—a mechanism for hydrogen-related fracture,” *Materials Science and Engineering: A*, vol. 176, pp. 191–202, mar 1994.
- [82] P. Ferreira, I. Robertson, and H. Birnbaum, “Hydrogen effects on the interaction between dislocations,” *Acta Materialia*, vol. 46, pp. 1749–1757, mar 1998.
- [83] I. Robertson, H. Birnbaum, and P. Sofronis, “Chapter 91 hydrogen effects on plasticity,” in *Dislocations in Solids*, pp. 249–293, Elsevier, 2009.

References

- [84] D. P. Abraham and C. J. Altstetter, “Hydrogen-enhanced localization of plasticity in an austenitic stainless steel,” *Metallurgical and Materials Transactions A*, vol. 26, pp. 2859–2871, nov 1995.
- [85] H. Matsui, H. Kimura, and S. Moriya, “The effect of hydrogen on the mechanical properties of high purity iron i. softening and hardening of high purity iron by hydrogen charging during tensile deformation,” *Materials Science and Engineering*, vol. 40, pp. 207–216, oct 1979.
- [86] Y. Jagodzinski, H. Hänninen, O. Tarasenko, and S. Smuk, “Interaction of hydrogen with dislocation pile-ups and hydrogen induced softening of pure iron,” *Scripta Materialia*, vol. 43, pp. 245–251, jul 2000.
- [87] J. Song and W. Curtin, “Mechanisms of hydrogen-enhanced localized plasticity: An atomistic study using α -Fe as a model system,” *Acta Materialia*, vol. 68, pp. 61–69, apr 2014.
- [88] R. Kirchheim, “Reducing grain boundary, dislocation line and vacancy formation energies by solute segregation. I. Theoretical background,” *Acta Materialia*, vol. 55, pp. 5129–5138, sep 2007.
- [89] R. Kirchheim, “Reducing grain boundary, dislocation line and vacancy formation energies by solute segregation. II. Experimental evidence and consequences,” *Acta Materialia*, vol. 55, pp. 5139–5148, sep 2007.
- [90] R. Kirchheim, “On the solute-defect interaction in the framework of a defactant concept,” *International Journal of Materials Research*, vol. 100, pp. 483–487, apr 2009.
- [91] R. Kirchheim, “Solid solution softening and hardening by mobile solute atoms with special focus on hydrogen,” *Scripta Materialia*, vol. 67, pp. 767–770, nov 2012.

References

- [92] A. Barnoush and H. Vehoff, “Recent developments in the study of hydrogen embrittlement: Hydrogen effect on dislocation nucleation,” *Acta Materialia*, vol. 58, pp. 5274–5285, sep 2010.
- [93] T. Michalske and J. Houston, “Dislocation nucleation at nano-scale mechanical contacts,” *Acta Materialia*, vol. 46, pp. 391–396, jan 1998.
- [94] M. Itakura, H. Kaburaki, and M. Yamaguchi, “First-principles study on the mobility of screw dislocations in BCC iron,” *Acta Materialia*, vol. 60, pp. 3698–3710, may 2012.
- [95] I. H. Katzarov, D. L. Pashov, and A. T. Paxton, “Hydrogen embrittlement i. analysis of hydrogen-enhanced localized plasticity: Effect of hydrogen on the velocity of screw dislocations in α -Fe.,” *Physical Review Materials*, vol. 1, aug 2017.
- [96] C. G. Broyden, “A class of methods for solving nonlinear simultaneous equations,” *Mathematics of Computation*, vol. 19, no. 92, pp. 577–577, 1965.
- [97] S. Sun, K. Shiozawa, J. Gu, and N. Chen, “Investigation of deformation field and hydrogen partition around crack tip in FCC single crystal,” *Metallurgical and Materials Transactions A*, vol. 26, pp. 731–739, mar 1995.
- [98] H. Gao, W. Cao, C. Fang, and E. R. Rios, “Analysis of crack tip hydrogen distribution under i/ii mixed mode loads,” *Fatigue & Fracture of Engineering Materials and Structures*, vol. 17, pp. 1213–1220, oct 1994.
- [99] J. Frenkel, “On the theory of elasticity and yield stress in crystalline bodies,” *Zeitschrift für Physik*, vol. 37, pp. 572–609, jul 1926.
- [100] M. Born and R. Oppenheimer, “Zur quantentheorie der moleküle,” *Annalen der Physik*, vol. 389, no. 20, pp. 457–484, 1927.

References

- [101] P.-O. Löwdin, “On the non-orthogonality problem connected with the use of atomic wave functions in the theory of molecules and crystals,” *The Journal of Chemical Physics*, vol. 18, pp. 365–375, mar 1950.
- [102] A. T. Paxton, “An introduction to the tight binding approximation – implementation by diagonalisation,” *NIC series*, vol. 42, pp. 365–375, 2009.
- [103] M. Finnis, *Interatomic Forces in Condensed Matter*. Oxford University Press, oct 2003.
- [104] J. C. Slater and G. F. Koster, “Simplified LCAO method for the periodic potential problem,” *Physical Review*, vol. 94, pp. 1498–1524, jun 1954.
- [105] A. T. Paxton and C. Elsässer, “Electronic structure and total energy of interstitial hydrogen in iron: Tight-binding models,” *Physical Review B*, vol. 82, dec 2010.
- [106] L. Goodwin, A. J. Skinner, and D. G. Pettifor, “Generating transferable tight-binding parameters: Application to silicon,” *Europhysics Letters (EPL)*, vol. 9, pp. 701–706, aug 1989.
- [107] R. S. Mulliken, “Electronic population analysis on LCAO–MO molecular wave functions. I,” *The Journal of Chemical Physics*, vol. 23, pp. 1833–1840, oct 1955.
- [108] D. J. Chadi, “Atomic and electronic structures of reconstructed Si(100) surfaces,” *Physical Review Letters*, vol. 43, pp. 43–47, jul 1979.
- [109] A. P. Sutton, M. W. Finnis, D. G. Pettifor, and Y. Ohta, “The tight-binding bond model,” *Journal of Physics C: Solid State Physics*, vol. 21, pp. 35–66, jan 1988.
- [110] R. A. Harris and L. R. Pratt, “A method for systematic inclusion of electron correlation in density functionals,” *The Journal of Chemical Physics*, vol. 83, pp. 4024–4028, oct 1985.

References

- [111] W. M. C. Foulkes, “Interatomic forces in solids.,” *PhD Thesis*, 1987.
- [112] N. Börnsen, B. Meyer, O. Grotheer, and M. Fähnle, “ e_{cov} - a new tool for the analysis of electronic structure data in a chemical language,” *Journal of Physics: Condensed Matter*, vol. 11, pp. L287–L293, jan 1999.
- [113] H. Hellmann, “Einführung in die quantenchemie,” *Deuticke*, 1987.
- [114] R. P. Feynman, “Forces in molecules,” *Physical Review*, vol. 56, pp. 340–343, aug 1939.
- [115] H. J. Monkhorst and J. D. Pack, “Special points for brillouin-zone integrations,” *Physical Review B*, vol. 13, pp. 5188–5192, jun 1976.
- [116] M. Methfessel and A. T. Paxton, “High-precision sampling for brillouin-zone integration in metals,” *Physical Review B*, vol. 40, pp. 3616–3621, aug 1989.
- [117] P. E. Blöchl, O. Jepsen, and O. K. Andersen, “Improved tetrahedron method for brillouin-zone integrations,” *Physical Review B*, vol. 49, pp. 16223–16233, jun 1994.
- [118] V. Heine, “Electronic structure from the point of view of the local atomic environment,” in *Solid State Physics*, pp. 1–127, Elsevier, 1980.
- [119] F. Ducastelle and F. Cyrot-Lackmann, “Moments developments and their application to the electronic charge distribution of d -bands,” *Journal of Physics and Chemistry of Solids*, vol. 31, pp. 1295–1306, jun 1970.
- [120] R. Haydock, V. Heine, and M. J. Kelly, “Electronic structure based on the local atomic environment for tight-binding bands,” *Journal of Physics C: Solid State Physics*, vol. 5, pp. 2845–2858, oct 1972.
- [121] R. Haydock, V. Heine, and M. J. Kelly, “Electronic structure based on the local atomic environment for tight-binding bands. II,” *Journal of Physics C: Solid State Physics*, vol. 8, pp. 2591–2605, aug 1975.

References

- [122] C. Lanczos, “Iterative solution of large-scale linear systems,” *Journal of the Society for Industrial and Applied Mathematics*, vol. 6, pp. 91–109, mar 1958.
- [123] T. Hammerschmidt, R. Drautz, and D. G. Pettifor, “Atomistic modelling of materials with bond-order potentials,” *International Journal of Materials Research*, vol. 100, pp. 1479–1487, nov 2009.
- [124] M. Aoki, “Rapidly convergent bond order expansion for atomistic simulations,” *Physical Review Letters*, vol. 71, pp. 3842–3845, dec 1993.
- [125] D. M. C. Nicholson, G. M. Stocks, Y. Wang, W. A. Shelton, Z. Szotek, and W. M. Temmerman, “Stationary nature of the density-functional free energy: Application to accelerated multiple-scattering calculations,” *Physical Review B*, vol. 50, pp. 14686–14689, nov 1994.
- [126] A. Girshick, A. M. Bratkovsky, D. G. Pettifor, and V. Vitek, “Atomistic simulation of titanium. I. a bond-order potential,” *Philosophical Magazine A*, vol. 77, pp. 981–997, apr 1998.
- [127] C. Priester, G. Allan, and M. Lannoo, “Tight-binding calculation of the band offset at the Ge-GaAs (110) interface using a local charge-neutrality condition,” *Physical Review B*, vol. 33, pp. 7386–7388, may 1986.
- [128] H. Hasegawa, “A spin fluctuation theory of degenerate narrow bands-finite-temperature magnetism of iron,” *Journal of Physics F: Metal Physics*, vol. 13, pp. 1915–1929, sep 1983.
- [129] E. C. Stoner, “Collective electron ferromagnetism. II. energy and specific heat,” *Proceedings of the Royal Society A: Mathematical, Physical and Engineering Sciences*, vol. 169, pp. 339–371, feb 1939.
- [130] G. Liu, D. Nguyen-Manh, B.-G. Liu, and D. G. Pettifor, “Magnetic properties of point defects in iron within the tight-binding-bond stoner model,” *Physical Review B*, vol. 71, may 2005.

References

- [131] M. W. Finnis, A. T. Paxton, M. Methfessel, and M. van Schilfgaarde, “Crystal structures of zirconia from first principles and self-consistent tight binding,” *Physical Review Letters*, vol. 81, pp. 5149–5152, dec 1998.
- [132] J. Spence, “The future of atomic resolution electron microscopy for materials science,” *Materials Science and Engineering: R: Reports*, vol. 26, pp. 1–49, oct 1999.
- [133] M. S. Daw and M. I. Baskes, “Semiempirical, quantum mechanical calculation of hydrogen embrittlement in metals,” *Physical Review Letters*, vol. 50, pp. 1285–1288, apr 1983.
- [134] M. W. Finnis and J. E. Sinclair, “A simple empirical n-body potential for transition metals,” *Philosophical Magazine A*, vol. 50, pp. 45–55, jul 1984.
- [135] D. Pettifor, M. Aoki, P. Gumbsch, A. Horsfield, D. N. Manh, and V. Vitek, “Defect modelling: the need for angularly dependent potentials,” *Materials Science and Engineering: A*, vol. 192-193, pp. 24–30, feb 1995.
- [136] A. Girshick, “Atomistic studies of dislocations in titanium and titanium-aluminum compound,” *Thesis*, 1997.
- [137] D. Bacon, D. Barnett, and R. Scattergood, “Anisotropic continuum theory of lattice defects,” *Progress in Materials Science*, vol. 23, pp. 51–262, jan 1980.
- [138] A. N. Stroh, “Dislocations and cracks in anisotropic elasticity,” *Philosophical Magazine*, vol. 3, pp. 625–646, jun 1958.
- [139] A. N. Stroh, “Steady state problems in anisotropic elasticity,” *Journal of Mathematics and Physics*, vol. 41, pp. 77–103, apr 1962.
- [140] G. Mills, H. Jónsson, and G. K. Schenter, “Reversible work transition state theory: application to dissociative adsorption of hydrogen,” *Surface Science*, vol. 324, pp. 305–337, feb 1995.

References

- [141] H. Jónsson, G. Mills, and K. W. Jacobsen, “Nudged elastic band method for finding minimum energy paths of transitions,” in *Classical and Quantum Dynamics in Condensed Phase Simulations*, World Scientific, jun 1998.
- [142] G. Henkelman and H. Jónsson, “Improved tangent estimate in the nudged elastic band method for finding minimum energy paths and saddle points,” *The Journal of Chemical Physics*, vol. 113, pp. 9978–9985, dec 2000.
- [143] G. Henkelman, B. P. Uberuaga, and H. Jónsson, “A climbing image nudged elastic band method for finding saddle points and minimum energy paths,” *The Journal of Chemical Physics*, vol. 113, pp. 9901–9904, dec 2000.
- [144] R. Gröger, “Differential displacement plot software (<http://groger.ipm.cz/download/ddplot/ddplot.html>),”
- [145] M. Wen and A. Ngan, “Atomistic simulation of kink-pairs of screw dislocations in body-centred cubic iron,” *Acta Materialia*, vol. 48, pp. 4255–4265, nov 2000.
- [146] P. Giannozzi, S. Baroni, N. Bonini, M. Calandra, R. Car, C. Cavazzoni, D. Ceresoli, G. L. Chiarotti, M. Cococcioni, I. Dabo, *et al.*, “Quantum espresso: a modular and open-source software project for quantum simulations of materials,” *Journal of physics: Condensed matter*, vol. 21, no. 39, p. 395502, 2009.
- [147] G. K. H. Madsen, E. J. McEniry, and R. Drautz, “Optimized orthogonal tight-binding basis: Application to iron,” *Physical Review B*, vol. 83, may 2011.
- [148] J. M. Soler, E. Artacho, J. D. Gale, A. García, J. Junquera, P. Ordejón, and D. Sánchez-Portal, “The SIESTA method for *ab-initio* order-n materials simulation,” *Journal of Physics: Condensed Matter*, vol. 14, pp. 2745–2779, mar 2002.
- [149] D. Caillard, “Kinetics of dislocations in pure Fe. part i. in situ straining experiments at room temperature,” *Acta Materialia*, vol. 58, pp. 3493–3503, may 2010.

References

- [150] D. Rodney, L. Ventelon, E. Clouet, L. Pizzagalli, and F. Willaime, “*Ab-initio* modeling of dislocation core properties in metals and semiconductors,” *Acta Materialia*, vol. 124, pp. 633–659, feb 2017.
- [151] Z. M. Chen, M. Mrovec, and P. Gumbsch, “Atomistic aspects of $\frac{1}{2}\langle 111 \rangle$ screw dislocation behavior in α -iron and the derivation of microscopic yield criterion,” *Modelling and Simulation in Materials Science and Engineering*, vol. 21, p. 055023, jun 2013.
- [152] Z. Xia, Z. Zhang, J. Yang, and Z. Zhang, “Quantitative analysis of the yield behavior of a $\frac{1}{2}\langle 111 \rangle$ screw dislocation in α -iron,” *Computational Materials Science*, vol. 148, pp. 207–215, jun 2018.
- [153] D. Brunner and J. Diehl, “The effect of atomic lattice defects on the softening phenomena of high-purity α -iron,” *physica status solidi (a)*, vol. 160, pp. 355–372, apr 1997.
- [154] Y. Aono, “Plastic deformation of high purity iron single crystals,” *Rep. Res. Inst. Appl. Mechanics*, vol. 24, p. 127, 1981.
- [155] V. V. Gröger R, “The effect of atomic lattice defects on the softening phenomena of high-purity α -iron,” *Bulletin of the American Physical Society*, mar 2006.
- [156] K. Ito and V. Vitek, “Atomistic study of non-schmid effects in the plastic yielding of BCC metals,” *Philosophical Magazine A*, vol. 81, pp. 1387–1407, may 2001.
- [157] W. Spitzig and A. Keh, “The effect of orientation and temperature on the plastic flow properties of iron single crystals,” *Acta Metallurgica*, vol. 18, pp. 611–622, jun 1970.
- [158] R. Gröger, A. Bailey, and V. Vitek, “Multiscale modeling of plastic deformation of molybdenum and tungsten: I. atomistic studies of the core structure and glide of $\frac{1}{2}\langle 111 \rangle$ screw dislocations at 0k,” *Acta Materialia*, vol. 56, pp. 5401–5411, nov 2008.

- [159] S. K. Bhattacharya, S. Tanaka, Y. Shiihara, and M. Kohyama, “*Ab-initio* perspective of the $\langle 110 \rangle$ symmetrical tilt grain boundaries in BCC Fe. application of local energy and local stress,” *Journal of Materials Science*, vol. 49, pp. 3980–3995, feb 2014.
- [160] H. Momida, Y. Asari, Y. Nakamura, Y. Tateyama, and T. Ohno, “Hydrogen-enhanced vacancy embrittlement of grain boundaries in iron,” *Physical Review B*, vol. 88, oct 2013.
- [161] N. Gao, C.-C. Fu, M. Samaras, R. Schäublin, M. Victoria, and W. Hoffelner, “Multiscale modelling of bi-crystal grain boundaries in BCC iron,” *Journal of Nuclear Materials*, vol. 385, pp. 262–267, mar 2009.
- [162] M. A. Tschopp, K. N. Solanki, F. Gao, X. Sun, M. A. Khaleel, and M. F. Horstemeyer, “Probing grain boundary sink strength at the nanoscale: Energetics and length scales of vacancy and interstitial absorption by grain boundaries in α -Fe,” *Physical Review B*, vol. 85, feb 2012.
- [163] H. Nakashima and M. Takeuchi, “Grain boundary energy and structure of α -Fe $\langle 110 \rangle$ symmetric tilt boundary,” *Tetsu-to-Hagane*, vol. 86, no. 5, pp. 357–362, 2000.
- [164] M. Mrovec, C. Elsässer, and P. Gumbsch, “Interactions between lattice dislocations and twin boundaries in tungsten: A comparative atomistic simulation study,” *Philosophical Magazine*, vol. 89, pp. 3179–3194, dec 2009.
- [165] M. Mrovec, T. Ochs, C. Elsässer, V. Vitek, D. Nguyen-Manh, and D. G. Pettifor, “Never ending saga of a simple boundary,” *Zeitschrift für Metallkunde*, vol. 94, pp. 244–249, mar 2003.
- [166] P. D. Bristowe and A. G. Crocker, “A computer simulation study of the structures of twin boundaries in body-centred cubic crystals,” *Philosophical Magazine*, vol. 31, pp. 503–517, mar 1975.

References

- [167] A. M. Papon, J. P. Simon, P. Guyot, and M. C. Desjonquères, “Calculation of $\{112\}$ twin and stacking fault energies in BCC transition metals,” *Philosophical Magazine B*, vol. 40, pp. 159–172, aug 1979.
- [168] C. T. Forwood and L. M. Clarebrough, “Rigid body displacements at a faceted $\Sigma 3$ boundary in α -iron,” *Physica Status Solidi (a)*, vol. 105, pp. 365–375, feb 1988.
- [169] V. Bulatov and W. Cai, “Computer simulations of dislocations,” 2006.
- [170] G. Monnet and D. Terentyev, “Structure and mobility of the $\frac{1}{2}\langle 111 \rangle\{112\}$ edge dislocation in BCC iron studied by molecular dynamics,” *Acta Materialia*, vol. 57, pp. 1416–1426, mar 2009.
- [171] K. Masuda, K. Kobayashi, A. Sato, and T. Mori, “Calculation of core structure and core energy of $\frac{1}{2}\langle 111 \rangle\{110\}$ and $\frac{1}{2}\langle 111 \rangle\{112\}$ edge dislocations in a BCC transition metal: moments approach,” *Philosophical Magazine B*, vol. 43, pp. 19–28, jan 1981.
- [172] M. Yamaguchi and V. Vitek, “Core structures of non-screw $\frac{1}{2}\langle 111 \rangle$ dislocations on (112) planes of BCC crystals. i. core structure in an unstressed crystal,” *Journal of Physics F: Metal Physics*, vol. 5, pp. 1–10, jan 1975.
- [173] K. Ingle and A. Crocker, “The interaction between vacancies and the $\frac{1}{2}\langle 111 \rangle\{110\}$ edge dislocation in body centred cubic metals,” *Acta Metallurgica*, vol. 26, pp. 1461–1469, sep 1978.
- [174] M. Yamaguchi and V. Vitek, “Core structure of nonscrew $\frac{1}{2}\langle 111 \rangle$ dislocations on (110) planes in BCC crystals. i. core structure in an unstressed crystal,” *Journal of Physics F: Metal Physics*, vol. 3, pp. 523–536, mar 1973.
- [175] B. L. Adams and J. P. Hirth, “Atomic simulation of the $\frac{1}{2}\langle 111 \rangle\{110\}$ edge dislocation in alpha-iron,” *Journal of Physics F: Metal Physics*, vol. 7, pp. 2021–2029, oct 1977.

References

- [176] J.-A. Yan, C.-Y. Wang, and S.-Y. Wang, “Generalized-stacking-fault energy and dislocation properties in BCC Fe: a first-principles study,” *Physical Review B*, vol. 70, nov 2004.
- [177] P. M. Derlet, D. Nguyen-Manh, and S. L. Dudarev, “Multiscale modeling of crowdion and vacancy defects in body-centered-cubic transition metals,” *Physical Review B*, vol. 76, aug 2007.
- [178] C. J. Först, J. Slycke, K. J. V. Vliet, and S. Yip, “Point defect concentrations in metastable Fe-C alloys,” *Physical Review Letters*, vol. 96, may 2006.
- [179] Y. Tateyama and T. Ohno, “Stability and clusterization of hydrogen-vacancy complexes in α -Fe: An *ab-initio* study,” *Physical Review B*, vol. 67, may 2003.
- [180] K. Masuda, “Vacancies and small vacancy clusters in BCC transition metals : calculation of binding energy, atomic relaxation and electronic and vibrational densities of states,” *Journal de Physique*, vol. 43, no. 6, pp. 921–930, 1982.
- [181] R. A. Johnson and W. D. Wilson, “Defect calculations for fcc and bcc metals,” *Interatomic Potentials and Simulation of Lattice Defects*, pp. 301–319, 1972.
- [182] A. Seeger, “Lattice vacancies in high-purity α -iron,” *physica status solidi (a)*, vol. 167, pp. 289–311, jun 1998.
- [183] C. Domain and C. S. Becquart, “*Ab-initio* calculations of defects in Fe and dilute Fe-Cu alloys,” *Physical Review B*, vol. 65, dec 2001.
- [184] L. de Schepper, D. Segers, G. Knuyt, L. Dorikens-Vanpraet, M. Dorikens, L. Stals, and P. Moser, “Determination of the ferromagnetic vacancy-formation enthalpy in α -iron by the positron method using the carbon-vacancy pair as a probe,” *Physics Letters A*, vol. 95, pp. 121–123, apr 1983.
- [185] H.-E. Schaefer, K. Maier, M. Weller, D. Herlach, A. Seeger, and J. Diehl, “Vacancy formation in iron investigated by positron annihilation in thermal equilibrium,” *Scripta Metallurgica*, vol. 11, pp. 803–809, sep 1977.

References

- [186] S. Li, Y. Li, Y.-C. Lo, T. Neeraj, R. Srinivasan, X. Ding, J. Sun, L. Qi, P. Gumbsch, and J. Li, “The interaction of dislocations and hydrogen-vacancy complexes and its importance for deformation-induced proto nano-voids formation in α -Fe.,” *International Journal of Plasticity*, vol. 74, pp. 175–191, nov 2015.
- [187] A. Stukowski, “Visualization and analysis of atomistic simulation data with OVITO—the open visualization tool (<http://ovito.org/>),” *Modelling and Simulation in Materials Science and Engineering*, vol. 18, p. 015012, dec 2009.
- [188] R. Bullough and R. C. Newman, “The kinetics of migration of point defects to dislocations,” *Reports on Progress in Physics*, vol. 33, pp. 101–148, jan 1970.
- [189] C. Li-Qun, W. Chong-Yu, and Y. Tao, “Atomistic simulation of kink structure on edge dislocation in BCC iron,” *Chinese Physics B*, vol. 17, pp. 662–668, feb 2008.
- [190] R. A. Johnson, “Interstitials and vacancies in α -iron,” *Physical Review*, vol. 134, pp. A1329–A1336, jun 1964.
- [191] M. A. Bhatia, S. Groh, and K. N. Solanki, “Atomic-scale investigation of point defects and hydrogen-solute atmospheres on the edge dislocation mobility in alpha iron,” *Journal of Applied Physics*, vol. 116, p. 064302, aug 2014.
- [192] A. B. Sivak, V. A. Romanov, and V. M. Chernov, “Diffusion of self-point defects in body-centered cubic iron crystal containing dislocations,” *Crystallography Reports*, vol. 55, pp. 97–108, jan 2010.
- [193] Y. Kamimura, T. Tsutsumi, and E. Kuramoto, “Calculations of positron lifetimes in a jog and vacancies on an edge-dislocation line in Fe.,” *Physical Review B*, vol. 52, pp. 879–885, jul 1995.
- [194] T. Lau, X. Lin, S. Yip, and K. Vanvliet, “Atomistic examination of the unit processes and vacancy-dislocation interaction in dislocation climb,” *Scripta Materialia*, vol. 60, pp. 399–402, mar 2009.

References

- [195] C.-C. Fu, J. D. Torre, F. Willaime, J.-L. Bocquet, and A. Barbu, “Multiscale modelling of defect kinetics in irradiated iron,” *Nature Materials*, vol. 4, pp. 68–74, dec 2005.
- [196] A. Vehanen, P. Hautojärvi, J. Johansson, J. Yli-Kauppila, and P. Moser, “Vacancies and carbon impurities in α -iron: Electron irradiation,” *Physical Review B*, vol. 25, pp. 762–780, jan 1982.
- [197] P. Sofronis, “The influence of mobility of dissolved hydrogen on the elastic response of a metal,” *Journal of the Mechanics and Physics of Solids*, vol. 43, pp. 1385–1407, sep 1995.
- [198] H. Fu, E. Galindo-Nava, and P. R.-D. del Castillo, “Modelling and characterisation of stress-induced carbide precipitation in bearing steels under rolling contact fatigue,” *Acta Materialia*, vol. 128, pp. 176–187, apr 2017.
- [199] H. Fu, W. Song, E. I. Galindo-Nava, and P. E. R.-D. del Castillo, “Strain-induced martensite decay in bearing steels under rolling contact fatigue: Modelling and atomic-scale characterisation,” *Acta Materialia*, vol. 139, pp. 163–173, oct 2017.
- [200] K. Tapasa, D. J. Bacon, and Y. N. Ossetsky, “Computer simulation of dislocation–solute interaction in dilute Fe–Cu alloys,” *Modelling and Simulation in Materials Science and Engineering*, vol. 14, pp. 1153–1166, aug 2006.
- [201] Y. Niu, S.-Y. Wang, D.-L. Zhao, and C.-Y. Wang, “The electronic effect in the $\langle 100 \rangle$ edge dislocation core system with a carbon atom in α -iron: a first-principles study,” *Journal of Physics: Condensed Matter*, vol. 13, pp. 4267–4276, apr 2001.
- [202] N. Hatcher, G. K. H. Madsen, and R. Drautz, “DFT-based tight-binding modeling of iron-carbon,” *Physical Review B*, vol. 86, oct 2012.
- [203] L. Ventelon, F. Willaime, and P. Leyronnas, “Atomistic simulation of single

References

- kinks of screw dislocations in α -Fe.,” *Journal of Nuclear Materials*, vol. 386-388, pp. 26–29, apr 2009.
- [204] W. Cai, V. V. Bulatov, J. F. Justo, A. S. Argon, and S. Yip, “Kinetic Monte Carlo approach to modeling dislocation mobility,” *Computational Materials Science*, vol. 23, pp. 124–130, apr 2002.
- [205] D. Cereceda, A. Stukowski, M. R. Gilbert, S. Queyreau, L. Ventelon, M.-C. Marinica, J. M. Perlado, and J. Marian, “Assessment of interatomic potentials for atomistic analysis of static and dynamic properties of screw dislocations in w,” *Journal of Physics: Condensed Matter*, vol. 25, p. 085702, jan 2013.
- [206] W. Cai, V. V. Bulatov, S. Yip, and A. S. Argon, “Kinetic Monte Carlo modeling of dislocation motion in BCC metals,” *Materials Science and Engineering: A*, vol. 309-310, pp. 270–273, jul 2001.
- [207] A. Stukowski, D. Cereceda, T. D. Swinburne, and J. Marian, “Thermally-activated non-schmid glide of screw dislocations in W using atomistically-informed kinetic Monte Carlo simulations,” *International Journal of Plasticity*, vol. 65, pp. 108–130, feb 2015.
- [208] F. Louchet and B. Viguier, “Ordinary dislocations in γ -TiAl: Cusp unzipping, jog dragging and stress anomaly,” *Philosophical Magazine A*, vol. 80, pp. 765–779, may 2000.
- [209] M. Duesbery, “On kinked screw dislocations in the BCC lattice—i. the structure and peierls stress of isolated kinks,” *Acta Metallurgica*, vol. 31, pp. 1747–1758, oct 1983.
- [210] P. A. Gordon, T. Neeraj, Y. Li, and J. Li, “Screw dislocation mobility in BCC metals: the role of the compact core on double-kink nucleation,” *Modelling and Simulation in Materials Science and Engineering*, vol. 18, p. 085008, nov 2010.

References

- [211] L. Proville, L. Ventelon, and D. Rodney, “Prediction of the kink-pair formation enthalpy on screw dislocations in α -iron by a line tension model parametrized on empirical potentials and first-principles calculations,” *Physical Review B*, vol. 87, apr 2013.
- [212] D. Brunner and J. Diehl, “Temperature and strain-rate dependence of the tensile flow stress of high-purity α -iron below 250 K. I. stress/temperature regime III,” *Physica Status Solidi (a)*, vol. 124, pp. 455–464, apr 1991.
- [213] I. Katzarov and A. Paxton, “Is the pinning of ordinary dislocations in γ -TiAl intrinsic or extrinsic in nature? a combined atomistic and kinetic Monte Carlo approach,” *Acta Materialia*, vol. 59, pp. 1281–1290, feb 2011.
- [214] W. Cai, V. V. Bulatov, and S. Yip *Journal of Computer-Aided Materials Design*, vol. 6, no. 2/3, pp. 175–183, 1999.
- [215] J. E. Sinclair, P. C. Gehlen, R. G. Hoagland, and J. P. Hirth, “Flexible boundary conditions and nonlinear geometric effects in atomic dislocation modeling,” *Journal of Applied Physics*, vol. 49, pp. 3890–3897, jul 1978.
- [216] S. Rao, C. Hernandez, J. P. Simmons, T. A. Parthasarathy, and C. Woodward, “Green's function boundary conditions in two-dimensional and three-dimensional atomistic simulations of dislocations,” *Philosophical Magazine A*, vol. 77, pp. 231–256, jan 1998.
- [217] D. G. Anderson, “Iterative procedures for nonlinear integral equations,” *Journal of the ACM*, vol. 12, pp. 547–560, oct 1965.
- [218] D. D. Johnson, “Modified broyden's method for accelerating convergence in self-consistent calculations,” *Physical Review B*, vol. 38, pp. 12807–12813, dec 1988.
- [219] D. Vanderbilt and S. G. Louie, “Total energies of diamond (111) surface reconstructions by a linear combination of atomic orbitals method,” *Physical Review B*, vol. 30, pp. 6118–6130, nov 1984.

References

- [220] R. P. Gangloff, "Hydrogen assisted cracking of high strength alloys," tech. rep., Aluminum co. of America, Alcoa center PA, Alcoa technical center, 2003.
- [221] I. Robertson, "The effect of hydrogen on dislocation dynamics," *Engineering Fracture Mechanics*, vol. 64, pp. 649–673, nov 1999.
- [222] S. Wang, N. Hashimoto, and S. Ohnuki, "Effects of hydrogen on activation volume and density of mobile dislocations in iron-based alloy," *Materials Science and Engineering: A*, vol. 562, pp. 101–108, feb 2013.
- [223] R. Fletcher and M. J. D. Powell, "A rapidly convergent descent method for minimization," *The Computer Journal*, vol. 6, pp. 163–168, aug 1963.
- [224] D. E. Jiang and E. A. Carter, "Diffusion of interstitial hydrogen into and through BCC Fe from first principles," *Physical Review B*, vol. 70, aug 2004.
- [225] G. Henkelman, B. P. Uberuaga, and H. Jónsson, "A climbing image nudged elastic band method for finding saddle points and minimum energy paths," *The Journal of Chemical Physics*, vol. 113, pp. 9901–9904, dec 2000.
- [226] M. I. A. Ramasubramaniam and E. A. Carter, "Interatomic potentials for hydrogen in α -iron based on density functional theory," *Physical Review B*, vol. 79, may 2009.
- [227] A. Ramasubramaniam, M. Itakura, M. Ortiz, and E. Carter, "Effect of atomic scale plasticity on hydrogen diffusion in iron: Quantum mechanically informed and on-the-fly kinetic Monte Carlo simulations," *Journal of Materials Research*, vol. 23, pp. 2757–2773, oct 2008.
- [228] J. P. Hirth, "Effects of hydrogen on the properties of iron and steel," *Metallurgical Transactions A*, vol. 11, pp. 861–890, jun 1980.
- [229] W. E, W. Ren, and E. Vanden-Eijnden, "String method for the study of rare events," *Physical Review B*, vol. 66, aug 2002.

References

- [230] J. Hirth and J. Lothe, “Theory of dislocations, 2nd,” *Ed.: John Wiley & Sons*, 1982.
- [231] W. C. C. Deo, D. Srolovitz and V. Bulatov, “Stochastic simulation of dislocation glide in tantalum and Ta-based alloys,” *Journal of the Mechanics and Physics of Solids*, vol. 53, pp. 1223–1247, jun 2005.
- [232] A. Y. Kuksin and A. V. Yanilkin, “Atomistic simulation of the motion of dislocations in metals under phonon drag conditions,” *Physics of the Solid State*, vol. 55, pp. 1010–1019, may 2013.
- [233] H. Kimura and H. Matsui, “Mechanism of hydrogen-induced softening and hardening in iron,” *Scripta Metallurgica*, vol. 21, pp. 319–324, mar 1987.
- [234] D. Caillard, “Kinetics of dislocations in pure Fe. part II. in situ straining experiments at low temperature,” *Acta Materialia*, vol. 58, pp. 3504–3515, may 2010.
- [235] D. Bombac, I. H. Katzarov, D. L. Pashov, and A. T. Paxton, “Theoretical evaluation of the role of crystal defects on local equilibrium and effective diffusivity of hydrogen in iron,” *Materials Science and Technology*, vol. 33, pp. 1505–1514, apr 2017.
- [236] Y. Hayashi and W. Shu, “Iron (ruthenium and osmium)-hydrogen systems,” *Solid State Phenomena*, vol. 73-75, pp. 65–114, aug 2000.
- [237] H. Kimizuka and S. Ogata, “Slow diffusion of hydrogen at a screw dislocation core in α -iron,” *Physical Review B*, vol. 84, jul 2011.
- [238] M. I. Mendelev, S. Han, D. J. Srolovitz, G. J. Ackland, D. Y. Sun, and M. Asta, “Development of new interatomic potentials appropriate for crystalline and liquid iron,” *Philosophical Magazine*, vol. 83, pp. 3977–3994, dec 2003.
- [239] H. Grabke and E. Riecke, “Absorption and diffusion of hydrogen in steels,” *Mater. technol.*, vol. 34, no. 6, p. 331, 2000.

References

- [240] M. Legros, G. Dehm, E. Arzt, and T. J. Balk, “Observation of giant diffusivity along dislocation cores,” *Science*, vol. 319, pp. 1646–1649, mar 2008.
- [241] W. Cai, V. V. Bulatob, J. Chang, J. Li, and S. Yip, “Periodic image effects in dislocation modelling,” *Philosophical Magazine*, vol. 83, pp. 539–567, jan 2003.
- [242] R. M. Nieminen, “From atomistic simulation towards multiscale modelling of materials,” *Journal of Physics: Condensed Matter*, vol. 14, pp. 2859–2876, mar 2002.
- [243] N. Reuter, A. Dejaegere, B. Maigret, and M. Karplus, “Frontier bonds in QM/MM methods: A comparison of different approaches,” *The Journal of Physical Chemistry A*, vol. 104, pp. 1720–1735, mar 2000.
- [244] V. Théry, D. Rinaldi, J.-L. Rivail, B. Maigret, and G. G. Ferenczy, “Quantum mechanical computations on very large molecular systems: The local self-consistent field method,” *Journal of Computational Chemistry*, vol. 15, pp. 269–282, mar 1994.
- [245] M. J. Field, P. A. Bash, and M. Karplus, “A combined quantum mechanical and molecular mechanical potential for molecular dynamics simulations,” *Journal of Computational Chemistry*, vol. 11, pp. 700–733, jul 1990.
- [246] N. Bernstein, C. Várnai, I. Solt, S. A. Winfield, M. C. Payne, I. Simon, M. Fuxreiter, and G. Csányi, “QM/MM simulation of liquid water with an adaptive quantum region,” *Phys. Chem. Chem. Phys.*, vol. 14, no. 2, pp. 646–656, 2012.
- [247] A. W. Duster, C.-H. Wang, C. M. Garza, D. E. Miller, and H. Lin, “Adaptive quantum/molecular mechanics: what have we learned, where are we, and where do we go from here?,” *Wiley Interdisciplinary Reviews: Computational Molecular Science*, vol. 7, p. e1310, apr 2017.
- [248] A. J. Fisher, “Methods of embedding for defect and surface problems,” *Journal of Physics C: Solid State Physics*, vol. 21, pp. 3229–3249, jun 1988.

References

- [249] I. H. Katzarov, “Embedding tight binding in bond order potential,” *Private communications*.
- [250] D. L. Pashov, “Electronic structure of certain titanium-aluminium superalloys: from first principles to bond order potentials,” *PhD Thesis*, nov 2012.
- [251] G. A. Baraff and M. Schluter *Journal of Physics C: Solid State Physics*, vol. 19, pp. 4383–4391, aug 1986.
- [252] “Archer uk national supercomputing service (<http://www.archer.ac.uk>),”
- [253] N. Bernstein, J. R. Kermode, and G. Csányi, “Hybrid atomistic simulation methods for materials systems,” *Reports on Progress in Physics*, vol. 72, p. 026501, jan 2009.
- [254] A. Togo and I. Tanaka, “First principles phonon calculations in materials science,” *Scripta Materialia*, vol. 108, pp. 1–5, nov 2015.
- [255] S. Klotz and M. Braden, “Phonon dispersion of BCC iron to 10 GPa,” *Physical Review Letters*, vol. 85, pp. 3209–3212, oct 2000.
- [256] P. Schelling, N. Yu, and J. Halley, “Self-consistent tight-binding atomic-relaxation model of titanium dioxide,” *Physical Review B*, vol. 58, no. 3, p. 1279, 1998.
- [257] E. Margine, A. Kolmogorov, M. Reese, M. Mrovec, C. Elsässer, B. Meyer, R. Drautz, and D. Pettifor, “Development of orthogonal tight-binding models for Ti-C and Ti-N systems,” *Physical Review B*, vol. 84, no. 15, p. 155120, 2011.
- [258] H. Amara, J.-M. Roussel, C. Bichara, J.-P. Gaspard, and F. Ducastelle, “Tight-binding potential for atomistic simulations of carbon interacting with transition metals: Application to the Ni-C system,” *Physical Review B*, vol. 79, no. 1, p. 014109, 2009.

References

- [259] S. Naka, A. Lasalmonie, P. Costa, and L. P. Kubin, “The low-temperature plastic deformation of α -titanium and the core structure of a-type screw dislocations,” *Philosophical Magazine A*, vol. 57, pp. 717–740, may 1988.
- [260] B. Barkia, J. Couzinié, S. Lartigue-Korinek, I. Guillot, and V. Doquet, “In situ TEM observations of dislocation dynamics in α titanium: Effect of the oxygen content,” *Materials Science and Engineering: A*, vol. 703, pp. 331–339, aug 2017.
- [261] Q. Yu, L. Qi, T. Tsuru, R. Traylor, D. Rugg, J. W. Morris, M. Asta, D. C. Chrzan, and A. M. Minor, “Origin of dramatic oxygen solute strengthening effect in titanium,” *Science*, vol. 347, pp. 635–639, feb 2015.
- [262] N. Chaari, D. Rodney, and E. Clouet, “Oxygen-dislocation interaction in titanium from first principles,” *Scripta Materialia*, vol. 162, pp. 200–203, mar 2019.